



HAL
open science

Atomic layer deposition on three dimensional silicon substrates for optical biosensors applications

Viktoriia Fedorenko

► **To cite this version:**

Viktoriia Fedorenko. Atomic layer deposition on three dimensional silicon substrates for optical biosensors applications. Chemical Sciences. Univ. Montpellier, 2017. English. NNT: . tel-01681308v1

HAL Id: tel-01681308

<https://hal.umontpellier.fr/tel-01681308v1>

Submitted on 11 Jan 2018 (v1), last revised 3 Sep 2018 (v2)

HAL is a multi-disciplinary open access archive for the deposit and dissemination of scientific research documents, whether they are published or not. The documents may come from teaching and research institutions in France or abroad, or from public or private research centers.

L'archive ouverte pluridisciplinaire **HAL**, est destinée au dépôt et à la diffusion de documents scientifiques de niveau recherche, publiés ou non, émanant des établissements d'enseignement et de recherche français ou étrangers, des laboratoires publics ou privés.



THÈSE

Pour obtenir le grade de
Docteur

Délivré par l'Université de Montpellier

Préparée au sein de l'école doctorale
Sciences Chimiques Balard (ED459)
Et de l'unité de recherche Institut Européen des
Membranes (IEM)

Spécialité : Chimie séparative matériaux et
procédés

Présentée par Fedorenko Viktoriia

**Atomic layer deposition on three
dimensional silicon substrates for
optical biosensors applications**

Soutenue le 23 octobre 2017 devant le jury composé de

M. Philippe MIELE , Professeur IEM, Montpellier	Examineur
M. Arunas RAMANAVICIUS , Professeur Vilnius University, Lithuania	Rapporteur
M. Fabien PICAUD , Chargé de Recherche University of Franche-Comté, Besançon	Rapporteur
M. Roman VITER , Chargé de Recherche University of Riga, Latvia	Examineur
M. Sebastien BALME , Assistant professor IEM, Montpellier	Directeur de these
M. Valentyn SMYNTYNA , Professeur Odessa National I.I. Mechnikov University, Ukraine	Directeur de these



Acknowledgments

This thesis is a result of the international collaboration between European Membrane Institute (IEM), University of Montpellier, Montpellier, France (host university) and Experimental Physics Department, physical faculty, Odessa National I.I. Mechnikov University, Ukraine (home university).

I am very thankful to my supervisor Prof. Valentyn Smyntyna and co-supervisors Dr. Roman Viter and Dr. Igor Iatsunskyi from the home university, thanks to their efforts to establish this collaboration, the opportunity to come and to do joint French-Ukrainian PhD became possible for me.

I would like to say great thanks to my director thesis Dr. Sebastien Balme and co-supervisor Dr. Mikhael Bechelany from the host university, who always were ready to help with any challenges, for their immense support, fruitful scientific discussions and for their great experience, which they shared with me during the whole period of my PhD study at IEM. Thanks to them the work atmosphere was really nice, and it was to pleasure to work at IEM, and this thesis became a result of this work.

I would like to show my gratitude to Dr. Vincent Rouessac, who provided the attestation for the utilization oxygen plasma reactor to me. I would like to thank all the team, who work at IEM.

I am very grateful to Dr. Jean-Marc Janot, Dr. Roman Viter and Dr. Igor Iatsunskyi for their effort to analyze all my results by epifluorescence microscopy, reflectance and photoluminescence spectroscopy, XRD, TEM, and Raman spectroscopy.

I am also thankful to the research staff from the NanoBioMedical Centre at Adam Mickiewicz University, Poznan, Poland (Dr. Igor Iatsunskyi, Dr. Mateusz Kempinski, Dr. Grzegorz Nowaczyk, Dr. Karol Załęski, and Prof. Stefan Jurga), University of Latvia, Riga (Dr. Donats Erts, and Dr. Roman Viter), and State Research Institute Center for Physical Sciences and Technology, Vilnius, Lithuania (Dr. Saulius Tumenas, Dr. Zigmantas Balevicius, and Prof. Arunas Ramanavicius), who participated in discussion of experimental results and writing of scientific papers.

I am very grateful to the reviewers of this thesis, Prof. Arunas Ramanavicius and Dr. Fabien Picaud, for their effort to revise this thesis and for their contribution to improve the work.

I am very thankful to the Erasmus Mundus Action 2, Backis program for the great opportunity to do my PhD in France, at IEM. The mobility gave me great experience not only in improving my scientific skills, but also in case of communication and work in team. It was

pleasure to discover Montpellier and the region Languedoc-Roussillon. I had really a pleasant and fruitful continuation of my mobility at IEM.

Abstract

This thesis manuscript presents the investigations and potential applications as a (bio)sensor platform of the conform thin layers of ZnO and/or Al₂O₃/ZnO nanolaminates, deposited by atomic layer deposition (ALD) on the various substrates. First, a study of the optical properties of ZnO thin films (20 and 50 nm) deposited by ALD technique on the large areas of ordered silicon nanowires (SiNWs), produced by combining nanosphere lithography and metal-assisted chemical etching, was performed. These methods allowed the morphology and the organization control of SiNWs on a large area. The detailed study of structural and optical properties of core-shell SiNWs/ZnO heterostructure was done by utilizing XRD, SEM, reflectance and photoluminescence spectroscopy, respectively. Integration of SiNWs arrays as core and ZnO as shell can have a strong impact on the development of sensing elements with improved properties. In the further investigations, ZnO films formed by ALD as an optical biosensor platform for the detection of Grapevine virus A-type proteins (GVA-antigens) were represented. The GVA-antigen detection was performed using the changes in the GVA related PL band behavior. The biosensor selectivity has been proved. The possibility to detect GVA-antigens without additional labels has been demonstrated. Thus, label free and sensitive photoluminescence based biosensor for GVA-antigens has been developed. Another part of our study is a specific control of protein anchoring by the development of multifunctional surface with large-scale array of polystyrene spheres (PSS), which produced by nanosphere lithography and further blocking the unspecific adsorption of protein on the surface of the PSS by PEG SAMs. The epifluorescence microscopy was used to confirm that after immersion of sample on target protein (avidin and anti-avidin) solution, the latter are specifically located on polystyrene sphere. These results are meaningful for exploration of devices based on large-scale nanoarray of PS spheres and can be used for detection of target proteins or simply to pattern a surface with specific proteins. Our research also includes the tuning of structural properties and the enhancement of electronic and optical properties of 1D PAN ZnO/Al₂O₃ nanolaminates designed by atomic layer deposition (ALD) and electrospinning. The structural and optical properties of Al₂O₃/ ZnO determined from the XPS, TEM, FTIR, XRD and PL analysis. The enhancement of electronic and optical properties would allow application in different fields such sensors and biosensors.

Table of Contents

Acknowledgments.....	ii
Abstract.....	iv
Table of Contents.....	v
List of figures.....	viii
List of tables.....	xiii
List of abbreviations.....	xiv
CHAPTER 1. GENERAL INTRODUCTION.....	1
1.1. Background.....	1
1.2. Research objectives.....	1
1.3. Study plan.....	2
CHAPTER 2. LITERATURE REVIEW.....	3
2.1. General introduction.....	3
2.2. Introduction to ALD: brief history.....	3
2.3. Reactants (precursors) for ALD.....	6
2.3.1. Synthesis of ZnO from DEZ and H ₂ O.....	9
2.3.2. Synthesis of Al ₂ O ₃ from TMA and H ₂ O.....	22
2.3.3. Al ₂ O ₃ /ZnO nanolaminates produced by ALD.....	31
2.4. Temperature window of the ALD process.....	37
2.5. ALD applications in nanotechnology.....	40
2.5.1. Applications of ALD coatings as active functional layers for different areas.....	40
2.6. ALD applications in sensors and biosensors.....	46
2.6.1. ALD applications for gas and optical sensors.....	46
2.6.2. ALD applications for biosensors.....	48
2.7. Advantages and limitations of ALD.....	57
2.8. Prospects of ALD.....	59
2.9. Conclusion.....	74
CHAPTER 3. LARGE-SCALE PROTEIN/ANTIBODY PATTERNING WITH LIMITING UNSPECIFIC ADSORPTION.....	75
3.1. Abstract.....	76
3.2. Introduction.....	76
3.3. Materials and methods.....	78
3.3.1. Materials.....	78

3.3.2. Protein labeling.....	79
3.3.3. Polystyrene sphere deposition on the Si/Cr/Au surface.....	79
3.3.4. Functionalization of nanoarrays.....	79
3.3.5. Microscopy.....	80
3.4. Results and discussion.....	80
3.5. Conclusion.....	86
CHAPTER 4. ZNO FILMS FORMED BY ATOMIC LAYER DEPOSITION AS AN OPTICAL BIOSENSOR PLATFORM FOR THE DETECTION OF GRAPEVINE VIRUS A-TYPE PROTEINS.....	88
4.1. Abstract.....	89
4.2. Introduction.....	89
4.3. Materials and Methods.....	91
4.3.1. ZnO thin film synthesis and characterizations.....	91
4.3.2. Chemical and physical characterizations of ZnO thin films.....	91
4.3.3. Functionalization of ZnO thin films.....	91
4.3.4. Evaluation of biosensor performance.....	92
4.4. Results and Discussion.....	92
4.4.1. Photoluminescence-based characterization of ZnO films deposited on Si substrate.....	93
4.4.2. Immobilization of anti-GVA on the surface of ZnO films.....	94
4.4.3. Performance of immunosensor.....	97
4.5. Conclusions.....	101
CHAPTER 5. OPTICAL PROPERTIES OF ZNO DEPOSITED BY ATOMIC LAYER DEPOSITION (ALD) ON SI NANOWIRES.....	102
5.1. Abstract.....	103
5.2. Introduction.....	103
5.3. Materials and methods.....	105
5.3.1. Materials.....	105
5.3.2. Synthesis of SiNWs.....	105
5.4. Synthesis of ZnO coating Si nanowires arrays.....	106
5.5. Characterization.....	107
5.6. Results and discussion.....	108
5.7. Conclusion.....	114
5.8. Supporting information.....	115

CHAPTER 6. ENHANCEMENT OF ELECTRONIC AND OPTICAL PROPERTIES OF ZNO/AL ₂ O ₃ NANOLAMINATE COATED ELECTROSPUN NANOFIBERS.....	116
6.1. Abstract.....	117
6.2. Introduction.....	117
6.3. Materials and methods.....	119
6.3.1. Electrospinning of PAN Nanofibers.....	119
6.3.2. ALD Deposition of Nanolaminates.....	119
6.3.3. Structural, Chemical, and Optical Characterizations.....	120
6.4. Results and discussion.....	121
6.4.1. Chemical and Structural Characterizations.....	121
6.4.2. Band Gap Energy Determination.....	126
6.4.3. Work Function Determination.....	126
6.4.4. Photoluminescence of PAN-Al ₂ O ₃ /ZnO Nanolaminates.....	129
6.5. Conclusion.....	131
6.6. Supporting information.....	132
CHAPTER 7. GENERAL CONCLUSION.....	136
7.1. General conclusion.....	136
SCIENTIFIC CONTRIBUTIONS.....	138
References.....	140

List of figures

Figure 2-1. Schematic illustration of one ALD reaction cycle [12].....	5
Figure 2-2. Cross-sectional SEM image of an Al ₂ O ₃ ALD film with a thickness of 300 nm on a Si wafer with a trench structure [24].....	6
Figure 2-3. Overview of the materials grown by ALD [25].....	7
Figure 2-4. a) SEM images of a cross section of ZnO ALD films deposited on Si substrates by 200, 500, and 1000 cycles; b) EDX; c) GIXRD of ZnO ALD films deposited by 100, 200, 500, and 1000 cycles; d) grain size and lattice strain in ZnO ALD films of different thickness [109].	19
Figure 2-5. a) Transmittance spectra, and b) band gap and Urbach energies of ZnO ALD films of different thickness [109].....	20
Figure 2-6. (a) SEM image of 1D ZnO NSs obtained with 300 s electrospinning time and coated with 50 cycles ALD ZnO at 100 °C. (b) XRD spectra of the obtained 1D NSs. (c) TEM image of 1D ZnO NSs [110].....	21
Figure 2-7. SEM images of ZnO thin film of 100 nm thickness and Al ₂ O ₃ /ZnO nanolaminates with different sequences (a), EDX of Al ₂ O ₃ /ZnO nanolaminates (b), and GIXRD of ZnO thin film of 100 nm thickness and Al ₂ O ₃ /ZnO nanolaminates with different sequences (c) [165].....	33
Figure 2-8. Blue square, roughness vs the film thickness of single layer of ZnO; black square, roughness vs the top layer of ZnO in the Al ₂ O ₃ /ZnO nanolaminates [165].....	34
Figure 2-9. Transmittance spectra of Al ₂ O ₃ /ZnO nanolaminates with different bilayer thickness and single ZnO thin film [165].....	34
Figure 2-10. Refractive index (real part) of Al ₂ O ₃ single thin film and Al ₂ O ₃ in Al ₂ O ₃ /ZnO nanolaminates with different bilayer thicknesses [165].....	35
Figure 2-11. Photoluminescence spectra of 50 nm thick single ZnO film and Al ₂ O ₃ /ZnO nanolaminates with different bilayer thicknesses [165].....	36
Figure 2-12. Schematic of possible behavior for the ALD growth per cycle versus temperature showing the “ALD” window [23].....	38
Figure 2-13. ALD growth per cycle for Al ₂ O ₃ (a) and ZnO (b) as a function of deposition temperature for reactor pressures of 2 and 760 Torr. The gas pulse conditions used for deposition are identified in the figure [92].....	39
Figure 2-14. Potential applications of ALD in various research fields [172].....	40
Figure 2-15. Cross-sectional view SEM image of a) macroporous silicon surface fabricated by MACE, b) mesoporous layer of PSi, c) mesoporous silicon surface (high magnification); d) cross-sectional view of as-prepared PSi/TiO ₂ nanostructure after 150 ALD cycles, e) plane view SEM image of the individual macropore in the PSi/TiO ₂ nanostructure after 150 ALD cycles, f)	

surface of the macropore in the P <i>Si</i> /TiO ₂ nanostructure (high magnification).....	41
Figure 2-16. SEM images of co-centric hollow nanotubes with different contents of ZnO and Al ₂ O ₃	43
Figure 2-17. Photodegradation of Methylorange by double, triple and quadruple cocentric nanotubes of ZnO/ZnAl ₂ O ₄	44
Figure 2-18. a,b) SEM images of a self-assembled monolayer of PS microspheres on a TCO substrate; a) tilted (458) low magnification and b) top view. The lower inset of (a) presents the digital image of the same sample. c,d) SEM images of an ordered hollow urchin-like structure of ZnO nanowires after the removal of PS; c) top view, the inset is a higher magnification, and d) tilted view (708). The inset is a high-magnification SEM image of the top of a nanowire grown at the top of the urchin-like structure. e,f) Cross-sectional SEM images of two urchin-like structures treated by FIB at different magnifications. g,h) High-magnification SEM images of a mechanically scratched structure for cross-section and internal surface observations, respectively [33].....	45
Figure 2-19. PL sensitivity test of ethanol vapor (150 ppm of ethanol) using 1D ZnO NSs obtained with 300 s electrospinning time and coated with 50 cycles ALD ZnO at 100 °C [110].....	47
Figure 2-20. Schematic process for hybrid membrane synthesis [4].....	56
Figure 2-21. Measurement scheme of ALD-based pore biosensor.....	56
Figure 2-22. Evolution of nanopore conductance with and without confined gA under NaCl symmetrical concentration in ALD-based pores with different diameters :(a) 10 nm pore (b) 6 nm pore and (c) 2 nm pore. Black squares and gray rounds show signal with and without gA in the pores, respectively [4].....	57
Figure 2-23. Atomic layer deposition reactor.....	61
Figure 2-24. Schematic diagram of set up of electrospinning apparatus [255].....	62
Figure 2-25. The scheme of floating-transferring technique.....	72
Figure 2-26. Scheme of processes involved in metal-assisted chemical etching.....	73
Figure 3-1. The schematic diagram of overall process for protein immobilization.....	81
Figure 3-2. Diameter of PS spheres as the function of the O ₂ plasma etching: The insets show PS spheres with different O ₂ plasma etching times: 1 (a), 5 (b), 10 (c) and 15 (d) min, respectively, as determined by SEM (scale bars 500 nm).....	82
Figure 3-3. Fluorescent images of Cy5-PEG-NHS-modified polystyrene spheres (the inset indicates a zoom).....	83

Figure 3-4. Fluorescent images of PS spheres functionalized with Biotin-PEG-NH ₂ (a) and mPEB (b) after addition of avidin (labeled with alexa fluor 647).....	84
Figure 3-5. Fluorescent images of PS spheres functionalized with Biotin-PEG-NH ₂ and avidin (unlabelled) after AntiAvidin*(labeled with Alexafluor 488).....	85
Figure 3-6. Fluorescent images of PS spheres functionalized with Biotin-PEG-NH ₂ and avidin (labeled with alexa fluor 647) after AntiAvidin (labeled with Alexafluor 488) addition recorded with FTIC cube (a) Cy5cube (b).....	86
Figure 4-1. a) SEM cross section images and b) GIXRD of ZnO ALD films deposited on Si substrates by different numbers of cycles (250 and 500).....	93
Figure 4-2. PL spectra of the ZnO samples with 57 and 110 nm layer thicknesses (a), PL spectra of anti-GVA deposited on glass (b).....	94
Figure 4-3. The scheme of PL based immunosensor.....	95
Figure 4-4. PL spectra of bare ZnO _{110nm} and ZnO _{110nm} functionalized with anti-GVA using 1/100 diluted initial anti-GVA solution (a), PL spectra (normalized intensity) of bare ZnO _{110nm} and ZnO _{110nm} functionalized with anti-GVA using solutions containing different concentrations of anti-GVA (b), PL intensity at 425 nm as a function of concentration of anti-GVA solutions used for the modification of ZnO-based substrates (c), absorbance spectra of anti-GVA deposited on glass from two solutions containing different concentrations of anti-GVA antibodies (d).....	96
Figure 4-5. The dependence of ZnO _{110nm} /anti-GVA/Ag ⁺ PL spectra (normalized intensity) after incubation of ZnO _{110nm} /anti-GVA-based immunosensor in different GVA-antigen concentrations containing specimens (specimens – Ag ⁺) (a), PL spectra dependence (normalized intensity) of ZnO _{110nm} /anti-GVA-based immunosensor under different concentrations of proteins separated from healthy vine grape plants, which not contains antigen for anti-GVA (specimens – Ag ⁻) (b).....	98
Figure 4-6. PL intensity at 425 nm as a function of GVA-antigen concentration in Ag ⁺ specimen, inset – biosensor response (<i>S</i>) as a function of GVA-antigen concentration in Ag ⁺ specimen (a), PL intensity at 425 nm as a function of different concentrations of proteins separated from healthy vine grapes, which not contain any antigen capable to bind with anti-GVA (specimens – Ag ⁻), inset - biosensor response (<i>S</i>) as a function of Ag ⁻ specimen concentration (b).....	99
Figure 5-1. The schematic diagram of overall process for the synthesis of SiNWs by combining MACE and NSL techniques.....	106
Figure 5-2. Diameter of PSS as the function of the O ₂ plasma etching: Inset consists of SEM images of the PSS as-prepared by floating transferring technique (a) and with different O ₂ plasma etching times: 1 (b), 5 (c) and 10 (d) min, respectively. And photographs of the	

monolayer of PSS on the water surface (e) and 2x2 cm ² silicon wafer covered with monolayer built from 1 μm PS latex beads by the mentioned before technique (f).....	108
Figure 5-3. SEM images of SiNWs (etching time is 5 min) and deposited by 50 nm ZnO.....	109
Figure 5-4. XRD spectra of SiNWs/ZnO with different thicknesses (20 and 50 nm) ZnO layers on SiNWs at 7 min etching.....	109
Figure 5-5. Cross-sectional view TEM image of ZnO-Si nanowires with different ZnO layer thicknesses: (a) 20 nm and (b) 50 nm.....	110
Figure 5-6. The Raman spectra of the Si NWs as-prepared (etching time is 7 min) and after deposition of ZnO 20 nm and 50 nm, respectively.....	111
Figure 5-7. The reflection spectra of the SiNWs prepared at different etching time (2, 5 and 7 min) and after deposited of ZnO 20 nm (a) and 50 nm (b), respectively.....	112
Figure 5-8. Band gap estimation of SiNWs covered with 20 (a) and 50 nm ZnO (b) by ALD, respectively.....	113
Figure 5-9. Photoluminescence spectra of SiNWs prepared at different etching time – 2, 5 and 7 minutes, and after ALD of 20 (a) and 50 nm ZnO (b), respectively.....	114
Figure SI5-1. Deconvolution of PL peaks spectra of SiNWs prepared at different etching time - 2, 5 and 7 minutes, and after ALD of 20 and 50 nm ZnO.....	115
Figure 6-1. TEM images of PAN-Al ₂ O ₃ /ZnO nanolaminates with different bilayers thicknesses: (a) 20 nm, (b) 10 nm, (c) 5.2 nm, and (d) 2 nm. Insets show the corresponding high-magnification images.....	121
Figure 6-2. (a) Absorbance spectra and (b) XRD spectra of PAN-Al ₂ O ₃ /ZnO nanolaminates at various bilayers thicknesses. Spectra are shifted for clarity.....	122
Figure 6-3. XPS survey spectra of ZnO/Al ₂ O ₃ nanolaminates coated polymer fiber with different bilayer thicknesses: (a) 1.2 nm, (b) 2 nm, (c) 5.2 nm, (d) 10 nm, and (e) 20 nm. Main core levels are labeled. Data are normalized to each O 1s peak maximum and separated vertically.....	123
Figure 6-4. XPS survey spectra of ZnO/Al ₂ O ₃ nanolaminates coated polymer fiber with different bilayers thicknesses: (a) 1.2 nm, (b) 2 nm, (c) 5.2 nm, (d) 10 nm, and (e) 20 nm. Main core levels are labeled. Data are normalized and separated vertically.....	124
Figure 6-5. O 1s energy-loss spectra for band gap determination of Al ₂ O ₃ of ZnO/Al ₂ O ₃ nanolaminate coated polymer fiber with different bilayers thicknesses.....	125
Figure 6-6. UPS results of work function measurements of ZnO/Al ₂ O ₃ nanolaminate coated polymer fiber with different bilayer thicknesses.....	126
Figure 6-7. Zone diagram of Al ₂ O ₃ /ZnO nanolaminate formation: (a) single layers before contact, (b) 1 bilayer, and (c) n bilayers.....	127

Figure 6-8. Room temperature PL spectra of PAN-Al ₂ O ₃ /ZnO nanolaminates with different bilayer thicknesses; Al ₂ O ₃ /ZnO nanolaminate 50 (2 nm × 2 nm) deposited on silicon was added for comparison.....	130
Figure SI6-1. EDS mapping of PAN-nanolaminates. Blue color – Zn and green color – Al.....	132
Figure SI6-2. TEM image of the end face of PAN fiber coated by the nanolaminates.....	133
Figure SI6-3. De-convolution of XPS peaks using CasaXPS software.....	134
Figure SI6-4. De-convolution of PL peaks spectra of PAN-Al ₂ O ₃ /ZnO nanolaminates with different bilayers thicknesses.....	135

List of tables

Table 2-1. Different names of ALD [12].....	4
Table 2-2. ALD processes reported for the growth of ZnO thin films. The growth per cycle (GPC) values displayed in the table are from inside the ALD window; if no ALD window is reported, representative values from the entire tested temperature range are displayed instead (The table is adopted from [45]).....	11
Table 2-3. ALD processes reported for the growth of Al ₂ O ₃ thin films.....	24
Table 2-4. Band gap of Al ₂ O ₃ /ZnO nanolaminates with different bilayer thicknesses and ZnO single thin film of 50 nm thickness [165].....	35
Table 2-5. Deposition sequences of Al ₂ O ₃ and ZnO cycles on the PAN nanofibers.....	42
Table 2-6. ALD for biosensors applications.....	50
Table 2-7. Selected properties of the most common noble metal oxides.....	60
Table 2-8. The process list for the ZnO ALD.....	62
Table 2-9. The experimental tools used for the study of the samples prepared at the present thesis.....	64
Table 5-1. Band gap of SiNWs covered with 20 and 50 nm ZnO.....	113
Table 6-1. Al ₂ O ₃ /ZnO Ultrathin Nanolaminates Synthesis by ALD.....	120
Table 6-2. Electronic parameters of Al ₂ O ₃ /ZnO Ultrathin Nanolaminate Synthesis by ALD...	127

List of abbreviations

ALD	Atomic layer deposition
ALE	Atomic layer epitaxy
Al ₂ O ₃	Aluminum Oxide
BEL	Band-edge laser
BSA	Bovine serum albumin
CB	Conduction band
CNT	Carbon nanotubes
CVD	Chemical vapor deposition
DEZn	Diethylzinc
DLE	Deep level emission
DMF	Dimethylformamide
DMZn	Dimethylzinc
EDX	Energy-dispersive X-ray spectroscopy
ELISA	Enzyme linked immune-sorbent assay
FET	Field effect transistors
FTIR	Fourier-transform infrared
FWHM	Full width half maximum
HF	Hydrofluoric acid
MACE	Metal-assisted chemical etching
NBE	Near band emission
NSL	Nanosphere lithography
GIXRD	Grazing Incidence X-ray Diffraction
GMRF	Guided Mode Resonance Filter
GPC	Growth per cycle
GVA	Grapevine Virus A-type
IC	Integrated circuits
SAMs	Self-assembled monolayers
SDS	Sodium dodecyl sulfate
SEM	Scanning electron microscopy
SiNWs	Silicon nanowires
SRI	Surrounding refractive index
TDMAT	Tetradimethylaminotitanium
TEM	Transmission electron microscopy

TFEL	Thin-film electroluminescent flat-panel displays
TMA	Trimethylaluminum
ZnO	Zinc Oxide
PAN	Polyacrylonitrile
PEG	Polyethylene glycol
PL	Photoluminescence
PSS	Polystyrene spheres
PVD	Physical vapor deposition
UPS	UV photoelectron spectroscopy
VB	Valence band
VOC	Volatile organic compound
XPS	X-ray photoelectron spectroscopy
XRD	X-ray diffraction analysis

CHAPTER I

General introduction

1.1. Background

Atomic layer deposition (ALD) is an attractive method to deposit thin films for advanced technological applications such as microelectronics and nanotechnology [1]. ALD is generally well-suited for the deposition of oxide thin films and overlayers for various applications [2]. The oxides may be insulating, semiconducting, conducting or even superconducting. They can also be used as catalysts, light-emitting phosphors, or gas sensors. Among various methods used to form ZnO thin films, atomic layer deposition (ALD) is an innovative technique, which allows the deposition of ultrathin metal oxide films with controlled thickness, grain size, chemical composition, texture, surface morphology and defect concentration. The mentioned structural parameters make a strong impact on optical, electrical and mechanical properties [3].

Different studies report the growth of Al₂O₃/ZnO nanolaminates as well as the incorporation of Al doping in ZnO using ALD [4-8]. Using ALD methods, ZnO grows as a conducting, polycrystalline film with a rough surface topography resulting from the individual crystallites. In contrast, Al₂O₃ grown by ALD is an excellent insulating, amorphous film that deposits with high conformality. The wide disparity in physical properties between ZnO and Al₂O₃ suggests that nanolaminates formed from alternating ZnO/Al₂O₃ layers may possess properties that span a wide range in surface roughness and conductivity. The advanced properties of the nanolaminates such as biocompatibility, easy surface modification, and enhanced photoluminescence at room temperature could provide good capacity for the development of nanolaminates-based optical sensors and biosensors.

1.2. Research objectives

The objectives of this study are the following:

- Optimization of the procedures for the preparation of silicon nanowires (SiNWs) by combining metal-assisted chemical etching (MACE) and nanosphere lithography (NSL) to fabricate large areas of ordered SiNWs. After the properties of the SiNWs will be improved by utilizing ALD for the deposition of ZnO thin films. Control of the morphology and organization of SiNWs on a large area by the above-mentioned techniques.
- Development of the novel, label free and sensitive photoluminescence based biosensor for GVA-antigens. The direct immobilization of anti-GVA antibodies was performed on the ZnO surface and resulted in the formation of biosensing structure (ZnO/anti-GVA)
- Specific control of protein anchoring by the development of multifunctional surface with large-scale array of polystyrene spheres (PSS), which produced by nanosphere

lithography and further blocking the unspecific adsorption of protein on the surface of the PSS by PEG SAMs.

- Tuning of structural properties and the enhancement of electronic and optical properties of 1D PAN ZnO/Al₂O₃ nanolaminates designed by atomic layer deposition (ALD) and electrospinning. The enhancement of electronic and optical properties will allow application in different fields such sensors and biosensors.

1.3. Study plan

To achieve the above objectives, the following topics were investigated:

- Overview of the recently investigations in the area of atomic layer deposition (ALD) of ZnO, Al₂O₃, and Al₂O₃/ZnO nanolaminates, and potential applications of ALD in various research fields (Chapter 2).
- Study of the optical properties of ZnO deposited by atomic layer deposition (ALD) on Si nanowires (Chapter 3).
- ZnO films formed by ALD as an optical biosensor platform for the detection of Grapevine Virus A-type Proteins (Chapter 4).
- Large-scale protein/antibody patterning with limiting unspecific adsorption (Chapter 5).
- Enhancement of electronic and optical properties of ZnO/Al₂O₃ nanolaminate coated electrospun nanofibers (Chapter 6).

CHAPTER II

Literature review

2.1. General introduction

ALD is known as a unique among thin-film deposition techniques, offering conformal deposition of ultra-thin films on high-aspect-ratio nanostructures at temperatures below 100 °C. The recently investigations in the area of ALD of ZnO, Al₂O₃, and Al₂O₃/ZnO nanolaminates, and potential applications of ALD in various research fields are overviewed in this chapter. As ALD is a thermally activated process in order to produce self-limiting reactions on the surface of a substrate, the processing temperature range for ALD - “ALD window” is represented as well. In this chapter, the key features of ALD are described. In summary, the collected information about ALD technology is emphasized with the advantages and limitations. Finally, at conclusion part of this chapter the prospects of the ALD are presented. With devices becoming ever smaller and increasingly structured into complex three dimensional shapes, the need for controllable and conformal thin films has never been greater. ALD, with its sequential self-limiting reactions, is able to meet these demands in one of the most effective methods possible.

2.2. Introduction to ALD: brief history

Atomic layer deposition (ALD), a thin film deposition process, was first emerged as atomic layer epitaxy (ALE) and introduced in 1970s by Suntola and Antson in Finland [9]. The motivation for the development of ALD was the desire to make thin-film electroluminescent (TFEL) flat-panel displays.

From the beginning of ALD development, its applications were limited to the deposition of epitaxial layers of II–VI or III–V semiconductors, mainly for display devices, as inherently low growth rate was considered as a major obstacle for other applications [10, 11].

The transition from ALE to ALD occurred as a result of the fact that most films grown using sequential, self-limiting surface reactions were not epitaxial to their underlying substrates. Moreover, amorphous films were most preferred for dielectric and diffusion barrier applications. Consequently, the use of ALD grew in preference and now dominates with the practitioners in the field.

In Table 2-1 some mostly used names of ALD technique are presented. The name “atomic layer deposition (ALD)” dates back to the early 1990s.

Since the mid-1990s, an increasing interest to ALD has originated from the silicon-based microelectronics. This increase is a consequence of the ever decreasing device dimensions and increasing aspect ratios in the integrated circuits (IC), which require the introduction of new materials and thin-film deposition techniques. In addition, the required thickness of the films has

decreased, in many cases, to the order of a few nanometers and therefore the main drawback of ALD, the low deposition rate, is becoming less important.

Currently, ALD is considered as one of the most promising thin film deposition techniques for enabling nanoscale device fabrication [1]. The benefits of ALD include thickness control at the atomic scale, production of highly conformal films, low temperature growth, and wide-area uniformity. Due to these benefits, ALD is finding ever more applications.

Distinguished from other deposition techniques such as chemical vapor deposition (CVD), physical vapor deposition (PVD), and other solution-based methods, ALD as a chemical vapor method operates with a unique mechanism relying on two gas-solid half-reactions to produce an ultimate material [2]. The reactions of ALD feature the characteristics of surface-controlled and self-terminating nature. In return, ALD performs the deposition of films in a layer-by-layer mode and it is especially superior in controlling films at the atomic level. As a result, ALD provides the deposited films with excellent uniformity and unrivalled conformality. In essence, ALD works with a temperature lower than the decomposition of the used precursors typically lower than 400 °C even down to room temperature. In addition, ALD requires no catalysts and has no needs on solvents. All the aforementioned characteristics contribute ALD to be a unique but precise deposition technique.

Table 2-1. Different names of ALD [12].

Name	Abbreviation	Refs.
Atomic layer deposition	ALD	[13]
Atomic layer epitaxy	ALE	[9]
Atomic layer evaporation	ALE	[14]
Atomic layer growth	ALG	[15]
Chemical assembly		[16]
Molecular deposition		[17]
Molecular lamination		[18]
Molecular layer epitaxy	MLE	[19]
Molecular layering	ML	[20]
Molecular stratification		[21]

In an ideal ALD growth process, different precursors are pulsed alternately onto the substrate surface in different steps. The non-reacted reactants and the reaction by-products are removed by the following inert gas purge step. This feature keeps the precursors strictly

separated from each other in the gas phase. As a result, there is only the reaction of a gaseous compound reactant with the solid surface in the ALD process, which is defined as the gas-solid reaction. A general ALD process is illustrated in Figure 2-1. The typical two-reactant ALD process is characteristically consists of four steps: Pulse step of the first reactant (A) and subsequent self-terminating gas-solid reaction. Then the second step is the purge step with an inert carrier gas (typically N₂ or Ar) to remove excess reactants and gaseous reaction by-products. Pulse step of the second reactant (B) and subsequent self-terminating gas-solid reaction. And the last step is purge of the unreacted precursor B and of the byproducts. During each reaction cycle a fixed amount of material having a corresponding nominal thickness is deposited, known as growth per cycle (GPC), due to the self-limiting nature of the reactions.

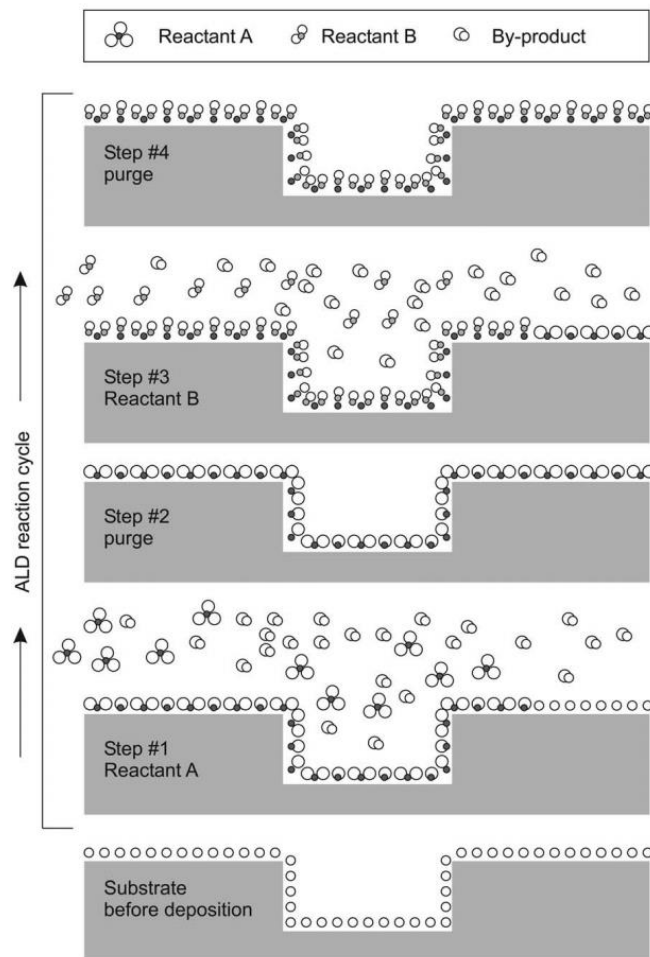


Figure 2-1. Schematic illustration of one ALD reaction cycle [12].

Because the GPC is fixed, a desired film thickness can be deposited simply by adjusting the number of reaction cycles. As the reactions are self-terminating, no tuning of reactant dose or flux is necessary provided that the dose is sufficient for the complete saturation of surface sites.

This surface control is responsible for ALD's inherent characteristics of extreme film thickness controllability and uniformity.

In addition, ALD has the capability to coat complex shapes with a conformal material layer of high quality, as illustrated by the cross-sectional scanning electron microscopy (SEM) image in Figure 2-2. Furthermore, ALD can make accuracy thickness control, facile doping, large area uniformity, and pinhole free film [22]. ALD processes have been developed to manufacture many types of solid inorganic materials for a wide range of applications, such as oxides, nitrides, sulphides, selenides, tellurides and pure elements (Figure 2-3). Among these materials, oxides have been the type most often investigated. Typically, Al_2O_3 can be used as a dielectric, protective or ion barrier layer in electronic and optoelectronic devices [12].

Over the past ten years, research advances have expanded the use of ALD technology to include deposition of films on materials for microelectronics applications (e.g. large area silicon substrates), materials for medical device applications and biologically derived materials. A variety of materials, such as metal oxides, metal nitrides, metal sulphides, metals, polymers and inorganic-organic hybrid materials, have been successfully grown using ALD [23].

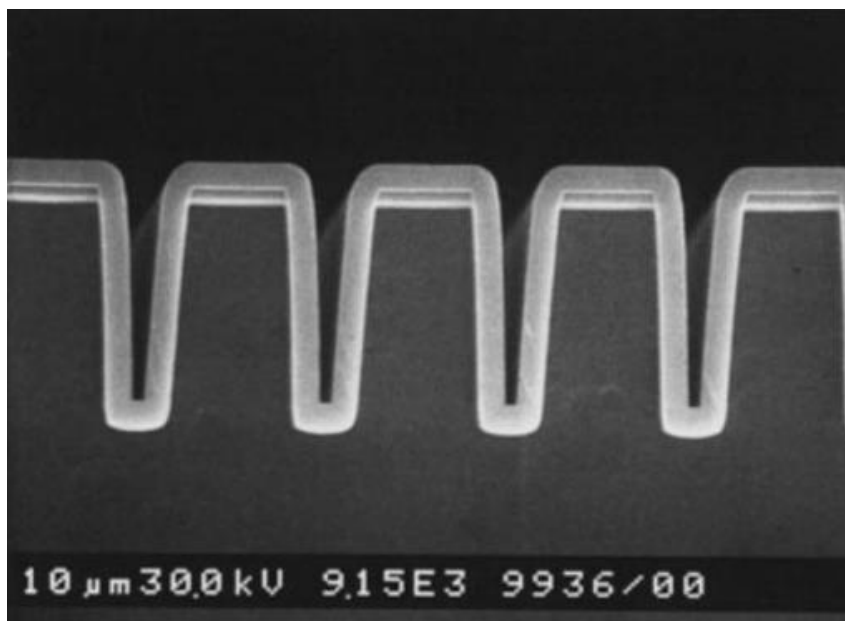


Figure 2-2. Cross-sectional SEM image of an Al_2O_3 ALD film with a thickness of 300 nm on a Si wafer with a trench structure [24].

2.3. Reactants (precursors) for ALD

Precursor chemistry plays an important role in a successful design of an ALD process [22]. Several requirements are taken into consideration when choosing a chemical precursor. They must be volatile to produce a high enough vapor pressure (at least above 0.1 Torr) so they can

easily be transported into the reaction zone of the process chamber. However, many precursors are low vapor liquids or even solids at room temperature and therefore require higher temperatures to raise their vapor pressure. The evaporating pressure of the precursor is an important parameter. The temperature will affect the precursor vapor pressure, which will influence the dose optimization together with pulsing length and methods. Due to various precursor states such as gas, solid and liquid, different pulsing methods should also be considered. Gas precursors are easy to pulse to the reactor. Liquid and solid precursor can be heated to achieve higher vapor pressure. If the vapor pressure is not possible to increase with raising temperature, different pulse methods can be applied to improve the precursor dose. Precursors must be thermally stable in that they do not decompose in the source or on the substrate. Reactions due to the decomposition of reactants are likely to produce non-self-limited reaction with higher growth rates and possible film contamination of C, H, N or halide atoms depending on the precursor used.

Precursors also must react rapidly and aggressively with surface groups from the previous exposure and not with its own adsorbates in order to achieve a saturated self-limiting surface in a short time (usually < 1s). The aggressive reaction requirement is contrary to traditional CVD precursors.

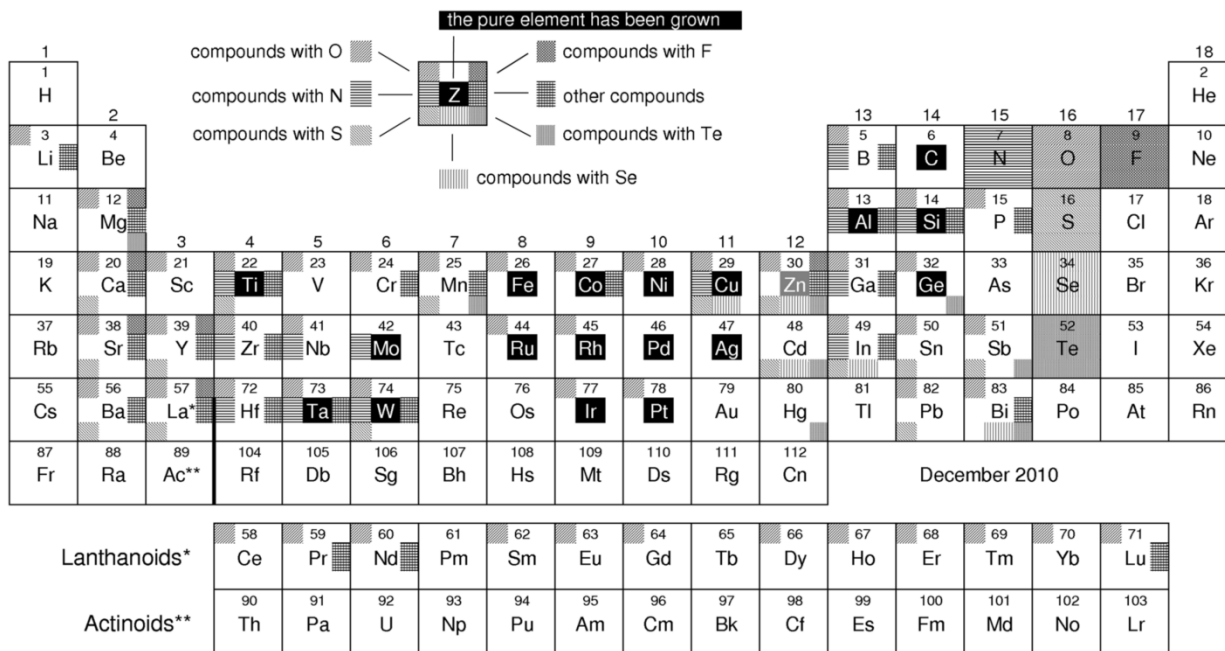


Figure 2-3. Overview of the materials grown by ALD [25].

It is also preferable if the reactants are small in size to avoid reduced surface coverage due to steric hindrance. Finally, the choice of reactants has economic implications, as some are

expensive and synthesis can be time consuming. Unfortunately, there are no perfect reactants, so the choice of reagents typically involves making trade-offs between cost, availability, safety, volatility and reactivity.

Different precursors have been employed for the deposition of an oxide ALD chemistry including metal halides and several types of organometallics for the metal containing precursor and water, O₂ plasma, and ozone for some of the more common oxidizers. Halides have been the most widely studied of all the metal containing precursors, however, their main drawback lies in the corrosive nature of the HCl byproduct that is often produced causing etching of the deposited films and the encasing reactor. Several organometallic precursors have been investigated including metal alkyls, amides, alkoxides, and cyclopentadienyls, however, growth rates are usually low due to the steric hindrance associated with the large ligands attached to the molecules.

Typical metal precursors used in ALD are halides, especially chlorides, alkyl compounds, and alkoxides. Organometallic compounds, such as cyclopentadienyl complexes and alkyl and silyl amides have gained more attention recently. The nonmetal precursors used are: water, hydrogen peroxide, and ozone for oxygen; hydrides for chalcogens; ammonia, hydrazine, and amines for nitrogen; hydrides for group V elements.

The precursors should be safe and easy to handle, preferably non-toxic and noncorrosive towards the substrate and the reactor materials. For industrial use, price is also an issue. High purity is needed for some applications. While it in principle does not matter whether the reactants are gases, liquids, or solids at room temperature, the phase affects the reactor construction: Solids and low-vapor-pressure liquids require special source designs. The list of preferred properties is long, and it is evident that not many reactants in actual use fulfill all the criteria. Compromises often need to be made regarding, for example, the reactivity and corrosiveness of the by-products

One of the major advantages in ALD precursor chemistry compared with CVD, for instance, is the fact that because ALD is based on surface saturation exact precursor dosage is not needed. The only requirement is that there are enough precursor molecules to cover the adsorption sites on the surface; the excess will be blown away by the inert gas purge. This makes it possible to use *in situ*-generation of the precursors and thus have a fresh supply of otherwise instable precursor molecules onto the substrate surface.

2.3.1. Synthesis of ZnO from DEZ and H₂O

In general, metal oxides offer a variety of interesting properties for technical applications. The oxides may be insulating, semiconducting, conducting or even superconducting. They can also be used as catalysts, light-emitting phosphors, or gas sensors. By doping, the properties can be changed or enhanced. ALD is generally well-suited for the deposition of oxide thin films and overlayers for various applications [2].

Zinc oxide (ZnO) has been widely studied since 1935 [26]. ZnO is a semiconductor with a wide band gap (3.37 eV) and large exciton binding energy (60 meV), making it an attractive optoelectronic material with unique optical, electronic, catalytic and photoelectrical properties [27]. It is one of few oxides showing confinement effects in an accessible size range [28].

Many of the technological applications of ZnO thin films rely on producing films with high optical quality. ZnO has been commonly used for different applications, such as optical coatings [29], light emitting diodes [30], sensors [31], photovoltaics [32-34], and biosensors [35]. Recent approaches in nanotechnology allow one to fabricate ZnO nanostructures with high surface-to-volume aspect ratios, which is significantly important for sensor and biosensor applications.

First ALD process of ZnO was based on zinc acetate and H₂O [36]. More recently, processes based on zinc alkyls (dimethylzinc = DMZn and diethylzinc = DEZn) have been developed [37]. Because of the reactivity of the organometallics, the processes based on DMZn and DEZn and water can be operated at relatively low temperatures (below 200 °C) [38].

Zinc oxide as deposited by ALD is a polycrystalline n-type semiconductor material that despite having a large band gap possesses low resistivity [39, 40].

The most studied precursor combination for ZnO ALD is DEZ–water. The deposition temperature range lies from around 100 to 350°C. Zinc oxide thin films are typically crystalline even when deposited at low temperature. Amorphous zinc oxide films can be deposited only as very thin films on certain substrate materials [41-43].

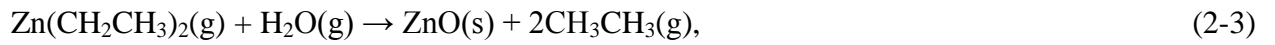
ALD can be used to deposit ZnO by subsequently exposing a substrate to DEZ, Zn(C₂H₅)₂ and deionized water vapor.



where asterisks denote surface species [44]. Between the exposure to the precursor and the deionized water vapor, purge steps are applied to remove excess gases and reaction products. Each ALD cycle consists therefore of a precursor step, a purge step, a deionized water vapor step, and another purge step. A Zn-O Lewis acid-base complex is formed during each half

reaction, with ethane formed as a reaction byproduct with the surface alternating between being ethyl-terminated and hydroxyl terminated.

The simplified DEZ/H₂O reaction can be generalized with the following reaction equation:



where (g) is the gas phase of byproducts.

In the Table 2-2 some overview of the ZnO deposited by ALD technique is demonstrated.

Table 2-2. ALD processes reported for the growth of ZnO thin films. The growth per cycle (GPC) values displayed in the table are from inside the ALD window; if no ALD window is reported, representative values from the entire tested temperature range are displayed instead (The table is adopted from [45])

Zn precursors	O precursors	Substrates	Deposition T (°C)	ALD window (°C)	GPC (Å/cycle)	References
Zn(CH ₃ COO) ₂	H ₂ O	Soda glass	290–360	-	0.9-1.2	[36]
Zn(CH ₃ COO) ₂	H ₂ O	Sapphire (0001)	350	-	0.4-3.0	[46]
Zn, ZnCl ₂ , Zn(CH ₃ COO) ₂	O ₂ , H ₂ O	Sapphire, Si, GaN/sapphire, soda glass	480-500 300-360	-	-	[47]
Zn(CH ₃ COO) ₂	H ₂ O	Sapphire, glass	280-400	-	0.8-4.0	[48]
Zn(CH ₃ COO) ₂ , Zn(CH ₃) ₂ ,	H ₂ O	-	60-350	280-350, 80-150,	1.8	[49]

Zn(C ₂ H ₅) ₂				100-180		
Zn(CH ₃) ₂ , Zn(C ₂ H ₅) ₂	H ₂ O	Soda glass	120-350	-	0.5-2.5	[37]
Zn(C ₂ H ₅) ₂	H ₂ O	Borosilicate	90-235	105-165	2.7	[50-52]
Zn(C ₂ H ₅) ₂	H ₂ O	PET, glass, sapphire, Si	100-210	-	1.4-1.9	[53]
Zn(C ₂ H ₅) ₂	H ₂ O	Au, glass	RT-220	130-180	2.2	[38]
Zn(C ₂ H ₅) ₂	H ₂ O	Si (100)	100-220	-	2.0	[8]
Zn(C ₂ H ₅) ₂	H ₂ O, O ₂	Al ₂ O ₃ - coated Si	180	-	2.06	[54]
Zn(C ₂ H ₅) ₂	O ₃	SiO ₂ /Si	230-300	230-250	1.9	[55]
Zn(C ₂ H ₅) ₂	O ₂	Si	180, 270	-	-	[56]
Zn(C ₂ H ₅) ₂	O ₂ plasma	Si (100)	75-150	100-150	2.2	[57]

Zn(C ₂ H ₅) ₂	H ₂ O	Sapphire (0001)	100-250	130-180	2.7	[58]
Zn(C ₂ H ₅) ₂	H ₂ O	Glass, Si (100)	90-200	100-180	1.9	[59]
Zn(C ₂ H ₅) ₂	H ₂ O	Si (100)	70-350	70-200	1.9	[60]
Zn(C ₂ H ₅) ₂	N ₂ O	Sapphire (0001)	600	-	-	[61]
Zn(C ₂ H ₅) ₂	H ₂ O	Glass	140	-	2.5-2.7	[62]
Zn(C ₂ H ₅) ₂	H ₂ O	Si (100)	60-300	125-150	1.9	[63]
Zn(C ₂ H ₅) ₂	O ₂ plasma	ZnO- coated Si	150	-	-	[64]
Zn(CH ₃) ₂ , Zn(C ₂ H ₅) ₂	H ₂ O	Glass	90-270	120-170, 130-170	1.4, 1.3	[65]
Zn(CH ₃) ₂ , Zn(C ₂ H ₅) ₂	H ₂ O	Glass, Si, sapphire, GaAs	60-250	110-180	1.8, 1.9	[66]

Zn(CH ₃) ₂	O ₂ plasma	Si	25-120	85-120	2.9	[67]
Zn(C ₂ H ₅) ₂	N ₂ O	Sapphire (0001)	250-340	290-310	2.6-2.7	[68, 69]
Zn(C ₂ H ₅) ₂	N ₂ O	Sapphire (11-20)	600	-	-	[70]
Zn(C ₂ H ₅) ₂	H ₂ O plasma	Si (100), quartz	100-300	150-200	2.0-2.2	[71]
Zn(C ₂ H ₅) ₂	H ₂ O	Glass, Si	120-240	120-150	1.8	[72]
Zn(C ₂ H ₅) ₂	H ₂ O	Glass, Si, GaN/Al ₂ O ₃	100-300	100-200	-	[73]
Zn(C ₂ H ₅) ₂	H ₂ O	PVP/Si	80-140	-	2.0	[74]
Zn(C ₂ H ₅) ₂	H ₂ O	Borosilicat e	100-250	-	1.2	[75]
Zn(C ₂ H ₅) ₂	H ₂ O	Si, SiO ₂ /Si	150-400	-	0.5-2.0	[76]
Zn(C ₂ H ₅) ₂	O ₂ plasma	Glass, Si	100-300	200-250	2.8	[77]

Zn(C ₂ H ₅) ₂	H ₂ O	Si (100)	25-200	-	-	[78]
Zn(C ₂ H ₅) ₂	O ₂ plasma, H ₂ O	Si (100)	100	-	1.5-2	[79, 80]
Zn(C ₂ H ₅) ₂ , Zn(CH ₃) ₂	H ₂ O	Glass, Si	100-200	120-170	2.1, 2.7	[81]
Zn(C ₂ H ₅) ₂	H ₂ O	GaAs	180	-	1.8	[82]
Zn(C ₂ H ₅) ₂	H ₂ O	Si (100)	RT-140	-	0.8-2.2	[83]
Zn(C ₂ H ₅) ₂	H ₂ O	Glass, Si, GaN	100-240, 250-300	-	-	[84]
Zn(C ₂ H ₅) ₂	O ₂ , H ₂ O	Si (111)	150-300	190-210, 200-225	4.8, 3.0	[85]
Zn(C ₂ H ₅) ₂	H ₂ O	Si (100)	80-240	100-160	2.3	[86]
Zn(C ₂ H ₅) ₂	H ₂ O	6H-SiC	180-300	-	-	[87]
Zn(C ₂ H ₅) ₂	H ₂ O	Si (001)	25-150	-	1.2-1.6	[88]
Zn(C ₂ H ₅) ₂	H ₂ O	SiO ₂ /Si, MgO	70-190	130-170	2.35	[89]

Zn(C ₂ H ₅) ₂	H ₂ O	Al ₂ O ₃ /Si	200	-	-	[90]
Zn(C ₂ H ₅) ₂	H ₂ O	Glass, Si	75-250	200-250	1.8	[91]
Zn(C ₂ H ₅) ₂	H ₂ O + O ₂ plasma	Si	40-200	110-160	1.7, 2.5	[92]
Zn(C ₂ H ₅) ₂	H ₂ O	Glass, Si (100)	200	-	1.5	[93]
Zn(C ₂ H ₅) ₂	H ₂ O	Si (111)	150, 300	-	1.8-2.1	[94]
Zn(C ₂ H ₅) ₂	H ₂ O	Si, GaN, graphene sapphire	150-300	-	-	[95]
Zn(C ₂ H ₅) ₂	O ₂ plasma	SiO ₂ /Si	150	-	-	[96]
Zn(C ₂ H ₅) ₂	H ₂ O plasma	SiO ₂ /Si	100-250	100-250	1.1	[97]
Zn(C ₂ H ₅) ₂	H ₂ O	Glass	50-200	-	0.7-1.9	[98]
Zn(C ₂ H ₅) ₂	H ₂ O	Polyacrylo nitrile (PAN)	50-130	-	2	[31]

Zn(C ₂ H ₅) ₂	H ₂ O	nanofibers Si (100)	200	-	2.2	[99]
Zn(C ₂ H ₅) ₂	H ₂ O	graphene powders	120	-	2	[100]
Zn(C ₂ H ₅) ₂	H ₂ O	Soda lime glass (SLG)	100-130	-	2	[101]
Zn(C ₂ H ₅) ₂	H ₂ O	Si (100), glass, optical fibers	100	-	2.5	[102]
Zn(C ₂ H ₅) ₂	H ₂ O	Anodic Aluminum Oxide (AAO) templates, polyvinyl acetate (PVA)	200 80	-	1	[103]

Zn(C ₂ H ₅) ₂	N ₂ O	nanowires Si (001) (a-SiO ₂), Al ₂ O ₃ (001) (c- Al ₂ O ₃),	250	-	-	[104]
Zn(C ₂ H ₅) ₂	H ₂ O	Si, quartz, PEN	40, 80, 120	-	0.94	[105]
Zn(C ₂ H ₅) ₂	H ₂ O	Si (100)	280	-	-	[106]
		Si (100), fused quartz (SiO ₂)	200	-	1.6	[107]
Zn(C ₂ H ₅) ₂	H ₂ O	Si	100	-	2	[108]

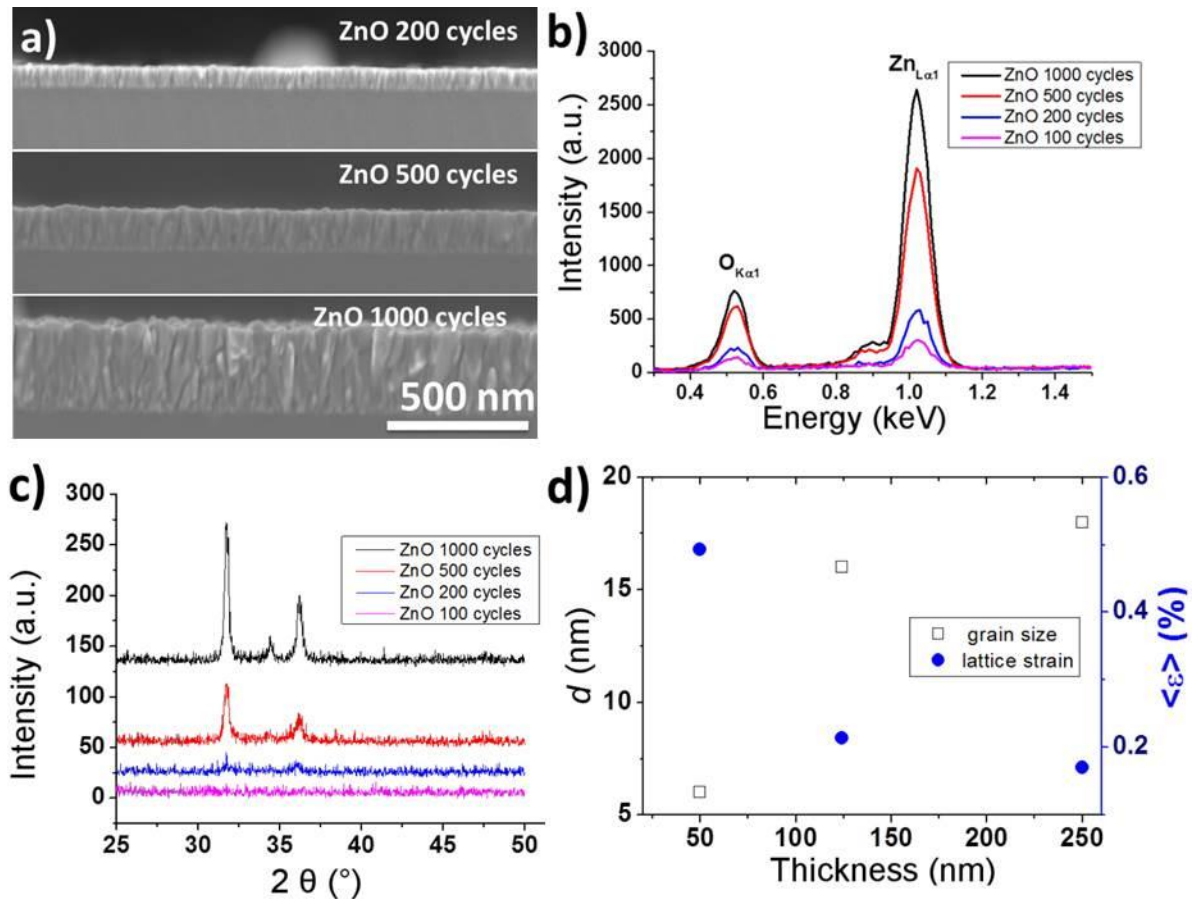


Figure 2-4. a) SEM images of a cross section of ZnO ALD films deposited on Si substrates by 200, 500, and 1000 cycles; b) EDX; c) GIXRD of ZnO ALD films deposited by 100, 200, 500, and 1000 cycles; d) grain size and lattice strain in ZnO ALD films of different thicknesses [109].

Chaaya *et al.* [109] reported a study of transmittance and photoluminescence spectra on the growth of oxygen-rich ultra-thin ZnO films prepared by atomic layer deposition. They observed the structural transition from an amorphous to a polycrystalline state upon increasing the thickness. Figure 2-4a demonstrates the SEM images which indicate a conformal coating of ZnO thin films at 200, 500 and 1000 cycles deposited by ALD on the Si substrates. A rough surface of columnar growth of the films developed with an increase of the film thickness.

EDX measurements were done for the evaluation of ZnO films (Figure 2-4b). An analysis of the results show a monotonous decrease of the O/Zn ratio with a growth of the film while remaining greater than unity, which points to an oxygen-rich stoichiometry of the studied samples.

GIXRD diffraction patterns of thin ZnO films are shown in Figure 2-4c. The structure of ZnO ALD films strongly depends on the thickness. The ZnO samples obtained by 100 cycles were amorphous, had a smooth surface, and did not exhibit any XRD peaks. The increase of the

film thickness was assisted by the growth of vertically oriented columns with well-defined boundaries, an improvement of the crystalline structure (narrowing of XRD peaks), a crystalline growth and an alleviation of lattice strain, and an enhancement of the surface roughness and the texture coefficient (Figure 2-4d).

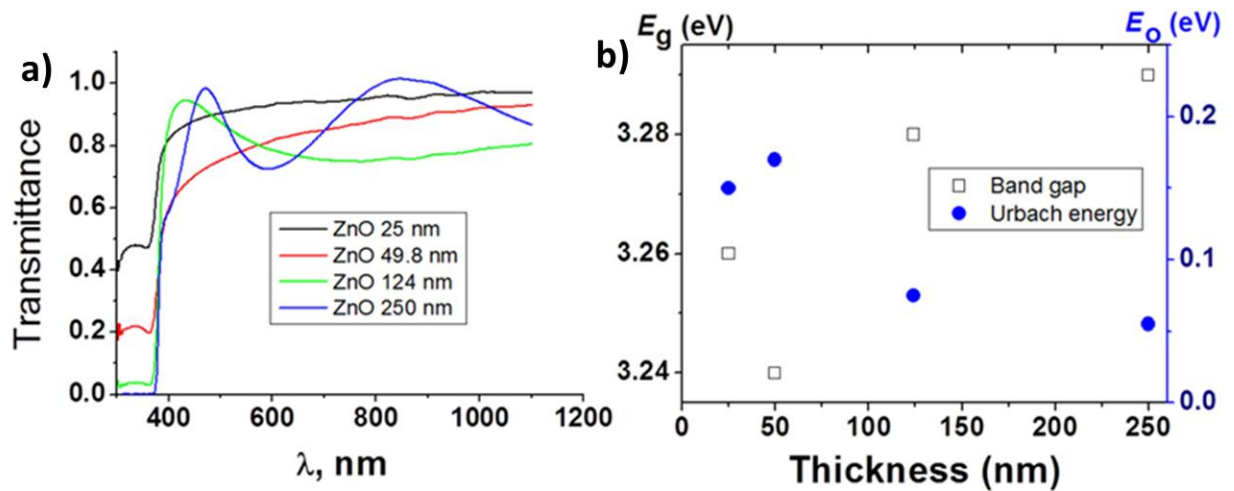


Figure 2-5. a) Transmittance spectra, and b) band gap and Urbach energies of ZnO ALD films of different thicknesses [109].

The same group of scientists proposed that the unusual behavior of the energy gap (Figure 2-5b) with thickness reflected by optical properties was attributed to the improvement of the crystalline structure resulting from a decreasing concentration of point defects at the growth of grains. Compared with the bulk ZnO crystals, the values of the energy gap of the films are lower due to structural defects. In summary, the authors concluded that the ultra-thin ZnO ALD films could be attractive for optical sensor/biosensor applications due to their high oxygen to zinc ratio and variable optical properties. In addition, the presence of hydroxyl terminals leads to the hydrophilicity of the films and improves the immobilization of selected kinds of bio-molecules, thus increasing the suitability for biosensor applications.

Viter *et al.* [110] investigated for the first time the ability of a three-dimensional polyacrylonitrile (PAN)/ZnO material - prepared by a combination of electrospinning and atomic layer deposition (ALD) as a new material with a large surface area - to enhance the performance of optical sensors for volatile organic compound (VOC) detection. The photoluminescence (PL) peak intensity of these one dimensional nanostructures has been enhanced by a factor of 2000 compared to a flat Si substrate. In addition, a phase transition of the ZnO ALD coating from amorphous to crystalline has been observed due to the properties of a PAN nanofiber template surface strain, roughness, and an increased number of nucleation sites in comparison with a flat

Si substrate. The greatly improved PL performance of these nanostructured surfaces could produce exciting materials for implantation in VOC optical sensor applications.

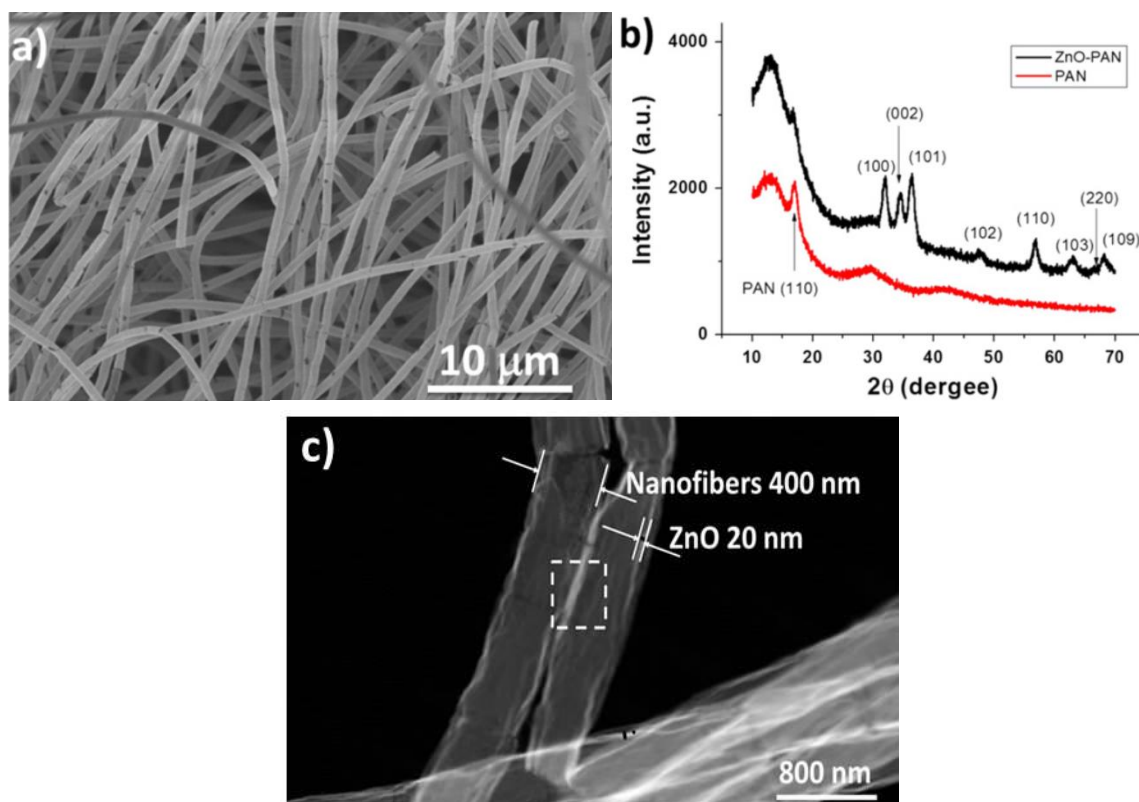


Figure 2-6. (a) SEM image of 1D ZnO NSs obtained with 300 s electrospinning time and coated with 50 cycles ALD ZnO at 100 °C. (b) XRD spectra of the obtained 1D NS and (c) TEM image of 1D ZnO NSs [110].

The conformal coating of 1D ZnO NSs, prepared with electrospinning (300 s) and after deposited with 50 cycles of ZnO by ALD, confirmed with the SEM-image (Figure 2-6a) and low-resolution TEM image (Figure 2-6c).

XRD shows peaks which correspond to the hexagonal wurtzite phase of ZnO, as generally observed with the ZnO thin films deposited by ALD (Figure 2-6b). Deposition of an ALD layer over PAN nanofibers led to the shift of the XRD peak toward lower values of 2θ .

The authors also overviewed a number of works with deposition of ZnO by ALD on different substrates (and influence of the substrate on the growth of ALD films) such as polyethylene-terephthalate (PET), polyethersulfone (PES) substrates, carbon nanotubes (CNTs), an organic polymer sublayer, and PAN (which was studied in their work).

The amorphous-to-crystalline phase transition in ZnO nanolayers deposited on Si and PAN nanofiber substrates, the authors explained by the higher value of nucleation sites on PAN nanofiber surfaces and the surface strain of PAN nanofibers.

2.3.2. Synthesis of Al₂O₃ from TMA and H₂O

Aluminum oxide (Al₂O₃) is one of the most widely studied and used material grown by ALD. Al₂O₃ is a well-behaved ALD system that can be accomplished with a variety of precursors and relatively short cycle times. The deposition is usually performed using trimethylaluminum (Al(CH₃)₃, TMA) and water as precursors [111-115]. This is almost an ideal self-limiting ALD process and considered as a model system for ALD [12]. The first report dates back to late 1980s [116] but since then the process has been extensively studied and characterized in detail. Aluminum oxide is probably the most extensively studied ALD material for numerous diverse applications. ALD Al₂O₃ films are widely used as protective, barrier, and dielectric layers as such or as component in nanolaminates [117, 118].

The surface chemistry during Al₂O₃ ALD can be described as the following binary reaction sequence [119, 120]:



where the surface species are designated by asterisks.

The Al₂O₃ ALD growth occurs during alternating exposures to TMA and H₂O. Al₂O₃ ALD is a model system because the surface reactions are very efficient and self-limiting. The main driver for the efficient reactions is the formation of a very strong Al-O bond. An Al-O Lewis acid-base complex is formed during each half reaction, with methane as a reaction byproduct, and the surface switches between methyl-terminated and hydroxyl-terminated.

During the first TMA half reaction (2-4), TMA molecules are exposed to the surface and will adsorb on the active ligands present on the surface, in the case of TMA and water these are hydroxyl –OH* groups. A thermally activated reaction will occur splitting the (Al(CH₃)₃) molecules on the surface. The CH₃ ligands will combine with the hydroxyl surface groups and form a volatile organic compound, such as methane CH₄, which will desorb from the surface. The remaining part of the molecule chemisorbs to the surface chemically bonding the aluminum atom with either one or two oxygen atoms on the surface in order to deposit a stoichiometric Al₂O₃ film. This reaction is referred to as a ligand exchange reaction. When all the hydroxyl active sites that are physically accessible to the (Al(CH₃)₃) molecules then the surface is

considered saturated and the half cycle is complete. Excess TMA molecules that could not react on the surface as well as desorbed reaction by-products are purged out of the reactor. For the 2nd half cycle, for this case water, water molecules will bind to the methyl groups through another ligand exchange reaction causing the release of more CH₄ molecules.

The net effect of one (2-4)-(2-5) cycles is to deposit one monolayer of Al₂O₃ on the surface. ALD can deposit a wide variety of materials including oxides, nitrides, sulfides, and metals.

The overall reaction for Al₂O₃ ALD is:



$$\Delta H = 376 \text{ kcal}$$

This reaction has an extremely high reaction enthalpy, one of the highest reaction enthalpies occurring for any ALD reaction.

The fundamental aspect of ALD is that after the completion of the 2 half reactions, the surface is functionalized again to react with TMA, therefore depositing a new layer by repeating the cycle. This four step sequence constitutes a full reaction cycle in which a fixed amount of material is deposited, referred to as the “growth rate” (thickness/cycle). Ideally, if sufficient doses are applied to saturate the surface and purge times are adequate to avoid parasitic CVD-like reactions, one monolayer of film is deposited [58] However, most processes are limited by the steric hindrance of the metal containing precursor due to their relatively large size, therefore, blocking active surface sites from being chemisorbed by other metal precursor molecules. Thus, only a fraction of a monolayer (1/2 ML) is actually deposited [121]. In the case of Al₂O₃ the growth rate is ~0.1 nm/cycle [23].

Many previous investigations have confirmed the conformal growth using TMA and H₂O [112]. In Table 2-3 the recent investigations of Al₂O₃ thin films produced by ALD technique are represented.

Table 2-3. ALD processes reported for the growth of Al₂O₃ thin films.

Al precursors	O precursors	Substrates	Deposition T (°C)	GPC (Å/cycle)	References
Al(CH ₃) ₃ (trimethylaluminum [TMA])	H ₂ O	Si (100)	250-400	0.45	[122]
Al(CH ₃) ₃	H ₂ O	Si (100)	227	1.1	[123]
Al(CH ₃) ₃	H ₂ O	Si (100), SiO ₂ / Si (100)	150	1.9	[124]
Al(CH ₃) ₃	D ₂ O	glass	150-400	1	[125]
Al(CH ₃) ₃	H ₂ O	n-type Si (100) wafers	125-425	1.18±0.04	[112]
Al(CH ₃) ₃	H ₂ O	p-type Si (001)	300	0.88	[126]
Al(CH ₃) ₃	H ₂ O	multiwalle	300	2	[127]

		d carbon nanotubes (MWNTs) were synthesized on a Si (100) substrate			
Al(CH ₃) ₃	H ₂ O	flat Si substrates, and Si MEMS structures	168	1.01	[128]
Al(CH ₃) ₃	H ₂ O	Si(100)	33, 177	1.33	[111]
Al(CH ₃) ₃	H ₂ O	Low-density polyethylene (LDPE) particles	77	2.0 - 3.3	[129]

Al(CH ₃) ₃	H ₂ O	Si (100)	85	1.1 - 1.2	[130]
Al(CH ₃) ₃	H ₂ O	polyethylene naphthalate (PEN) and Kapton® polyimide substrates	100-175	1.2-1.3	[117]
Al(CH ₃) ₃	H ₂ O	AgFON (silver film-over- nanosphere) substrates	50	1	[131]
Al(CH ₃) ₃	O ₂ plasma	poly (2,6- ethylenephthalate) (PEN)	RT-100	0.97-0.17	[132]

Al(CH ₃) ₃	O ₃	Si (100)	150-300	0.4-0.9	[133]
Al(CH ₃) ₃	H ₂ O	electrospun poly(vinyl alcohol) microfiber templates	45	0.7	[134]
Al(CH ₃) ₃	O ₃	ZrO ₂ particles	90-377	1.1	[135]
Al(CH ₃) ₃	O ₃	highly oriented pyrolytic graphite (HOPG) surface	200	0.95	[136]
Al(CH ₃) ₃	H ₂ O	Si (100)	200	1.2	[137]
Al(CH ₃) ₃	H ₂ O	Natural graphite (NG) and	180	1.1	[138]

Al(CH ₃) ₃	H ₂ O	LiCoO ₂ particles			
Al(CH ₃) ₃	H ₂ O	SnO ₂ photoanodes	200	1.1	[139]
Al(CH ₃) ₃	chromatography-grade water	copper substrates	177	1.2	[140] 2011
Al(CH ₃) ₃	H ₂ O	heat-stabilized polyethylene naphthalate (HSPEN) substrates	155	1.1-1.2	[141]
Al(CH ₃) ₃	H ₂ O	cellulose cotton fibers	60-90	1.2-1.3	[142]

Al(CH ₃) ₃	H ₂ O	black silicon	200	1.026±0.002	[143]
Al(CH ₃) ₃	H ₂ O	polymer films	80	1.1	[144]
Al(CH ₃) ₃	H ₂ O	MoS ₂	200	1.0	[145]
Al(CH ₃) ₃	O ₃	Si (100)	205	1.1	[146]
Al(CH ₃) ₃	O ₂	Li metal	150	1.2	[147]
Al(CH ₃) ₃	O ₂	black phosphorus	200	1	[148]
Al(CH ₃) ₃	H ₂ O	p-Si (100)	300	1	[149]
Al(CH ₃) ₃	O ₃	Li-ion (LiNi _{0.5} Mn _{0.3} Co _{0.2} O ₂) battery electrodes	50	0.66	[150]
Al(CH ₃) ₃	H ₂ O	CH ₃ NH ₃ P	RT	1.4	[151]

		bI ₃ perovskite film			
Al(CH ₃) ₃	H ₂ O	silver film over nanospher e (AgFON) substrates	55	1.1	[152]
Al(CH ₃) ₃	O ₃	2G glass Si (100)	100	0.9	[153]
Al(CH ₃) ₃	H ₂ O	WSe ₂	120	1	[154]
Al(CH ₃) ₃	H ₂ O	Si (100)	100-250	0.8-1.02	[155]
Al(CH ₃) ₃	H ₂ O	AgFONs	70	1.1	[156]
Al(CH ₃) ₃	H ₂ O	TiO ₂ nanotube layers	200	1.1	[157]
Al(CH ₃) ₃	O ₃	Si (100)	100	1.6	[158]

2.3.3. Al₂O₃/ZnO nanolaminates produced by ALD

Atomic layer deposition (ALD) is a powerful tool to fabricate different oxide materials [159]. The recent ALD oxide studies have often dealt with growth mechanism investigations, but also the structural properties of the films have been of interest. One important material type of ALD oxides is nanolaminates. Nanolaminates are unique nanocomposites that allow various thin film properties to be tuned by changing the composition and interfacial density. Nanolaminates are composite films comprised of alternating layers of different materials, which have individual layer thicknesses on the nanometer scale [160-162]. The multilayered structure often imparts unique properties to the nanolaminates film. In some cases, the nanolaminates may have physical properties that are superior to those of the constituent materials.

In addition, surface reactions can be devised that promote good nucleation and adhesion between the different nanolayers. Once the physical properties of the nanolaminates have been optimized, ALD allows objects with diverse sizes and shapes to be coated with the desired nanolaminates film.

The ALD of nanolaminates and alloys has many applications in semiconductor device fabrication and nanostructure engineering. The first report of nanolaminates fabricated using ALD examined HfO₂/Ta₂O₅ nanolaminates as low leakage dielectric films [163]. In nanolaminates the advantageous properties of each component can be retained, for example, in insulators: high permittivity, low leakage current density, and high charge storage capacity.

The Al₂O₃/ZnO NLs can be grown by alternating between the trimethylaluminum (TMA) and H₂O reaction cycles for Al₂O₃ ALD and the DEZ and H₂O reaction cycles for ZnO ALD [8]. Different studies report the growth of Al₂O₃/ZnO nanolaminates as well as the incorporation of Al doping in ZnO using ALD [4-8].

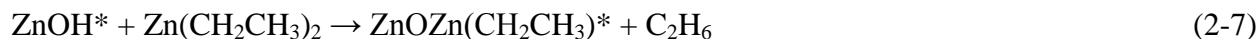
Using ALD methods, ZnO grows as a conducting, polycrystalline film with a rough surface topography resulting from the individual crystallites. In contrast, Al₂O₃ grown by ALD is an excellent insulating, amorphous film that deposits with high conformality. The wide disparity in physical properties between ZnO and Al₂O₃ suggests that nanolaminates formed from alternating ZnO/Al₂O₃ layers may possess properties that span a wide range in surface roughness and conductivity.

Although there are nucleation issues upon initiating the Al₂O₃ ALD cycles following the ZnO ALD cycles, the relative number of Al₂O₃ ALD and ZnO ALD cycles can be changed to define a wide range of alloy compositions [7]. Since Al₂O₃ ALD films are insulating and ZnO ALD films are conducting, variable resistivity films can be fabricated using Al₂O₃/ZnO alloys. Al₂O₃ thin films deposited by ALD are amorphous in nature independently of their thickness, whereas ZnO

nanolayers show a transition from amorphous to nanocrystalline phases when bilayer spacing increased [6]. Thin amorphous Al₂O₃ layers work as stopping layers for ZnO crystal growth [164].

The ZnO ALD films are deposited using alternating exposures to DEZ and H₂O.

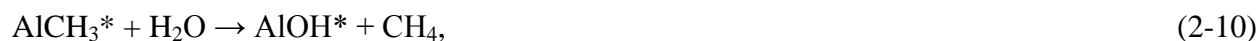
The (2-7) and (2-8) surface reactions that define the cycle can be written as:



where the asterisks designate the surface species.

The Al₂O₃ ALD films are deposited using alternating TMA and H₂O exposures.

The (2-9) and (2-10) surface reactions that define the cycle for Al₂O₃ ALD are:



The ALD methods allow the tailoring of structural and optical parameters of the nanolaminates, including single layer thickness, grain size, band gap, and PL [165].

Chaaya *et al.* reported on the tuning of optical and structural properties of Al₂O₃/ZnO nanolaminates designed by atomic layer deposition (ALD). The SEM images (Figure 2-7a) indicate a conformal coating by ALD of the Si substrate in case of ZnO thin film of 100 nm thickness as well as for Al₂O₃/ZnO nanolaminates with different sequences. The SEM cross-section proves as well that the sequence of alternating Al₂O₃ and ZnO interlayers was achieved throughout the total film thickness of the nanolaminates. The SEM images show that the single layer of ZnO developed a rough surface of columnar growth where the nanolaminates consist of alternating layers of amorphous Al₂O₃ and nanocrystalline ZnO [6, 90].

The EDX of nanolaminates Al₂O₃/ZnO 10 (10/10 nm) consisting of alternating ZnO/Al₂O₃ films (Figure 2-7b) grown at 100 °C by ALD showed the presence of Al, Zn, and O.

GIXRD patterns of Al₂O₃/ZnO 50 (2/2 nm) nanolaminates with the thinnest bilayer thickness showed weak broad X-ray diffraction peak at 34.26° (Figure 2-7c) which can result from their amorphous structure or their crystalline size below 2 nm. The increase of the bilayer thickness in the nanolaminates, Al₂O₃/ZnO 10 (10/10 nm), led to the appearance of XRD peaks at 2θ = 31.82° and 34.35° and a weak peak at 2θ = 36.1° corresponding to (100), (002), and (101) reflections of ZnO, respectively. A change in the preferential growth orientation (strong (002) and negligible (101) XRD peaks) is observed when comparing the thicker nanolaminates Al₂O₃/ZnO 2 (50/50 nm) to the single ZnO film (100 nm).

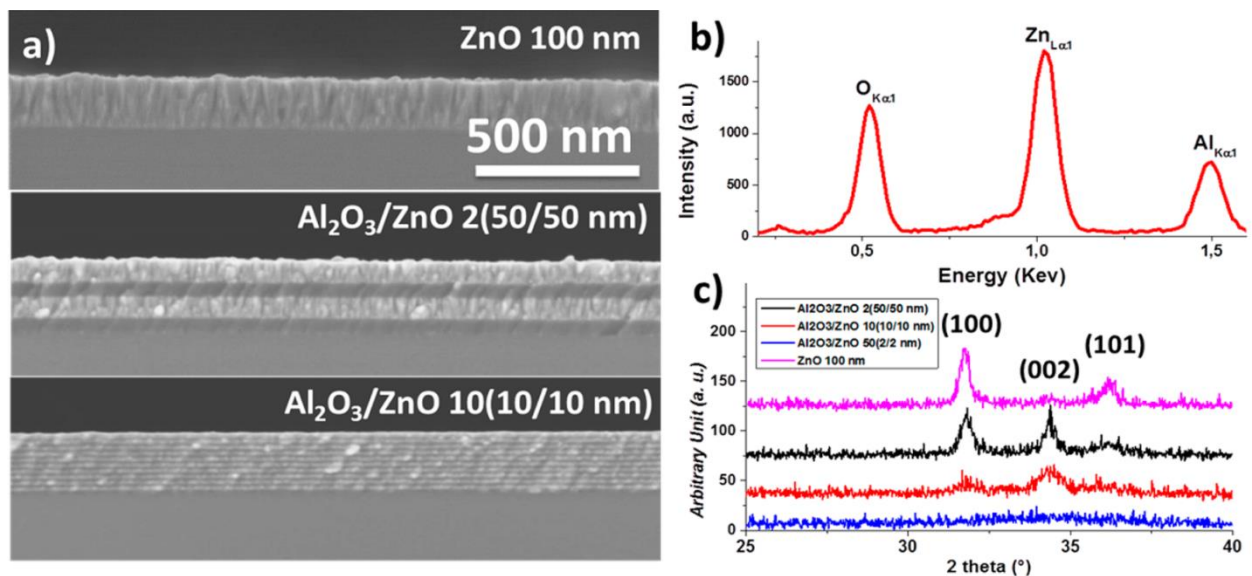


Figure 2-7. SEM images of ZnO thin film of 100 nm thickness and Al₂O₃/ZnO nanolaminates with different sequences (a), EDX of Al₂O₃/ZnO nanolaminates (b), and GIXRD of ZnO thin film of 100 nm thickness and Al₂O₃/ZnO nanolaminates with different sequences (c) [165].

The authors concluded that in the first stage, vertical growth of ZnO on amorphous Al₂O₃ was initiated. At low bilayer thickness Al₂O₃/ZnO 50 (2/2 nm), wurtzite ZnO with low crystalline quality was observed. The lattice parameter increased, matching possible interstitial Al incorporation in ZnO structure at least at the interface between ZnO and Al₂O₃ [165].

It was shown a linear behavior of the mean square roughness vs the increase of bilayer thickness (Figure 2-8). Amorphous Al₂O₃ blocks the ZnO crystal growth and forces the ZnO to renucleate on the Al₂O₃ surface. It was noted that surface roughness of nanolaminates was lower than that for 200 nm thick ZnO (Figure 2-8).

Transmittance spectra of Al₂O₃/ZnO nanolaminates are shown in Figure 2-9. All measured samples were transparent in the range of 550-1100 nm. The absorption edge of the samples was found in the region of 370-410 nm. Blue shift of absorption edge was observed particularly with the decrease of nanolaminates bilayer thickness. The band gap value of the samples was calculated considering that Al₂O₃ was totally transparent and the observed absorption edge was related to ZnO layers.

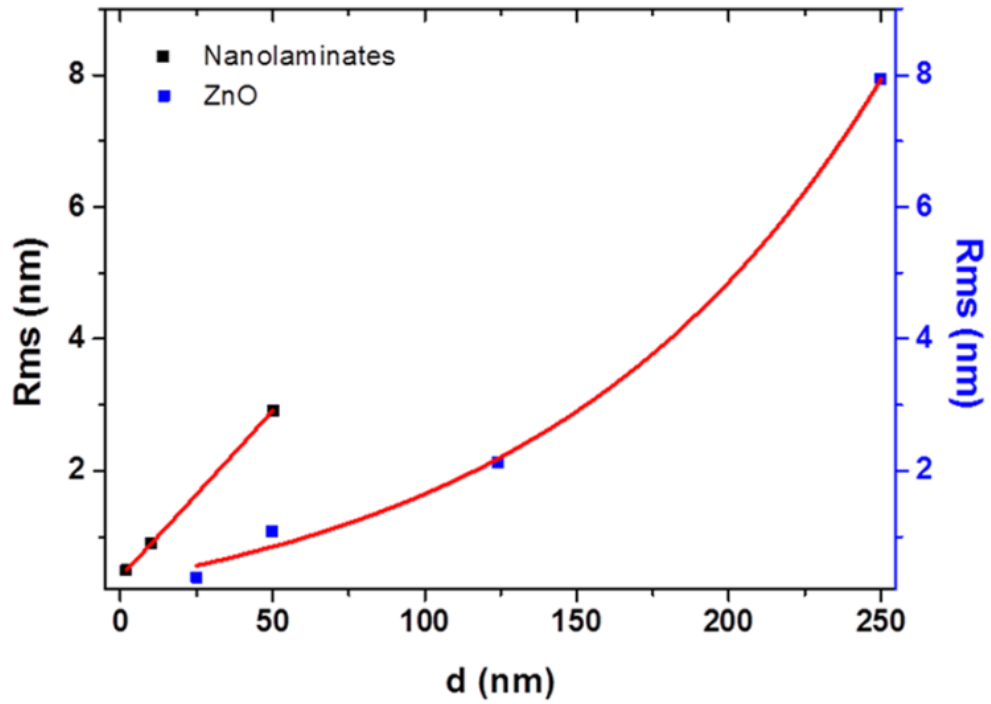


Figure 2-8. Blue square, roughness vs the film thickness of single layer of ZnO; black square, roughness vs the top layer of ZnO in the $\text{Al}_2\text{O}_3/\text{ZnO}$ nanolaminates [165].

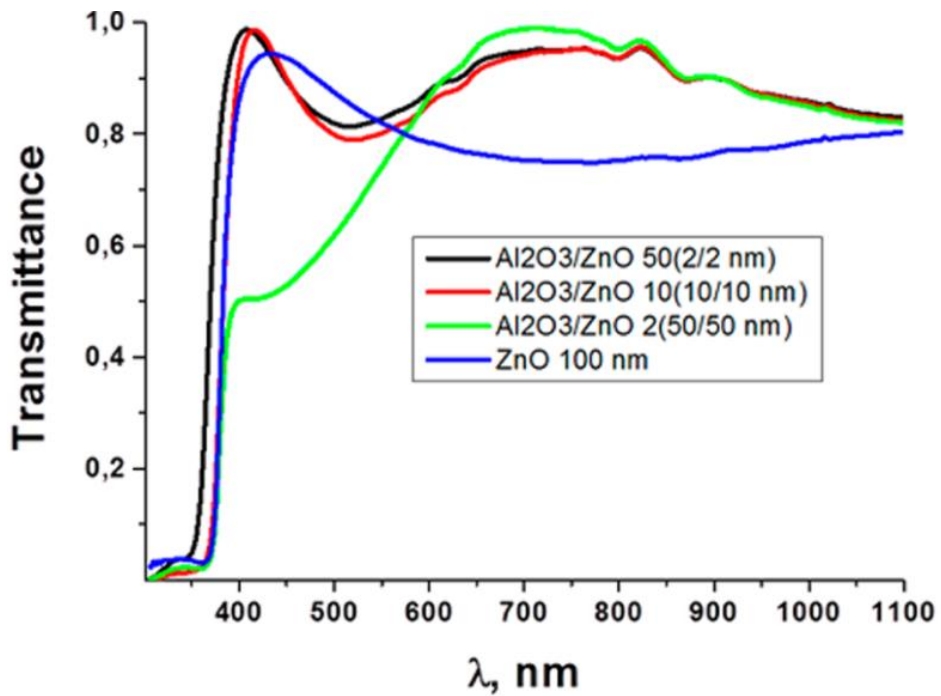


Figure 2-9. Transmittance spectra of $\text{Al}_2\text{O}_3/\text{ZnO}$ nanolaminates with different bilayer thicknesses and single ZnO thin film [165].

The calculated band gap values E_g are presented in Table 2-4. The band gap increased with the decrease of the bilayer thickness in the nanolaminates. The obtained E_g values can be affected by structural defects (interstitials, vacancies, etc.) and impurities.

Table 2-4. Band gap of $\text{Al}_2\text{O}_3/\text{ZnO}$ nanolaminates with different bilayer thicknesses and ZnO single thin film of 50 nm thickness [165]

	E_g (eV) from transmittance	E_g (eV) from ellipsometry
$\text{Al}_2\text{O}_3/\text{ZnO}$ 50 (2/2 nm)	3.41	3.45
$\text{Al}_2\text{O}_3/\text{ZnO}$ 10 (10/10 nm)	3.3	3.36
$\text{Al}_2\text{O}_3/\text{ZnO}$ 2 (50/50 nm)	3.28	3.31
ZnO (50 nm)	3.24	3.25

The authors proposed three physical phenomena for the determination of the observed blue shift, such as quantum confinement effect of small nanograins, doping of ZnO by Al, and improvement of crystalline quality of the single layer.

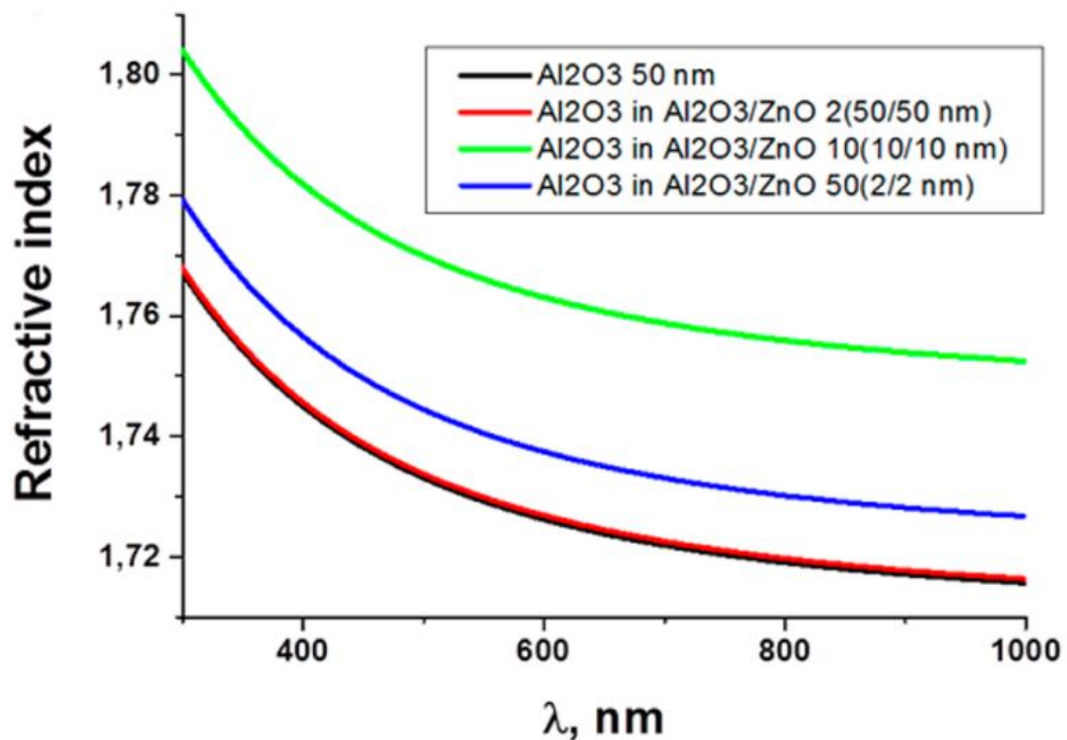


Figure 2-10. Refractive index (real part) of Al_2O_3 single thin film and Al_2O_3 in $\text{Al}_2\text{O}_3/\text{ZnO}$ nanolaminates with different bilayer thicknesses [165].

Chaaya *et al.* investigated the thickness and the optical constants (refractive index and extinction coefficients) of single ZnO and Al₂O₃ layers and the evaluation of nanolaminates (Figure 2-10) by a spectroscopic ellipsometry. They found that Al₂O₃ was transparent in the whole UV and VIS range of the wavelength (Figure 2-10). It was noted that ellipsometry allows obtaining the optical constants *n* (real part of refractive index) and *k* (imaginary part of refractive index). It was mentioned that in case of deposition of ZnO on Al₂O₃, lateral growth can take place. The deviation from the columnar growth can change then the microstructure and increase the packing density and the refractive index.

It was shown that the refractive index of Al₂O₃ single layer in nanolaminates increased in comparison to single layer of Al₂O₃ deposited on Si (Figure 2-10). This layer had amorphous structure. The authors considered the improvement of the structure in amorphous Al₂O₃, similar to ZnO, which resulted in the increase of the refractive index and/or the Zn incorporation at the ZnO/Al₂O₃ interface.

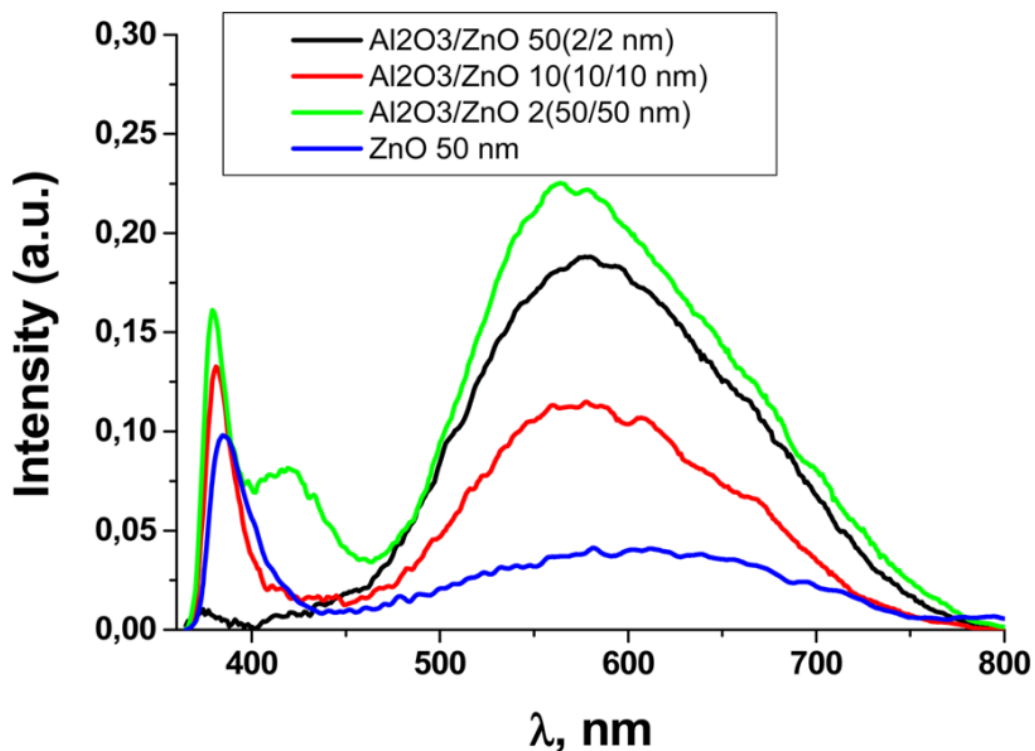


Figure 2-11. Photoluminescence spectra of 50 nm thick single ZnO film and Al₂O₃/ZnO nanolaminates with different bilayer thicknesses [165].

The study of PL of nanolaminates was also performed (Figure 2-11). The UV peak corresponds to free exciton emission, and the VIS peak was observed due to defect level emission. The intensity of UV peak increased with the increase of the bilayer thickness in the nanolaminates.

The intensity of the VIS band does not follow the same tendency. The ratio of UV/vis emission could be a parameter of the crystalline structure quality of ZnO inside the nanolaminates.

It was mentioned that UV/vis intensity of nanolaminates did not increase monotonically with the increase of the single layer thickness (Figure 2-11). It could be affected by structural changes during the layer growth and/or doping by Al. Blue shift of band gap and excitonic peak position of ZnO single layers were explained by quantum confinement effect and the improvement of crystalline quality of ZnO layer.

The advanced properties of the nanolaminates such as biocompatibility, easy surface modification, and enhanced photoluminescence at room temperature could provide good capacity for the development of nanolaminates-based optical sensors and biosensors.

Viter *et al.* reported on the optical and structural properties of ultrathin $\text{Al}_2\text{O}_3/\text{ZnO}$ nanolaminates (lower than 20 nm) deposited by ALD technique [166]. The one of the proposed way to explain amorphous nature of ultrathin nanolaminates is the minimum thickness required to allow crystallization in a thin film. The proposed crystallization model for ultrathin layers and superlattices was taking into account the interface energies, the thickness of the layers, the melting point of the system, and the bulk amorphous crystallization temperature. It was shown that exponential increase of the crystallization temperature leads to the decrease of the minimal thickness at which crystallization occurs.

Mechanisms of growth of ultrathin $\text{ZnO}/\text{Al}_2\text{O}_3$ nanolaminates were studied using AFM and ellipsometry. On the basis of the analysis of optical methods such as transmission, spectroscopic ellipsometry and photoluminescence of ultrathin nanolaminates, the amorphous nature of them has been proven. These results allowing not only to determine optical properties of $\text{Al}_2\text{O}_3/\text{ZnO}$ nanolaminates but also to get some inside on the formation processes of ultrathin films of $\text{Al}_2\text{O}_3/\text{ZnO}$ [166].

2.4. Temperature window of the ALD process

ALD is a thermally activated process in order to produce self-limiting reactions on the surface of a substrate [167]. The processing temperature range for ALD or the so-called “ALD window” is the region of nearly ideal ALD behavior between the non-ideal regions. The ALD temperature window is presented in Figure 2-12, which indicated the temperature range where thin film growth proceeds by the self-limiting reaction in an ALD mode [121]. At lower temperatures, the reactants could condense on the surface or the surface reactions may not have enough thermal energy to reach completion. At higher temperature, the surface species could decompose and allow additional reactant adsorption. This behavior is similar to CVD by unimolecular decomposition. The surface

species needed for ALD could also desorb from the surface at higher temperatures and be unavailable for additional surface reactions. This desorption would lead to the decrease of the ALD growth per cycle at higher temperatures. This behavior is observed for Al_2O_3 ALD [12]. One system that displays dramatic non-ideal ALD behavior is TiN ALD using tetradimethylaminotitanium (TDMAT) and NH_3 . Although this ALD system was initially presented as a working ALD process, additional studies revealed that the surface reactions did not reach completion, impurities were left in the resulting films, and the films had significant porosity that led to their easy oxidation [168, 169]. TiN ALD using TDMAT and NH_3 has no “ALD window” where the ALD process is reasonable. In contrast, TiN ALD using TiCl_4 and NH_3 is a well-defined ALD process that occurs at higher temperatures and produces HCl as a reaction product [170].

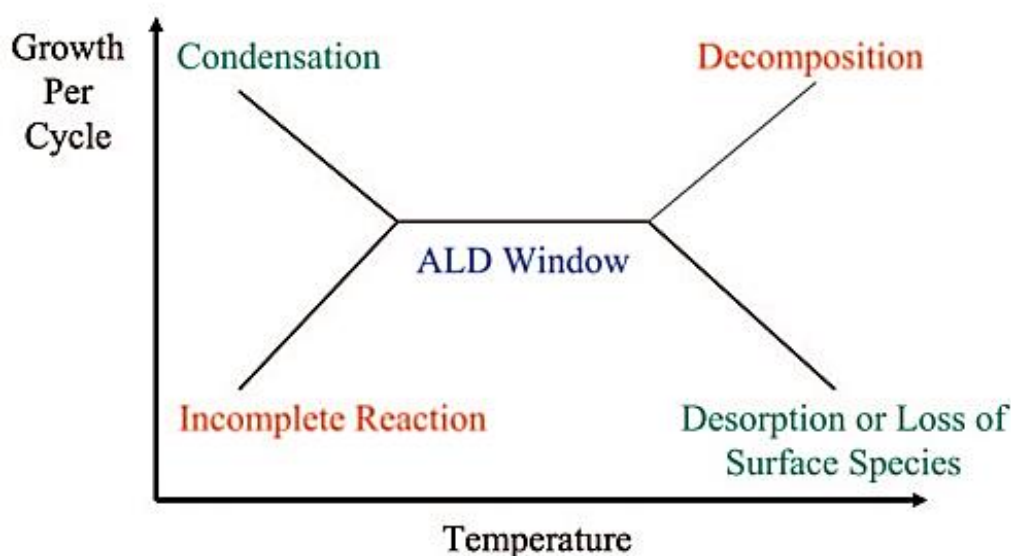


Figure 2-12. Schematic of possible behavior for the ALD growth per cycle versus temperature showing the “ALD” window [23].

Outside the temperature window at lower temperatures there occurs either less growth due to insufficient thermal energy for reactions to occur or more growth due to condensation of precursor(s). At higher temperatures, if the material is volatile, desorption can occur which results in a reduced GPC. Alternatively, at sufficiently high temperatures reactant decomposition can occur which will cause an enhancement of growth. It is important to recognize that for true ALD growth all reactants have to be operating within their respective temperature windows. This requirement has the important consequence of restricting reactant pairs and thus potentially materials, particularly if strictly ALD growth is desired. It is however worth recognizing that operating outside of the temperature window may be tolerable as the non-ALD growth components may be

sufficiently small. For example, the reactant pair of TMA and NH_3 may appear unsuitable candidates for ALD of AlN due to a mismatched temperature window between the two reactants. TMA starts decomposing at a temperature of 600 K which is below the necessary temperature for reasonable reactivity of NH_3 . Nevertheless, one can still achieve reasonable ALD-like growth if the decomposition rate is sufficiently low.

The above considerations imply that with proper reactor design and careful process tuning one can achieve high quality ALD-like layers. On the low end of the temperature spectrum, the effects of condensation and poor reactivity can be mitigated with sufficiently long purges and reactant exposure times, respectively. There can be a considerable departure from the ideal ALD window. Within the temperature window, the GPC is often not fixed due to temperature influencing available reactive surface sites, migration of ad molecules, or even change in the favored reaction mechanism. For example, the Al_2O_3 process based on TMA and H_2O displays a progressive decrease in GPC from 175 to 300 °C due to dehydroxylation.

Mousa *et al.* investigated an effect of temperature and gas velocity on growth per cycle during Al_2O_3 and ZnO atomic layer deposition at atmospheric pressure [92].

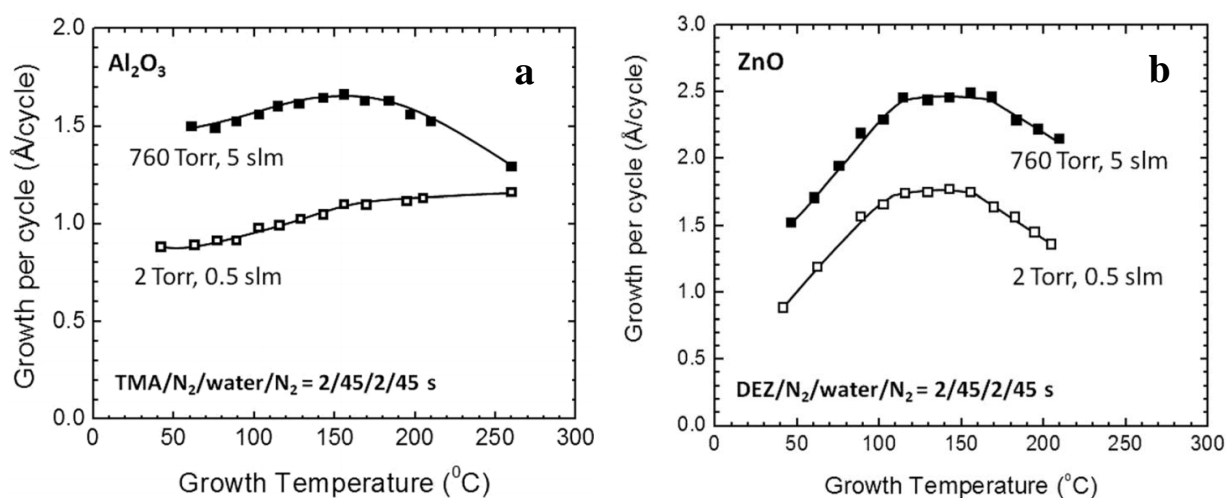


Figure 2-13. ALD growth per cycle for Al_2O_3 (a) and ZnO (b) as a function of deposition temperature for reactor pressures of 2 and 760 Torr. The gas pulse conditions used for deposition are identified in the figure [92].

The resulting film growth per cycle for Al_2O_3 and ZnO are presented in Figure 2-13 a and b, respectively. It was shown that at low pressure, the ALD temperature “window” follows the trend expected for Al_2O_3 and ZnO [111, 171]. For Al_2O_3 , growth is limited by thermal activation at lower temperatures, whereas at higher temperatures it is determined by the number of active Al-OH and Al-CH₃ surface sites. The temperature profile results in Figure 2-13 a, b indicate that the higher

growth rate at high pressure results primarily from gas transport mechanisms that are not strongly temperature dependent, whereas at higher temperatures, thermally activated processes also become important allowing the growth rates nearly convergence at $T > 250$ C for Al_2O_3 ALD. A reasonable explanation is that the excess growth results from additional physisorbed water at high pressure, and the water desorbs more readily at $T > 150$ C, decreasing the growth rate difference. This is consistent with previous studies that show that large water doses produce additional growth per cycle during alumina ALD.

2.5. ALD applications in nanotechnology

ALD coatings have been widely used for different nanotechnology applications (Figure 2-14). They worked as supporting layers and as principal elements of the developed nanostructures.

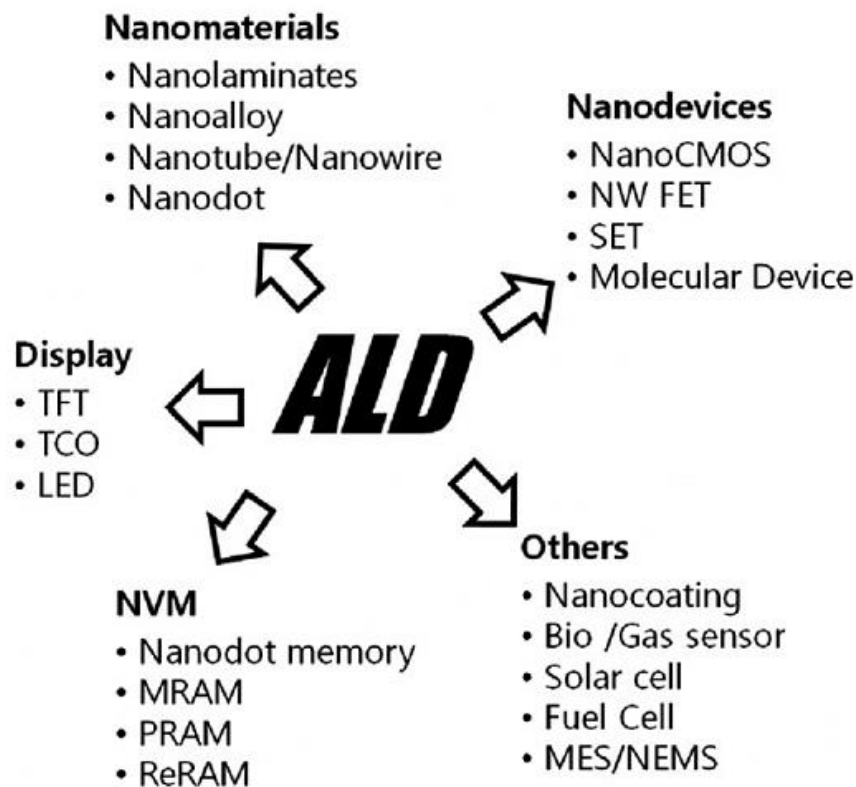


Figure 2-14. Potential applications of ALD in various research fields [172]

2.5.1. Applications of ALD coatings as active functional layers for different areas

Chaaya *et al.* [109, 165] and Iatsunskyi *et al.* [173, 174] proposed methodologies for integration of ALD deposited ZnO , TiO_2 , $\text{ZnO}/\text{Al}_2\text{O}_3$ and $\text{TiO}_2/\text{Al}_2\text{O}_3$ nanolaminate structures with tailored properties into Si and porous Si substrates (Figure 2-15). It resulted to development of

principally new materials, based on ZnO/graphene nanolaminates, with novel unique properties, reported by Baitimirova *et al.* [175].

Viter *et al.* reported on successful integration of ALD ZnO with plasmonic Au nanolayers for surface plasmon resonance applications [176]. In addition, methodologies for analysis of fundamental properties of metal oxide nanolaminates have been proposed [166, 173, 174].

ALD coatings have been used as active functional layers for different applications. Viter *et al.* combined 1D PAN electrospun nanofibers with ZnO-based ultrathin coatings for sensor applications [110, 177]. New properties, such as high crystallinity and room temperature photoluminescence were achieved. Mechanisms of physical properties in such structures have been proposed [110, 177].

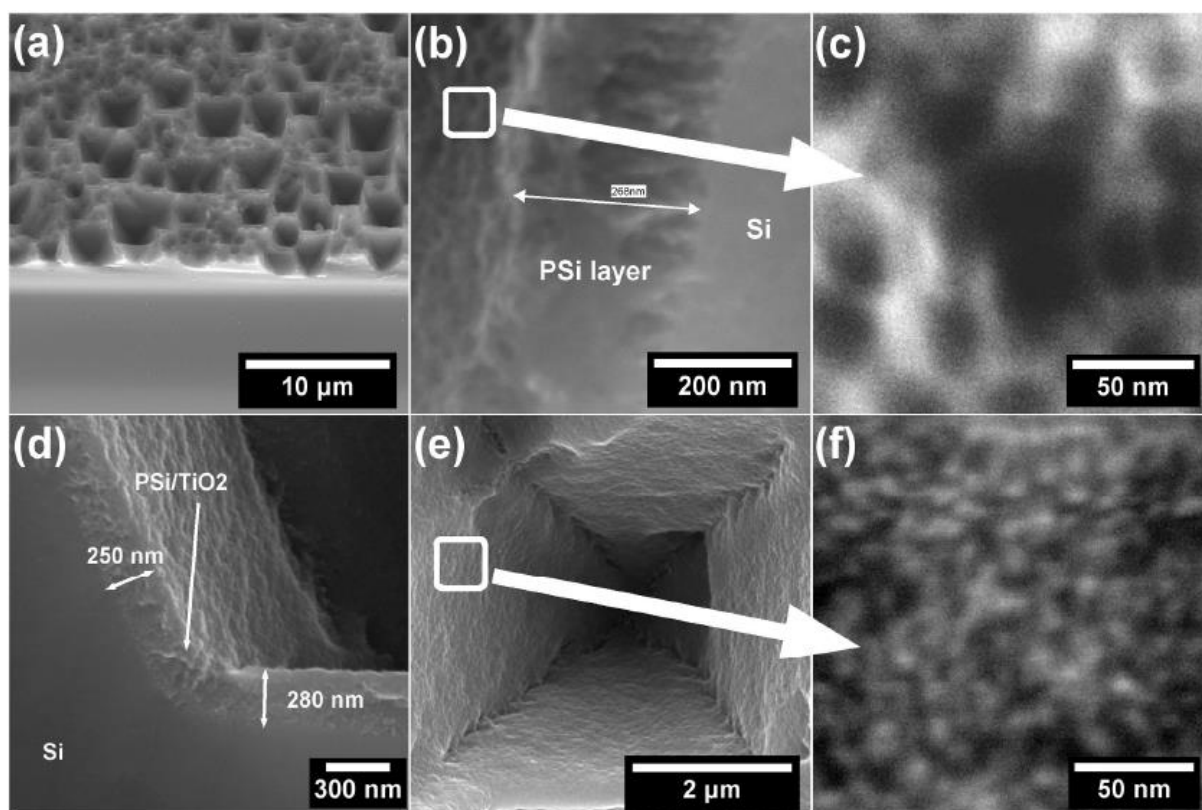


Figure 2-15. Cross-sectional view SEM image of a) macroporous silicon surface fabricated by MACE, b) mesoporous layer of PSi, c) mesoporous silicon surface (high magnification); d) cross-sectional view of as-prepared PSi/TiO₂ nanostructure after 150 ALD cycles, e) plane view SEM image of the individual macropore in the PSi/TiO₂ nanostructure after 150 ALD cycles, f) surface of the macropore in the PSi/TiO₂ nanostructure (high magnification).

Nasr *et al.* used ZnO and ZnO/Al₂O₃ to form novel ZnO/ZnAl₂O₄ multi co-centric nanotubes for photocatalytic application [178]. Electrospun PAN nanofibers were used as template for deposition of ALD layers. Altering ZnO and Al₂O₃ layers were deposited as shown in Table 2-5.

Calcination at high temperatures ($T > 650$ °C) was performed to remove the organic core and initiate phase transitions. SEM images of the obtained hollow nanotubes are shown in Figure 2-16.

Table 2-5. Deposition sequences of Al₂O₃ and ZnO cycles on the PAN nanofibers.

Double	20 nm Al ₂ O ₃ /40 nm ZnO/20 nm Al ₂ O ₃
Triple	20 nm Al ₂ O ₃ /40 nm ZnO/20 nm Al ₂ O ₃ /40 nm ZnO/20 nm Al ₂ O ₃
Quadruple	Al ₂ O ₃ /40 nm ZnO/20 nm Al ₂ O ₃ /40 nm ZnO/20 nm Al ₂ O ₃ /40 nm ZnO/20 nm Al ₂ O ₃

Due to a temperature induced phase transitions, new phase of ZnAl₂O₄ has been formed. The presence of new phase was confirmed using XRD measurements. PL quenching of ZnAl₂O₄/ZnO nanotubes was observed with the increase of ZnAl₂O₄ content. The developed ZnO/ZnAl₂O₄ nanotubes showed good photocatalytic performance for organic pollutants degradation. Particularly, the increase of ZnAl₂O₄ content supported charge separation. Clear increase of photocatalytic performance was observed for samples with high ZnAl₂O₄ content (Figure 2-17).

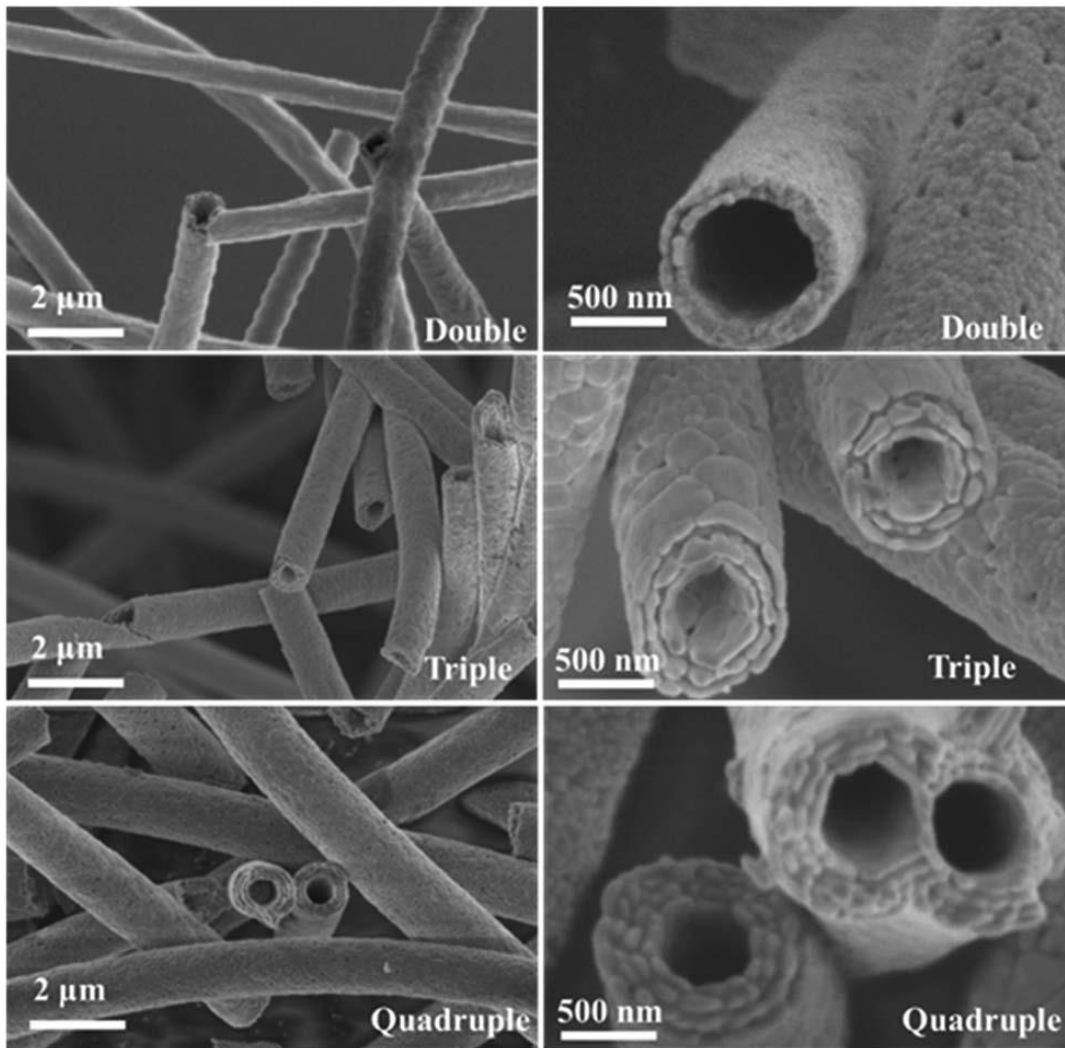


Figure 2-16. SEM images of co-centric hollow nanotubes with different contents of ZnO and Al₂O₃.

As ALD provides conformal coatings, solar cells are one of important application areas of ALD nanomaterials. Niu *et al.* reported on ALD TiO₂ nanolayers for solar cells applications [179]. Moret *et al.* reported on ZnO applications with different Al doping for solar cells [101]. More applications and prospects of ALD materials in solar cells are reported by Zardetto *et al.* [180]. Good prospects of development ALD perovskite materials are demonstrated.

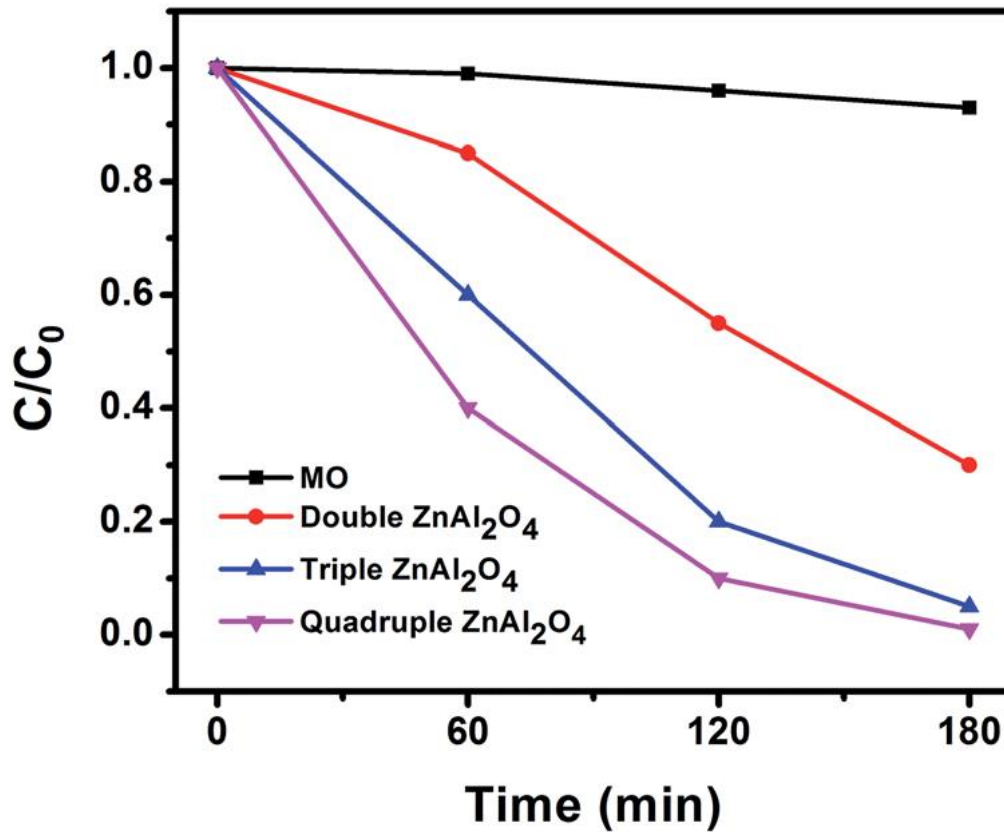


Figure 2-17. Photodegradation of Methylorange by double, triple and quadruple cocentric nanotubes of ZnO/ZnAl₂O₄.

Elias *et al.* [32, 34] and Guerin *et al.* [181] used ALD ZnO nanolayers as seed layers on polystyrene microspheres for further growth of urchin-like ZnO nanostructures (Figure 2-18). The developed urchin-like ZnO nanostructures have been applied for hybrid solar cells. ALD deposited metal oxides and nanolaminates are also used in barrier applications for food packaging and electronics [182-184]. It was found that nanolaminate materials showed higher resistance to oxygen and applied strain rather than single layers.

ALD deposited metal oxide and metal oxide nanolaminates such as Al₂O₃, HfO₂ and HfO₂/Al₂O₃ are used as gates in MOSFET transistors [185, 186].

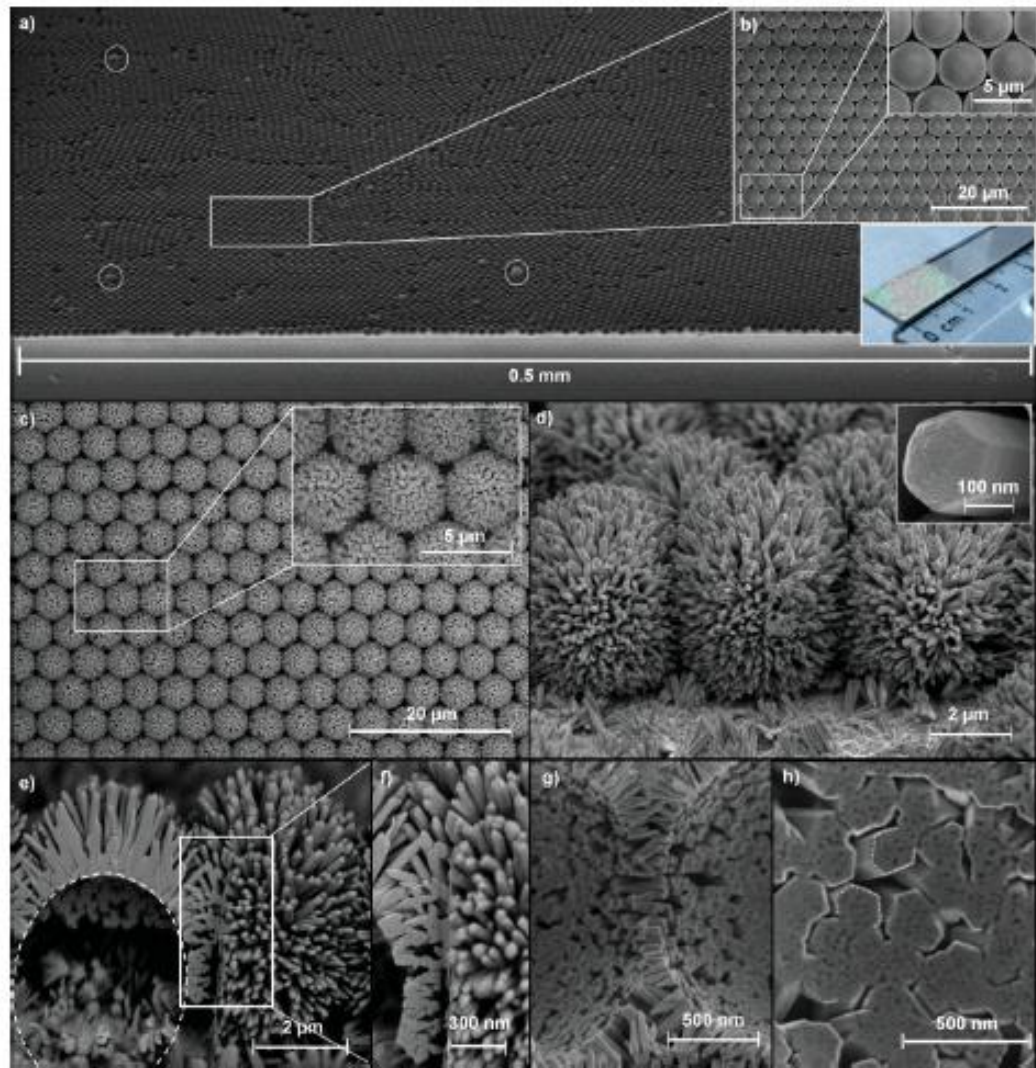


Figure 2-18. a,b) SEM images of a self-assembled monolayer of PS microspheres on a TCO substrate; a) tilted (458) low magnification and b) top view. The lower inset of (a) presents the digital image of the same sample. c,d) SEM images of an ordered hollow urchin-like structure of ZnO nanowires after the removal of PS; c) top view, the inset is a higher magnification, and d) tilted view (708). The inset is a high-magnification SEM image of the top of a nanowire grown at the top of the urchin-like structure. e,f) Cross-sectional SEM images of two urchin-like structures treated by FIB at different magnifications. g,h) High-magnification SEM images of a mechanically scratched structure for cross-section and internal surface observations, respectively [33].

ALD is a powerful tool for modification of porous structures [4, 187]. Due to high reactivity, the internal surface of pores (Si, polymer, etc.) can be coated with metal oxide nanolayers. It was shown good coating of pores with Al_2O_3 and $\text{ZnO}/\text{Al}_2\text{O}_3$ nanolayers. The ALD coated pores were used for single pore biosensor [4, 187, 188].

Thus, ALD technique fits well with micro- and nanofabrication and shows a number of useful applications.

2.6. ALD applications in sensors and biosensors

2.6.1. ALD applications for gas and optical sensors

ZnO based ALD nanostructures have good prospects for applications in optical sensors [189]. Due to conformal coating of ALD layer, combination of ZnO ALD nanolayers with optical fibers and 1D templates had a significant impact for sensor development.

Jędrzejewska-Szczerska *et al.* developed new fiber-optic Fabry–Perot interferometer supplied with ALD thin ZnO layer as an active medium for temperature measurements [102]. Interference fringes in ZnO layer depended on optical thickness of the film. Due to thermal expansion of the ZnO the fringes position shifted. The developed sensor was tested in the range of temperatures of 50-300 °C. It showed sensitivity of 0.05 nm/°C.

Majchrowicz *et al.* reported on application of 200 nm ZnO ALD layers on optical fibers for measurement of the refractive index of following chemical substances: cyclohexane, benzene, toluene, issue oil, paraffin [190]. The developed ALD optical sensor showed different responses to the target analytes.

ZnO ALD nanostructures have been applied for gas sensors. Humayun *et al.* reported on resistive sensors, based on carbon nanotubes/ZnO for methane detection [191]. ZnO nanoparticles were deposited on the surface of carbon nanotubes with ALD method at 175 °C. Room temperature sensitivity tests showed repeatable sensor response towards 2-10 ppm of methane. Boyadjiev *et al.* demonstrated performance of ZnO thin films, formed by ALD on quartz microbalance crystal to nitrogen oxide detection [192]. The sensor showed high sensitivity to 150-500 ppm of NO₂ at room temperature. Yun *et al.* showed that deposition of ZnO layer by ALD technique over thin-film transistor transducer enhanced sensor performance to ammonia [193]. Recent advances in ZnO ALD sensors were summarized by Marichy *et al.* [194]. Improvement of sensitivity and selectivity of ALD layers, decrease of operation temperature and reduction of time constants of the sensors within doping, deposition of catalyst and forming hybrid structures are discussed in details.

Due to unique optical properties such as room temperature photoluminescence and optical absorption edge in UV region, ZnO-based ALD nanocoatings could be applied of optical sensing [109, 110, 165, 176, 177].

Novel 1D core/shell polyacrylonitrile/ZnO nanofibers have been applied as UV detectors [31]. ZnO layers were deposited over dielectric organic core by ALD technique. Current measurements were performed in dark and under UV excitation. The measured photocurrent of 1D

ZnO nanofibers was enhanced by a factor of 250 compared to the same ZnO layers, deposited on Si substrate. Shao *et al.* 2014 showed high efficiency of UV detection by hybride carbon nanotubes/ZnO paper [195]. Combination of 1D organic fibers and ZnO ALD layers showed good prospects due to high surface-to-volume aspect ratio of the developed 1D nanostructures.

Viter *et al.* reported on photoluminescence sensors for ethanol vapours, based on 1D core/shell PAN/ZnO nanostructures [110]. The UV and visible emission bands of ZnO were studied before and after ethanol adsorption. Good sensitivity was found to 150 ppm of ethanol. Modeling of the surface properties was performed [196]. Tailoring of structure, electronic and sensor properties of 1D ZnO nanostructures was proposed.

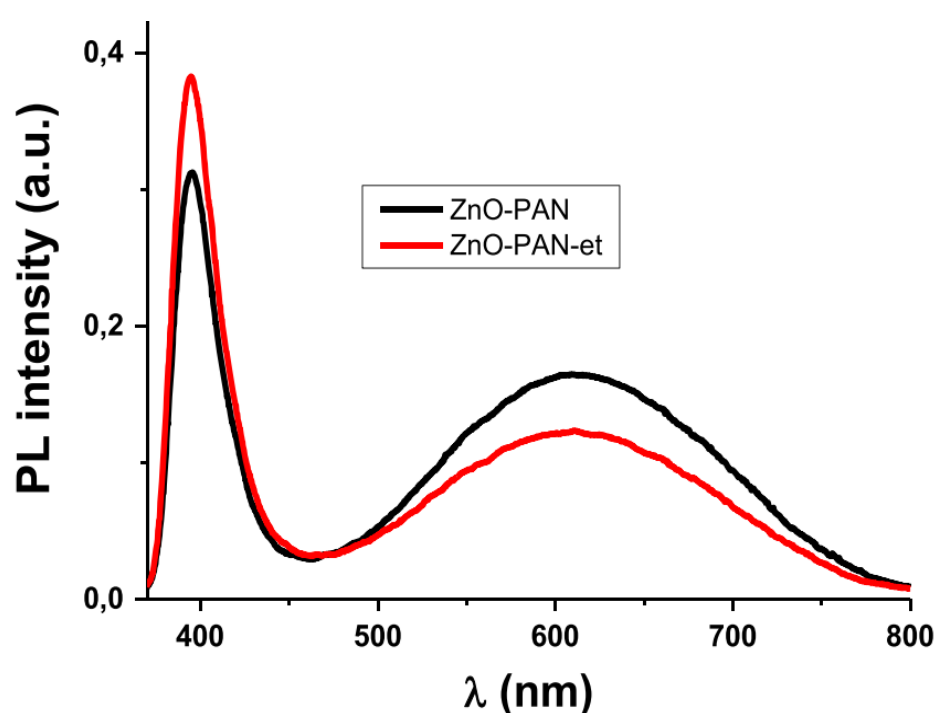


Figure 2-19. PL sensitivity test of ethanol vapor (150 ppm of ethanol) using 1D ZnO NSs obtained with 300 s electrospinning time and coated with 50 cycles ALD ZnO at 100 °C [110].

ZnO/PAN 1D nanostructures showed changes in PL intensity induced by ethanol adsorption (Figure 2-19). Ethanol increases the conductivity of ZnO due to the electron transfer to its conductance band. In the present work, ethanol adsorption increased NBE and decreased DLE emission. The authors suggested two possible mechanisms which could induce these phenomena: (i) Ethanol was adsorbed on optical defects and passivated them, and (ii) surface-bend bending decreased due to the ethanol adsorption. The presence of two peaks in the ZnO PL spectrum and their simultaneous changes due to the ethanol adsorption can make ZnO PL nanostructures suitable

for recognition of different VOCs by analyzing the integrated parameters of the NBE and DLE peaks.

2.6.2. ALD applications for biosensors

The applications of ALD metal oxides for biosensor devices are not well studied. A number of published papers on ALD metal oxides for biosensors is not compatible with the number of reports on the other techniques [197, 198]. Application of metal oxide ALD nanolayers for FET sensing devices were reported by Nakashima *et al.* and Sultan *et al.* [199, 200]. Nakashima *et al.* reported on use of HfO₂ as a gate in carbon nanotubes (CNT)-FET biosensor device [199]. Sultan *et al.* reported on ALD ZnO FET sensitivity to oxygen and possible applications in biosensors [200].

Ramesh *et al.* reported on ALD Al₂O₃, used in capacitance biosensors for protein sensing [201]. Couniot *et al.* developed on an advanced label free microfluidic capacitance biosensor, based on ALD Al₂O₃ nanolayers for the whole-cell bacteria detection [202]. Bajpai *et al.* reported on ALD ZnO nanorod resonators, used as mass biosensors [203].

Guo *et al.* reported on Al₂O₃, TiO₂, and SiO₂ ALD nanolayers, coated over GaN nanowires [204]. Protein adsorption was studied by dye-label fluorescence spectroscopy. SiO₂ nanolayer showed the best properties for protein adsorption due to the high content of hydroxyl groups on their surface [204].

The ALD deposited Al₂O₃ nanolayer was used to enhance the sensitivity of optical fiber cladding mode to surrounding refractive index (SRI) variation [205]. Applications in chemical sensors were discussed [205]. Purniawan *et al.* reported on TiO₂ ALD nanolayers as evanescent waveguides for biomedical sensing applications [206].

ALD-SiO₂ nanolayers have been used for biosensor applications [207]. The developed silica layers were deposited on InGaAsP lasing system, and a lasing shift was observed after adsorption of the biomolecules on the silica surface [207].

The developed ALD sensitive layers were compatible with the silane-based surface chemistry for covalent binding [207]. Watanabe *et al.* showed the application of ALD deposited ZrO₂ nanolayers for biosensor applications. Similarly to the methodology, reported by Cha *et al.*, the shift of the lasing was observed due to DNA adsorption on the ZrO₂ surface which was deposited over GaInAsP emitting system [208]. The developed sensor showed also good sensitivity to pH changes [208].

ALD deposited Al₂O₃ nanolayers were combined with plasmonic nanostructures to work as an active biosensor surface [115]. Another application of the Al₂O₃ nanolayer was to enhance the SERS signal [115].

Some of the recent investigations of ALD in biosensors applications are represented in the Table 2-6.

Table 2-6. ALD for biosensors applications.

Type of materials	Applications	References
ZnO	nanorod resonators, used as mass biosensors	[203]
SiO ₂	study of protein adsorption	[204]
HfO ₂	gate in carbon nanotubes (CNT) field effect transistors (FET) biosensor device	[199]
TiO ₂	evanescent waveguides for biomedical sensing applications	[206]
ZnO	the effects of oxygen adsorption by measuring FET characteristics	[200]
Al ₂ O ₃	capacitance biosensors for protein sensing	[201]
Al ₂ O ₃	enhancement of the sensitivity of optical fiber cladding mode to surrounding refractive index	[205]

	(<i>SRI</i>) variation	
Al ₂ O ₃	an advanced label free microfluidic capacitance biosensor for the whole-cell bacteria detection	[202]
SiO ₂	protection of the InGaAsP band-edge laser (BEL) devices from harsh chemicals; ALD-passivated BEL devices as label-free biosensors	[207]
ZrO ₂	GaInAsP photonic crystal nanolaser sensor independently detected the environmental index and surface charges on the basis of the variation in emission wavelength and intensity, respectively.	[208]
SiO ₂	a stacked structure of high-k materials (Al ₂ O ₃ and HfO ₂) with an ultrathin SiO ₂ to	[209]

	enhance biomolecular sensibility in Si-NW biosensors	
ZnO	Cholesterol ZnO biosensors	[210]
TiO ₂	TiO ₂ based Guided Mode Resonance Filter (GMRF) biomolecular sensor	[211]
CoO	NPG/CoO composite exhibits high catalysis activity for glucose as well as excellent sensitivity and selectivity for the detection of H ₂ O ₂ , which holds unique promise for applications in nonenzymatic H ₂ O ₂ biosensors	[212]
Alumina	the quantify performances of a biofunctionalization layer to bind proteins	[213]
Al ₂ O ₃	the native-silicon-oxide coating with aluminum oxide of	[214]

	<p>nanometer thickness insignificantly lowers the femtomole sensitivity of nanowire-transistor biosensors, but provides their stability in bioliquids</p>	
HfO ₂	<p>MoS₂ transistor sensor for characterizing the real-time association/dissociation kinetics of the (TNF-α)-antibody reaction</p>	[215]
Al ₂ O ₃	<p>low-cost and label-free technique for qualitative and quantitative detection of specific biointeractions - visualization of biosensors using enhanced surface plasmon resonances in capped silver nanostructures</p>	[216]
TiO ₂	<p>improving of the performance</p>	[217]

Al_2O_3	of extrinsic Fabry-Pérot interferometers	
-------------------------	---	--

ALD coatings have important application in nanopore biosensors [4]. The latter methods permit to detect single object such as protein, DNA or nanoparticle. ALD, it is a powerful technique to fashion nanostructure with complex shapes and high aspect ratio [159]. These methods have several advantages. Indeed, they permit (i) a perfect control of the final diameter, (ii) an increase of the reactivity of the surface and (iii) a homogenous coating inside a nanopore with high aspect ratio.

ALD permits to deposit different oxide or non-oxide materials which broaden the scale of nanopore functionalization. In the area of nanopore, ALD was used to tune SiN [218, 219], with oxide metals such as Al₂O₃ [220], Al₂O₃/ZnO bilayers [221, 222], TiO₂. HfO₂ [223], Al₂O₃/ZnO were deposited on alumina pores [224]. For polymeric materials Al₂O₃ [220, 225], Al₂O₃/ZnO [222, 226], can be used, however, the processes have been done at low temperature (60°C). In order to limit the roughness due to the crystallinity, Al₂O₃/ZnO nanolaminates are used to reduce the diameter of the nanopore up to 1 nm in PET nanopores [227]. Another advantage from metal oxide- deposition by ALD is the possible functionalization of the surface, thanks to the –OH function, by silanisation in gas phase for instance [222]. However, the functionalization is not only located inside the nanopore. This permit to obtain a homogeneous functionalisation inside and outside the nanopore [228, 229].

For single molecule sensing, Al₂O₃ was the most used. It increases the detection capabilities of the nanopore by adjusting precisely its surface properties [219], by reducing the noise [220, 230], and by neutralizing the surface charges to increase the capture rate of DNA [231] or other negative poly-electrolyte. Using alternate bilayers of Al₂O₃/ZnO on PET nanopores creates a low roughness of the deposited layers. Using this functionalization, completed by a cover by trimethyl silane, it have been show how the surface charge of nanopore influence the polynucleotide translocation [232, 233].

The scheme of preparation of nanopore biosensors is shown in Figure 2-20. A periodic mask was formed on a polymer (poly(ethyleneterephthalate) (PET)) using UV lithography. The film was etched in KOH solution to form pores. The pores were coated with Al₂O₃/ZnO nanolaminates. Gramicidin (gA), solved in methanol, was added to pure water (pH=8) to reach a final concentration of 10⁻⁴ M. Then, the porous PET/nanolaminate was filled with gA solution. The gA incubation procedure was performed during 72 h at 6 °C. A gA confinement throughout in PET/nanolaminate pores was achieved.

Measurement scheme of the ALD pore-based nanostructures is shown in Figure 2-21.

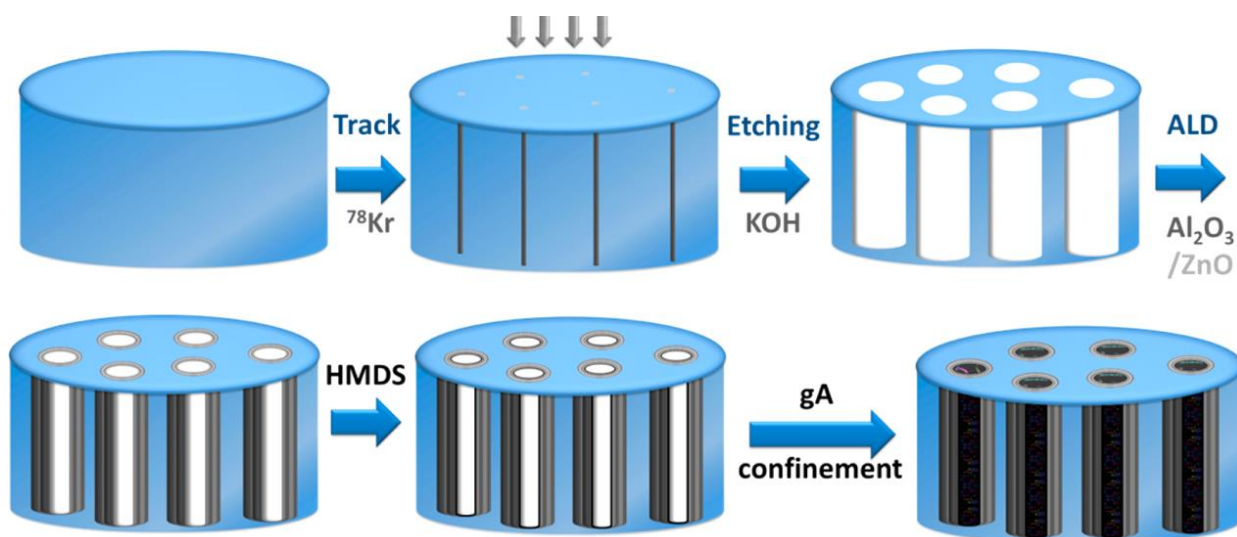


Figure 2-20. Schematic process for hybrid membrane synthesis [4].

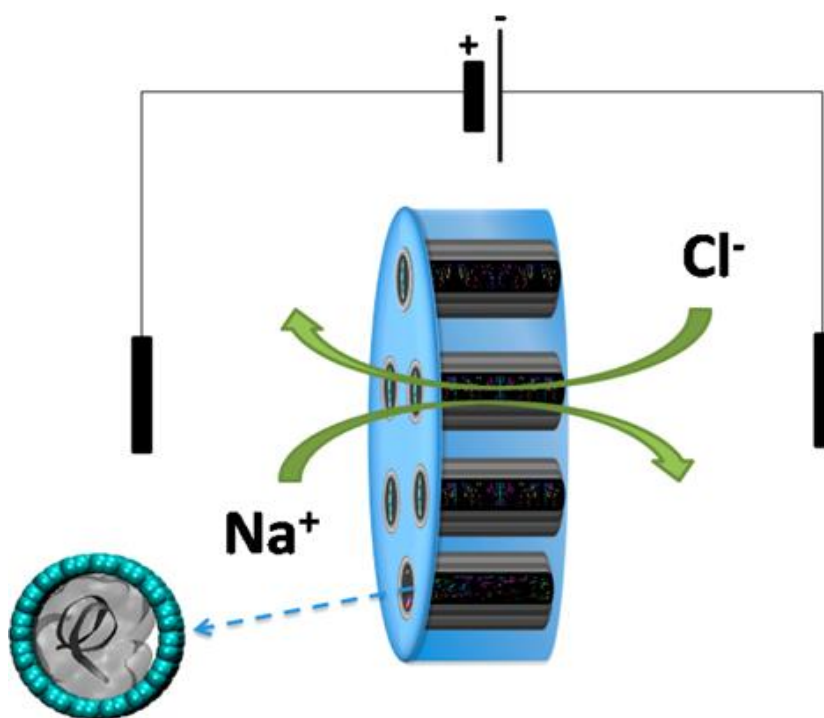


Figure 2-21. Measurement scheme of ALD-based pore biosensor.

Conductance measurements were studied before and after gA incubation in the ALD based nanopores (Figure 2-22). It was shown that gA confinement in the ALD-based pores significantly changed.

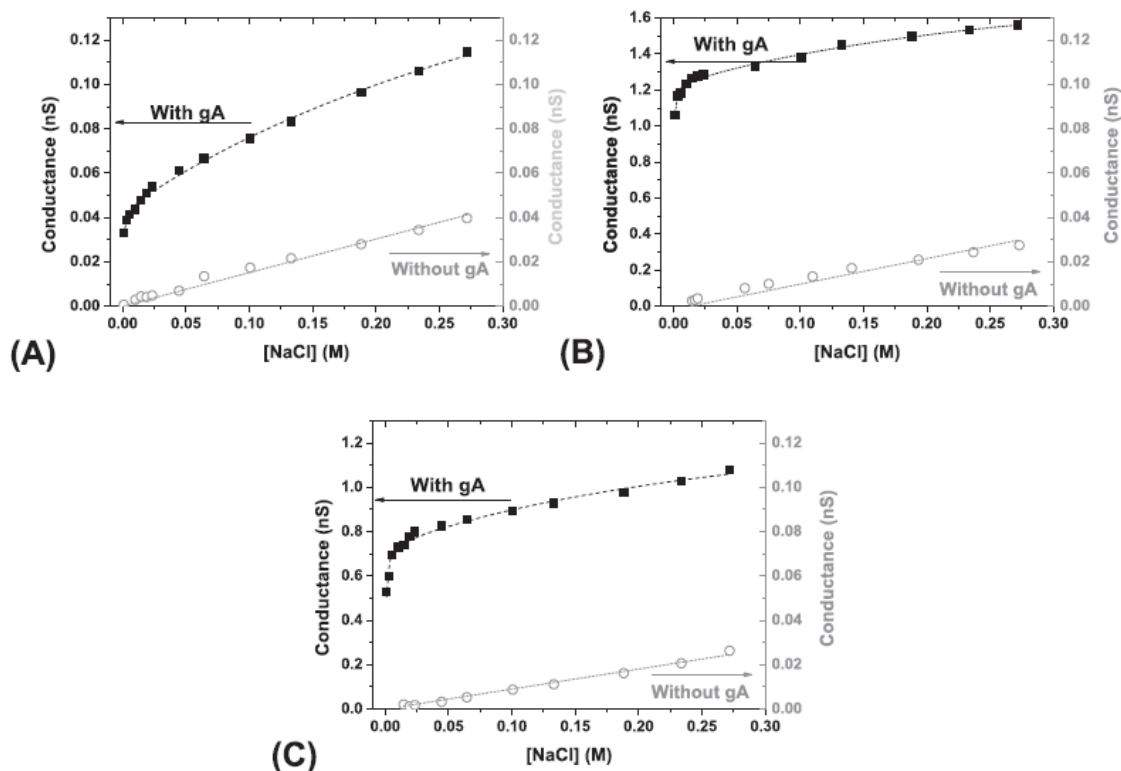


Figure 2-22. Evolution of nanopore conductance with and without confined gA under NaCl symmetrical concentration in ALD-based pores with different diameters : (a) 10 nm pore (b) 6 nm pore and (c) 2 nm pore. Black squares and gray rounds show signal with and without gA in the pores, respectively [4].

The advanced approaches were also shown on single pore, modified with ALD technique for α -hemolysin capturing at the entrance of a long biomimetic nanopore of diameter 5 nm [5]. Similarly, to the study of Chaaya *et al.* [4] pore conductivity was measured at different concentrations of α -hemolysin.

2.7. Advantages and limitations of ALD

Summarizing the collected information about ALD technology we can emphasize following advantages:

1. Conformal coating on the surface;
2. Compatibility with non-standard (optical fibers, capillaries, etc.) substrates;
3. Tailored structure, electronic and optical properties of deposited ALD layers.
4. Compatibility with electrospinning and lithography for deposition of 1D nanostructures with high surface-to-volume aspect ratio;

5. Wide range of applications (sensors, protective coatings, photodetectors, solar cells, etc.)
6. Good potential for development of novel materials.

While ALD has many promising features, it also suffers from slow deposition rates, usually only a fraction of a monolayer is deposited in one cycle. Because of the long cycle times involved in pulsing and purging precursors and the layer-by-layer nature of the deposition, most ALD rates are on the order of 100–300 nm/h [234, 235]. This rate is strongly dependent on the reactor design and the aspect ratio of the substrate. As the surface area and volume of an ALD reactor increase, so does the time needed for pulsing and purging. High aspect ratio substrates also require longer pulse and purge times to allow for the precursor gas to disperse into trenches and other three dimensional features. To combat this shortcoming, spatial ALD has emerged as a promising technique that may significantly improve throughput [236-238]. Spatial ALD operates by eliminating the traditional pulse/purge chamber and replacing it with a spatially-resolved head, which exposes the substrate to a specific gas precursor based on location. In one design, as the head translates around the substrate, it alters the exposed precursor, resulting in film growth. Alternatively, spatial ALD has also been demonstrated in which the substrate moves past stationary precursor nozzles, which are arranged so that by passing by them, precursor cycling is achieved and the film is grown. Overall, with spatial ALD techniques, deposition rates around 3600 nm/h are possible [235].

It is not very practical to grow micrometer-thick films by ALD. The slow growth rate can be compensated by processing large batches of substrates in one process, as is done in TFEL production. In microelectronics, however, single-wafer processing is preferred. Fortunately the films needed for future-generation ICs are very thin and thus the slowness of ALD is not such an important issue.

Another limiting factor in the application of ALD to thin film processing includes: processing of ternary and more complicated compounds requires the constituent precursors to volatilize and then react at a common temperature ('ALD window') because during the growth process the reactor temperature cannot be changed.

As a chemical process, ALD has a risk of impurities. The impurities can come from gas precursors and/or a carrier gas, the process requires material with a high degree of cleanliness. Impure chemicals can lead to the incorporation of impurities and to the growth of poor quality films [234].

2.8. Prospects of ALD

With devices becoming ever smaller and increasingly structured into complex three dimensional shapes, the need for controllable and conformal thin films has never been greater. ALD, with its sequential self-limiting reactions, is able to meet these demands in one of the most effective methods possible. Comparable techniques, such as CVD and PVD, cannot always provide the same level of uniformity, conformality and thickness control at the Angstrom level. Because of the advantages of ALD, ALD processes have been developed for a wide variety of materials, ranging from metals to metal oxides to complex ternary materials, allowing ALD to become incorporated into industrial procedures.

Atomic layer deposition (ALD) provides a unique tool for the growth of thin films with excellent conformity and thickness control down to atomic levels. The deposition of noble metals by ALD technique is one of the perspective directions of ALD method [239-249]. Research on thermal ALD of noble metal thin films has been very active since the first reports (2003). Noble metals, which include ruthenium, osmium, rhodium, iridium, palladium, platinum, silver, and gold, have proven to be of wide technological importance. A group of authors headed by Hamalainen has reviewed a thermal ALD of noble metals and their oxides [250]. In this review, reaction mechanisms in various types of processes were discussed and issues in nucleation were addressed. Deposition temperatures, film growth rates, and purities as well as evaporation temperatures used for noble metal precursors were tabulated for comparison.

The authors summarized the selected properties of the noble metal oxides in Table 2-7.

Atomic layer deposition (ALD) is a vapour-phase deposition technique capable of depositing high quality, uniform and conformal thin films at relatively low temperatures. These outstanding properties can be employed to face processing challenges for various types of next-generation solar cells [179]. Hence, ALD for photovoltaics (PV) has attracted recently great interest in academic and industrial research. The use of ALD for several PV applications has been studied from the early 1990s to the present day [251].

van Delft *et al.* [252] overviewed the recent progress of ALD layers applied to various solar cell concepts and discussed their future prospects. The intention is to focus on results obtained with actual solar cells with at least one layer deposited by ALD and to address the viability of this technique for the PV industry. ALD is being introduced in the PV industry and it is expected that it will be part of the standard solar cell manufacturing equipment in the near future.

The remarkable advances and increasing interest in ALD technology in the last years establish ALD as a promising tool for addressing different aspects of nanostructured photovoltaics [253].

Table 2-7. Selected properties of the most common noble metal oxides.

noble metal	metal oxide	density (g cm ⁻³)	melting point (°C) ^a	resistivity (μΩ cm) ^b
Ru	RuO ₂	7.1	1300 dec.	35, 50
	RuO ₄	3.3	25 (bp 40)	
Os	OsO ₂	11.4	500 dec.	15, 60
	OsO ₄	5.1	41 (bp 131)	
Rh	Rh ₂ O ₃	8.2	1100 dec.	5 × 10 ⁶
	RhO ₂	7.2		100
Ir	Ir ₂ O ₃		1000 dec.	
	IrO ₂	11.7	1100 dec.	35 ^[011] , 49 ^[001] , 60
Pd	PdO	8.3	750 dec.	
Pt	PtO	14.1	325 dec.	
	PtO ₂	11.8	450	1 × 10 ¹²
Ag	Ag ₂ O	7.2	~200 dec.	
	AgO	7.5	>100 dec.	
	Ag ₂ O ₂	7.4	>100	
Au	Au ₂ O ₃		~150 dec.	

ALD is well known due to its success in preparing Al₂O₃-based surface passivation layers for c-Si homojunction cells in the field of PV. Macco *et al.* [254] provide an overview of the new concepts, and highlights both the current role and prospects of ALD in this field. ALD is a versatile technique capable of preparing many of the metal oxide thin films that are ubiquitous in the field of passivating contacts. The main advantages of ALD such as thickness, compositional control and large-area uniformity make it highly likely that ALD will continue to play a pervasive role in this field.

The present PhD thesis is a result of the international collaboration between not only University of Montpellier (France) and Odessa National I.I. Mechnikov University (Ukraine), but as well such education centers as Adam Mickiewicz University (Poland), University of Latvia and Vilnius University (Lithuania). And all of these research centers participated in the investigation of the prepared samples and in discussion of the gained experimental results for the further writing of publications.

In more details, all experimental procedures for the preparation such samples as silicon nanowires by metal-assisted chemical etching in combination with nanosphere lithography

methods, polyacrylonitrile (PAN) fibers by electrospinning technique, and the production of a large surface of nanoarrays functionalized with proteins for antibody detection were done at European Membrane Institute (IEM). The deposition of ZnO thin layers and Al₂O₃/ZnO nanolaminates by ALD technique was carried out at IEM as well. The custom-made ALD reactor, which was used for the synthesis of the ultrathin ZnO films and Al₂O₃/ZnO nanolaminates, is represented in the Figure 2-23.

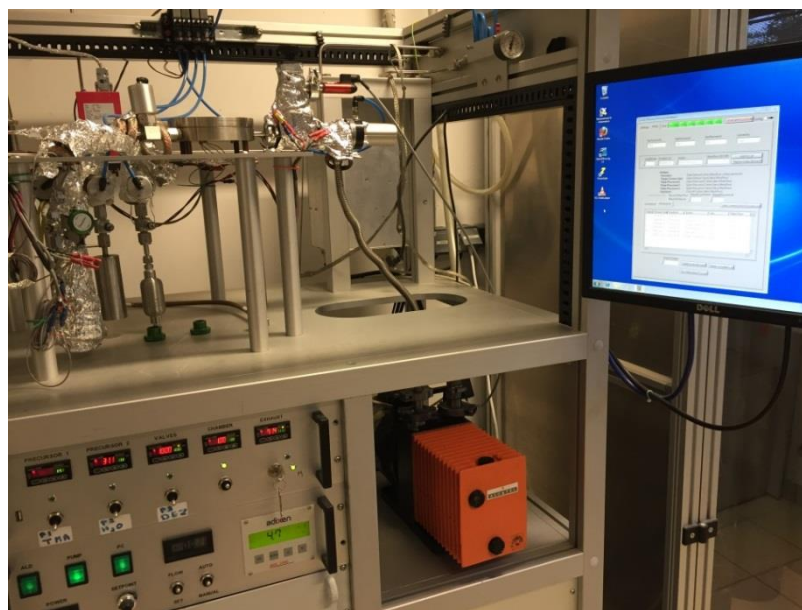


Figure 2-23. Atomic layer deposition reactor.

ALD was performed using sequential exposures of TMA (DEZ) and H₂O separated by a purge of Argon with a flow rate of 100 standard cubic centimeters per minute (sccm) to deposit ZnO and Al₂O₃/ZnO. The deposition regime for ZnO and Al₂O₃ consisted of 0.2 s pulse of TMA (DEZ), 30 s of exposure to TMA (DEZ), 30 s of purge with argon followed by 2 s pulse of H₂O, 30 s of exposure to H₂O, and finally 40 s purge with argon. Al₂O₃/ZnO ultrathin nanolaminates with different numbers of cycles were deposited on electrospun PAN nanofibers. The deposition temperature was fixed to 100 °C. GPC of ~0.2 nm/cycle has been observed for Al₂O₃ and ZnO coating. The typical process list for the ALD of ZnO films is represented in the Table 2-8.

In this thesis, polyacrylonitrile (PAN) nanofibers were produced by electrospinning technique and after coated with ZnO/Al₂O₃ nanolaminates by ALD method to enhance the electronic and optical properties.

Electrospinning is a simple, versatile, and cost-effective technology, which generates fibers with high surface area to volume ratio. The schematic diagram of set up of electrospinning is

presented in the Figure 2-24. The used electrospinning machine was a homemade device using an HPx 600 605 generator (physical instruments) and a KDS 100 syringe pump.

Table 2-8. The process list for the ZnO ALD

Index	Process Time	Duration	Action	Gas	Mass Flow
0	00:00:00,00	00:00:00,20	Pulse Precursor3	DEZ	25,0
1	00:00:00,20	00:00:40,00	Exposure	DEZ	0,0
2	00:00:40,20	00:01:00,00	Purge (Carrier Gas)	Argon	100,0
3	00:01:40,20	00:00:02,00	Pulse Precursor2	H ₂ O	25,0
4	00:01:42,20	00:00:40,00	Exposure	H ₂ O	0,0
5	00:02:22,20	00:01:00,00	Purge (Carrier Gas)	Argon	100,0

The polymer solution (Polyacrylonitrile (10 wt % PAN) was dissolved in dimethylformamide (DMF)) is electrospun in ambient air atmosphere under a high voltage (25 kV) using a syringe connected to the positive output of the generator. A fix collector was placed 25 cm from the tip of the syringe and was related to the negative output of the generator. The droplet is transformed to a Taylor cone due to the electrostatic field applied between the syringe and the collector. The evaporation of the solvent during the process induces the formation of a net of submicron fiber.

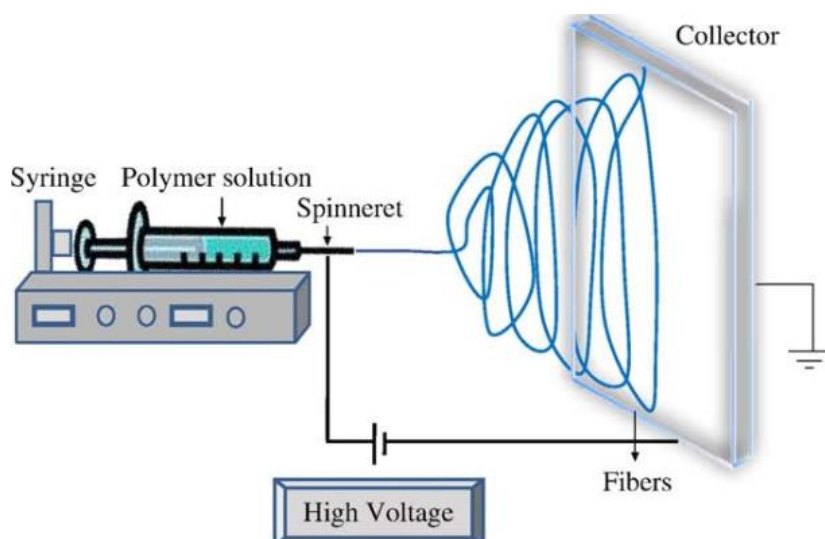


Figure 2-24. Schematic diagram of set up of electrospinning apparatus [255].

PAN nanofibers are good chemically stable material for 1D core/shell nanostructure design [256]. It was shown that PAN nanofibers have good mechanical and thermal stability. The

adsorption sites present on the surface of the PAN fibers would facilitate the nucleation of the metal oxide layers by ALD. Thus, integration of metal oxide ALD technique and PAN nanofibers has a good perspective.

The study of the prepared samples, which were mentioned above, was done in European Membrane Institute (IEM), University of Montpellier, (Montpellier, France), Adam Mickiewicz University (Poznan, Poland), University of Latvia (Riga) and Vilnius University (Lithuania). The details of the performed investigations are represented in the Table 2-9.

Table 2-9. The experimental tools used for the study of the samples prepared at the present thesis.

The studied sample	Analysis	Device	Notes	Place
Silicon nanowires (SiNWs) covered with 20 and 50 nm of ZnO by ALD	Structural and chemical compositions of the SiNWs/ZnO	Scanning electron microscopy (SEM, S-4800, Hitachi)		European Membrane Institute (IEM), University of Montpellier, Montpellier, France
	Crystallographic structure of the films	X-Ray diffraction (XRD, PANalyticalXpert-PRO diffractometer equipped with a X'celerator detector using Ni-filtered Cu-radiation)	The XRD spectra were measured in the 2θ angular region between 10° and 60° .	NanoBioMedical Centre at Adam Mickiewicz University, Poznan, Poland
	Structural properties	Transmission electron microscopy (TEM, JEOL ARM 200F high-resolution transmission electron microscope)	The cross-sections and lamellas for TEM investigations were prepared by Focused Ion Beam (FIB). The FIB milling was carried out with a JEOL, JIB-4000.	

		(200 kV) with an EDX analyzer)		
	Raman scattering measurements	Renishaw micro-Raman spectrometer equipped with a confocal microscope (Leica)	The samples were measured in backscattering geometry with a spectral resolution of 1.0 cm^{-1} . The incident light was not polarized and also the light detector contained no polarization filters. The Raman scattering spectra were excited by a 488 nm laser. The beam was focused on the samples with a 50 x microscope objective with a numerical aperture of 0.4. The incident optical power was changed by using neutral density filters in the beam path.	
	Optical properties by diffuse reflectance	Standard Shimadzu UV-3600 spectrophotometer	The spectral range 200-1400 nm. Scanning step of 1 nm.	State Research Institute Center for Physical Sciences and Technology, Vilnius, Lithuania

	spectroscopy			
	Photoluminescence spectroscopy	Standard fluorometer (FS5 Spectrofluorometer (Edinburg instruments Ltd, 2 Bain Square, Kirkton Campus, EH54 7DQ, UK))	Photoluminescence spectroscopy was studied in spectral range of 350–800 nm. The excitation of luminescence was performed at wavelength of 280 nm.	
ZnO films on Si substrates; ZnO/anti-GVA samples	Optical properties were characterized by photoluminescence (PL) study of ZnO films	The spectrometer TRIAX 550 made by Jobin Yvon (New Jersey, USA)	The samples were excited by a solid state laser with a wavelength of 355 nm. The excited ZnO photoluminescence entered a spectrometer with the slit entrance of 1 by 1 mm, a focal length of 550, a 600 gr/mm grating and a liquid nitrogen cooled CCD as the detector. The large, 0.4 mm wide, excitation area was produced in order to obtain an average	Department of Physics, Chemistry and Biology, Linköping University, Linköping, Sweden

<p>by etching in O₂ plasma</p> <p>Cy5-PEG-NHS-modified polystyrene spheres</p> <p>PS spheres functionalized with:</p> <ul style="list-style-type: none"> - Biotin-PEG-NH₂ and mPEB after addition of avidin (labeled with alexa fluor 647) - Biotin-PEG-NH₂ and avidin (unlabelled) after AntiAvidin*(labeled with Alexafluor 488) 		<p>Epifluorescence microscope DM6000</p>	<p>The alexa fluor 647 and 488 were detected using CY5 and FTIC cube respectively.</p>	
---	--	--	--	--

<p>Polyacrylonitrile (PAN) nanofibers coated with ZnO/Al₂O₃ nanolaminates</p>	<p>Structural and chemical compositions</p>	<p>JEOL ARM 200F high-resolution transmission electron microscope (200 kV) with an EDX analyzer (JED2300, at least 30 accumulations, matrix 512 × 512 points in STEM mode).</p> <p>FTIR spectra were obtained with the Bruker VERTEX 70v vacuum spectrometer using the RT-DLaTGS detector (spectral resolution of 4 cm⁻¹).</p> <p>X-ray diffraction measurements were performed with PANalytical Xpert-</p>	<p>Dark and bright field detectors were used.</p>	<p>NanoBioMedical Centre at Adam Mickiewicz University, Poznan, Poland</p>
---	---	--	---	--

	Surface structural and chemical properties	<p>PRO diffractometer equipped with a X'celerator detector using Ni-filtered Cu-radiation.</p> <p>XPS/UPS technique mounted within the Omicron Nanotechnology multiprobe UHV system, using a monochromatized Al Kα X-ray as the excitation source ($h\nu = 1486.6$ eV) and choosing C 1s (284.6 eV) as the reference line. XPS was conducted under ultrahigh vacuum (10^{-7}</p>	CasaXPS software was used to analyze the XPS data.	
--	--	--	--	--

	Optical properties	Pa). PL spectroscopy (in the spectral range of 370-800 nm).	The excitation of luminescence was performed by a solid state laser source (Nd:YAG, 355 nm, 13 mW cm ⁻²).	
--	--------------------	--	---	--

In the present work, we used a simple method based on metal-assisted chemical etching (MACE) in combination with nanosphere lithography (NSL) to produce highly ordered silicon nanowires (SiNWs) arrays [257].

These methods have a number of advantages. MACE is a simple, inexpensive process, and able to control various parameters of the etched nanostructures, such as cross-sectional shape, diameter, length, and crystallographic orientation. In parallel, the main advantages of NSL consist of a short preparation time, a high level of hexagonal structure orientation and a possibility of application of large, monolayered masks directly onto any kind of surfaces.

Nanosphere lithography is a powerful fabrication technique to produce nanoparticle arrays with controlled shape, size, and interparticle spacing. The need for monodisperse, reproducible, and materials general nanoparticles has driven the development and refinement of the most basic NSL architecture as well as many new nanostructure derivatives. In this technique the submicron latex particles self-organized into hexagonal pattern, which was used as template to create ordered 2D array of desired materials.

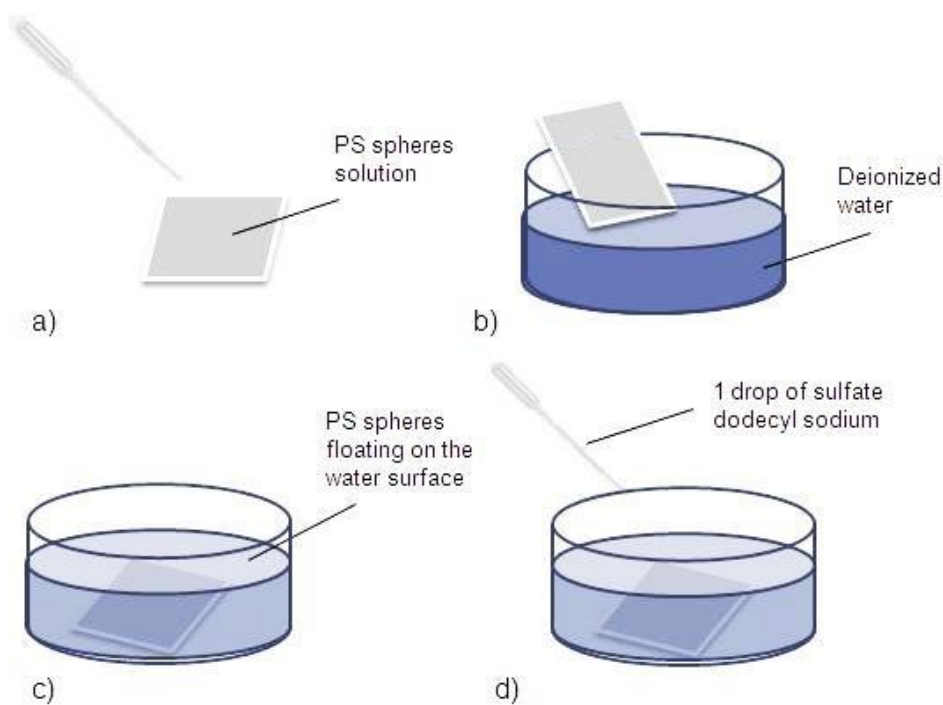


Figure 2-25. The scheme of floating-transferring technique.

Several methods were developed for the production of colloid monolayers, such as Langmuir-Blodgett, spin-coating, vertical deposition and floating-transferring technique. Generally, the floating-transferring technique is simple and can create compact hexagonal patterns over large area on any surface. Figure 2-25 shows the general floating-transferring technique and the obtained 2D

polystyrene latex patterns. In this indirect methods, high quality monolayers are first formed on an intermediate surface (like water) that allows for better particle ordering, after addition of sodium dodecyl sulfate solution to consolidate the particles and then transferred to the target substrate. After, the sample is dried in air at room temperature and spheres self-assembled into a close-packed, two-dimensional ordered lattice via attractive capillary forces.

Basically, MACE is based on electrochemical processes where a Si wafer covered by a noble metal layer is immersed in the etching solution consist of etchant and oxidizing agent. The scheme of the overall etching process is represented in Figure 2-26.

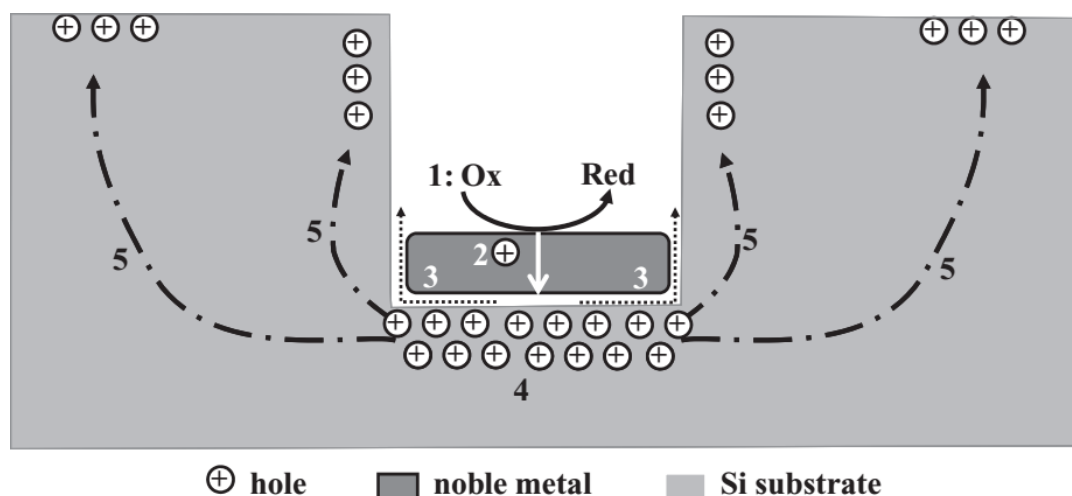


Figure 2-26. Scheme of processes involved in metal-assisted chemical etching [258].

In our case, the Si substrate covered by spheres is in contact with Au antidot arrays and etched in a mixed solution of hydrogen fluoride (HF) and hydrogen peroxide (H_2O_2), in Figure. The noble metal acts as a microscopic cathode on which the reduction of the oxidant occurs. The first step of the reaction might be the reduction of the H_2O_2 at the metal/solution interface that can be called cathodic site. The reduction is like following:



Electrons are taken from the gold that dissolved in ions following the dissolution reaction



Au is more electronegative than Si, so Au ions are able to recover into gold by catching electrons from Si bulk. That involves an injection of positives charge carriers, called holes. They are locally injected underneath the gold layer. On this weakness site, Si is oxidized into SiO_2 and the attack by HF occurs afterward, and the SiO_2 becomes an aqueous byproduct.



The Au layer sinks into the tracks around the PS and the SiNWs appear in this way.

2.9. Conclusion

Atomic layer deposition (ALD) is a vapour-phase deposition technique capable of depositing high quality, uniform and conformal ultra-thin films at relatively low temperatures (below 100 °C). Currently, ALD is considered as one of the most promising thin film deposition techniques for enabling nanoscale device fabrication. The recently investigations in the area of ALD of ZnO, Al₂O₃, and Al₂O₃/ZnO nanolaminates, and potential applications of ALD in various research fields were overviewed in this chapter. With devices becoming ever smaller and increasingly structured into complex three dimensional shapes, the need for controllable and conformal thin films has never been greater. ALD, with its sequential self-limiting reactions, is able to suit to these demands. The requirements, which have to be taken into consideration for choosing a chemical precursor for ALD process, were presented. The precursors for the ALD deposited ZnO and Al₂O₃ thin films were overviewed and presented in the Tables 2-2 and 2-3, respectively. The applications of ALD metal oxides for biosensor devices are not well studied. Some recent investigations of ALD biosensor applications were presented in the Table 2-6. The collected information about ALD technology was emphasized with the advantages and limitations. Finally, at conclusion part of this chapter the prospects of the ALD are presented.

In this thesis, the ALD technique was used for the deposition of ZnO and Al₂O₃/ZnO nanolaminates thin films on the different substrates. The following tasks were performed:

- Improvement of the properties of SiNWs, which were prepared by the combination of NSL and MACE techniques, by the ALD deposited ZnO thin films (20 and 50 nm); morphology and the organization control of SiNWs on a large area;
- ZnO films formed by ALD as an optical biosensor platform for the detection of Grapevine virus A-type proteins (GVA-antigens);
- A specific control of protein anchoring by the development of multifunctional surface with large-scale array of polystyrene spheres (PSS), which produced by NSL and further blocking the unspecific adsorption of protein on the surface of the PSS by PEG SAMs
- The tuning of structural properties and the enhancement of electronic and optical properties of 1D PAN ZnO/Al₂O₃ nanolaminates designed by atomic layer deposition (ALD) and electrospinning.

CHAPTER III

Large-scale protein/antibody patterning with limiting unspecific adsorption

This chapter has been published in *Journal of Nanoparticle research* as:

Viktoriia Fedorenko^{1,2}, Mikhael Bechelany¹, Jean-Marc Janot¹, Valentyn Smyntyna², Sebastien Balme¹, *Large-scale protein/antibody patterning with limiting unspecific adsorption*, *Journal of Nanoparticle research*, 2017, 19(10), 351

¹ Institut Européen des Membranes (IEM UMR5635), Université de Montpellier, CNRS, ENSCM, Place Eugène Bataillon, F-34095 Montpellier Cedex 5, France

² Faculty of Physics, Experimental Physics Department, Odessa National I. I. Mechnikov University, 42, Pastera, Odessa 65026, Ukraine

In this chapter we report the synthesis of multifunctional surface with polystyrene spheres and selective functionalization ability. We aim to attach specifically the protein directly to the PS spheres and to limit its unspecific adsorption. In our work we use a silicon wafer coated with a thin adhesion layer of chromium (15 nm) and a layer of noble metal (50 nm) as a substrate. PS spheres are deposited on the gold surface using the floating-transferring technique. The PS spheres were then functionalized with PEG-biotin and the defects by self-assembly monolayers (SAMs) PEG to prevent unspecific adsorption. The schematic diagram of overall process for protein immobilization is represented in Figure a.

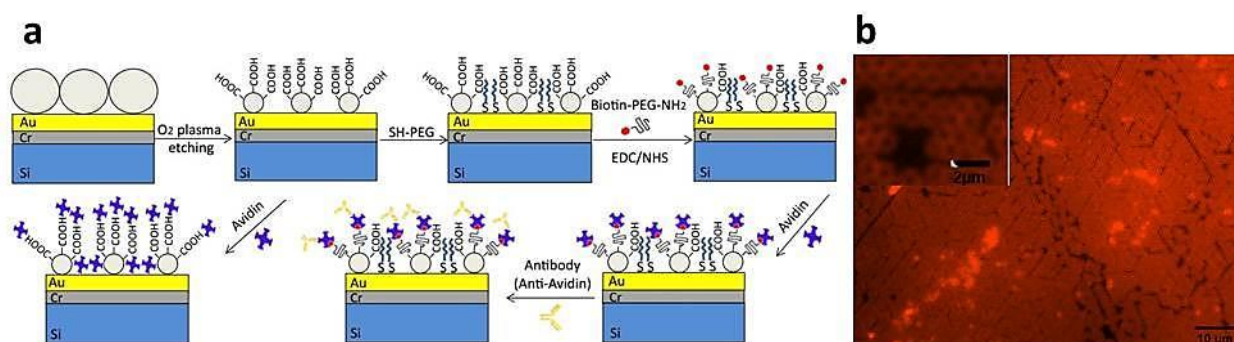


Figure. The schematic diagram of overall process for protein immobilization (a), fluorescent images of Cy5-PEG-NHS-modified polystyrene spheres (the inset indicates a zoom).

In order to confirm that the fluorescence comes from the dyes we performed some additional experiments. And we proved that our strategy allows designing a large scale of monolayer of PS spheres and that our strategy of functionalization is relevant to functionalize PS spheres surface and gold surface with different functions.

In order to prove that the large-scale nanoarrays are suitable for antibody detection, different samples were functionalized with PEG-biotin and unlabeled avidin.

Using epifluorescence microscopy, we confirmed that after immersion of sample on target protein (avidin and anti-avidin) solution, the latter are specifically located on polystyrene sphere. Figure b shows a fluorescence microscopy image of the prepared sample.

Thus, in this chapter we present the fabrication of large-scale nanoarrays which permit to control protein grafting and limit the unspecific adsorption. These results are meaningful for exploration of devices based on large-scale nanoarray of PS spheres and can be used for detection of target proteins or simply to pattern a surface with specific proteins.

3.1. Abstract

A simple synthetic route based on nanosphere lithography has been developed in order to design a large-scale nanoarray for specific control of protein anchoring. This technique based on two-dimensional (2D) colloidal crystals composed of polystyrene spheres allows the easy and inexpensive fabrication of large arrays (up to several centimeters) by reducing the cost. A silicon wafer coated with a thin adhesion layer of chromium (15 nm) and a layer of gold (50 nm) is used as a substrate. PS spheres are deposited on the gold surface using the floating-transferring technique. The PS spheres were then functionalized with PEG-biotin and the defects by self-assembly monolayer (SAM) PEG to prevent unspecific adsorption. Using epifluorescence microscopy, we show that after immersion of sample on target protein (avidin and anti-avidin) solution, the latter are specifically located on polystyrene sphere. Thus, these results are meaningful for exploration of devices based on large-scale nanoarray of PS spheres and can be used for detection of target proteins or simply to pattern a surface with specific proteins.

Keywords: Nanosphere, Avidin, Large-scale nanoarrays, Biosensor applications.

3.2. Introduction

In the area of biosensing and bioengineering, one of challenges is to produce large-scale patterning for specific anchoring of target protein. This challenge requires an ability to manipulate nano-objects, to order them on large surface areas and to control the location of protein attachment. One of the strategies for the deposition of a large-scale array is the nanosphere lithography using two-dimensional (2D) colloidal crystals that is composed of microscale polystyrene spheres (PS spheres). This technique as introduced by Deckman and Dunsmuir [259] allows the synthesis of large arrays (several millimeters) [260, 261]. This method is fascinating because it is rather easy in comparison to the traditional lithographical methods. Using this process, well-ordered and controlled micro/nanostructures could be designed on a large-area substrate using a mono or several layers of PS spheres.

Polystyrene is one of the most extensively used types of plastic, and the number of its applications is growing over the past 20 years. It is an aromatic polymer obtained by polymerization of styrene monomers [262]. It is also biocompatible and is not expected to adversely affect interactions of nanoparticles with biological systems. Polystyrene nanoparticles have been used to fashion large-scale nanoarray for various applications, such as biosensors [263], photonics [264], and self-assembling of nanostructures [265]. Specifically surface-modified polystyrene nanoparticles are homogeneous, exhibit a low polydispersity index, and form stable colloids in

biological fluids [266]. Because polystyrene nanoparticles can be easily synthesized in a wide range of sizes with distinct surface functionalization, they are perfectly suited as model particles to study the effects of the particle surface characteristics on various biological parameters. The protein micro/nano patterning using PS spheres has been previously reported. In most of case, the strategy consists to remove the sphere in order to adsorb the proteins [267-269]. There are several limitations for this strategy because the adsorption is an unspecific process which is not suitable to develop specific biosensor. This process does not allow controlling the protein orientation and denaturation.

Thus, the development of large-scale nanoarray requires an effort to control the protein location, integrity, and selectivity; this includes preventing the unspecific adsorption and the grafting of specific probe on the surface. The adsorption process is regulated by the properties of the protein as well as those of the surface of the material, the environmental conditions, and the kinetics of the process [270, 271]. In the case of biosensor, unspecific protein adsorption may limit the effectiveness of the surface that provides the active component of the biosensors. This induces a low signal from the sensor and often causes a high background (noise) signal. Thus, control of the adsorption process is even more critical for applications that use nanostructured substrates with large relative surface areas, such as nanoparticles, microchannels, and thin porous membranes, due to their large surface.

There are different strategies to prevent unspecific adsorption of proteins, such as coating by bovine serum albumin (BSA), grafting of phospholipids, and use of non-ionic detergents like Tween 20 or of polymeric materials like polyethylene glycol (PEG), as well as combinations of these elements [272, 273]. PEG is one of the most studied materials used in order to obtain antibioadherent coatings, especially in the pharmaceutical, cosmetic, and biomedical fields [274-276]. The interest of this polymer is due to its unique physical and chemical properties. Indeed, it is highly hydrophilic and has a significant chain flexibility [277]. It has also excellent solubility in aqueous and organic and has a low toxicity to living cells [278]. Preventing unspecific adsorption *via* its strong hydration layer and its steric stabilization effect is one of the most widespread applications of PEG [278, 279]. This coating by PEG is used to control the interaction of biological molecules with the surface of biosensors. This functionalization is commonly done by thiol-PEG self-assembled monolayers (SAM) on gold surface [280-282].

The SAMs produced on various substrates have been extensively investigated for the surface functionalization with active molecules or for protecting them from adsorption of species present in the environment [283, 284]. The SAM formation is induced by the strong chemisorption between the substrate and the head group of the selected organic molecules. This allows making stable

ultrathin organic films with controlled thickness [285, 286]. These advantages make the SAMs particularly suited to the development of applications in the field of biosensors [287]. This makes them an ideal model in many areas such as bioanalytical, organometallic, physical organic, bioorganic and electrochemistry [284, 285, 288]. Usually, SAMs formed on gold material or surface are attached using thiol-modified molecules. The self-assembled monolayers of alkanethiols on gold are probably one of the best surfaces currently available to obtain the functionalization and the patterning of biosensors with advantages such as flexibility and stability. The gold-thiol monolayers are stable when exposed to air, to water or to ethanolic solutions for several months [289]. They are also quite easy to produce, quickly assembled and well ordered.

This work aims to produce a large surface of nanoarray functionalized with proteins for antibody detection. Herein, we report the synthesis of multifunctional surface with polystyrene spheres and selective functionalization ability. We aim to attach specifically the protein directly to the PS spheres and to limit its unspecific adsorption. In our work we used a silicon wafer coated with a thin adhesion layer of chromium (15 nm) and a layer of noble metal (50 nm). PS spheres are deposited on the gold surface using the floating-transferring technique. We design a multifunctional surface with array of polystyrene spheres. We used PEG SAMs to block the unspecific adsorption of protein on the surface of these polystyrene spheres. Another interesting point is relative to the stability of PS sphere layer regarding the multistep functionalization which could create defects on the surface.

3.3. Materials and method

3.3.1. Materials

Avidin from egg white (A9275), Poly(ethylene glycol) 2-aminoethyl ether biotin (PEG) $M_n = 5300 \text{ g mol}^{-1}$ (757772), N-Hydroxysuccinimide (NHS) $M_w = 115.09 \text{ g mol}^{-1}$ (130672), Ethylenediamine $M_w = 60.10 \text{ g mol}^{-1}$ (E26266), Anti-Avidin, antibody produced in rabbit (A5170), Ethanol (absolute alcohol, without additive (02860)), phosphate buffered saline (P4417) and Micro particles based on polystyrene, (size $1 \mu\text{m}$, 10 wt% aqueous solution (89904)) were purchased from Sigma Aldrich. Thiol PEG, mPEG-SH $M_w = 2000 \text{ g mol}^{-1}$ (PG1-TH-2k), Cy5-PEG-NHS $M_w = 5000 \text{ g mol}^{-1}$ (PG2-NSS5-5k) and Succinimidyl PEG, mPEG-NHS $M_w = 2000 \text{ g mol}^{-1}$ (PG1-SC-2k) were purchased from Nanocs. N-(3-Dimethylaminopropyl)-N-ethylcarbodiimide hydrochloride (EDC) $M_w = 191.70 \text{ g mol}^{-1}$ (03449) was purchased from Fluka Analytical. Alexa Fluor 488 TFP ester (A37570) and Alexa Fluor 647 NHS (A37573) were purchased from ThermoFisher Scientific.

3.3.2. Protein labeling

Avidin was labeled with Alexa Fluor 647 NHS. Typically, 100 μ L of protein solution (1 mg Avidin and 100 μ l PBS pH = 8.3) was added to dry fluorophore Alexa-647 and allowed to react for 0.5 h at 20 °C. Anti-Avidin was labeled using Alexa Fluor 488 TFP ester. One hundred microliters of protein solution (5 μ L Anti-Avidin and 100 μ l PBS pH = 8.3) was added to dry fluorophore Alexa-488 and allowed to react for 0.5 h at 20 °C. Then the unreacted dyes and proteins were separated by centrifugation (16000 g, 1 min) using filter (Biospin P6) according to the supplier of the kit.

3.3.3. Polystyrene sphere deposition on the Si/Cr/Au surface

The nanoarrays of polystyrene spheres were designed using the following procedure. A deposition of 15 nm of Cr and 50 nm of Au were performed on p-type Si (100) wafers (2x2 cm² pieces of boron doped (8 – 25 Ω cm)). The substrates were treated by O₂ plasma using a pressure of 0.6 mbar and a power supply at 0.15 A in order to eliminate all the organic matters from the surface. The polystyrene spheres (PS spheres) were then deposited using the floating-transferring technique.

Typically, the monolayers of spheres were prepared using monodisperse polystyrene particles with the diameter of 1 μ m. Forty microliters of the polystyrene solution (10 wt%) diluted by an equal amount of ethanol. The solution was applied onto the Si substrate and displayed over the Si surface. The Si substrate was maintained stationary for few seconds in order to allow a good dispersion of the PS spheres. The Si wafer was then slowly immersed into a glass vessel filled with deionized water (80 ml). A non-ordered monolayer of PS spheres was formed on the water surface. A droplet of 10% sodium dodecyl sulfate (SDS) solution was added to the water in order to modify the surface tension. This step targets to consolidate the PS spheres. A large monolayer of PS spheres was transferred to our target substrate (Si/Cr(15 nm)/Au(50 nm)). After drying, the Si substrate covered with the PS was heated at 100 °C for 10 min in order to sinter the PS spheres and to improve their adhesion into the Si substrate. After sintering, the diameter of the PS spheres was reduced with etching by O₂ plasma for different times: 1, 5, 10 and 15 min. In this experiment, the utilized pressure of O₂ plasma is 0.6 mbar and the power supply is 0.15 A.

3.3.4. Functionalization of nanoarrays

The PEGylating of gold surface by SAMS The nanoarray was placed into 1 ml of solution of thiol PEG, (mPEG-SH) (4 mg) in unmodified ethanol for 2 days. Then, the samples were rinsed with ethanol.

Polystyrene sphere biotinylation After PEGylation by SAMS, the nanoarrays were placed in a solution of 0.5 mg mL^{-1} PEG-biotin-NH₂, 2 mg mL^{-1} EDC, and 1 mg mL^{-1} NHS for 24 h. After this period, the sample is rinsed with ethanol to remove the absorbed PEG.

mPEG-NHS and Cy5-PEG-NHS grafting on polystyrene sphere In order to link mPEG-NHS or Cy5-PEG-NHS on the polystyrene surface, we have firstly grafted ethylenediamine on COOH groups as follows:(i) the nanoarrays were immersed in 1 ml ethanol solution which contained 2 mg mL^{-1} EDC and 1 mg mL^{-1} NHS for 2 h. (ii) Then, the sample is rinses with ethanol and it is placed in solution of mPEG-NHS or Cy5-PEG-NHS (0.2 mg mL^{-1}) for 1 h. (iii) Finally, the samples were rinsed with ethanol.

Protein attachment assays For protein attachment assay, we used Avidin, Avidin labeled with Alexa Fluor 647 NHS (noted Avidin*), and Anti-Avidin labeled with Alexa Fluor 488 TFP ester (noted Anti-Avidin*). The nanoarrays were immersed for 30 min in 1 ml of protein ($10 \text{ } \mu\text{g mL}^{-1}$) in PBS (0.01 M phosphate buffer, 0.0027 M potassium chloride, and 0.137 M sodium chloride, pH 7.4, at 25°C). Then, the samples were rinsed with PBS.

3.3.5. Microscopy

The morphology of the samples was observed with scanning electron microscopy (SEM, Hitachi S-4800). Fluorescence images were performed using an epifluorescence microscope DM6000. The Alexa Fluor 647 and 488 were detected using CY5 and FTIC cube respectively.

3.4. Results and discussion

The present work aims to produce large-scale nanoarrays which permit to control protein grafting and limit the unspecific adsorption. The large-scale nanoarrays can be produced by nanospheres lithography using the floating-transferring technique of polystyrene sphere. These spheres can serve as anchor site for protein attachment. However, the main limitation comes from the unspecific adsorption between the spheres. In order to tackle this limitation, one way is the functionalization of these free spaces with a high density of PEG molecules. This can be achieved by thiol PEG SAM strategies on gold surface since it is a well-known strategy to limit the non-specific adsorption of protein. The overall process for nanoarrays design is presented in the schematic diagram (Figure 3-1).

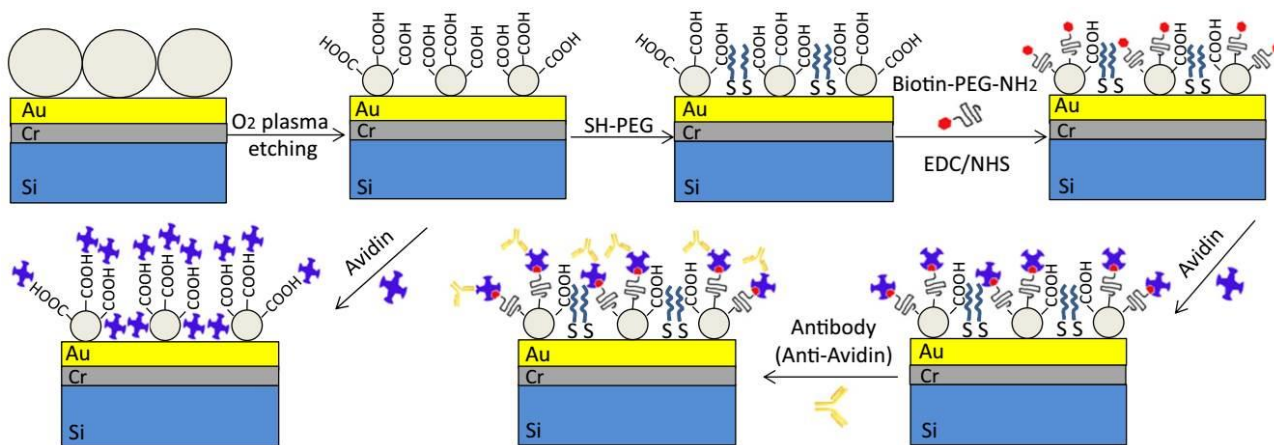


Figure 3-1. The schematic diagram of overall process for protein immobilization.

The first step consists to deposit a thin layer of gold (50 nm) on Si wafer. In order to improve the stability of this layer, 15 nm of Cr is deposited on the Si substrate before the Au deposition. The Si/Cr/Au substrates were treated by O₂ plasma to remove all organic matter from the surface. After the pretreatment, an ordered monolayer of polystyrene spheres (PS spheres) was prepared and deposited on the substrate by floating transferring technique [290, 291]. The sample was prepared as described in the experimental section and dried in air at room temperature. The obtained spheres were self-assembled into a close-packed two-dimensional ordered area via attractive capillary forces [292]. After drying, the Si substrate covered with PS was heated in an oven at 100 °C for 10 min to sinter the PS and to improve their adhesion to the Si/Cr/Au substrate. The diameter of spheres was decreased with etching by O₂ plasma. This step permits also as well to oxidize the polystyrene surface to create a COOH group on their surface. The latter step is essential for further functionalization of PS spheres. The SEM image (Figure 3-2) of PS spheres shows the unformal decrease of the diameter with plasma treatment. In addition, it confirms that the transfer permits to obtain the monolayer of PS spheres. The dependence mean diameter of PS spheres as the function of different times of etching by O₂ plasma is also reported in Figure 3-2. The characterization of protein and antibody on the nanoarrays is performed by epifluorescence microscopy. The minimum size required to detect the PS spheres is around 900 nm. Thus, we have fixed etching time to 5 min. This time permits to decrease the PS spheres diameter from 956 nm to 933 nm.

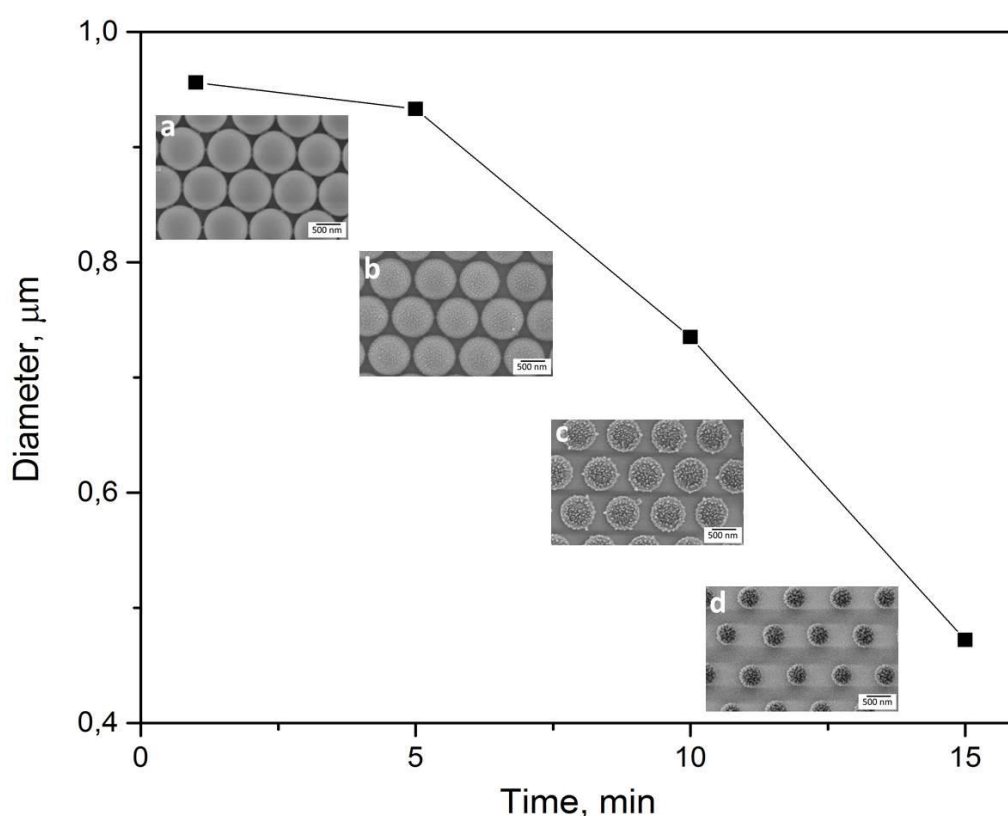


Figure 3-2. Diameter of PS spheres as the function of the O₂ plasma etching: The insets show PS spheres with different O₂ plasma etching times: 1 (a), 5 (b), 10 (c) and 15 (d) min, respectively, as determined by SEM (scale bars 500 nm).

After the plasma etching, the sample is composed by zone. The first one is the gold metallic surface which is uncovered by polystyrene spheres. The second one is the surface of PS spheres with exhibits COOH group. These two parts of the sample could be functionalized differently because we expect to graft protein and antibodies specifically on PS spheres. This imposes to prevent the absorption between the PS spheres. To do it, the gold surface between PS spheres was functionalized by SAMS of PEG-thiol.

After this step, we are able to have two different functionalizations on spheres and between them on the gold surface. We attached on polystyrene spheres PEG-Cy5 following two steps. The first one consists to link ethylene diamine on carboxyl groups using EDC/NHS and the second one is the addition of NHS-PEG-Cy5. Figure 3-3 shows a fluorescence microscopy image of the prepared sample. We can observe that fluorescence came only from the spheres and there is no fluorescence between them. The diameter of spheres around 0.9 μm is in good agreement with the one determined by SEM.

Several additional experiments were performed as blank to confirm that the fluorescence comes from the dyes. PS spheres do not exhibit self-fluorescence under excitation wavelength of 590-650 nm provided by Cy5 cube. In addition, the images performed after each step of functionalization (after reduction by plasma, gold coating and PEG-biotin grafting) do not reveal fluorescence emission under the same condition. A weak autofluorescence of PS sphere was only observed under excitation wavelength lower than 450 nm (using Hoechst and CFT cubes). According to that, we can conclude that the PEG-Cy5 is attached on PS spheres. Between the PS spheres, we observe some defects. However, PS spheres cover the majority of the surface of the sample (here the $90.48 \times 67.6 \mu\text{m}^2$). At this step, our results prove that our strategy allows designing a large scale of monolayer of PS spheres and that our strategy of functionalization is relevant to functionalize PS spheres surface and gold surface with different functions.

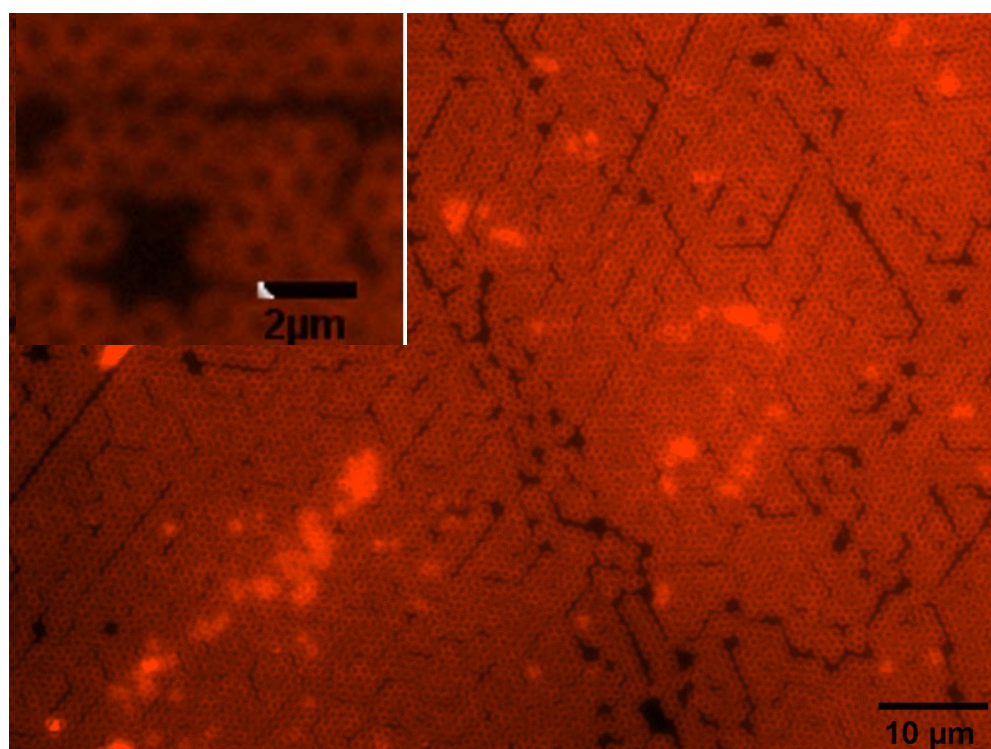


Figure 3-3. Fluorescent images of Cy5-PEG-NHS-modified polystyrene spheres (the inset indicates a zoom)

We wanted to use similar strategy to attach the protein directly to the spheres, but not between them. To do it, we have done a variety of experiments using the avidin-biotin strategy. The latter is commonly used to design biosensor devise. The first step consists to graft PEG-biotin on PS spheres. This was performed using PEG-biotin-NH₂ and EDC/NHS. In the second step, the avidin labeled with Alexa-647 was added and their localization was investigated by epifluorescence

spectroscopy (Figure 3-4). As expected, the fluorescence comes specifically from the PS spheres. The lack of fluorescence between the spheres proves that there is no protein. Thus, the functionalization of gold surface is efficient to prevent the unspecific adsorption of protein. In order to prove that the avidin is on PS spheres due to the presence of biotin, a similar functionalization with mPEG on PS spheres was performed. After immersion, under labeled avidin, the epifluorescence reveals a weak fluorescence. Since the PS spheres and the functionalization do not reveal fluorescence emission using the CY5 cube, we can admit that the signal is due to avidin likely adsorbed on sphere. Actually, this is not surprising because PEG layer has to be dense to prevent the protein adsorption. In the case of PS spheres, the PEGs are grafted on carboxylate group. Thus, the density of these groups is likely too weak to induce a dense layer of PEG. In this case, proteins could be adsorbed on the defects and/or between the PEG chains.

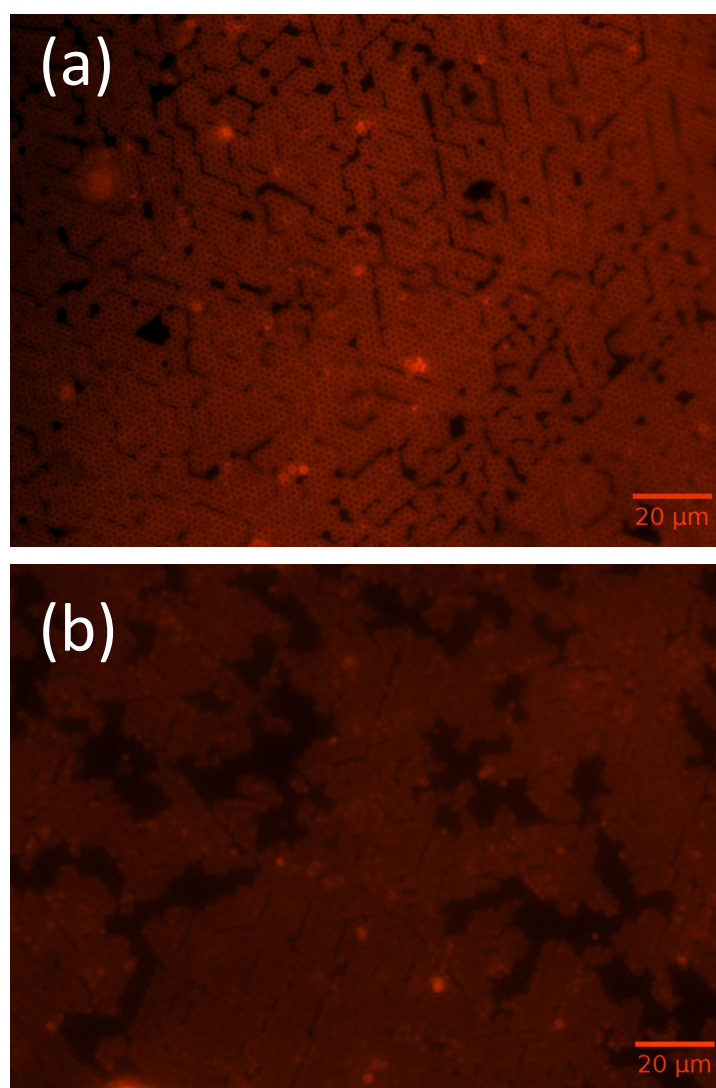


Figure 3-4. Fluorescent images of PS spheres functionalized with biotin-PEG-NH₂ (a) and mPEG (b) after addition of avidin (labeled with Alexa Fluor 647).

In order to prove that the large-scale nanoarrays are suitable for antibody detection, different samples were functionalized with PEG-biotin and unlabeled avidin. After this first step, no fluorescence can be detected under excitation wavelength of 460–500 nm as well as 590– 650 nm. Then, they were immersed in solution containing Anti-Avidin* labeled with Alexa Fluor 488. As expected, the epifluorescence image shows that anti-avidin is specifically located on PS spheres (Figure 3-5). The functionalization with SAMs of PEG prevents the antibody as well as the avidin adsorption. We can observe that some microspheres have different intensity of green fluorescence. This could be explained by the following: (i) the number of dyes on antibodies is not homogeneous or (ii) the number of antibodies attached on microspheres is different.

The Figure 3-6 depicts the fluorescence image of a sample where both avidin* and anti-avidin* are labeled with Alexa Fluor 647 and 488 respectively. The first one is characterized with CY5cube and the second one with FTIC cube. The perfect superposition of both images confirms that both avidin and anti-avidin are located on PS spheres.

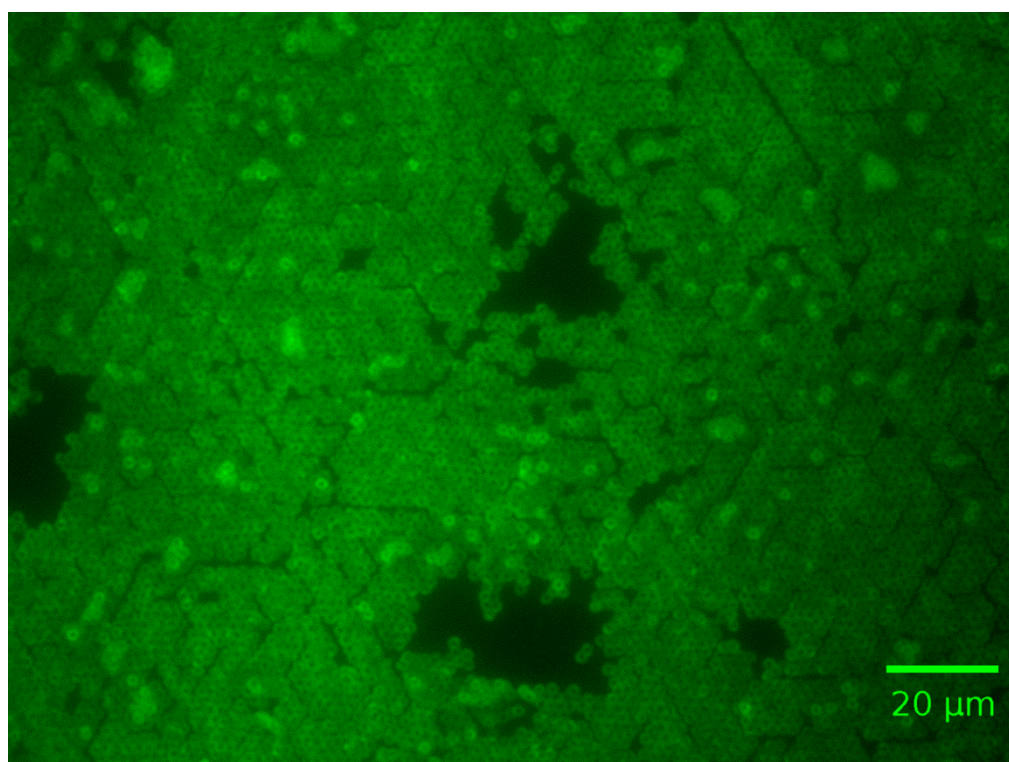


Figure 3-5. Fluorescent images of PS spheres functionalized with biotin-PEG-NH₂ and avidin (unlabeled) after Anti-Avidin*(labeled with Alexa Fluor 488).

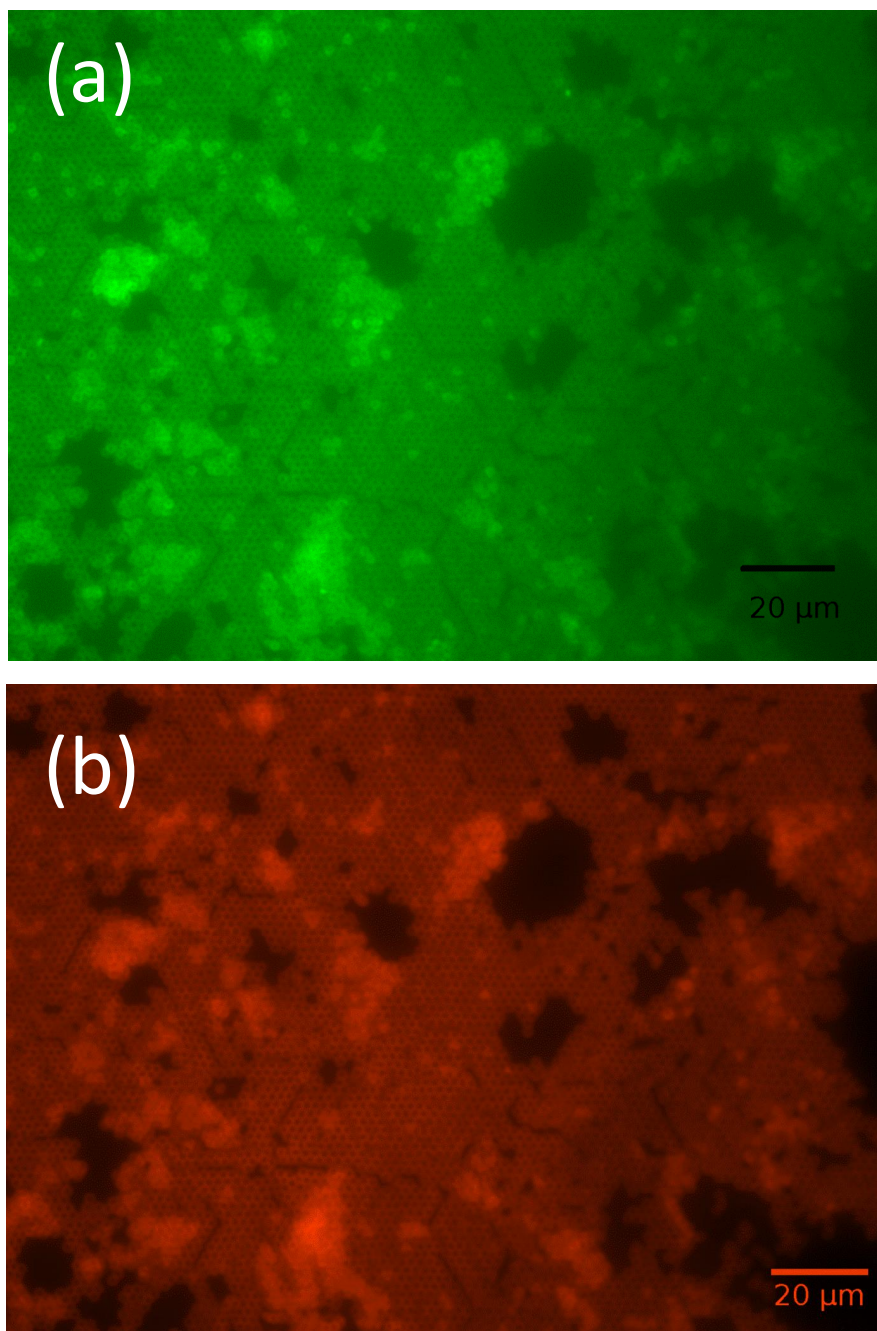


Figure 3-6. Fluorescent images of PS spheres functionalized with biotin-PEG-NH₂ and avidin (labeled with Alexa Fluor 647) after Anti-Avidin (labeled with Alexa Fluor 488) addition recorded with FTIC cube (a) Cy5 cube (b).

3.5. Conclusion

In summary, we have presented a novel method based on nanosphere lithography in order to design a large-scale protein patterning. This technique based on two-dimensional (2D) colloidal crystals (polystyrene sphere (PS spheres)) allows the fast synthesis of large arrays (up to several

centimeters) by reducing the cost. The nanoarrays are formed by a monolayer of polystyrene sphere deposit by floating-transferring technique on gold surface. On the one hand, the gold surface between spheres was functionalized with SAMs of PEG to prevent the unspecific adsorption. On the other hand, the PS spheres were functionalized with PEG biotin. After addition of avidin and anti-avidin, the proteins are located only on PS spheres confirming that our strategy is suitable to control their location. Our results are meaningful for exploration of devices based on large-scale protein patterning on PS spheres. Regarding the versatility of avidin/biotin system, this strategy can be extended for biosensor development as well as for other applications which require large-surface patterning of proteins.

CHAPTER IV

ZnO Films Formed by Atomic Layer Deposition as an Optical Biosensor Platform for the Detection of Grapevine Virus A-type Proteins

This chapter has been published in *Biosensors & Bioelectronics* as:

Alla Tereshchenko¹, Viktoriia Fedorenko^{1,2}, Valentyn Smyntyna¹, Igor Konup³, Anastasiya Konup⁴, Martin Eriksson⁵, Rositsa Yakimova⁵, Arunas Ramanavicius⁶, Sebastien Balme², Mikhael Bechelany², *ZnO films formed by atomic layer deposition as an optical biosensor platform for the detection of Grapevine virus A-type proteins*, *Biosensors and Bioelectronics*, 2017, 92, 763-769

¹ Faculty of Physics, Experimental physics department, Odessa National I. I. Mechnikov University, 42, Pastera, 65026, Odesa, Ukraine

² Institut Européen des Membranes IEMM, ENSCM UM CNRS UMR5635, Place Eugène Bataillon, F-34095 Montpellier Cedex 5, France

³ Department of Microbiology, Virology and Biotechnology, Odessa National I. I. Mechnikov University, 2, Shampanskiy lane, 65000, Odesa, Ukraine

⁴ National Scientific Centre “Institute of Viticulture and Wine Making Named After V. Ye. Tairov”, 27, 40 Let Pobedy str., 65496, Odesa, Ukraine

⁵ Department of Physics, Chemistry and Biology, Linköping University, 58183 Linköping, Sweden

⁶ Department of Physical Chemistry, Vilnius University, Naugarduko str. 24, LT-03225 Vilnius, Lithuania

In this chapter, we performed the novel optical biosensor based on thin films of ZnO deposited by ALD for the determination of *Grapevine virus A-type* (GVA) proteins (GVA-antigens).

GVA is a plant vitivirus that is the most regularly detected virus in grapevine. Figure a represents the vine-grapes infected with GVA. Such vine-grapes have poor health, poor quality and low-yielding fruit.

Among a large variety of biosensors, immunosensors are based on specific interaction between antibody – antigen couple. The scheme of PL based immunosensor, which was used in the present work, is shown in Figure b. ZnO is suitable for the immobilization of biomaterials, which are applied as biological recognition parts in biosensors. The detection of GVA-antigens was performed through direct immobilization of anti-GVA antibodies on the ZnO thin film surface, forming the biosensitive layer.

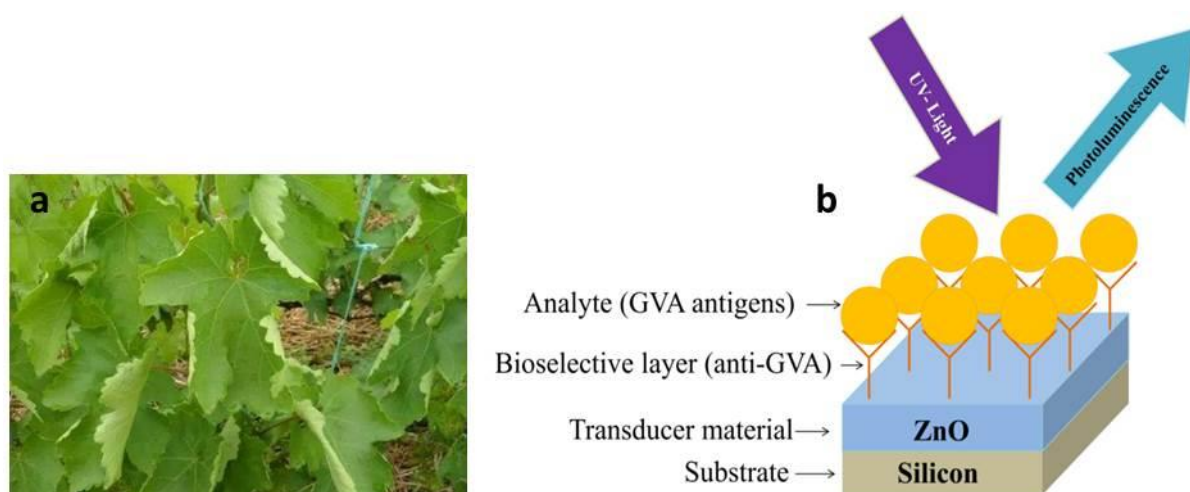


Figure. Vine-grapes infected with Grapevine virus A-type (GVA) (a), and the scheme of PL based immunosensor (b).

In summary, label free and sensitive photoluminescence based biosensor for GVA-antigens has been developed. The decrease of the deposition time of immobilized layers has been achieved. Optical properties of ZnO films obtained by ALD method were applied for the detection of GVA-antigens. The GVA-antigen detection was performed by the evaluation of changes and behavior of corresponding luminescence band. The changes in the photoluminescence of ZnO/anti-GVA caused by the formation of complex between immobilized anti-GVA antibodies and GVA-antigens were interpreted as analytical signal. Thus, a good performance and simplicity of the described immunosensor ZnO-modified substrates could be applied as a platform for the development of other immunosensors based on immobilized antibodies, which would be sensitive to selected analyte.

4.1. Abstract

Novel sensitive optical biosensor for the determination of *Grapevine virus A-type* (GVA) proteins (GVA-antigens) has been designed. This biosensor was based on thin films of Zinc oxide (ZnO) deposited by atomic layer deposition (ALD). The ZnO-based films have demonstrated favorable surface-structural properties for the direct immobilization of antibodies against GVA-antigens in order to form a biosensitive layer sensitive to GVA-antigens. The immobilization was confirmed by intensity changes in the main near band emission (NBE) peak of ZnO and by the formation of intense PL band, discovered in the visible range around 425 nm, caused by the immobilized proteins. The GVA-antigen detection was performed by the evaluation of changes and behavior of corresponding luminescence band. The sensitivity of as-formed label-free biosensor towards the GVA-antigens was determined in the range from 1 pg/ml to 10 ng/ml; in addition, the selectivity of biosensor was evaluated.

Keywords: ZnO, Atomic layer deposition, Photoluminescence, Optical Biosensor, Grapevine virus A-type.

4.2. Introduction

Grapevine virus A-type (GVA) is a plant vitivirus that is the most regularly detected virus in grapevine. Such viruses are easily transmitted from infected to healthy plants during grafting and by insect pests common in vineyards. Vine-grapes infected with GVA have poor health, poor quality and low-yielding fruit [293-295]. Even if GVA virus was identified more than 30 years ago, it is still common in vineyards worldwide. In addition, its origin is relatively unknown and it has negative economic impact on vineyard productivity. Up to date the monitoring and diagnostics of GVA are based on the study of its genome, genomic organization and replication mechanism [294, 295]. For example, complete genome sequence of a natural mutant of GVA was determined by Goszczynski *et al.* However, up to date, the determination of GVA is based on serological methods (e.g. ELISA tests) and nucleic acid-based methods (variety of PCR-based approaches). These methods provide high sensitivity, up to 100 % detection, however they are time consuming, labor-intensive and relatively expensive. Therefore, there is a need to develop rapid, sensitive, inexpensive and simple in use biosensor for the determination of GVA.

Advances in Zinc Oxide (ZnO) growth technology allow the formation of nanostructures with desired optical, structural, morphological and electrical properties that are exploited in the range of biosensors [296, 297]. Due to its high isoelectric point (~ 9.5), biocompatibility, high chemical

stability, strong adsorption ability, high catalytic efficiency along with nontoxicity and abundance in nature, ZnO is suitable for the immobilization of biomaterials, which are applied as biological recognition parts in biosensors [296, 297]. As a wide and direct band gap (3.37 eV) semiconductor that has intense photoluminescence at room temperature, ZnO is widely applied in optical biosensors [298-302] particularly photoluminescence based biosensors [303-305]. In this type of biosensors, the changes in the photoluminescence signal of nanostructured material are used for the detection of analyte and the determination of its amount by the characterization of photoluminescence spectra. Therefore recently, a wide range of photoluminescence biosensors based on ZnO nanostructures have been developed [296, 303-305].

Among various methods used to form ZnO thin films, atomic layer deposition (ALD) is an innovative technique, which allows the deposition of ultrathin metal oxide films with controlled thickness, grain size, chemical composition, texture, surface morphology and defect concentration. The mentioned structural parameters make a strong impact on optical, electrical and mechanical properties [109]. In previous studies [109, 110, 306-308], we investigated the tuning of the optical and the structural properties of ultrathin ZnO films deposited by ALD along with their potential applications in sensors and biosensors [109].

In the wide range of studies, the influence of adsorption and immobilized proteins on the optical properties of ZnO was investigated [302-305, 309-311]. The majority of results reports on the changes in photoluminescence intensity and peak positions of near band emission (NBE) and/or deep level emission (DLE) of ZnO after interaction with biomolecules. In rare cases, the immobilized proteins induce new photoluminescence peak or line in the spectra [302, 310] but the photoluminescence caused by protein adsorption was not strong enough to be used as a biosensor response. In the present work, the influence of immobilized GVA-antibodies (against GVA-antigens) on the photoluminescence spectra of ZnO was investigated for the first time. The direct immobilization of anti-GVA antibodies on the ZnO surface was performed and resulted in the formation of biosensing structure (ZnO/anti-GVA), which was characterized by increased intensity of the main NBE peak of ZnO and photoluminescence band appearance in the range around 425 nm. The changes in the photoluminescence of ZnO/anti-GVA caused by the formation of complex between immobilized anti-GVA antibodies and GVA-antigens were interpreted as analytical signal. In this way, novel, label free and sensitive photoluminescence based biosensor for GVA-antigens has been developed.

4.3. Materials and Methods

4.3.1. ZnO thin film synthesis and characterizations

ZnO layers of 57 and 110 nm thicknesses were synthesized by ALD method using lab-made ALD reactor at the same conditions as described elsewhere. ALD was performed using sequential exposures of Diethyl zinc (DEZ) ($\text{Zn}(\text{CH}_2\text{CH}_3)_2$, 95% purity, CAS: 557-20-0) and H_2O separated by a purge of Argon with a flow rate of 100 sccm. The deposition regime for ZnO consisted of 0.2 s pulse of DEZ, 30 s of exposure and 30 s of purge with Argon followed by 2 s pulse of H_2O , 30 s of exposure to H_2O and finally 40 s purge with Argon. ZnO ultrathin films with different numbers of cycles were deposited at 100 °C.

4.3.2. Chemical and physical characterizations of ZnO thin films

Structural properties of ZnO films were characterized by Scanning Electron Microscopy (SEM), Ellipsometry and Grazing Incidence X-ray Diffraction (GIXRD). Optical properties were characterized by photoluminescence (PL) study of ZnO films that was used further as a biosensor signal.

In order to investigate the photoluminescence of the studied samples, they were excited by a solid state laser with a wavelength of 355 nm. The excited ZnO photoluminescence entered a spectrometer with the slit entrance of 1 by 1 mm, a focal length of 550, a 600 gr/mm grating and a liquid nitrogen cooled CCD as the detector. The large, 0.4 mm wide, excitation area was produced in order to obtain an average photoluminescence of each sample. The spot size on the sample was a diameter of roughly 1 mm. The laser power was 1.2 mW. All photoluminescence experiments were recorded at room temperature, with a spectral resolution of 3.3 nm, using the spectrometer TRIAX 550 made by Jobin Yvon (New Jersey, USA). The laser was blocked by a 364 nm long pass filter after the sample, with full transmission from 368 nm.

4.3.3. Functionalization of ZnO thin films

The biological samples used in the experiment were provided by National Scientific Centre “Institute of Viticulture and Wine Making named after V. Ye. Tairov” (Odesa, Ukraine). The used proteins were part of the immunoassay-based KIT for the determination of GVA produced by Agritest (Valenzano, Italy) and consisted from anti-GVA antibodies containing serum, which in deed was a real sample extracted from GVA-infected grape plants; control sample of GVAantigens, containing extract of GVA-infected grape plants (further in the text it is marked as ‘Ag+’) and real

sample of non-infected plant extract, which does not contain any proteins of GVA virus capsid (further in the text it is marked as 'Ag-'). The molecular weight of GVA capsid proteins, which were present in Ag+ sample is ~ 27 kDa (Monette and Green, 1992).

The anti-GVA antibody immobilization procedure was the following: 5 μ l of anti-GVA antibodies containing sample was diluted by 50, 100, 200, 400, 600, 800, 1000 times that corresponds 1/50, 1/100, 1/200, 1/400, 1/600, 1/800, 1/1000 respectively, were dissolved in 0.01 mol/l PBS (pH=7.4) and this solution was equally distributed on the surface of as grown ZnO film modified substrates with the size 5 \times 5 mm, and it was kept for 1 hour in humid environment at room temperature. After this, the samples were washed with PBS and with deionized water and then they were dried in air for 1 hour at room temperature. By above mentioned procedure biosensing structure (ZnO/anti-GVA) was formed. After all, the photoluminescence signal of ZnO/anti-GVA was recorded.

4.3.4. Evaluation of biosensor performance

The procedure for the determination of GVA-antigens was following: 5 μ l of GVA-antigens containing samples of different concentrations from 1 pg/ml to 1 μ g/ml dissolved in PBS (pH=7.4) and this solution was equally distributed on the surface of ZnO film modified substrates (ZnO/anti-GVA) and it was kept for 1 hour in humid environment at room temperature. After this, the samples were washed with PBS and with deionized water and then they were dried in air for 1 hour at room temperature. After all, the photoluminescence signals of ZnO/anti-GVA/GVA-antigen samples were recorded.

Before biosensor test, optical properties (absorbance and PL) of anti-GVA-based substrates were studied. The absorbance spectra were recorded with UV-VIS spectrophotometer Shimadzu UV-1700 (Kyoto, Japan) in the range of 250-600 nm. The photoluminescence spectra were registered using setup described above.

4.4. Results and Discussion

The SEM images of ALD ZnO thin films deposited on Si substrates with different numbers of cycles are represented in figure 4-1a. The SEM images show a conformal coating of the Si substrate by the ALD formed the ZnO films. With increasing thickness of ZnO films, a rough surface with columnar growth has been observed. Ellipsometry-based measurements confirmed that ZnO films of 57 and 110 nm thickness (these films in the further text are noted as ZnO_{57nm} and ZnO_{110nm}) were obtained respectively by 250 and 500 ALD cycles, which correspond to a growth of 2.2 Å per one

cycle. GIXRD diffraction patterns of ZnO thin films are shown in figure 1b. It demonstrates the diffraction peaks at $2\theta = 31.80^\circ$, 34.54° and 36.16° , which are corresponding to (100), (002), and (101) reflection planes of hexagonal wurtzite structure of ZnO respectively.

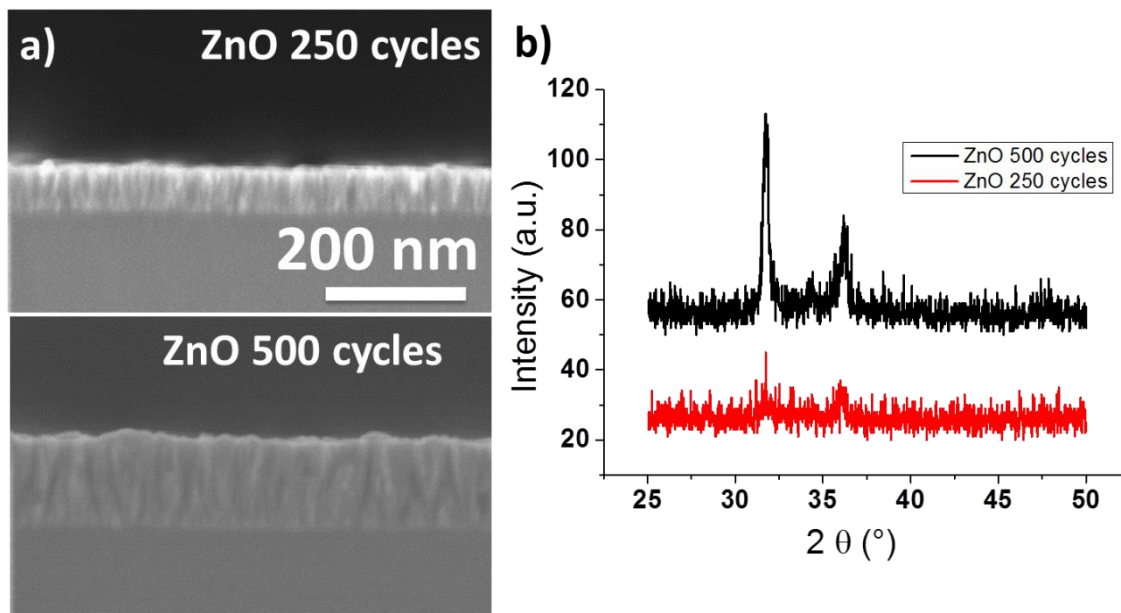


Figure 4-1. a) SEM cross section images and b) GIXRD of ZnO ALD films deposited on Si substrates by different numbers of cycles (250 and 500).

4.4.1. Photoluminescence-based characterization of ZnO films deposited on Si substrate

Photoluminescence (PL) spectra of the samples were characterized by NBE peak at 378 nm (Fig. 4-2a). The films with the layer thickness of 110 nm ($\text{ZnO}_{110\text{nm}}$) demonstrate more intense PL emission than $\text{ZnO}_{57\text{nm}}$ films (Fig. 4-2a, inset) and weak DLE emission in the visible range.

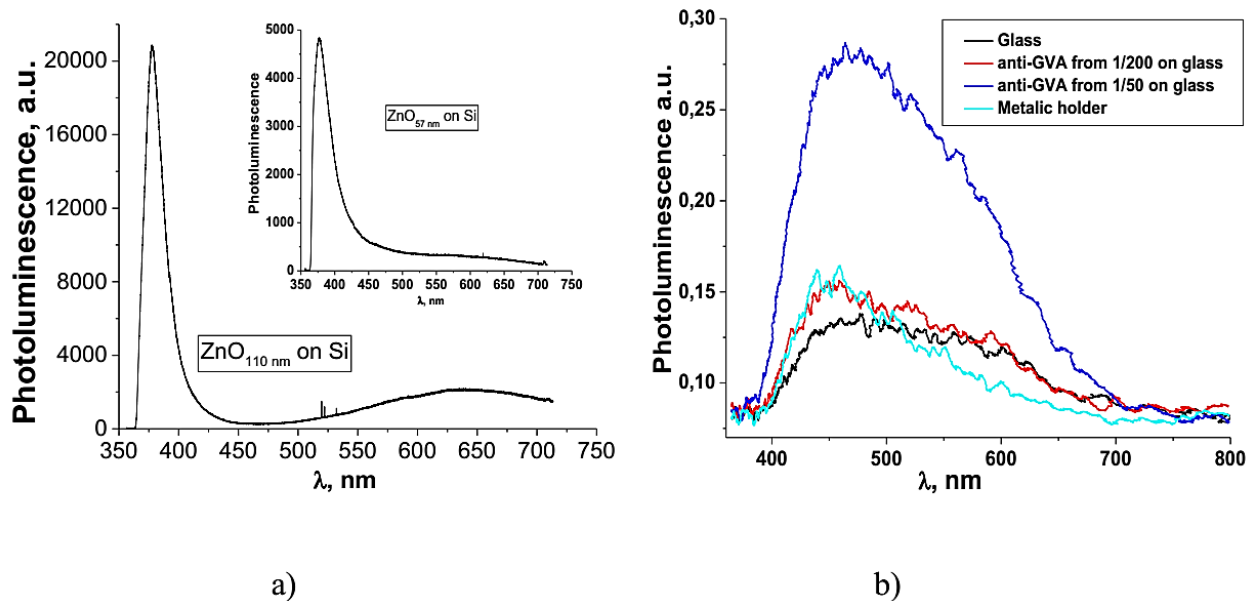


Figure 4-2. PL spectra of the ZnO samples with 57 and 110 nm layer thicknesses (a), PL spectra of anti-GVA deposited on glass (b)

4.4.2. Immobilization of anti-GVA on the surface of ZnO films

Among a large variety of biosensors, immunosensors are based on specific interaction between antibody – antigen couple [298]. The interaction between antibody and antigen couple has high specificity and sensitivity to detect analytes what makes immunosensors suitable for accurate and precise analysis with different types of transducers. Optical transducers are simple, fast and accurate, therefore they are very suitable for the detection of target analyte. Out of many optical approaches, photoluminescence based methods are among the most sensitive and simple ones [302, 304, 309, 310]. In PL-based sensors nanostructured photoluminescent materials are often used as transducers due to their ability to convert molecular interactions into PL-signals without contamination or deterioration of samples [310]. The principle of the PL-based biosensor action is based on the changes of PL signal before and after interaction of immobilized bio-recognition sites with analyte [296, 304, 310], see figure 4-3.

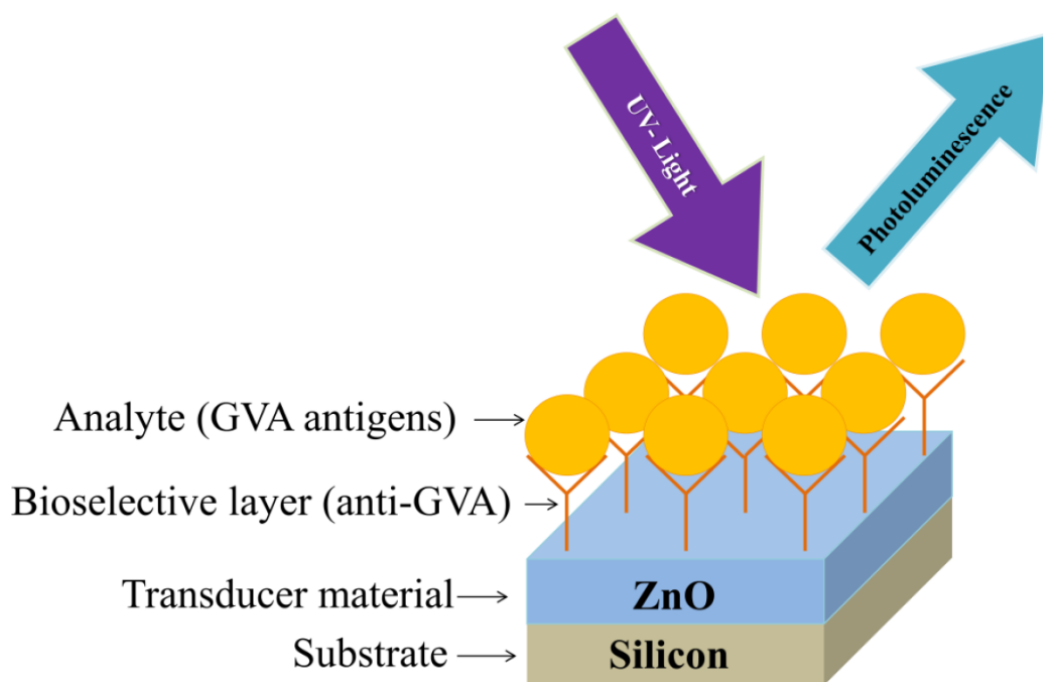


Figure 4-3. The scheme of PL based immunosensor

In order to investigate the possibility of application of ZnO films, which were deposited by ALD method, as an optical transducer of immunosensor and to determine the optimal surface concentration of anti-GVA antibodies immobilized in the biosensitive layer, anti-GVA solutions of different concentrations were deposited on the surface of ZnO-modified substrates. For both ZnO_{110nm} and ZnO_{57nm} samples, the immobilization of anti-GVA has resulted in appearance of PL band in the range from 400 to 550 nm along with the intensity increase of the NBE peak in the average by 35% (Fig. 4-4a). The shift of NBE peak was not observed and no significant difference in the PL spectra after the immobilization of the same anti-GVA concentration on the surface of ZnO_{110nm} and ZnO_{57nm} modified substrates was observed (the spectra are not shown here). Considering the fact that the PL signal from the ZnO_{110nm} films was much more intense than the signal from ZnO_{57nm} the films with the layer thickness of 110 nm were chosen for the further immunosensor design.

Figure 4-4b presents the PL spectra of the ZnO_{110nm} films with immobilized anti-GVA antibodies (ZnO_{110nm}/anti-GVA) from the solutions with different concentrations of anti-GVA, which are ranging from the lowest concentration (at 1/1000 dilution of initial anti-GVA containing solution) to the highest concentration (at 1/50 dilution). The initial PL signal intensity among all ZnO films was varying from 16000 to 19000 arbitrary units. Thus, the PL spectra (Fig. 4-4b) were normalized in order to eliminate the fluctuation of this varying initial signal and to compare the

influence of protein adsorption on ZnO. Such immobilization of anti-GVA has resulted in the appearance of PL emission in the range from 400 to 550 nm.

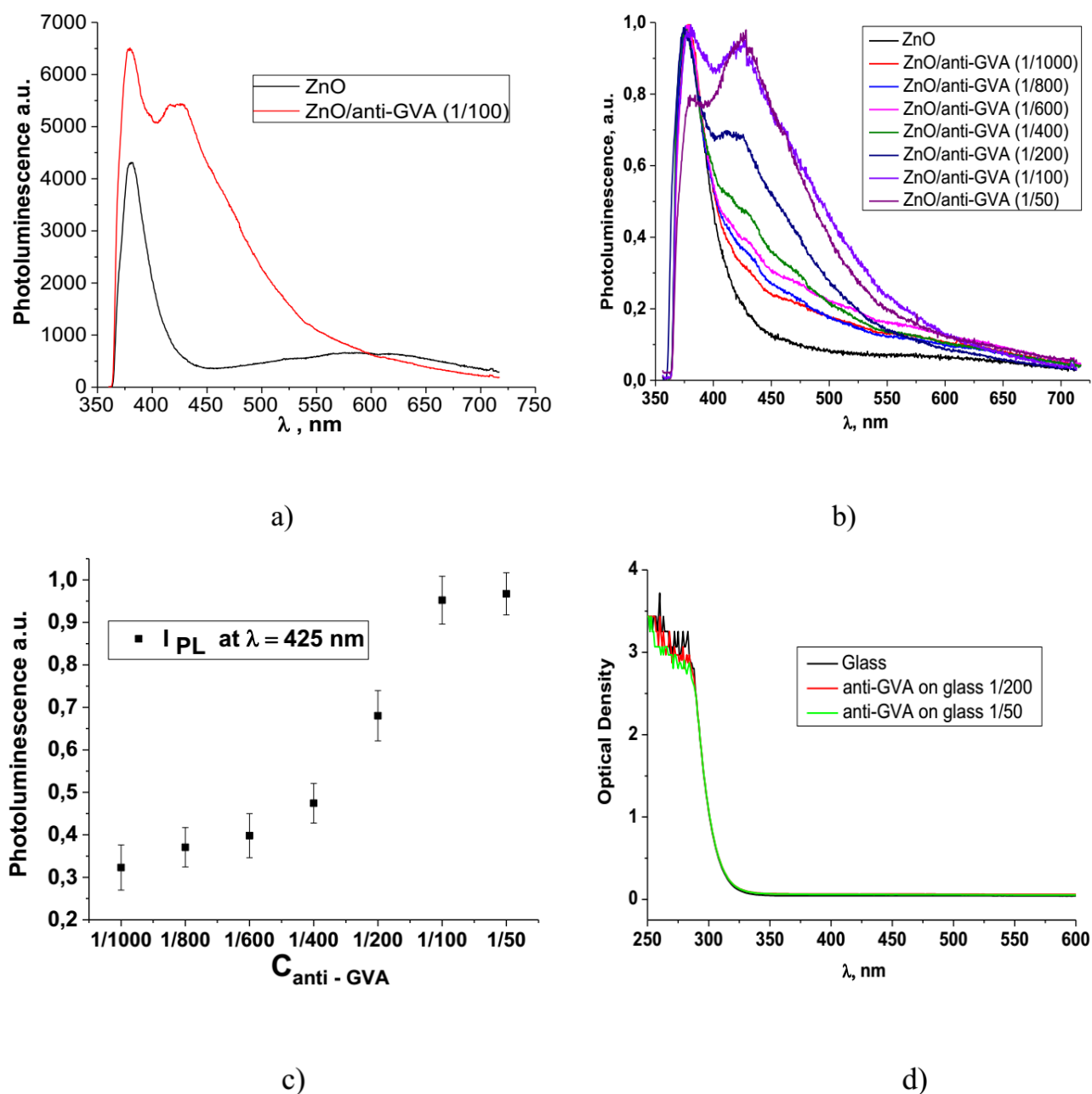


Figure 4-4. PL spectra of bare ZnO_{110nm} and ZnO_{110nm} functionalized with anti-GVA using 1/100 diluted initial anti-GVA solution (a), PL spectra (normalized intensity) of bare ZnO_{110nm} and ZnO_{110nm} functionalized with anti-GVA using solutions containing different concentrations of anti-GVA (b), PL intensity at 425 nm as a function of concentration of anti-GVA solutions used for the modification of ZnO-based substrates (c), absorbance spectra of anti-GVA deposited on glass from two solutions containing different concentrations of anti-GVA antibodies (d).

This intensity increases with the increase of surface-concentration of anti-GVA adsorbed from solutions containing different antiGVA concentrations (Fig. 4-4b). For low surface-concentrations of anti-GVA (adsorbed from initial anti-GVA solutions diluted by 1/1000 to 1/400 times), the PL caused by protein adsorption looks like PL band, which intensity increases with anti-GVA surface-concentration. In the ZnO_{110nm}/anti-GVA films, which were formed by immobilization of anti-GVA from 1/200 diluted initial anti-GVA solution, the PL emission turns to the formation of PL peak, which is centered at 425 nm, with the intensity increasing proportionally to the immobilized anti-GVA surface concentration. For the ZnO_{110nm}/anti-GVA films formed from the highest concentration (1/50 diluted initial anti-GVA sample) of anti-GVA containing sample, a redistribution of the peak intensities was observed between the PL peak attributed to the protein emission and the peak related to NBE of ZnO. The dependence of PL intensity vs anti-GVA concentration at the $\lambda=425$ nm (protein attributed PL) is shown in figure 4-4c. This dependence indicates that the saturation of the PL signal of ZnO_{110nm}/anti-GVA films appears for the films formed from 1/100 diluted initial sample of anti-GVA. Therefore, the optimal concentration of anti-GVA for the formation of biosensitive layer was in the 1/200 diluted sample.

Optical properties of anti-GVA were investigated by PL and optical absorbance measurements. The PL spectra of anti-GVA deposited on glass substrates are shown in figure 4-2b. No PL line around 425 nm was observed for the samples formed using solutions with highest antiGVA concentrations from 1/200 and 1/50 diluted samples. The spectra of optical absorbance of the same samples (Fig. 4-4d) demonstrate that anti-GVA antibodies do not have optical activity by themselves in the UV-VIS range of spectra. Therefore, the PL line at 425 nm is caused by the luminescence, resulted from the interaction of anti-GVA with ZnO.

4.4.3. Performance of immunosensor

The sensitivity of immunosensor was tested using ZnO_{110nm} film modified by anti-GVA (ZnO_{110nm}/ anti-GVA) formed using 1/200 diluted initial anti-GVA sample. The target analyte used in the experiment was GVA-antigen (Ag⁺) that is specifically bounding to the immobilized anti-GVA, because both, immobilized anti-GVA and GVA-antigen, which is present in Ag⁺ specimen, are complementary to each other and by interaction they are forming an 'immune complex'. The concentration of GVA-antigen in Ag⁺ specimen was in the range from 1 pg/ml to 1 μ g/ml (Fig. 4-5a). The interaction between ZnO_{110nm}/anti-GVA and GVA-antigen, which is present in Ag⁺ sample, resulted in the decrease of the NBE peak intensity by 20 % in average for all ZnO_{110nm}/anti-GVA/Ag⁺-based structures. However, the initial variation of NBE peak intensity for all ZnO_{110nm} samples disabled the application of NBE intensity changes as a sensor signal. Therefore, the spectra

were normalized and the response of the biosensor was based on the change in the intensity of PL band at 425 nm corresponding to the luminescence of anti-GVA (Fig. 4-5a). The response of the as formed immunosensor was observed at the Ag⁺ concentrations from 1 pg/ml to 10 ng/ml, where the intensity of protein related PL line decreased with the increase of the Ag⁺ concentration (Fig. 4-6). The further increase of the Ag⁺ concentrations led to the increasing PL intensity and full saturation of the PL signal at the 1 μg/ml.

The biosensor response (*S*) was calculated using the equation 4-1 [304, 305, 309]:

$$S = \frac{I_{Ab} - I_{Ab-Ag}}{I_{Ab}}, \quad (4-1)$$

where: *I*_{Ab} is a PL intensity at 425 nm of ZnO_{110nm} with immobilized anti-GVA; *I*_{Ab-Ag} is the PL intensity at 425 nm of ZnO_{110nm} with immobilized anti-GVA and GVA-antigen (Ag).

The sensitivity of obtained biosensor to the GVA Ag⁺ is in the range from 1 pg/ml to 10 ng/ml (Fig. 4-6, inset).

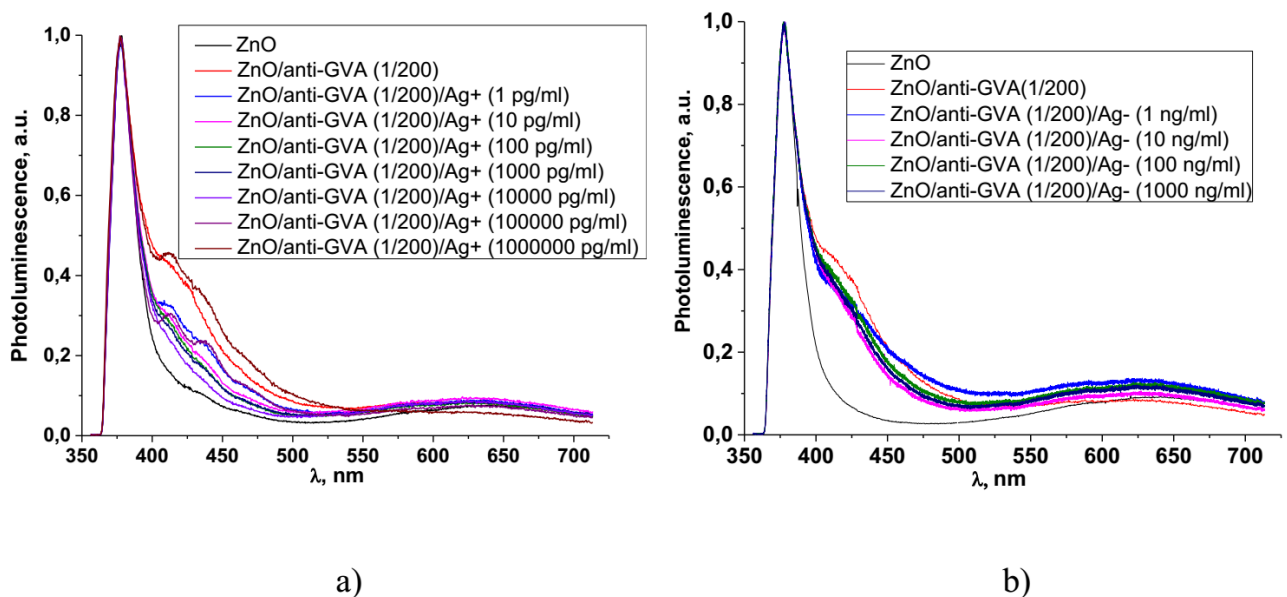


Figure 4-5. The dependence of ZnO_{110nm}/anti-GVA/Ag⁺ PL spectra (normalized intensity) after incubation of ZnO_{110nm}/anti-GVA-based immunosensor in different GVA-antigen concentrations containing specimens (specimens – Ag⁺) (a), PL spectra dependence (normalized intensity) of ZnO_{110nm}/anti-GVA-based immunosensor under different concentrations of proteins separated from healthy vine grape plants, which not contains antigen for anti-GVA (specimens – Ag⁻) (b).

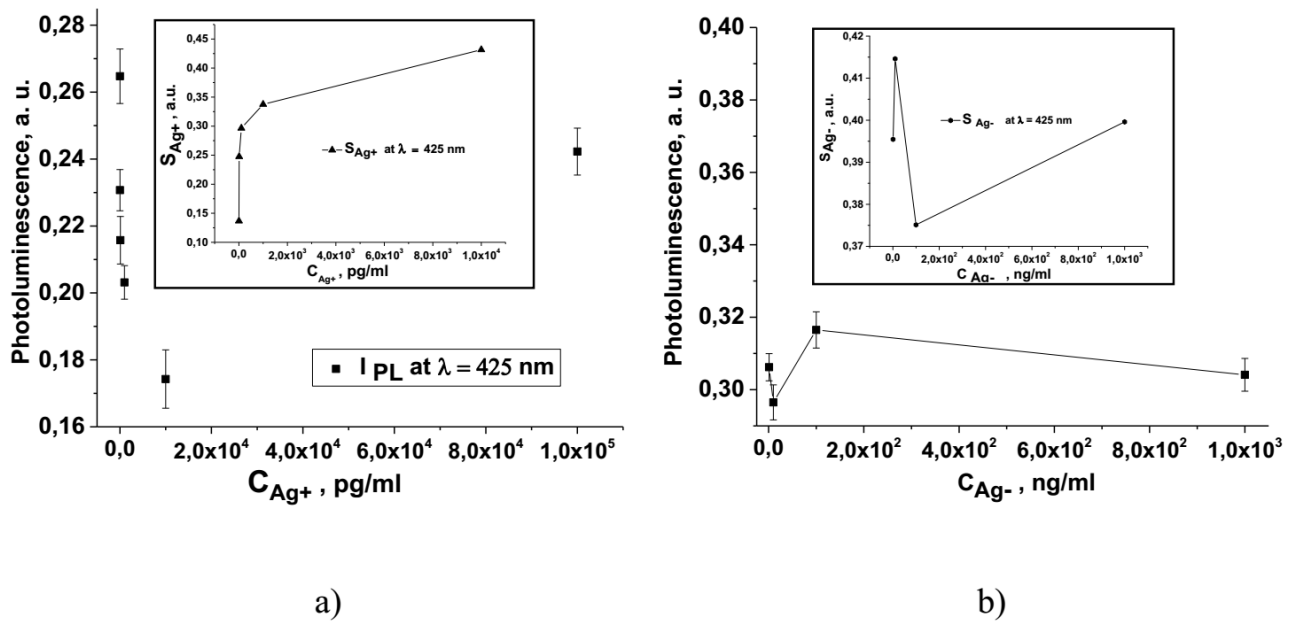


Figure 4-6. PL intensity at 425 nm as a function of GVA-antigen concentration in Ag+ specimen, inset – biosensor response (S) as a function of GVA-antigen concentration in Ag+ specimen (a), PL intensity at 425 nm as a function of different concentrations of proteins separated from healthy vine grapes, which not contain any antigen capable to bind with anti-GVA (specimens – Ag-), inset - biosensor response (S) as a function of Ag- specimen concentration (b).

The sensitivity of here proposed immunosensor cannot be compared directly with the one of already known and widely applied methods for GVA-antigen detection, which are based on enzyme linked immune-sorbent assay (ELISA) or real time polymerase chain reaction (RT-PCR) tests. Both (ELISA and RT-PCR) methods are providing very efficient detection of GVA, which is close to 100%, but these methods are based on a number of chemical/biochemical reactions and another analytical signal detection principles. Therefore both (ELISA and RT-PCR) methods in comparison with action of here proposed immunosensor are time-consuming, needs initial sample preparation and requires much more advanced equipment. In addition by both (ELISA and RTPCR) methods the quantitative determination of concentration of GVA-antigens is not very easy and is technically complicated. The detection of GVA-antigens using optical properties of ZnO film formed by ALD method proved to be relatively sensitive and selective analytical approach, which could be applied as an express method for the diagnosis of GVA infection, because it does not applies any additional labels, such as enzymes, which are used in ELISA, fluorescent-dyes, which are used in RT-PCR. Therefore here proposed immunosensor is simpler in use and much cheaper as well.

In order to check the selectivity of the biosensor, the control specimen – Ag-, which was isolated from the non-infected grapevine plants and not contained any GVA proteins, was deposited

and incubated on the biosensitive layer of immunosensor that was formed using 1/200 diluted sample of initial anti-GVA sample. Therefore in the latest specimen no proteins that could specifically bound to the anti-GVA were present. The incubation of ZnO/anti-GVA-based immunosensor with control-specimen Ag⁻ resulted in the decrease of NBE peak intensity and PL emission in the region of 400-500 nm (Fig. 4-5b). However, unlike the case of Ag⁺ specimen, PL lines, which are related to the GVA emission, have overlapped with each other and intersected at wavelength around 425 nm. Unlike the covalent binding, which is known as a 'strong' binding between protein and substrate that provides a significant structure of the bioselective layer and improves the bio-recognition, however it involves a cross-linking agent between ZnO surface and anti-GVA molecules forming the bioselective layer, which significantly complicates the general procedure, increases the cost of the experiment and partly damages immobilized anti-GVA antibodies. Therefore, in the absence of GVA-antigens no specific biosensor response was observed (Fig. 4-6b).

In the case of direct adsorption of biosensitive layer (anti-GVA antibodies) the binding between ZnO and biomolecules occurs due to Van der Waals forces and hydrogen bonds [296, 305]. The increase of PL intensity of NBE peak after the formation of biosensitive layer results from the charge transfer between anti-GVA molecules and conductance band of ZnO [296, 302, 305, 309, 310]. The phenomenon is known as an adsorption assisted increase of exciton-phonon interaction, which is evident from the change of NBE-related peak of ZnO. After 'biofunctionalization' of ZnO thin film surface, the PL emission increases since the molecular complexes can supply extra free electrons, which can participate in transitions between different surface energy levels [310].

The quenching of the main ZnO peak and the decrease of PL intensity related to anti-GVA antibodies (which are proteins) after their interaction with target-analyte (GVA antigen), which is present in Ag⁺ specimen, may be induced by several reasons. The surface reaction with a quencher may introduce non-radiative surface defects. In addition, the charge transfer from a radiative material to a quencher can also be one of the main mechanisms of the PL quenching [296]. Sodel *et al.* have suggested the collisional PL quenching mechanism, responsible for the recognition of the analyte. Under laser excitation, the carriers in ZnO are separated into conduction band (CB-electrons) and valence band (VB-holes). The carriers aim to recombine radiatively while emitting a photon with energy close to the ZnO band gap (~3.3 eV) for NBE emission or alternatively through the level defects with energies ~2.9 eV for the protein related emission [304].

The appearance of protein related luminescence band in the range of 400-500 nm can be caused by radiative transitions from defect states in the forbidden gap to valence band of ZnO. Zn interstitial states (~2.97 eV [312, 313]) and Zn vacancies (3.09 eV [304]) can play the role of

adsorption centers for the immobilized proteins. From the other side, the increase of PL peak at 425 nm, which is observed at high concentrations of anti-GVA antibodies, is in the same region as the blue emission peak of ZnS [314, 315]. This fact indicates that during the adsorption process the disulfide bonds, which are formed between the chains of anti-GVA, at least partly dissociates [316-321] and forms strong complexes (-OZn-S-anti-GVA) with Zn atoms, which are present in ZnO structure. The quenching of both NBE (378 nm) and protein related (425 nm) PL peaks after antigen-antibody interaction of ZnO/antiGVA with target analyte can be related to the partial elimination and/or weakening of interactions between anti-GVA and ZnO, which were formed during the immobilization of anti-GVA molecules on the ZnO surface.

4.5. Conclusions

Optical properties of ZnO films obtained by ALD method were applied for the detection of GVA-antigens for the first time. The detection of GVA-antigens was performed through direct immobilization of anti-GVA antibodies on the ZnO thin film surface, forming the biosensitive layer. The immobilization of anti-GVA antibodies resulted in new PL band appearance in the region of 400-550 nm that can be caused by the formation of Zn-S bound during the anti-GVA adsorption process. The GVA-antigen detection was performed using the changes in the GVA related PL band behavior. The sensitivity of obtained biosensor is in the range from 1 pg/ml to 10 ng/ml of protein. The biosensor selectivity has been proved by test based on the application of control specimen – Ag-, which was isolated from the non-infected grapevine plants and not contained any GVA proteins (antigens). The possibility to detect GVA-antigens without additional labels (e.g. enzymes, which are used in ELISA, or fluorescent dyes, which are used in RT-PCR) has been demonstrated. The decrease of the deposition time of immobilized layers has been achieved. The general duration of the experiment procedure is few times shorter than ELISA and RT-PCR. Due to good performance and simplicity of here described immunosensor ZnO-modified substrates could be applied as a platform for the development of other immunosensors based on immobilized antibodies, which would be sensitive to selected analyte.

CHAPTER V

Optical properties of ZnO deposited by atomic layer deposition (ALD) on Si nanowires

This chapter is in preparation for publication as:

Viktoriia Fedorenko^{1,2}, Roman Viter^{3,4}, Igor Iatsunskyi⁵, Grzegorz Nowaczyk⁵, Octavio Graniel¹, Karol Załęski⁵, Stefan Jurga⁵, Valentyn Smyntyna², Philippe Miele¹, Arunas Ramanavicius⁶, Sebastien Balme¹, Mikhael Bechelany¹, *Optical properties of ZnO deposited by atomic layer deposition (ALD) on Si nanowires.*

¹ Institut Européen des Membranes, UMR 5635, ENSCM, UM, CNRS, Université Montpellier, Place Eugene Bataillon, F-34095 Montpellier cedex 5, France

² Faculty of Physics, Experimental physics department, Odessa National I.I. Mechnikov University, 42, Pastera, 65026, Odessa, Ukraine

³ Institute of Atomic Physics and Spectroscopy, University of Latvia, 19, Raina Blvd., LV 1586, Riga, Latvia

⁴ State Research Institute Center for Physical Sciences and Technology, Savanoriuave. 231, LT-01108 Vilnius, Lithuania

⁵ NanoBioMedical Centre, Adam Mickiewicz University, 85 Umultowska str., 61-614, Poznan, Poland

⁶ Faculty of Electronics, Vilnius Gediminas Technical University, Sauletekio 11, LT-10223 Vilnius, Lithuania

In this chapter we represent the optimization procedures for the preparation of large areas ordered silicon nanowires (SiNWs) by combining metal-assisted chemical etching (MACE) and nanosphere lithography (NSL) techniques.

The aim of this study was to control the morphology and organization of SiNWs on a large area by the above-mentioned techniques, and to improve the properties of the SiNWs by utilizing ALD for the deposition of ZnO thin films. Figure a shows the scheme of metal-assisted chemical etching of Si wafer covered with polystyrene spheres, and the SEM image of SiNWs (etching time is 5 min) with 50 nm ZnO ALD layer. The TEM and SEM investigations confirmed the ability to produce highly uniform layers of ZnO covered SiNWs. The detailed study of structural and optical properties of core-shell SiNWs/ZnO heterostructure was done by utilizing XRD, SEM, reflectance and photoluminescence spectroscopy, respectively.

The X-ray diffraction analysis revealed the hexagonal wurtzite structure of all samples. The optical reflectance spectra for SiNWs/ZnO confirmed the low optical reflection of thin films. The study of photoluminescence (PL) spectra of SiNWs/ZnO showed the domination of defect emission bands, which points to deviations of stoichiometry of the prepared 3D ZnO nanostructures.

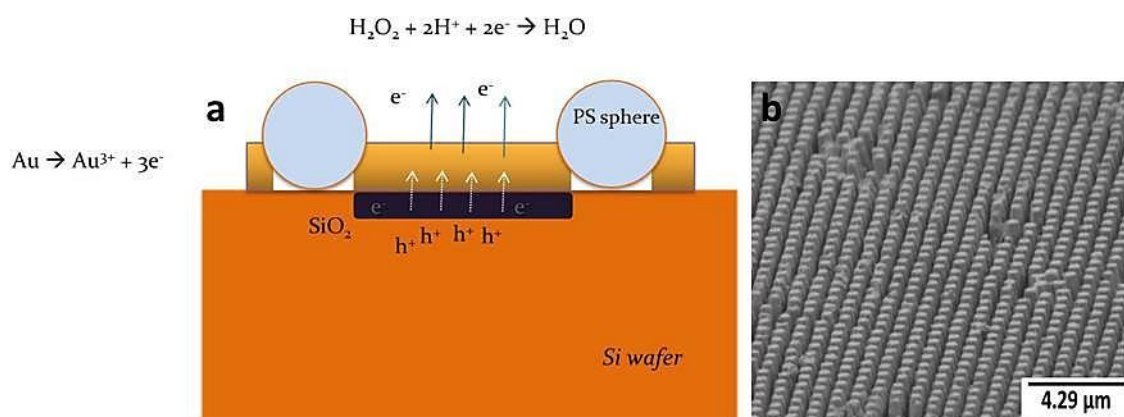


Figure. Scheme of metal-assisted chemical etching of Si wafer covered with PSS (a), and the SEM image of SiNWs/ZnO, 50 nm (b).

In summary, the conformal deposition of ZnO by ALD technique was done on highly-ordered vertical SiNWs array. The detailed study of structural and optical properties of core-shell SiNWs/ZnO heterostructure confirmed the highly uniform deposition of ZnO by ALD and the low optical reflection of the deposited thin films.

5.1. Abstract

Nowadays one dimensional silicon nanowires (SiNWs) are of great interest due to their abilities to scatter and trap incident light, large surface to volume ratio, and other special electronic and optical properties that make possible utilizing SiNWs as a promising blocks for a range of applications including electronic devices, energy storage devices, thermoelectrics, and biosensors. In this research, SiNWs were produced by combination of nanosphere lithography and metal-assisted chemical etching (MACE). After they were coated with ZnO layer by ALD method. These methods allow the morphology and the organization control of SiNWs on a large area. The structural and optical properties of the obtained nanostructures will be discussed. Structural properties of ZnO/SiNWs were studied by XRD and SEM. Optical characterization was performed by reflectance and photoluminescence spectroscopy.

The X-ray diffraction analysis revealed that all samples have hexagonal wurtzite structure. The grain sizes as measured using XRD data are found to be in the range of 7 - 14 nm. In order to confirm the composition of silicon nanowires covered by ALD ZnO, Raman spectroscopy have been used. The study of photoluminescence (PL) spectra of SiNWs/ZnO showed the domination of defect emission bands, which points to deviations of stoichiometry of the prepared 3D ZnO nanostructures. We observed also the reduction of the PL intensity of SiNWs/ZnO with the etching time for 7 minutes corresponding to a higher light scattering with the increase of the nanowire length.

Keywords: Silicon nanowires (SiNWs), metal-assisted chemical etching (MACE), nanosphere lithography (NSL), atomic layer deposition (ALD), ZnO.

5.2. Introduction

Since decades, silicon (Si) continues to be the most widely used semiconductor. Such great interest to this material is due to its beneficial features as high stability and non-toxicity, quantum confinement effects, high carrier mobility and well-established fabrication technique [322]. Because of morphological and energetic feature, silicon nanomaterials, known as one of the most important types of nanomaterials. Nowadays, one dimensional (1D) silicon nanostructures, *i.e.*, silicon nanowires (SiNWs) and Si nanopillars, are of great interest because of their abilities to scatter and trap incident light, large surface to volume ratio, and other special electronic and optical properties that make possible utilizing SiNWs as a promising blocks for a range of applications including electronic devices [323-325], energy storage devices [326, 327], thermoelectrics [328-330], and biosensors [331-334].

The first preparation of Si whiskers with $\langle 111 \rangle$ orientation, or filamentary Si crystals with macroscopic dimensions was reported in 1957 by Treuting and coworkers [335]. Thereafter, in 1964 by Wagner and Ellis performed the illuminating work and established the vapor-liquid-solid (VLS) mechanism of the Si whisker growth [336]. These pioneer studies open exciting possibilities for fabrication and investigation of SiNWs. In 2002, Peng and coworkers introduced a HF-etching-assisted nanoelectrochemical strategy to synthesize wafer-scale aligned SiNWs [337].

To date, there are a lot of different techniques to produce silicon nanowires such as chemical vapor deposition using the VLS (Vapor—Liquid—Solid) mechanism [338], laser ablation [339], molecular beam epitaxy [340], chemical etching [341], and solution growth [342]. Among various preparation methods, the metal-assisted chemical etching (MACE) of silicon substrates in combination with nanosphere lithography (NSL) has recently emerged as a promising method to fabricate large areas of ordered SiNWs [290, 343]. The combination of MACE and NSL techniques is under increasing attention, especially because MACE is a simple, inexpensive process, and able to control various parameters of the etched nanostructures, such as cross-sectional shape, diameter, length, and crystallographic orientation [258, 344, 345]. The main advantages of NSL consist of a short preparation time, a high level of hexagonal structure orientation and a possibility of application of large, monolayered masks directly onto any kind of surfaces [291, 346, 347].

Integration of SiNWs arrays as core and Zinc oxide (ZnO) as shell can have a strong impact on the development of sensing elements with improved properties. Si is an attractive substrate because of its low cost, good thermal conductivity, high crystalline quality, and availability of large size substrates with different types of conductivity (doping). In addition, silicon is the best candidate for miniaturized electronic devices for the development of modern nanoelectronic technology.

In parallel, ZnO is a wide bandgap (3.4 eV) II-VI compound semiconductor, that has a stable wurtzite structure with lattice spacing $a = 0.325$ nm and $c = 0.521$ nm [348]. It has attracted intensive research effort for its unique properties such as a thermal and chemical stability, optical transparency, piezoelectricity, etc. [349]. The attractiveness of ZnO is increased also due to its simplicity and the ease by which it can be synthesized as thin-film layer using a variety of techniques, including atomic layer deposition (ALD) [109, 350]. ALD is a special modification of chemical vapor deposition (CVD) method, capable of angstrom resolution, layer-by-layer growth of compound films [159]. The reaction between the incoming precursors and surface species is self-terminating. As a result, atomic level control of film growth can be achieved. Nowadays it is becoming a promising deposition method for growing uniform thin and ultra-thin films, especially

in the cases when precise film thickness control (should be determined by the number of reaction cycles), high reproducibility, thickness uniformity and excellent conformity are required [351].

In the present work, the silicon nanowires produced by utilizing gold-assisted chemical etching in combination with nanosphere lithography and after coated with ZnO layer by ALD method, were investigated. The structural and optical properties of the obtained nanostructures were discussed.

5.3. Materials and methods

5.3.1. Materials

Micro particles based on polystyrene, size 1 μm , 10 wt% aqueous solution (89904), sodium dodecyl sulfate (436143), Hydrofluoric acid HF 40% (47590), Perdrogen H_2O_2 30% (31642), Nitric acid (30709), Hydrochloric acid (258148), Diethyl zinc (DEZ) ($\text{Zn}(\text{CH}_2\text{CH}_3)_2$, 95% purity, CAS: 557-20-0) were purchased from Sigma Aldrich. Boron doped (8-25 $\Omega\text{ cm}$) p-type (100) crystal orientation, Si wafers were used as substrates.

5.3.2. Synthesis of SiNWs

The organized silicon nanowires were produced by utilizing gold-assisted chemical etching in combination with nanosphere lithography [290]. For this experiment, the monolayers were prepared using monodisperse polystyrene particles with the diameter of 1 μm .

The 1x1 and 2x2 cm^2 pieces of Si wafers are cleaned sequentially with deionized water (18.2 $\text{M}\Omega\text{ cm}$), ethanol and acetone by ultrasonication for 15 min each. Then the substrates were treated by O_2 plasma to have a hydrophilic surface. After the pretreatment, an ordered monolayer of polystyrene spheres (PSS) was prepared by self-assembly. The floating-transferring technique was utilized to deposit PSS on Si substrate. The polystyrene solution (40 μl) diluted by an equal amount of ethanol, was applied onto the modified substrate, which spread all over the substrate. After holding the substrate stationary for a while to obtain good dispersion of the suspension, the wafer was then slowly immersed into the glass vessel filled with deionized water and PSS started to form an unordered monolayer on the water surface. Then, one drop of 10% sodium dodecyl sulfate (SDS) solution was added to the water to change the surface tension and to consolidate the particles. The addition of SDS solution was an important step to produce 2D ordered colloidal array [352]. As a result, a large monolayer with highly ordered areas was obtained. Then this monolayer of PSS was transferred to the target substrate.

The quality of the PSS monolayer mask can be assessed right away by looking at the uniformity of the color throughout the whole area. The reflected color of the pattern varies with the size of the spheres and its quality.

After the sample was dried in air at room temperature and the spheres were self-assembled into a close-packed, two-dimensional ordered lattice *via* attractive capillary forces[353, 354]. Then the diameter of spheres was decreased by O₂ plasma etching for 5 min to expose the surface of wafer for metal deposition. Plasma etching is capable of uniform and fast modification of nanospheres, and it can control the sphere diameter by adjustment the etching time [355]. It is a convenient and efficient etching method. In order to stick the PS spheres at the Si surface, a heat treatment at 100 °C for 30 min was performed. On the next step a thin Au film was deposited by physical vapor deposition (PVD). The sputtering was carried out at a discharge of 25 mA in a vacuum with a pressure below 0.1 mbar. After the samples covered by Au were etched with the solution consisting of H₂O/H₂O₂/HF in the volume ratio 1:0.15:0.3 respectively, at room temperature for 1, 2, 5 and 7 minutes. The metal was removed with aqua regia solution; the PS spheres were etched by O₂ plasma.

Figure 5-1 represents the overall process for the synthesis of SiNWs.

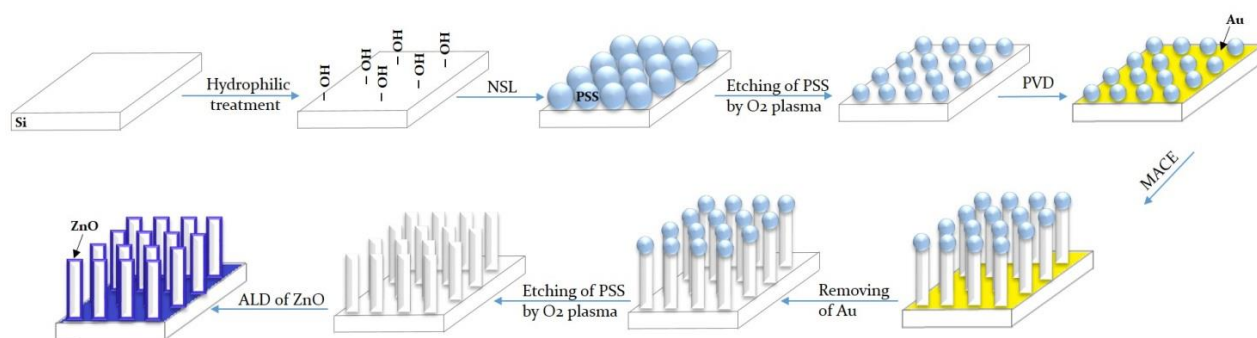


Figure 5-1. The schematic diagram of overall process for the synthesis of SiNWs by combining MACE and NSL techniques.

The samples with organized SiNWs were then placed into the ALD chamber for the synthesis of SiNWs/ZnO coating material.

5.4. Synthesis of ZnO coating Si nanowires arrays

A custom-made ALD reactor was used for the synthesis of ultrathin ZnO films. ALD was performed using sequential exposures of DEZ and H₂O separated by a purge of Argon with a flow rate of 100 standard cubic centimeters per minute (sccm). The deposition regime for ZnO consisted

of 0.2 s pulse of DEZ, 40 s of exposure to DEZ, 60 s of purge with argon followed by 2 s pulse of H₂O, 40 s of exposure to H₂O, and finally 60 s purge with argon. Thus, 20 and 50 nm thick ZnO layers were deposited on silicon nanowires using 100 and 250 ALD cycles, respectively. The deposition was performed at 100°C. The typical growth rate for ZnO coating during these cycles is found to be 0.2 nm per cycle.

5.5. Characterization

Structural and chemical compositions of the SiNWs/ZnO were analyzed by the scanning electron microscopy (SEM, S-4800, Hitachi), and the X-Ray diffraction (PANalyticalXpert-PRO diffractometer equipped with a X'celerator detector using Ni-filtered Cu-radiation). From the latter, the grain size was calculated by Debye-Scherrer equation.

The crystallographic structure of the films has been studied by X-ray diffraction (XRD). The analysis was performed using PANalyticalXpert-PRO diffractometer equipped with a X'celerator detector using Ni-filtered Cu-radiation. The XRD spectra were measured in the 2 θ angular region between 10° and 60°.

Structural properties of silicon nanowires covered by ALD ZnO were investigated by SEM and transmission electron microscopy (TEM) (JEOL ARM 200F high-resolution transmission electron microscope (200 kV) with an EDX analyzer). The cross-sections and lamellas for TEM investigations were prepared by Focused Ion Beam (FIB) by procedures described elsewhere.[356]. The FIB milling was carried out with a JEOL, JIB-4000.

Raman scattering measurements were performed using a Renishaw micro-Raman spectrometer equipped with a confocal microscope (Leica). The samples were measured in backscattering geometry with a spectral resolution of 1.0 cm⁻¹. The incident light was not polarized and also the light detector contained no polarization filters. The Raman scattering spectra were excited by a 488 nm laser. The beam was focused on the samples with a 50 x microscope objective with a numerical aperture of 0.4. The incident optical power was changed by using neutral density filters in the beam path.

Optical properties of the samples have been studied by diffuse reflectance spectroscopy (the spectral range 200-1400 nm). The diffuse reflectance spectroscopy has been performed using standard Shimadzu UV-3600 spectrophotometer with scanning step of 1 nm.

Photoluminescence spectroscopy was studied in spectral range of 350–800 nm. The measurements were performed at standard fluorometer (FS5 Spectrofluorometer (Edinburg instruments Ltd, 2 Bain Square, Kirkton Campus, EH54 7DQ, UK)). The excitation of luminescence was performed at wavelength of 280 nm.

5.6. Results and discussion

Figure 5-2 represents a dependence of the diameter of PSS as the function of different etching times (insets: 1 (b), 5 (c) and 10 (d) min, respectively) by O₂ plasma. The etching of PSS by O₂ plasma for 1 to 10 minutes permits to decrease the PSS diameter from 960±10 nm to 610±10 nm.

Figure 3-2a demonstrates the SEM image, which confirms the possibility to obtain a relatively large area, close-packed, hexagonal polystyrene monolayer, produced by floating-transferring technique.

Figure 3-2f shows a photograph of a monolayer pattern of PSS prepared by the mentioned before technique on 2x2 cm² silicon wafer. The color of the substrate observed in this photograph is due to the diffraction of light.

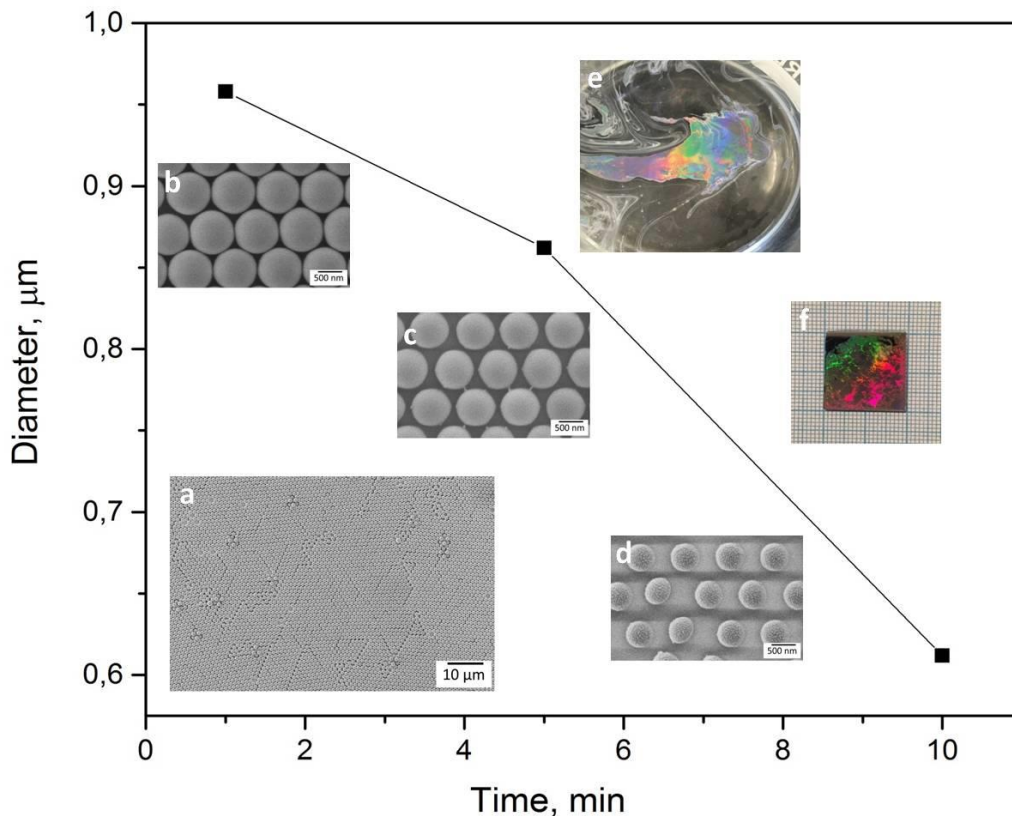


Figure 5-2. Diameter of PSS as the function of the O₂ plasma etching: Inset consists of SEM images of the PSS as-prepared by floating transferring technique (a) and with different O₂ plasma etching times: 1 (b), 5 (c) and 10 (d) min, respectively. And photographs of the monolayer of PSS on the water surface (e) and 2x2 cm² silicon wafer covered with monolayer built from 1 μm PS latex beads by the mentioned before technique (f).

Figure 5-3 shows the final structure after depositing 50 nm ZnO film on SiNWs array. The SEM images indicate a conformal coating by ALD of the Si substrate.

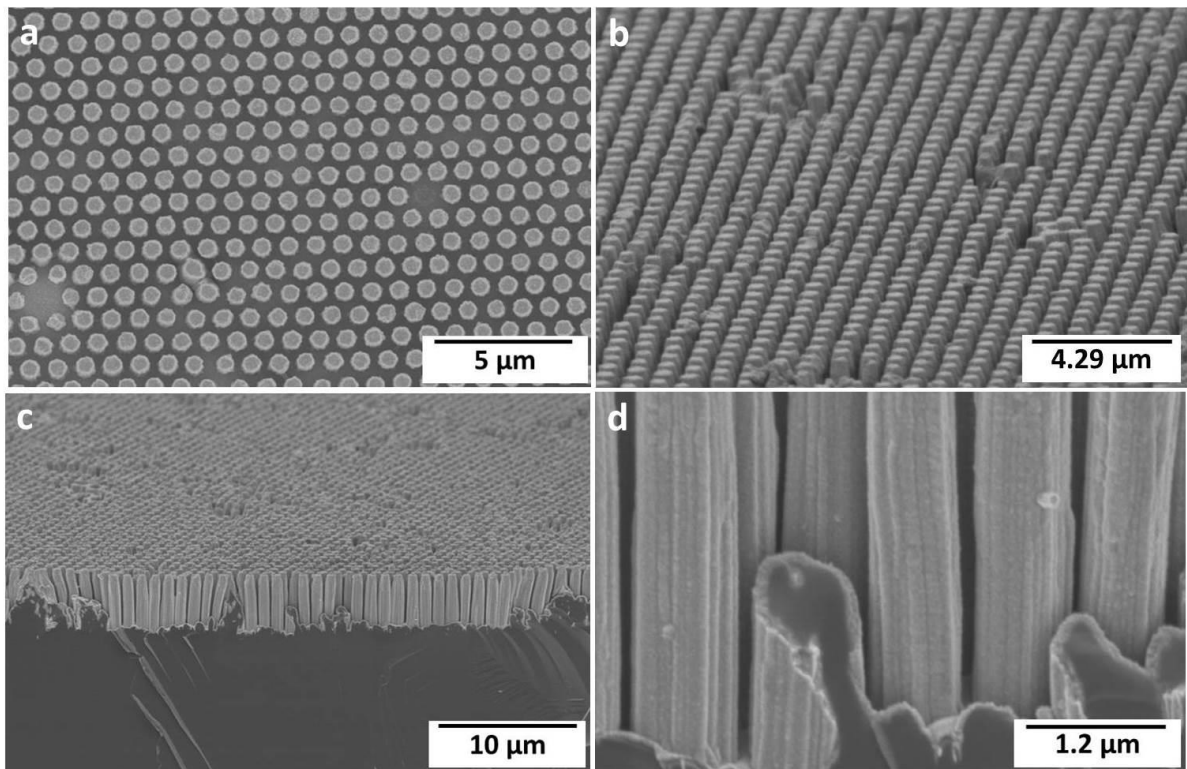


Figure 5-3. SEM images of SiNWs (etching time is 5 min) with 50 nm ZnO ALD layer.

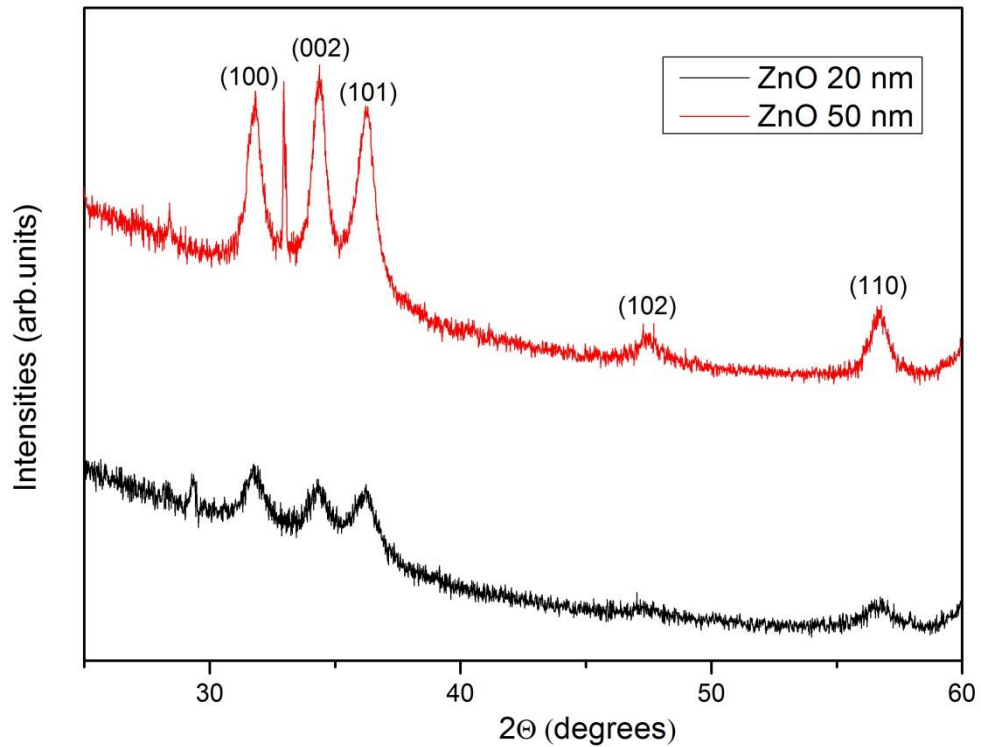


Figure 5-4. XRD spectra of SiNWs/ZnO with different thicknesses (20 and 50 nm) ZnO layers on SiNWs with 7 min etching.

Figure 5-4 shows the XRD spectra of 20 and 50 nm ZnO films deposited on the silicon nanowires substrate with 7 minute etching. All peaks in the recorded range were identified [109, 165, 357].

The respective positions of ZnO diffraction peaks show that all the films are polycrystalline with ZnO hexagonal wurtzite structure. The XRD patterns consists of the diffraction peaks of ZnO at 2θ values of 31.78° , 34.35° , 36.25° and 56.69° attributed to (100), (002), (101) and (110) planes, that have been observed for both ZnO thickness spectra (but with rather low intensity). The increase of the ZnO thickness (50 nm) led to the appearance of XRD peaks at $2\theta = 47.46^\circ$ corresponding to (102) reflections of ZnO.

The grain sizes (D) of the deposited films are estimated using the following formula [350]:

$$D = \frac{0.9\lambda}{\beta \cos(\theta)}$$

where λ is the wavelength of X-ray used ($\lambda = 0.154$ nm), β is the full width at half maximum intensity in radians, and θ is the Bragg angle. The average value of grain size is found to be 7.5 ± 0.45 nm and 14 ± 6.5 nm for samples etched for 7 minutes and covered with 20 and 50 nm ZnO, respectively.

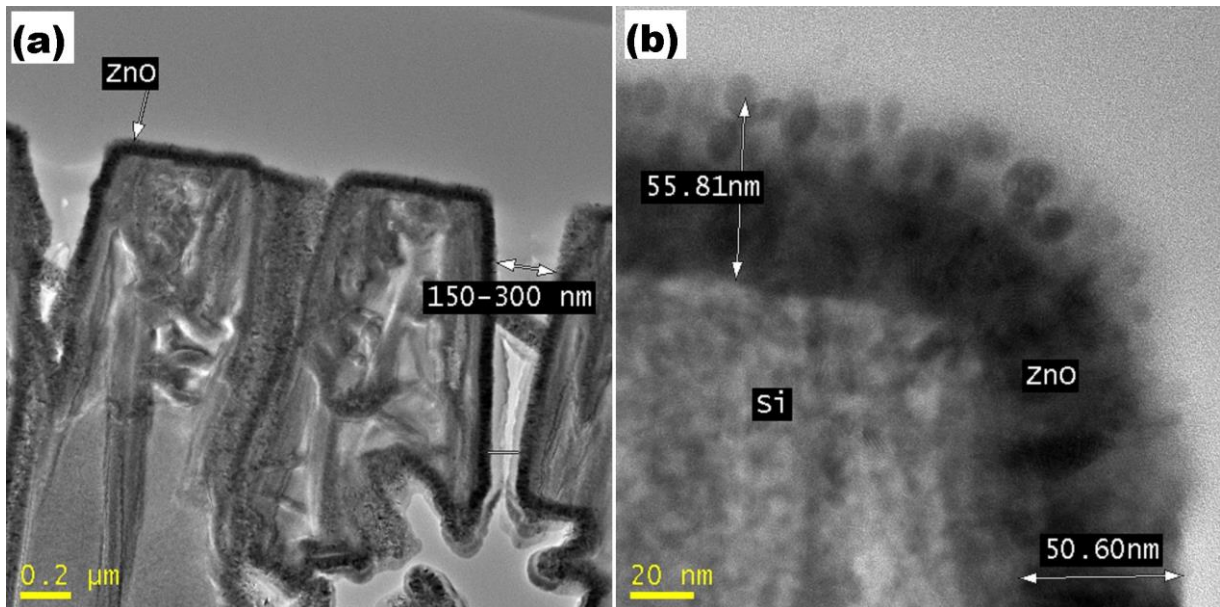


Figure 5-5. Cross-sectional view TEM image of ZnO-Si nanowires with different ZnO layer thicknesses: (a) 20 nm and (b) 50 nm.

Figure 5-5 shows the high-resolution TEM image of ZnO-Si nanowires with different ZnO layer thicknesses. Silicon nanowires coated with 20 nm of ZnO by ALD is presented in Fig 5-5a.

ZnO coating is seen to always be near the thickness of around 20 nm. It is clearly seen that the distance between the nearest wires is narrowed to the bottom from 150 to 300 nm. We can notice that the diameter of the wires is about 450 nm on the top and 850 nm at the bottom. Thus, wires have the shape of a truncated trapezoid. That would come from the longer exposure time of the top part to the etching solution according to Dawood *et al.* [358]. Macroporous structure of the wires could be also observed (Fig. 5-5 a). It can be explained by the lateral transport of the charge carriers [290].

Figure 5-5b shows a TEM image of individual silicon nanowires covered by 50 nm ALD ZnO layer. The total thickness of the layer is approximately 50 nm, having the maximum value on the top (55 nm). For both samples, the ZnO layers are in a polycrystalline phase. The size of nanocrystallites was estimated using elliptical shape fitting and the longer axis was used as the nanocrystallite size. The average grain size for 50 nm and 20 nm layer thicknesses was almost the same, 11.8 ± 2.5 nm and 10 ± 2.5 nm, respectively. These results confirmed the data obtained by XRD. The TEM images demonstrate the ability to produce highly uniform layers of ZnO covered silicon nanowires by the ALD processes.

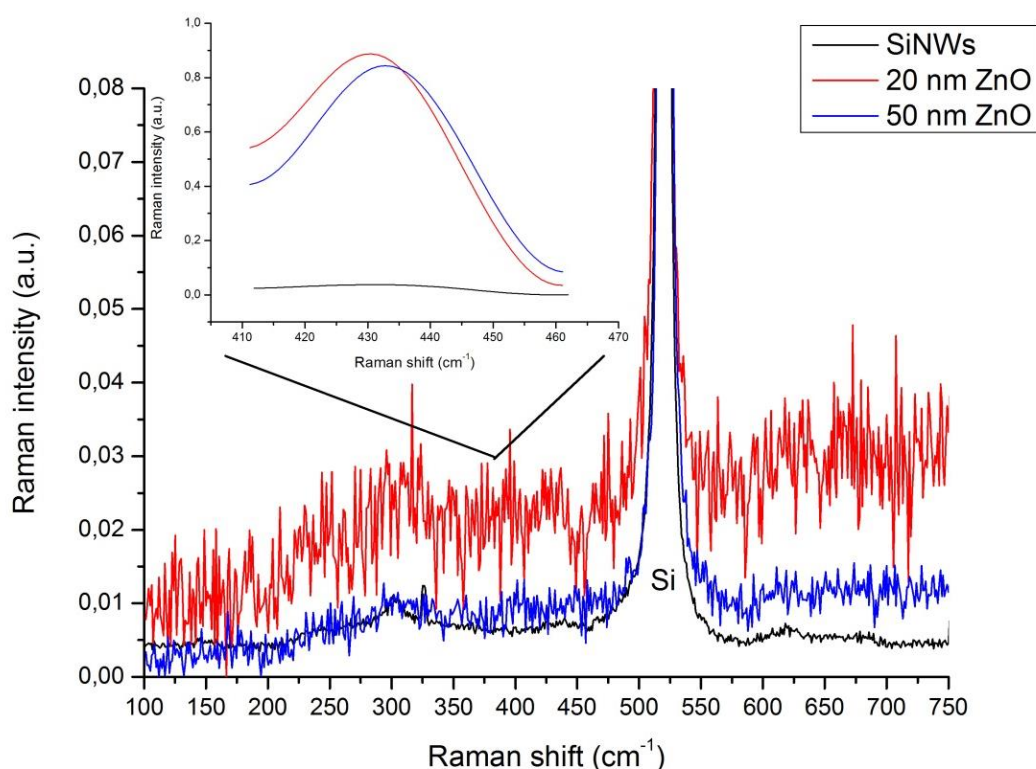


Figure 5-6. The Raman spectra of the Si NWs as-prepared (etching time is 7 min) and after deposition of ZnO 20 nm and 50 nm, respectively.

In order to confirm the composition of silicon nanowires covered by ALD ZnO, Raman spectroscopy have been used. Figure 5-6 shows the Raman spectra of Si nanowires (7 min. etching) with 20 and 50 nm ZnO layer. Raman spectra of the as-prepared ZnO-Si nanowires showed no significant peaks of ZnO in the background of the strong spectrum of the Si (520 cm^{-1}), indicating the small amount and/or the polycrystalline/amorphous phase of ZnO. However, increasing the number of accumulations allowed us to observe the Raman peak at about $432\pm 2\text{ cm}^{-1}$ (E_2^{high} mode), corresponding to the wurzite phase of ZnO, associated with the motion of oxygen atoms (inset of Figure 5-6) [359-361]. It is typical of the wurzite ZnO phase, but the peak is broader (full width half maximum – FWHM, is about 20 cm^{-1}) with respect to the bulk value (FWHM is less than 10 cm^{-1}) and blue-shifted [359-361]. This broadening and shifting could be explained by the quantum confinement effects in ZnO nanocrystals [360-362].

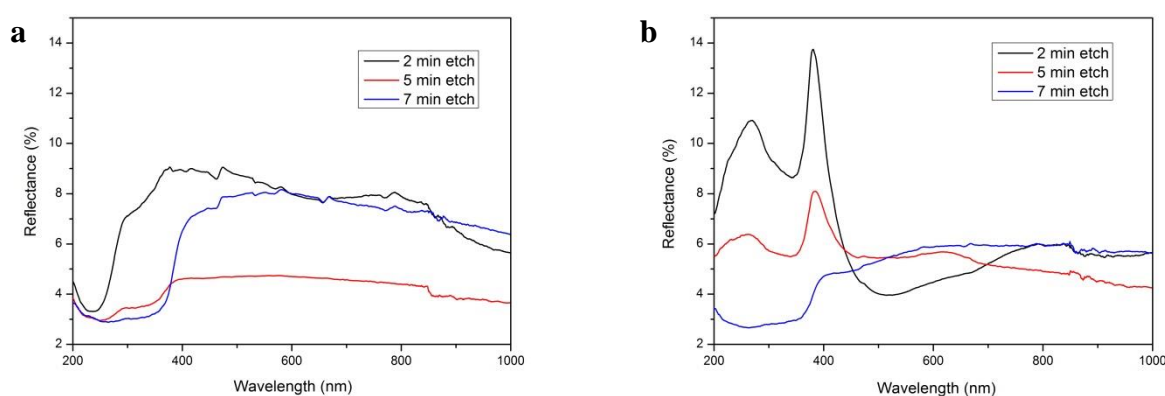


Figure 5-7. The reflection spectra of the SiNWs prepared at different etching times (2, 5 and 7 min) and after deposited of ZnO 20 nm (a) and 50 nm (b), respectively.

Figure 5-7 shows the reflectance of Si nanowires arrays etched for 2, 5 and 7 minutes and covered with 20 (a) and 50 nm (b) of ZnO, respectively. It was found that the reflectance decreases with increasing of etching time, for longer Si nanowires. This may be explained by the more effective light trapping and more absorption of longer nanowires. We observe that the reflectance is less than 5% and 8% for the SiNWs (etching time is 5 minutes) covered with ZnO 20 and 50 nm, respectively. Such low reflectance could be explained by the energy band structure of the sample. Various band gaps in the system causes a variety of near band-edge absorption from sunlight in different frequency ranges, reducing reflectivity. Also the change of the refractive indexes of the materials may effect on the reflection reduction [363]. The optical reflectance spectra for SiNWs/ZnO presented in Figure 5-7 confirm the low optical reflection of thin films. Layer of ZnO on SiNWs can work as antireflection coating.

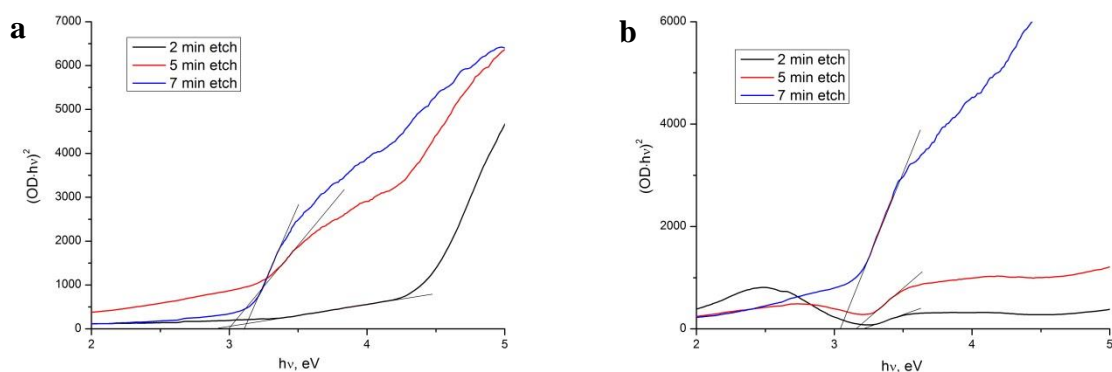


Figure 5-8. Band gap estimation of SiNWs covered with 20 (a) and 50 nm ZnO (b) by ALD, respectively.

Table 5-1. Band gap of SiNWs covered with 20 and 50 nm ZnO.

Etching time, min	2	5	7
	E_g (eV)		
ZnO 20 nm	$2,9 \pm 5-7 \%$	$3 \pm 5-7 \%$	$3,11 \pm 5-7 \%$
ZnO 50 nm	$3,22 \pm 5-7 \%$	$3,16 \pm 5-7 \%$	$3,05 \pm 5-7 \%$

The band gap values of SiNWs, prepared at different etching time (2, 5 and 7 minutes) and covered with 20 (a) and 50 nm ZnO (b) by ALD, were graphically calculated in the linear part of the absorption edge and showed in Figure 3-8. As we can see, the obtained values (presented in Table 5-1) are lower than the value typical of a ZnO single crystal ($E_g = 3.37$ eV). As was reported before, this difference should be due to the concentration of point defects (such as vacancies and interstitials of Zn and O) [109]. We can also observe a small increase of the band gap value with ZnO thickness, which could be associated with improvement of the crystalline structure of deposited samples [109].

PL of 3D ZnO nanostructures with different thicknesses is plotted in Figure 5-9. The PL spectra showed strong peaks in the range of 410-450 nm with long PL tail to higher wavelengths. Deconvolution of the PL spectra on separate lines has been performed using Gauss fitting in Origin software (see supporting information, Figure SI3-1). The spectra deconvolution showed peaks, centered at 376-379, 411-415, 434-437, 447-480, 490-540, 570-640 nm, 660-740 nm related to free exciton, Zn interstitials, Zn vacancies, neutral oxygen vacancies, single charged oxygen vacancies, double charged oxygen vacancies and surface defects, respectively [109, 165, 176, 177]. Domination of defect emission bands points to deviations of stoichiometry of the prepared 3D ZnO

nanostructures. The decrease of PL intensity for ZnO samples, deposited on 7 min etched Si nanowires could be related to higher light scattering with the increase of the nanowire length.

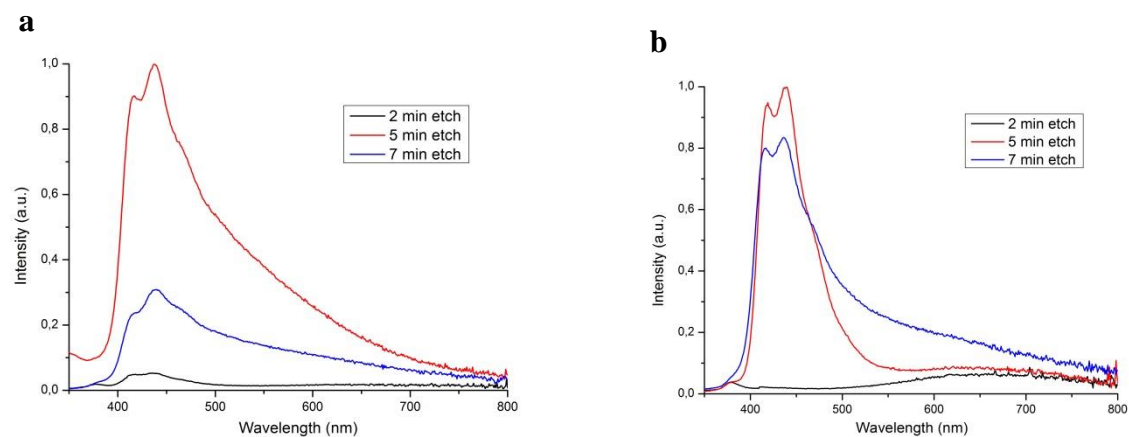


Figure 5-9. Photoluminescence spectra of SiNWs prepared at different etching times – 2, 5 and 7 minutes, and after ALD of 20 (a) and 50 nm ZnO (b), respectively.

5.7. Conclusion

In summary, we have demonstrated a simple and inexpensive method for the fabrication of ordered aligned SiNWs. The method utilizes 2D non-close-packed polystyrene sphere template for metal deposition in metal-assisted chemical etching of silicon. Here conformal deposition of ZnO was done on highly-ordered vertical SiNWs array by ALD technique. The ordered SiNWs readily produced by the present method may find myriad applications in array devices, such as field-effect transistors, sensors, electrodes, and two-dimensional photonic crystals. The high aspect ratio, anti-reflective characteristics inherent to nanowires structure can be exploited for fabricating future nanoelectronic and optoelectronic devices. The detailed study of structural and optical properties of core-shell SiNWs/ZnO heterostructure was represented.

The X-ray diffraction analysis revealed that all samples have hexagonal wurtzite structure. The grain sizes as measured using XRD data were found to be in the range of 7 - 14 nm, and confirmed by TEM measurement. The TEM and SEM images demonstrated the ability to produce highly uniform layers of ZnO covered silicon nanowires by the ALD processes. The optical reflectance spectra for SiNWs/ZnO confirmed the low optical reflection of thin films. Layer of ZnO on SiNWs can work as antireflection coating. The study of photoluminescence (PL) spectra of SiNWs/ZnO showed the domination of defect emission bands, which points to deviations of stoichiometry of the prepared 3D ZnO nanostructures. We observed also the reduction of the PL

intensity of SiNWs/ZnO with the etching time for 7 minutes that could be due to the higher light scattering with the increase of the nanowire length.

5.8. Supporting information

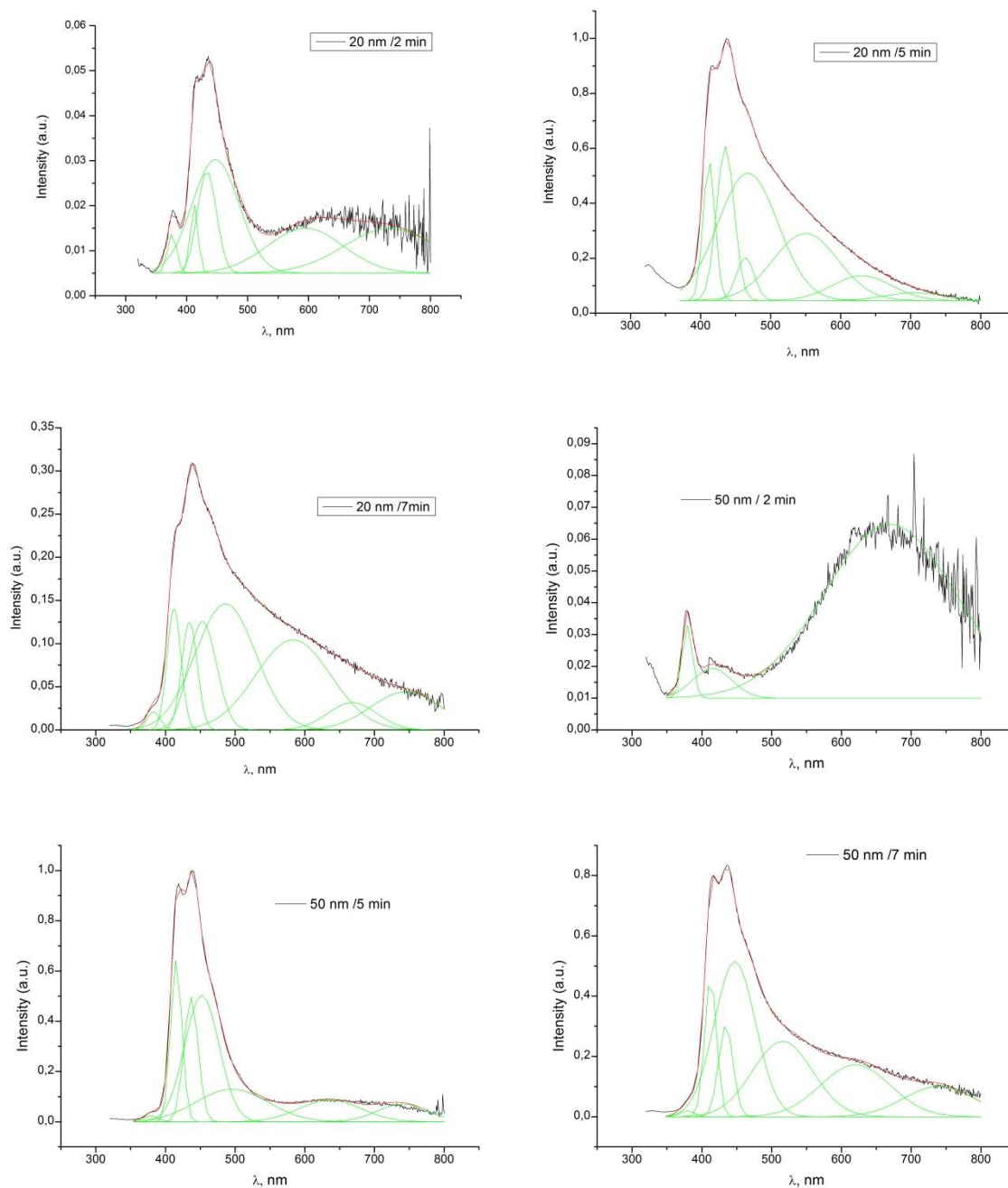


Figure SI5-1. Deconvolution of PL peaks spectra of SiNWs prepared at different etching time - 2, 5 and 7 minutes, and after ALD of 20 and 50 nm ZnO.

CHAPTER VI

Enhancement of Electronic and Optical Properties of ZnO/Al₂O₃ Nanolaminate Coated Electrospun Nanofibers

This chapter has been published in *The Journal of Physical Chemistry C* as:

Roman Viter^{1,5}, Igor Iatsunskiy², Viktoriia Fedorenko^{3,4}, Saulius Tumenas⁵, Zigmantas Balevicius^{5,6}, Arunas Ramanavicius⁵, Sebastien Balme³, Mateusz Kempniński², Grzegorz Nowaczyk², Stefan Jurga², Mikhael Bechelany³, *Enhancement of electronic and optical properties of ZnO/Al₂O₃ nanolaminate coated electrospun nanofibers*, *The Journal of Physical Chemistry C*, 2016, 120(9), 5124-5132

¹ Institute of Atomic Physics and Spectroscopy, University of Latvia, 19, Raina Blvd., LV 1586 Riga, Latvia

² NanoBioMedical Centre, Adam Mickiewicz University, 85 Umultowska str., 61-614 Poznan, Poland

³ Institut Européen des Membranes, UMR 5635 ENSCM UM CNRS, Université Montpellier, Place Eugene Bataillon, F-34095 Cedex 5 Montpellier, France

⁴ Faculty of Physics, Experimental physics department, Odessa National I.I. Mechnikov University, 42, Pastera, 65026 Odessa, Ukraine

⁵ State Research Institute Center for Physical Sciences and Technology, Savanoriuave. 231, LT-01108 Vilnius, Lithuania

⁶ Faculty of Electronics, Vilnius Gediminas Technical University, Sauletekio 11, LT-10223 Vilnius, Lithuania

⁷ Department of Macromolecular Physics, Adam Mickiewicz University, 85 Umultowska str., 61-614 Poznan, Poland

In this chapter, we report the enhancement of electronic and optical properties of 1D organic core with ZnO/Al₂O₃ nanolaminates designed by atomic layer deposition (ALD) and electrospinning.

Electrospinning is a simple, versatile, and cost-effective technology, which generates fibers with a high surface area to volume ratio. The schematic diagram of set up of electrospinning is shown in Figure a.

For our study we used polyacrylonitrile (PAN) as a core and ZnO/Al₂O₃ nanolaminates as a shell. PAN nanofibers have a number of advantages, as good mechanical and thermal stability, and the presence of the adsorption sites on the surface of the PAN fibers, which would facilitate the nucleation of the metal oxide layers by ALD. Nanolaminates are of great interest for their unique properties such as high dielectric constants and advanced mechanical, electrical, and optical properties. ZnO/Al₂O₃ nanolaminates allow the surface roughness to be controlled. TEM image of the PAN fiber coated by the ZnO/Al₂O₃ nanolaminates is shown in Figure b.

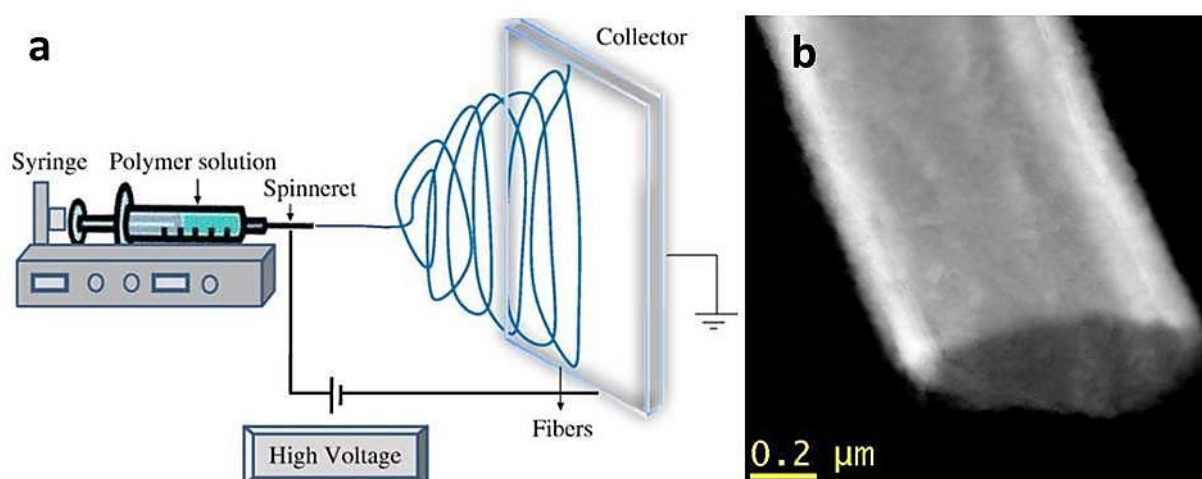


Figure 1. Schematic diagram of set up of electrospinning apparatus (a), and TEM image of the end face of PAN fiber coated by the nanolaminates (b).

We determined the structural and optical properties of Al₂O₃/ZnO from the XPS, TEM, FTIR, XRD and PL analysis, which provide important information about crystalline structure of nanolaminates on the 1D PAN substrate. A strong influence of the bilayer thicknesses on the crystallinity of ZnO nanolayers was shown. And we discussed the influence of structure parameters of ZnO/Al₂O₃ nanolaminates (thickness, grain size, number of bilayers, defect concentration) on the main electronic (work function) and optical (photoluminescence and band gap) properties. The observed enhanced photoluminescence of the 1D PAN ZnO/Al₂O₃ nanolaminates would allow applications in optical (bio)sensing field. Thus, the integration of metal oxide ALD technique and PAN nanofibers has a good perspective.

6.1. Abstract

Nanolaminates are new class of promising nanomaterials with outstanding properties. Here we explored on the tuning of structural properties and the enhancement of electronic and optical properties of 1D PAN ZnO/Al₂O₃ nanolaminates designed by atomic layer deposition (ALD) and electrospinning. The influence of ZnO/Al₂O₃ bilayer thicknesses on the fundamental properties of 1D PAN ZnO/Al₂O₃ nanolaminates has been investigated. Due to the quantum confinement effect, the shift of XPS peaks to higher energies has been observed. Work function of Al₂O₃ was mostly independent of the bilayers number, whereas the ZnO work function decreased with an increase of the bilayer number. Photoluminescence of the 1D PAN ZnO/Al₂O₃ nanolaminates corresponded to emission bands in ZnO nanolayers. Due to quantum confinement and surface band bending, no excitonic peaks were observed. The defect emission band was affected by the band bending and defect concentration. The enhanced photoluminescence of the 1D PAN ZnO/Al₂O₃ nanolaminates allows applications in optical (bio)sensing field.

6.2. Introduction

Nanolaminates are new class of promising nanomaterials with well-tailored properties. These materials are obtained by alternating layers with an individual thickness on the nanometer scale of different materials [165]. They manifest outstanding advanced mechanical [6], electrical, and optical properties [165] which depend from the constituent materials forming these nanolaminates. Zinc Oxide (ZnO) which can be incorporated in the nanolaminate material is a n-type semiconductor with wide band gap value (3.3 eV) and high exciton binding energy (0.06 eV). It also exhibited room temperature photoluminescence in UV-vis region [109, 165]. Among the different techniques to elaborate oxides based nanolaminates, atomic layer deposition (ALD) is a powerful tool to fabricate different oxide materials [159, 307]. It is based on two self-limiting surface reactions which allow growing continuous, smooth, and conformal ultrathin film on high aspect ratio and complex substrates such as the 1D nanostructures with a precise dimensional control. This paper deals with the investigation of electronic and optical properties of ZnO/Al₂O₃ nanolaminate coated electrospun nanofibers.

The design of Al₂O₃/ZnO nanolaminates as well as ZnO thin film doped with Al was widely investigated by ALD [4-6, 8, 164]. The ZnO deposited on Al₂O₃ thin films in the Al₂O₃/ZnO nanolaminates demonstrated a different growth direction in comparison to single ZnO thin film [364]. ZnO demonstrates as well a change from amorphous to nanocrystalline with the increase of the bilayers thickness where Al₂O₃ layer remains amorphous [6]. The change of the growth

direction, the crystallinity, and the Al doping influence the optical [165, 166], electrical [101], and mechanical properties [6] of the deposited thin films. Recently, we investigated the optical and the structure properties of ZnO/Al₂O₃ nanolaminates deposited on Si substrates by ALD [165]. We demonstrated the amorphous-to-crystalline phase transitions of ZnO in ZnO/Al₂O₃ nanolaminates as well as the quantum confinement and size dependent room temperature photoluminescence [165]. It was shown a correlation between structure (grain size and layer thickness) and optical (extinction coefficient and refractive index), pointing to the influence of growth conditions on the fundamental properties of the nanolaminates [165].

Different 1D nanostructures such as carbon nanotubes (CNTs) and polymer fibers have been investigated in order to design core/shell nanostructures using ALD of metal oxides [365-369]. Different studies were performed for the growth of oxides of Carbon nanotubes. Stano et al. reported the influence of CNTs type and the defect concentration on the ALD coating [369]. For low defect concentration, ALD coating cannot be realized. The functionalization of CNTs surface is needed to promote the nucleation of the oxide film. Carboxyl and hydroxyl groups are formed on the CNTs surface to initiate the ALD growth. Kemnade et al. showed that conformal growth of ALD ZnO layer on CNTs requested the modification of the CNTs with aromatic linking agents [366]. Lin et al. reported on the importance of CNT functionalization before deposition of ZnO nanolayers by ALD [367]. Kayaci et al. reported that ALD ZnO layers provided a conformal coating of nylon fibers [365]. However, Oldham et al. demonstrated that TMA and DEZ precursors could chemically react with polyamide-6 (PA-6) nylon nanofibers destroying their physical properties [368]. Therefore, the conformal and uniform ALD coating on 1D nanostructures could be achieved by the right choice of the core chemical composition and surface state of the 1D nanostructures. PAN nanofibers are good chemically stable material for 1D core/ shell nanostructure design [256]. PAN nanofibers have been successfully used for chemical deposition of different metal nanoparticles on their surface. It was shown that PAN nanofibers have good mechanical and thermal stability. The adsorption sites present on the surface of the PAN fibers would facilitate the nucleation of the metal oxide layers by ALD. Thus, integration of metal oxide ALD technique and PAN nanofibers has a good perspective.

Previously, we have reported on the fabrication of three-dimensional polyacrylonitrile/ZnO material prepared by the combination of electrospinning and atomic layer deposition (ALD) as new material with large surface area to enhance the optical properties [31, 110]. The study of room temperature photoluminescence (PL) spectrum exhibits peak intensity which enhance by a factor of 2000 compared to a flat Si substrate [110]. In the present work, we report on the enhancement of electronic and optical properties of 1D organic core with ZnO/Al₂O₃ nanolaminates shell

nanostructures. The influence of structure parameters of ZnO/Al₂O₃ nanolaminates (thickness, grain size, number of bilayers, defect concentration) on the main electronic (work function) and optical (photoluminescence and band gap) properties will be discussed. The enhancement of electronic and optical properties will allow application in different fields such sensors and biosensors.

6.3. Materials and methods

Polyacrylonitrile (PAN) nanofibers have been elaborated by electrospinning technique to be a template for the nanolaminates design by ALD.

6.3.1. Electrospinning of PAN Nanofibers. Polyacrylonitrile PAN (M_w = 150 000) and dimethylformamide (ACS reagent, ≥99.8%) were purchased from Sigma-Aldrich. Polyacrylonitrile (10 wt % PAN) was dissolved in dimethylformamide (DMF). The electrospinning solution was maintained under agitation for 1 h and then heated in an oil bath at 80 °C for 10 min. The used electrospinning machine was a homemade device using an HPx 600 605 generator (physical instruments) and a KDS 100 syringe pump. The polymer solution was electrospun in ambient air atmosphere under an applied voltage of 25 kV with a flow rate of 3 mL h⁻¹ using a 0.7 mm diameter syringe connected to the positive output of the generator. A fix collector was placed 25 cm from the tip of the syringe and was related to the negative output of the generator. The droplet was transformed to a Taylor cone due to the electrostatic field applied between the syringe and the collector. The evaporation of the solvent during the process induces the formation of a net of submicron fiber.

6.3.2. ALD Deposition of Nanolaminates. Diethyl zinc (DEZ) (Zn(CH₂CH₃)₂, 95% purity, CAS: 557-20-0) and trimethylaluminum (TMA) ((CH₃)₃Al) 98% purity, CAS: 75-124-1) were purchased from Sigma-Aldrich. A custom-made ALD reactor was used for the synthesis of ultrathin Al₂O₃/ZnO nanolaminates. ALD was performed using sequential exposures of TMA (DEZ) and H₂O separated by a purge of Argon with a flow rate of 100 sccm. The deposition regime for ZnO and Al₂O₃ consisted of 0.2 s pulse of TMA (DEZ), 30 s of exposure to TMA (DEZ), 30 s of purge with argon followed by 2 s pulse of H₂O, 30 s of exposure to H₂O, and finally 40 s purge with argon. Al₂O₃/ZnO ultrathin nanolaminates with different numbers of cycles were deposited on electrospun PAN nanofibers (Table 6-1). The deposition temperature was fixed to 100 °C. We note here that, in contrast to the deposition of thin films on flat surfaces, the reactants had to diffuse into the high-aspect-ratio structures. Therefore, an exposure time should be added and adapted in order to ensure the conformal coating of the PAN nanofibers. GPC of ~0.2 nm/cycle has been observed for Al₂O₃ and ZnO. These values are consistent with what has been reported elsewhere by Karvonen et al. [164] on ZnO/Al₂O₃ nanolaminates. The difference between the GPC of Al₂O₃

reported on single Al₂O₃ layers and the ZnO/Al₂O₃ nanolaminates has been attributed to the higher surface area of the rough crystalline ZnO interfaces [164].

Table 6-1. Al₂O₃/ZnO Ultrathin Nanolaminates Synthesis by ALD

samples	cycles of Al ₂ O ₃	cycles of ZnO	no. of bilayers	bilayer thickness (nm)
Al ₂ O ₃ /ZnO 20 (0.6/0.6 nm)	3	3	20	1.2
Al ₂ O ₃ /ZnO 10 (1/1 nm)	5	5	10	2
Al ₂ O ₃ /ZnO 4 (2.6/2.6 nm)	13	13	4	5.2
Al ₂ O ₃ /ZnO 2 (5/5 nm)	25	25	2	10
Al ₂ O ₃ /ZnO 1 (10/10 nm)	50	50	1	20

6.3.3. Structural, Chemical, and Optical Characterizations. Structural and chemical compositions of all PAN-nanolaminates were analyzed by transmission electron microscopy (TEM). Images were obtained with a JEOL ARM 200F high-resolution transmission electron microscope (200 kV) with an EDX analyzer (JED2300, at least 30 accumulations, matrix 512 × 512 points in STEM mode). Dark and bright field detectors were used.

FTIR spectra were obtained with the Bruker VERTEX 70v vacuum spectrometer using the RT-DLaTGS detector (spectral resolution of 4 cm⁻¹). X-ray diffraction measurements were performed with PANalytical Xpert-PRO diffractometer equipped with a X'celerator detector using Ni-filtered Cu-radiation. Surface structural and chemical properties of PAN-nanolaminates were analyzed by means of the XPS/UPS technique mounted within the Omicron Nanotechnology multiprobe UHV system, using a monochromatized Al K α X-ray as the excitation source ($h\nu = 1486.6$ eV) and choosing C 1s (284.6 eV) as the reference line. XPS was conducted under ultrahigh vacuum (10⁻⁷ Pa). CasaXPS software was used to analyze the XPS data. Optical properties of ultrathin nanolaminates have been studied by photoluminescence spectroscopy (in the spectral range of 370-800 nm). The excitation of luminescence was performed by a solid state laser source

(Nd:YAG, 355 nm, 13 mW cm⁻²). The registration of the emitted spectra was provided by an experimental setup described elsewhere [109, 110, 165].

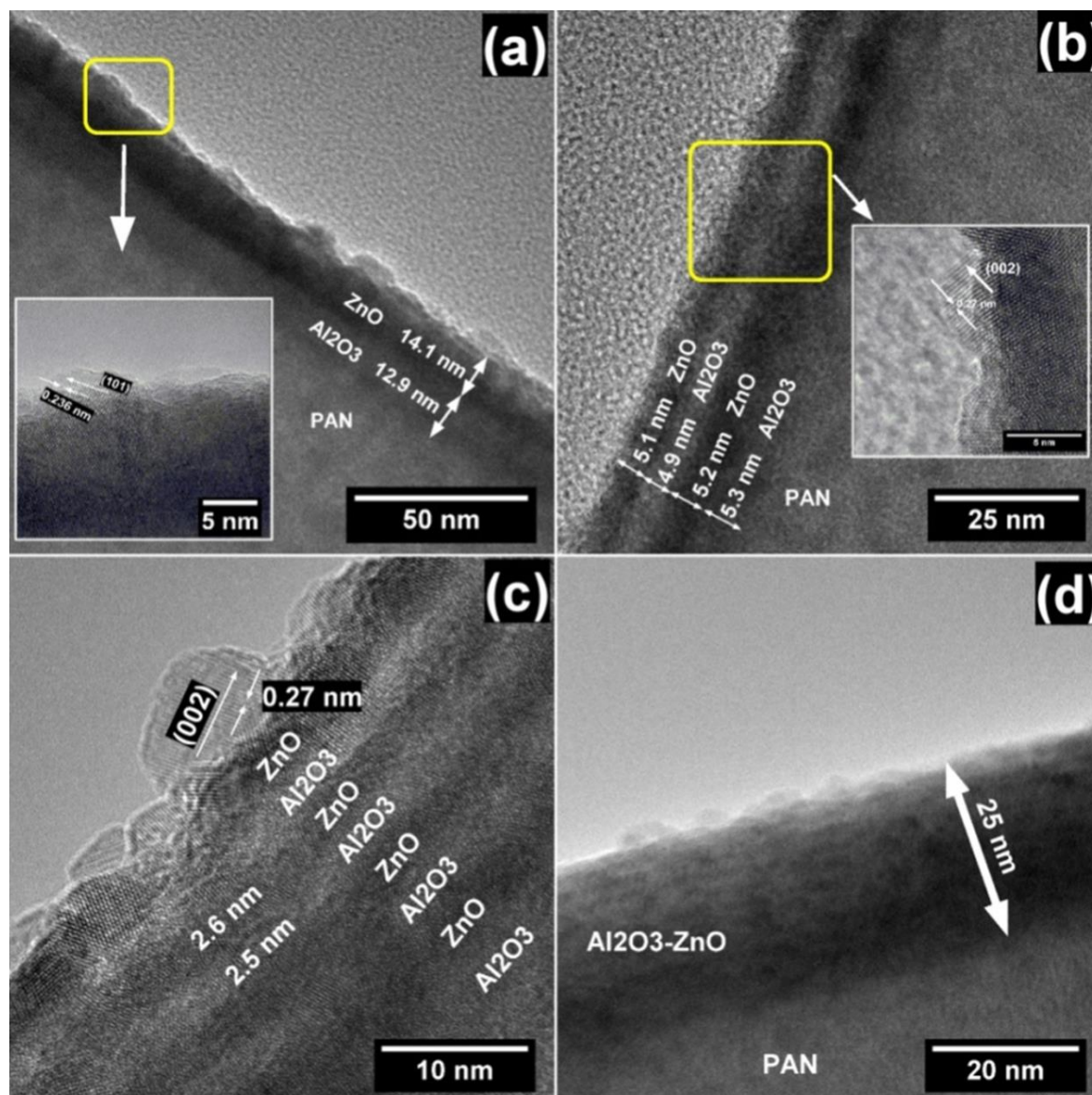


Figure 6-1. TEM images of PAN-Al₂O₃/ZnO nanolaminates with different bilayers thicknesses: (a) 20 nm, (b) 10 nm, (c) 5.2 nm, and (d) 2 nm. Insets show the corresponding high-magnification images.

6.4. Results and discussion

6.4.1. Chemical and Structural Characterizations. TEM images of PAN-Al₂O₃/ZnO nanostructures are presented in Figure 6-1 (TEM image of the end face of PAN fiber and TEM/EDX mapping in Supporting Information (Figures SI6-1 and SI6-2)). The TEM images confirm the conformal coating of the PAN nanofibers by ALD. It is clearly seen the nanolaminates formation (ZnO (dark stripes) and Al₂O₃ (light stripes)). The total thickness of nanolaminates layer is 25 nm

(Figure 6-1d). Lattice fringes seen in high-resolution TEM images reveal ZnO nanocrystals with (101) and (002) planes (Figure 6-1a and b insets). Using ImageJ software, the grain size and the interplane distances for (101) and (002) lattice planes were calculated (insets of Figure 6-1a-c). The grain size was calculated using elliptical shape fitting and the longer axis was used as the grain size. The average grain size for 20 nm, 10 and 5.2 nm bilayer thicknesses were 9.8 ± 2.5 nm, 6.5 ± 1.5 nm and 5.3 ± 2.1 nm, respectively. For 2 and 1.2 bilayer thicknesses, the grain size was not determined due to the quality of the image and the resolution of TEM. We suppose that in the case of 20, 10, and 5.2 nm bilayer thicknesses, the grains were elongated and limited by the layer thickness. The TEM analysis provided evidence that the Al_2O_3 layers are amorphous for all samples. The ZnO layers are in a polycrystalline phase. The TEM images demonstrate the ability to produce highly uniform layers of nanolaminates covered PAN fibers by the ALD processes.

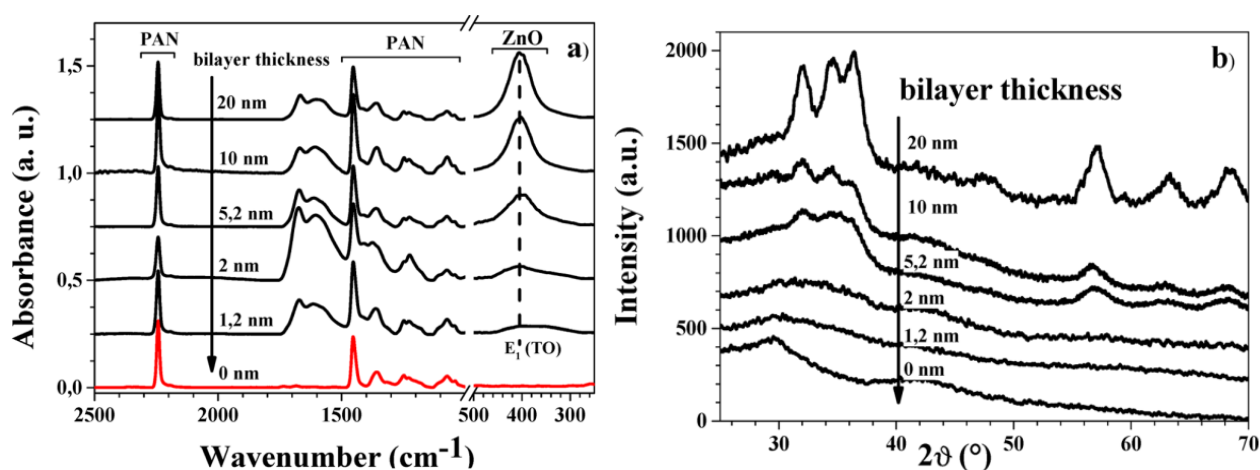


Figure 6-2. (a) Absorbance spectra and (b) XRD spectra of PAN- Al_2O_3 /ZnO nanolaminates at various bilayers thicknesses. Spectra are shifted for clarity.

The Fourier-transform infrared (FTIR) absorbance spectrum is presented in Figure 6-2a. The FTIR data reveals a presence of the main vibration bands of polyacrylonitrile (PAN) in investigated samples. The bands manifest themselves in the ranges of $2260\text{-}2240\text{ cm}^{-1}$ ($\text{C}\equiv\text{N}$ stretch) and $1485\text{-}1035\text{ cm}^{-1}$ (C-O and C-C stretch and aliphatic CH -group vibrations of different modes in CH , CH_2 and CH_3). Very sharp and strong peak at 2243 cm^{-1} is assigned to nitrile band. After deposition of Al_2O_3 /ZnO nanolaminates, two new bands appear in the $1670\text{-}1600\text{ cm}^{-1}$ spectral range which are attributed to carbonyl group vibrations [370]. In the spectral range $600\text{-}380\text{ cm}^{-1}$, the peak at 407 cm^{-1} is visible, which is related to ZnO $\text{E}_{1,\text{TO}}$ phonon mode. With a decrease of the nanolaminate thickness, the ZnO phonon related absorption decreases, and at the 1.2 nm bilayer thickness it is undetectable. This tendency implies the transition from the polycrystalline to amorphous phase of

the nanolaminates with low bilayer thicknesses. Similar tendency is shown by XRD spectra recorded from nanolaminates with the same bilayer thicknesses (Figure 6-2b). The ZnO related XRD peaks essentially decrease with a decrease of bilayer thickness. It is reasonable to assume that amorphous nature of ultrathin nanolaminates required minimum thickness to allow crystallization in a thin film [166]. The proposed crystallization model for ultrathin layers and superlattices is taking into account the interface energies, the thickness of the layers, the melting point of the system, and the bulk amorphous crystallization temperature [371]. It was shown that exponential increase of the crystallization temperature leads to the decrease of the minimal thickness at which crystallization occurs. From XRD (Figure 6-2b), HRTEM, and previous studies [6, 166], this bilayer thickness value was shown to be 2.5 nm for Al₂O₃/ZnO nanolaminates. So, we assume that close to this value is the point at which the crystallization process starts in Al₂O₃/ZnO nanolaminates. The ZnO grain size decreases with decreasing the bilayer thickness. The amorphous Al₂O₃ layer plays the role of stopping layer for ZnO growth. The ZnO layer is forced to renucleate on the underlying amorphous Al₂O₃ layer inducing the decrease of the grain size when the bilayer thickness decreases.

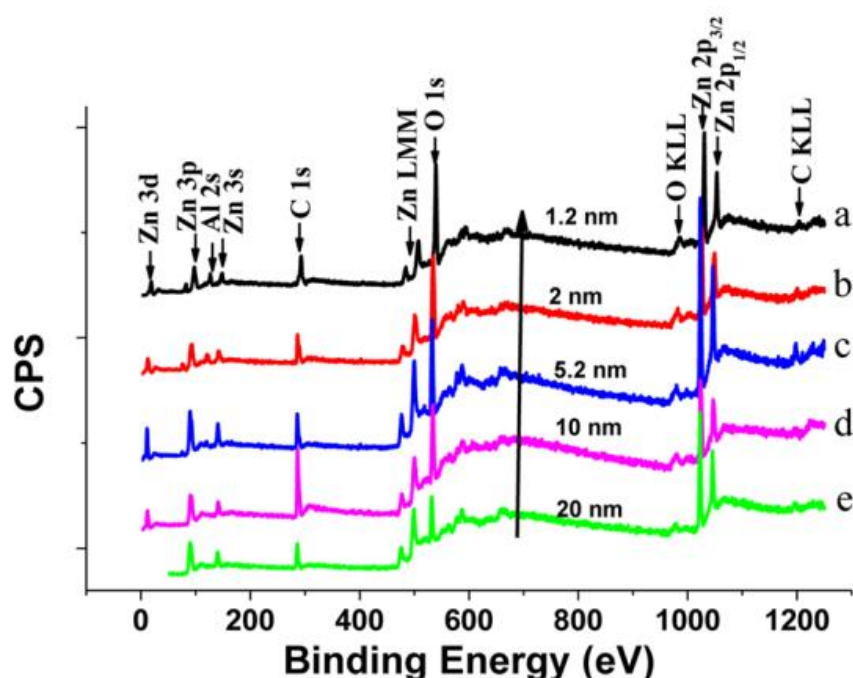


Figure 6-3. XPS survey spectra of ZnO/Al₂O₃ nanolaminates coated polymer fiber with different bilayer thicknesses: (a) 1.2 nm, (b) 2 nm, (c) 5.2 nm, (d) 10 nm, and (e) 20 nm. Main core levels are labeled. Data are normalized to each O 1s peak maximum and separated vertically.

The surface composition and chemical state polymer fiber coated with different bilayers thicknesses of ZnO/Al₂O₃ nanolaminates were studied by XPS (Figure 6-3). Samples depict zinc (Zn), aluminum (Al), oxygen (O), and carbon (C) components. It is worth to say that no peaks,

related to Al were observed for nanolaminates with 10 and 20 nm bilayer thicknesses (Figure 6-3d and e). It is related to the limit of the penetration depth of the excitation X-ray photons. As was shown in our previous work, the Auger parameter is a useful tool to determine the stoichiometry and the phase of obtained structures [372]. The main peak of the Zn (LMM) Auger series occurs at kinetic energy of 988 ± 0.5 eV. From this value and Zn $2p_{3/2}$ binding energy, we calculated the modified Auger parameter α' ($\alpha' = BE(\text{Zn } 2p_{3/2}) + KE(\text{Zn LMM})$, where BE and KE are a binding energy of the core level $2p_{3/2}$ and a kinetic energy of the Auger transition involving electrons from L3, M45, and M45 core levels) as defined by Wanger. For all samples, our calculations lead to a value of 2009.9 ± 0.5 eV corresponding to ZnO (wurtzite) [373]. This indicates the formation of stoichiometric ZnO in all samples.

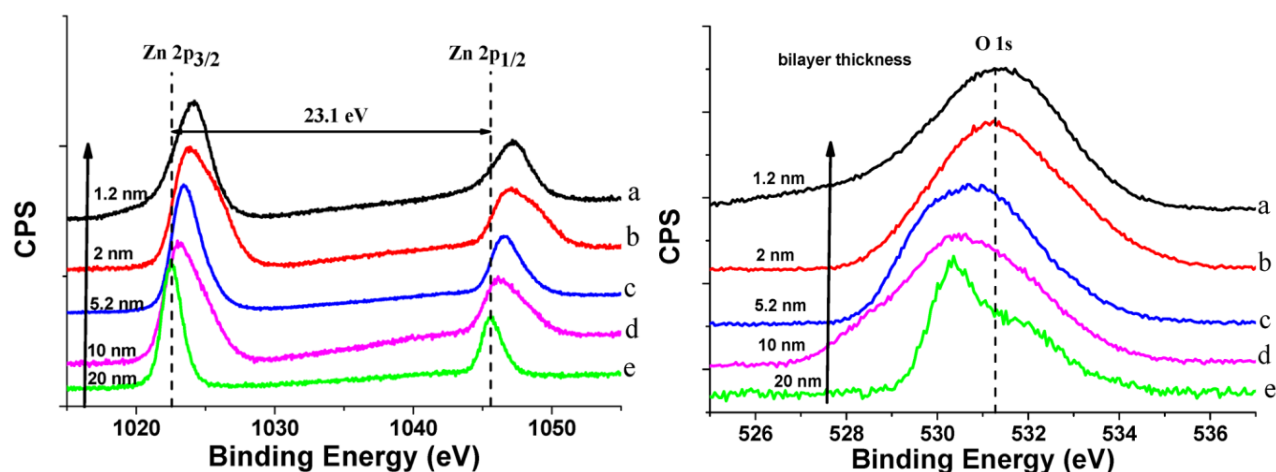


Figure 6-4. XPS survey spectra of ZnO/Al₂O₃ nanolaminates coated polymer fiber with different bilayers thicknesses: (a) 1.2 nm, (b) 2 nm, (c) 5.2 nm, (d) 10 nm, and (e) 20 nm. Main core levels are labeled. Data are normalized and separated vertically.

As the studied samples had a single ZnO layer thickness from 0.6 to 10 nm, their fundamental properties would change from the bulk materials to nanoscale [374]. In order to understand the surface role and quantum confinement effects, the energy ranges related to Zn and O lines were rescaled and analyzed. Figure 6-4 shows the core level of the Zn 2p spectra. The core level binding energies of Zn $2p_{3/2}$ and Zn $2p_{1/2}$ are about 1022.5 ± 0.1 and 1045.6 ± 0.1 eV (20 nm bilayer thickness). These peaks indicate the presence of ZnO phase [375-378]. The binding energy difference (doublet) between these components is about 23.1 ± 0.1 eV which could be attributed to the Zn²⁺ ions in ZnO. From Figure 6-4, we can see the shift of peak positions to higher energies with the decrease of bilayer thickness. However, the difference of 23.1 eV in all samples indicates the presence of the normal state of Zn²⁺ in the ZnO. The oxygen core level peak behaves similarly

(Figure 6-4 bottom image). The observed phenomenon of XPS size shift can be explained, by growth of surface to volume atoms relation and correspondingly relative increase of dangling bonds on the surface. This leads to change of electronic structure in nanocrystals, resulting in increase of binding energies [372, 374, 379].

The XPS peaks were analyzed by deconvolution of peaks using CasaXPS software (Supporting Information Figure SI6-3). It was found that Zn $2p_{1/2}$ peak of 1.2 nm bilayer thickness sample was well fitted with one peak, centered at 1045 eV, whereas other samples showed two peak fittings of the corresponding Zn $2p_{1/2}$ peak. The obtained peaks P1 and P2 were in the range of 1045 ± 0.6 eV and 1044 ± 0.6 eV, respectively. The ratio of Zn $2p_{1/2}$ (P2)/(P1) increased with a growth of a bilayer thickness, pointing to the decrease of surface-to-volume aspect ratio. The analysis of Zn $2p_{1/2}$ peaks showed similar results: the main peak was shifted toward lower energies and additional peak at 1022.3 ± 0.6 eV appeared in the spectra, pointing to the presence of Zn species (interstitials) or Zn-OH in ZnO [380].

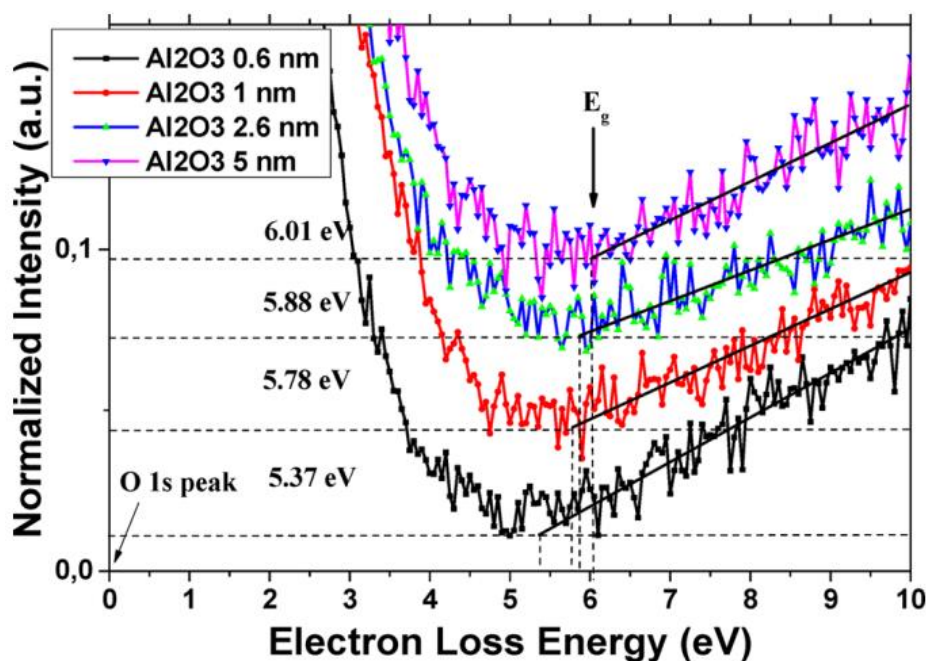


Figure 6-5. O 1s energy-loss spectra for band gap determination of Al_2O_3 of $\text{ZnO}/\text{Al}_2\text{O}_3$ nanolaminate coated polymer fiber with different bilayers thicknesses.

Analysis of O 1S peak has been fitted with three peaks, centered at 529.6 ± 0.5 (P1), 531.3 ± 0.2 (P2) and 532.1 ± 0.4 (P3) eV. The present oxygen at XPS spectrum peaks corresponded to chemisorbed surface oxygen and water (P1), surface adsorbed OH and/or oxygen vacancy (P2), and O_2^- (P3) in ZnO lattice [381]. It is worth to say that ratio P2/P3 decreased with the increase of the

bilayer thickness, pointing to the improvement of nanolaminates crystallinity and the decrease of the defect concentration.

6.4.2. Band Gap Energy Determination. It is well-known that the difference between the onset of inelastic electron losses (E_{loss}) energy and the core level peak (e.g., oxygen peak, $E_{\text{O } 1s}$) allows one to estimate the energy gap (E_g) of the material [382]. The intersection of the linear-fit line of the measured electron loss spectra near the core level peak and the background “zero” level gives us the onset of inelastic losses occurring in Al_2O_3 [149]. Then we can calculate the band gap energy of Al_2O_3 using the formula: $E_g = E_{\text{loss}} - E_{\text{O}}$. Applying this theory, we have calculated E_g of Al_2O_3 for PAN-nanolaminate samples (Figure 6-5). The following values were obtained: 5.37 ± 0.06 , 5.78 ± 0.09 , 5.88 , and 6.01 ± 0.08 eV for PAN-nanolaminate samples with 0.6, 1, 2.6, and 5 nm Al_2O_3 layer thickness, respectively. Unfortunately, it was impossible to calculate the E_g of Al_2O_3 for PAN- $\text{Al}_2\text{O}_3/\text{ZnO}$ (10 nm Al_2O_3 layer thickness) due to the thick top layer of ZnO under the Al_2O_3 layer. Our obtained value of about 6 eV is low compared to the one reported for amorphous Al_2O_3 (8.8 eV) [382]. This observation might be explained by the highly defected structure of Al_2O_3 layer in nanolaminates. Upon increasing the Al_2O_3 layer thickness in PAN-nanolaminates, the E_g gradually increases and tends to bulk value.

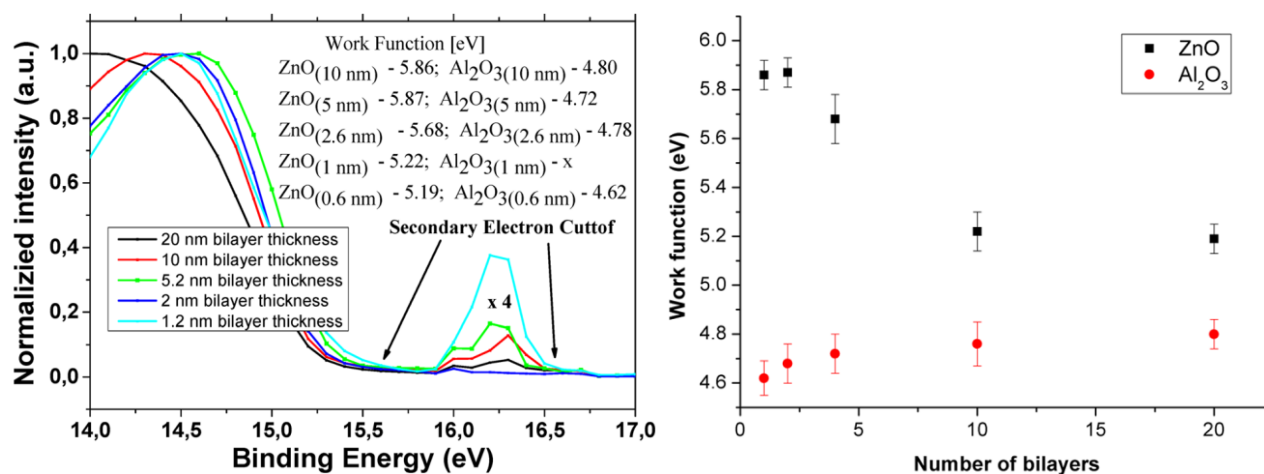


Figure 6-6. UPS results of work function measurements of ZnO/ Al_2O_3 nanolaminate coated polymer fiber with different bilayer thicknesses.

6.4.3. Work Function Determination. The electronic structure of PAN-ZnO/ Al_2O_3 nanolaminates as a function of the bilayer thicknesses was studied with UV photoelectron spectroscopy (UPS) (He I emission 21.22 eV). The work function (Φ) of the ZnO could be estimated by subtracting the secondary electron cutoff value from the He excitation source of 21.22 eV ($\Phi = 21.22$ eV, E_{SEC}). Figure 6-6 shows the UPS spectra of PAN-ZnO/ Al_2O_3 nanolaminates.

The calculated values of Φ are shown in the image. The Φ of ZnO decreases gradually from 5.86 eV (20 nm bilayer thickness) to 5.19 eV (1.2 nm bilayer thickness), which is possibly due to the morphology changes of the top ZnO layers in nanolaminates. The structure of ZnO layer in the 20 nm bilayer thickness sample is polycrystalline (TEM results; Figure 6-1); thus, the energy barriers presenting at the border of disorientated ZnO nanocrystallites increase the value of the Φ . The small peak corresponding to Al_2O_3 is also present in Figure 6-6. The average value of WF for Al_2O_3 is approximately 4.7 eV, and it changes insignificantly.

Work functions of ZnO and Al_2O_3 layers are plotted in Figure 6-6. The work function of Al_2O_3 was insignificantly changed whereas the ZnO work function significantly decreased with the bilayer thickness.

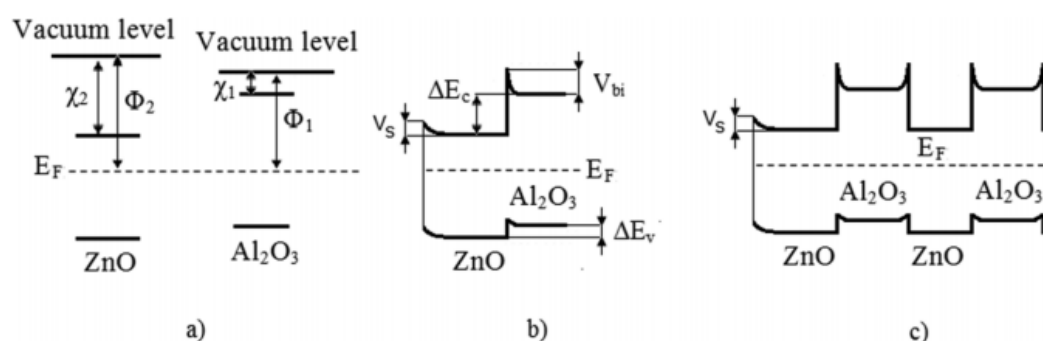


Figure 6-7. Zone diagram of $\text{Al}_2\text{O}_3/\text{ZnO}$ nanolaminate formation: (a) single layers before contact, (b) 1 bilayer, and (c) n bilayers.

The change of Φ could be explained by band bending, formed at the upper layer of the nanolaminates (ZnO-air interface) (Figure 6-7). Electron affinities of ZnO and Al_2O_3 were taken $\chi_{\text{ZnO}} = 4.37$ eV and $\chi_{\text{Al}_2\text{O}_3} = 1.35$ eV, respectively [383, 384].

Fermi level E_F position in each component of the nanolaminates was estimated:

$$E_F = \Phi - \chi \quad (6-1)$$

where Φ is the work function.

The conductance band and valence band gap offsets could be calculated as (Table 6-2):

Table 6-2. Electronic parameters of $\text{Al}_2\text{O}_3/\text{ZnO}$ Ultrathin Nanolaminate Synthesis by ALD^a

	electron affinity (eV)	band gap (eV)	work function (eV)	ΔE_c (eV)	ΔE_v (eV)	V_{bi} (eV)
Al_2O_3	1.35 [384]	6 ± 0.1	4.8 ± 0.1	3	0.3 ± 0.1	2 ± 0.1
ZnO	4.35 [383]	3.3 [383]	5.8 ± 0.1			

^aNumbers in square parentheses are references.

$$\Delta E_c = \chi_2 - \chi_1 \quad (6-2)$$

$$\Delta E_v = E_{g1} - E_{g2} - \Delta E_c \quad (6-3)$$

where $E_{g1,2}$ and $\chi_{1,2}$ are band gap values of Al_2O_3 and ZnO and electron affinity values of ZnO and Al_2O_3 , respectively.

The built in potential V_{bi} between two altering ZnO and Al_2O_3 layers was calculated due to (Table 6-2):

$$V_{bi}q = E_{F2} - E_{F1} \quad (6-4)$$

where q is an electron charge, and E_{F1} and E_{F2} are Fermi level positions in Al_2O_3 and ZnO, correspondently.

To estimate potential drops in ZnO and Al_2O_3 , the Debye lengths in the altering materials were estimated:

$$L_D = \sqrt{\frac{kT\epsilon\epsilon_0}{N_dq}} \quad (6-5)$$

where k , T , ϵ , and ϵ_0 are the Boltzmann's constant, absolute temperature, dielectric permittivity of ZnO ($\epsilon = 8.5$), and electric constant ($\epsilon_0 = 8.85 \times 10^{-12} \text{ F m}^{-1}$), respectively. The donor concentrations in ZnO and Al_2O_3 were taken as 10^{23} and 10^{16} m^{-3} , respectively [385, 386]. The estimated Debye lengths were 10^{-8} and $5 \times 10^{-5} \text{ m}$ for ZnO and Al_2O_3 , respectively.

The potential drops in ZnO and Al_2O_3 could be calculated as

$$V_{ZnO} = L_{DZnO} \frac{V_{bi}}{L_{DAl_2O_3} + L_{DZnO}}$$

$$V_{Al_2O_3} = V_{bi} - V_{ZnO} \quad (6-6)$$

Based on eqs 6-5 and 6-6, the potential drop in ZnO was 10^{-4} eV .

Therefore, the band bending in ZnO at the interface between ZnO and Al_2O_3 is significantly small and the potential drop will be mostly faced in Al_2O_3 layer. The estimated values of ZnO work function are strongly affected by the surface band bending in the upper ZnO layer. The later could be estimated from eq 6-7:

$$V_S = \Phi_{1bl} - \Phi_{20bl} \quad (6-7)$$

where $\Phi_{1\text{bl}}$ and $\Phi_{20\text{bl}}$ are the work function of ZnO in 1 bilayer and 20 bilayer samples, respectively. The obtained V_s value was 0.64 eV. The depletion width in ZnO could be calculated from eq 6-8 [387]:

$$W = \sqrt{\frac{2V_s \epsilon \epsilon_0}{qN_d}} \quad (6-8)$$

The estimated W value was around 50 nm. Therefore, the upper ZnO layer will be fully depleted and a double barrier structure will be formed on the borders of the ZnO layers, pointing to the confinement of the electrons in ZnO along Z-axis. The observed change of work function in ZnO layers results from the presence of hydroxyl and oxygen groups, adsorbed on ZnO surface. This is corroborated by the band at 3500 cm^{-1} observed in FTIR and XPS analysis. The change of the work function with the increase of the bilayer numbers is affected by ‘screening’ of the induced electric field on the surface of the middle Al_2O_3 layers. The part of the depleted ZnO layers will decrease and therefore, the average value of the work function will decrease.

6.4.4. Photoluminescence of PAN- $\text{Al}_2\text{O}_3/\text{ZnO}$ Nanolaminates. The photoluminescence of the PAN- $\text{Al}_2\text{O}_3/\text{ZnO}$ nanolaminates samples showed intense broad visible emission (Figure 6-8). The deconvolution of the peaks was performed using Gaussian fitting (Supporting Information; Figure SI6-4). Peaks at 473, 520, and 580 nm have been found. In ZnO, PL appears due to the photogenerated holes and electrons as the equilibrium holes concentration is too low. PL depends on the defects concentration. The visible PL intensity increases with the decrease of the layer thickness due to the growth of defects number. It was shown that PAN, as a template, induces the nucleation of pure ZnO during the growth affecting the optical properties [110]. However, in the present work, PAN template did not influence the PL of ZnO as since Al_2O_3 layer was the first layer deposited over PAN in all the analyzed samples. It is known that PL of ZnO is sensitive to surface band bending and grain size dimensions [109]. Due to the depleted layer, no exciton emission was observed in the samples with 20, 10, and 5.2 nm bilayers thicknesses. Moreover, the strong visible emission has been observed for all samples. The intensity of the measured emission was 1000-fold higher than the PL emission of the nanolaminates, deposited on Si substrates [110, 165]. The significant increase of the PL was found with the increase of the bilayer numbers. It has been reported that visible PL in ZnO nanostructures is resulted from defects, mostly from Zn and O vacancies and interstitials [109, 110, 165]. According to that, the observed peaks at 473, 520, and 580 nm could be assigned to neutral, single charged and double charged oxygen vacancies, respectively [109, 110, 165]. However, the peak at 473 nm could also be related to Zn vacancies [109, 110, 165]. Measuring only room temperature luminescence, we cannot discriminate the

observed peak at 473 nm between two different defect states. However, this fact does not change the nature of the emission.

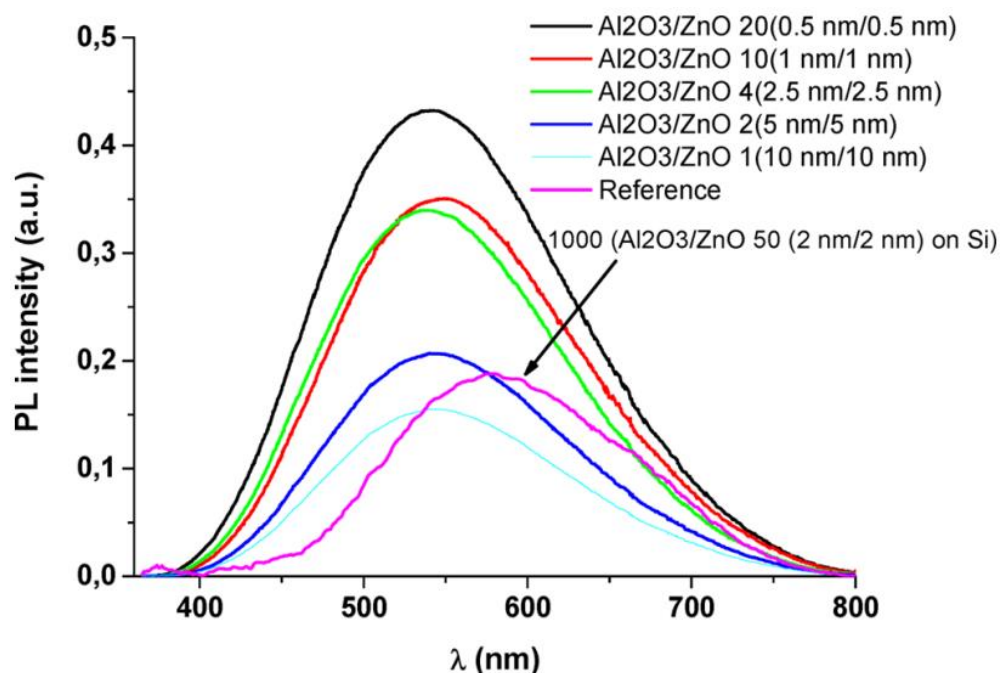


Figure 6-8. Room temperature PL spectra of PAN- $\text{Al}_2\text{O}_3/\text{ZnO}$ nanolaminates with different bilayer thicknesses; $\text{Al}_2\text{O}_3/\text{ZnO}$ nanolaminate 50 (2 nm \times 2 nm) deposited on silicon was added for comparison.

According to XPS data, the number of defects decreased with an increase of the bilayer thickness. Therefore, the 1.2 nm bilayer thickness sample showed the highest photoluminescence. The work function measurements of the samples showed the significant influence of the surface band bending in the upper ZnO layer. The band bending could stimulate the separation of photogenerated electrons and holes, increasing a role of nonradiative transitions. As shown above, the Al_2O_3 layers “screen” the influence of the surface charge in the upper layer and form heterostructures in which ZnO layers are electron-rich. Besides the decrease of the average value of ZnO work function, the increase of the emission intensity occurred.

The work function of ZnO is related to a width of the space charge and band bending [388, 389]. The change of WF can point to the adsorption/desorption, interface forming and other changes on the surface. In our case, WF demonstrates that the band bending decreases when more Al_2O_3 layers are introduced in the nanolaminates which induced the electron-rich area in ZnO. It is one of the factors which influences PL value.

In our previous works [109, 165], we observed similar results when no excitonic peaks were found for thin layers due to band bending and low grain size. This will result from the high concentration of defects, the low grain size (compatible with exciton Bohr radius for ZnO (2.6 nm)), and the surface band bending. Therefore, domination of defect level emission and low rate of exciton formation are observed.

The ZnO layers were polycrystalline with small grain size. We suppose that the grain boundaries will have the following effects in the optical properties of the nanolaminates: (i) Quantum confinement effect: due to the low grain size, the blue shift of the band gap is observed. (ii) Defects are formed on the grain boundaries [390]: XPS showed the higher concentration of the defects for low ZnO thickness, which enhanced visible photoluminescence. (iii) Grain boundaries influence light absorption, particularly, the Urbach tail [390]: a higher Urbach tail value is observed for low ZnO thickness due to the increasing of the grain boundaries active surface (more defects). In the present study, we have shown that the ZnO work function significantly decreased with the decreasing of the bilayer thickness. We explain this observation by band bending. It is well-known fact that grain boundaries can induce localized energy states within the band gap, leading to trapped, localized charges. These will form an electrostatic potential barrier, band bending, for the majority of carrier transport across grain boundaries and as well as enhanced recombination of photogenerated carriers, thus increasing the PL what we can observe on the PL spectra. Many other authors have shown that the formation of a nanocrystalline structure decreases the electron work function [391, 392].

6.5. Conclusion

Summarizing, the structural and optical properties of Al₂O₃/ ZnO determined from the XPS, TEM, FTIR, XRD and PL analysis provide an important information about crystalline structure of nanolaminates on the 1D PAN substrate. The amorphous-to crystalline transition has been observed for ZnO nanolayers at the thickness of 2.6 nm on the 1D PAN nanotemplate. In particular, strong influence of the bilayer thicknesses on the crystallinity of ZnO nanolayers has been found. Due to the quantum confinement effect, the shift of XPS peaks to higher energies has been observed. Work function of Al₂O₃ was mostly independent of the bilayers number whereas the ZnO work function decreased with an increase of the bilayer number. The observed phenomenon indicate surface band bending on the upper layer of ZnO and further charge “screening” by Al₂O₃ layers in internal ZnO layers of the nanolaminates.

Photoluminescence of the nanolaminates corresponded to emission bands in ZnO nanolayers. Due to low grain size, high defect concentration, and surface band bending, no excitonic peaks were

observed. The defect emission band was affected by the band bending and defect concentration. The observed XPS and PL data are in good correlation. The enhanced PL of the nanolaminates could be used for optical (bio)sensing.

6.6. Supporting information

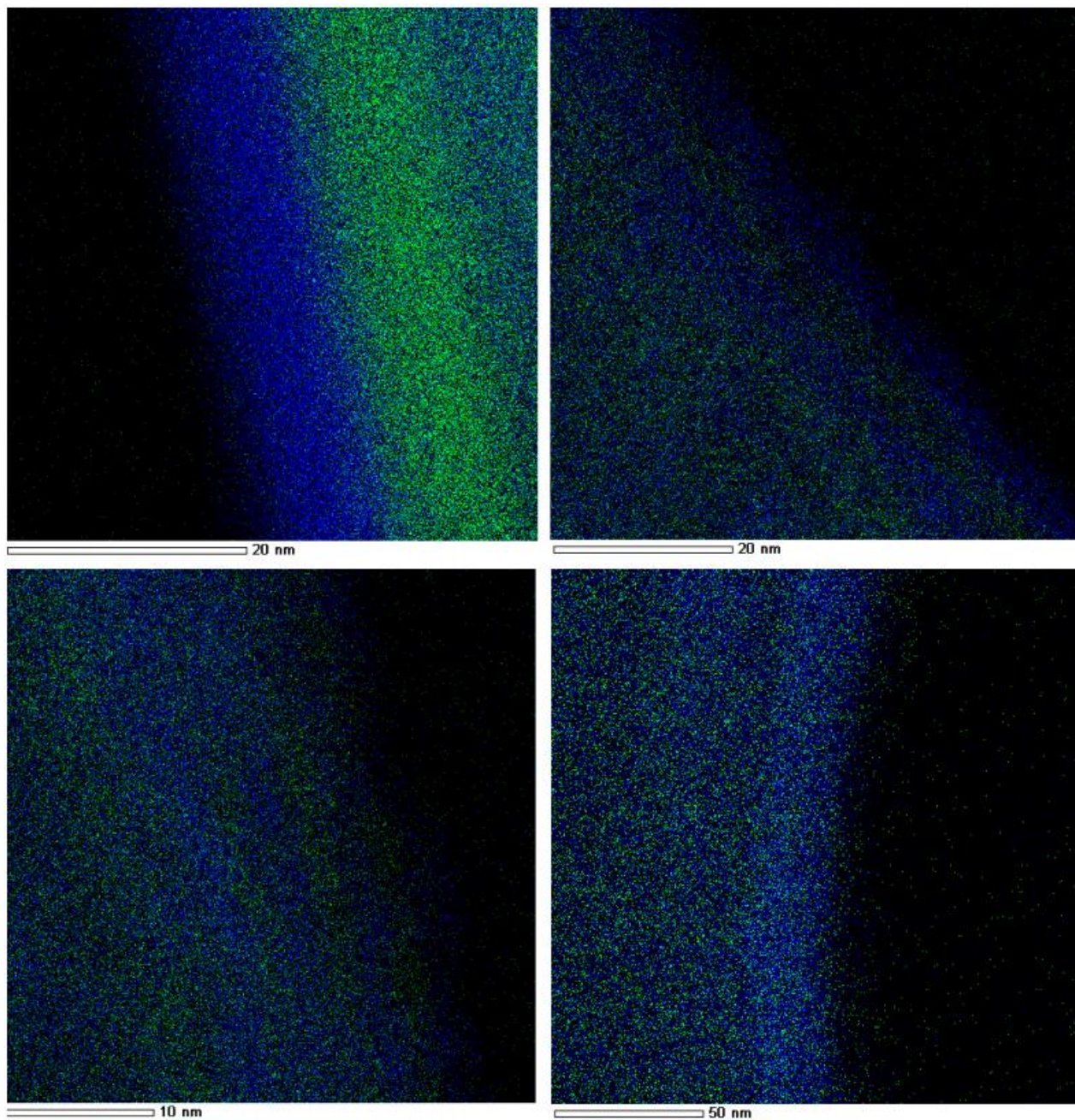


Figure SI6-1. EDS mapping of PAN-nanolaminates. Blue color – Zn and green color – Al.

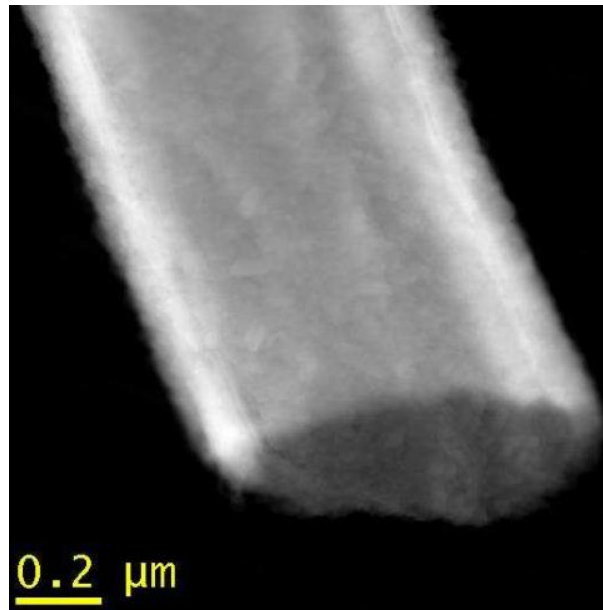


Figure SI6-2. TEM image of the end face of PAN fiber coated by the nanolaminates.

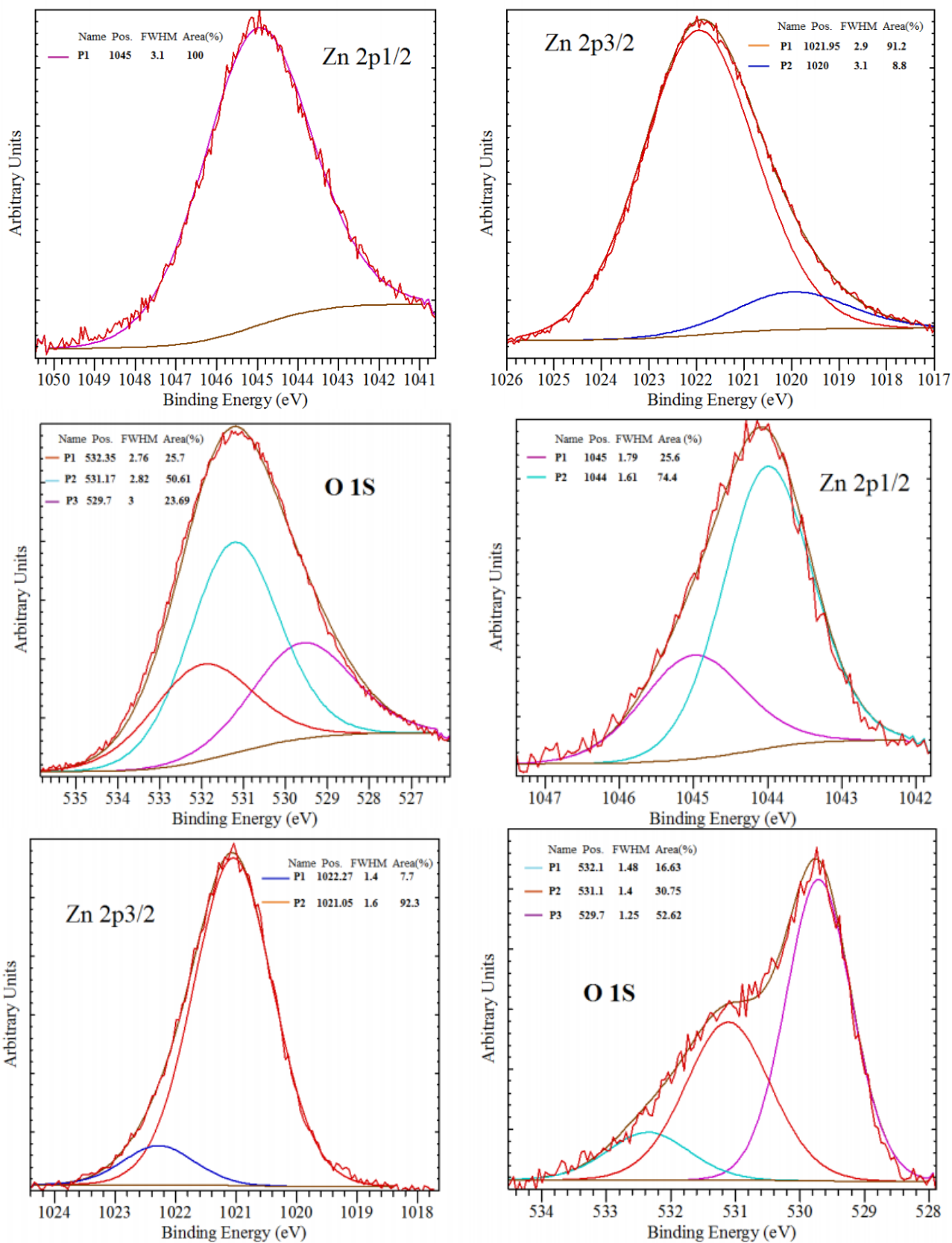


Figure SI6-3. De-convolution of XPS peaks using CasaXPS software.

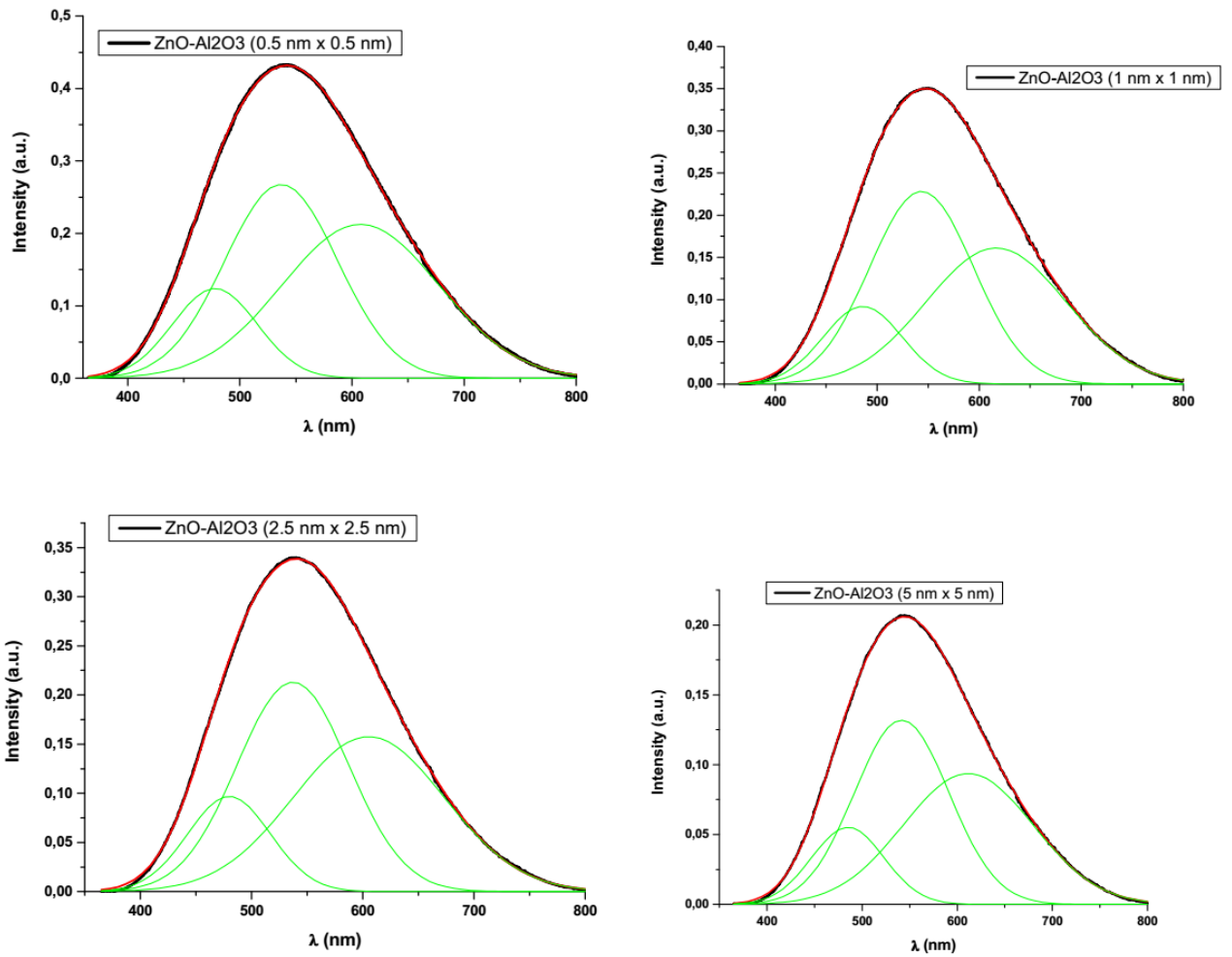


Figure SI6-4. De-convolution of PL peaks spectra of PAN-Al₂O₃/ZnO nanolaminates with different bilayers thicknesses.

CHAPTER VII

General conclusion

7.1. General conclusion

ALD is considered as one of the most promising thin film deposition techniques for enabling nanoscale device fabrication. In this study, we used the ALD technique for the deposition of ZnO and Al₂O₃/ZnO nanolaminates thin films on the different substrates, reached some interesting results and performed some tasks, as following:

(i) In this research, a simple and inexpensive method for the fabrication of ordered aligned SiNWs was proposed, which concluded the combination of nanosphere lithography and metal-assisted chemical etching. To improve the properties of the prepared highly-ordered vertical SiNWs array, it was coated with ZnO thin films (20 and 50 nm) by ALD method. These methods allow the morphology and the organization control of SiNWs on a large area. Structural properties of ZnO/SiNWs were studied by XRD and SEM. Optical characterization was performed by reflectance and photoluminescence spectroscopy. The X-ray diffraction analysis revealed that all samples have hexagonal wurtzite structure. The grain sizes as measured using XRD data were found to be in the range of 7 - 14 nm. In order to confirm the composition of silicon nanowires covered by ALD ZnO, Raman spectroscopy have been used. The study of photoluminescence (PL) spectra of SiNWs/ZnO showed the domination of defect emission bands, which points to deviations of stoichiometry of the prepared 3D ZnO nanostructures. We observed also the reduction of the PL intensity of SiNWs/ZnO with the etching time for 7 minutes corresponding to a higher light scattering with the increase of the nanowire length. The high aspect ratio, anti-reflective characteristics inherent to nanowires structure can be exploited for the fabricating future nanoelectronic and optoelectronic devices.

(ii) ZnO films formed by ALD as an optical biosensor platform for the detection of Grapevine virus A-type proteins (GVA-antigens) were represented. The detection of GVA-antigens was performed through direct immobilization of anti-GVA antibodies on the ZnO thin film surface, forming the biosensitive layer. The immobilization of anti-GVA antibodies resulted in new PL band appearance in the region of 400-550 nm that can be caused by the formation of Zn-S bound during the anti-GVA adsorption process. The GVA-antigen detection was performed using the changes in the GVA related PL band behavior. The sensitivity of obtained biosensor was in the range from 1 pg/ml to 10 ng/ml of protein. The biosensor selectivity has been proved by test based on the application of control specimen – Ag-, which was isolated from the non-infected grapevine plants and not contained any GVA proteins (antigens). The possibility to detect GVA-antigens without additional labels (e.g. enzymes, which are used in ELISA, or fluorescent dyes, which are used in RT-PCR) has been demonstrated. The decrease of the deposition time of immobilized layers has been achieved. The general duration of the experiment

procedure was few times shorter than ELISA and RT-PCR. Due to good performance and simplicity of the described immunosensor, ZnO-modified substrates could be applied as a platform for the development of other immunosensors based on immobilized antibodies, which would be sensitive to selected analyte.

(iii) We have presented a simple synthetic route based on nanosphere lithography to produce large-scale protein patterning. This technique based on two-dimensional (2D) colloidal crystals (polystyrene sphere (PS spheres)) allows the fast synthesis of large arrays (several millimeters) with low cost. The nanoarrays were formed by a monolayer of polystyrene spheres deposit by floating-transferring technique on gold surface. On one hand, the gold surface between spheres was functionalized with SAMs of PEG to prevent the unspecific adsorption. On the other hand, the PS spheres were functionalized with PEG biotin. After addition of avidin and anti-avidin, the proteins are located only on PS spheres confirming that our strategy is suitable to control their location. The epifluorescence microscopy was used to confirm this finding. Regarding the versatility of avidin/biotin system, this strategy can be extended for biosensor development as well as for other applications which require large surface patterning of proteins.

(iv) The tuning of structural properties and the enhancement of electronic and optical properties of 1D PAN ZnO/Al₂O₃ nanolaminates designed by atomic layer deposition (ALD) and electrospinning were performed in our research study as well. The structural and optical properties of Al₂O₃/ZnO determined from the XPS, TEM, FTIR, XRD and PL analysis provide important information about crystalline structure of nanolaminates on the 1D PAN substrate. The amorphous-to-crystalline transition has been observed for ZnO nanolayers at the thickness of 2.6 nm on the 1D PAN nanotemplate. In particular, strong influence of the bilayer thicknesses on the crystallinity of ZnO nanolayers has been found. Due to the quantum confinement effect, the shift of XPS peaks to higher energies has been observed. Work function of Al₂O₃ was mostly independent of the bilayers number whereas the ZnO work function decreased with an increase of the bilayer number. The observed phenomenon indicate surface band bending on the upper layer of ZnO and further charge “screening” by Al₂O₃ layers in internal ZnO layers of the nanolaminates. Photoluminescence of the nanolaminates corresponded to emission bands in ZnO nanolayers. Due to low grain size, high defect concentration, and surface band bending, no excitonic peaks were observed. The defect emission band was affected by the band bending and defect concentration. The observed XPS and PL data are in good correlation. The enhanced PL of the nanolaminates could be used for optical (bio)sensing.

SCIENTIFIC CONTRIBUTIONS

Publications

- Viter, R.; Iatsunskiy, I.; **Fedorenko, V.**; Tumenas, S.; Balevicius, Z.; Ramanavicius, A.; Balme, S.; Kempinski, M.; Nowaczyk, G.; Jurga, S.; Bechelany, M., *Enhancement of Electronic and Optical Properties of ZnO/Al₂O₃ Nanolaminate Coated Electrospun Nanofibers*. The Journal of Physical Chemistry C 2016, 120 (9), 5124-5132.
URL: <http://pubs.acs.org/doi/pdfplus/10.1021/acs.jpcc.5b12263>
- El Khoury, D., Arinero, R., Castellon, J., Laurentie, J. C., **Fedorenko, V.**, Bechelany, M., Balme, S., Fréchet, M. (2016, October). *Detection of shell coatings from core-shell like dielectric nanoparticles with electrostatic force microscopy*. In Electrical Insulation and Dielectric Phenomena (CEIDP), 2016 IEEE Conference on (pp. 755-758). IEEE.
URL: <http://ieeexplore.ieee.org/abstract/document/7785549/>
- El Khoury, D., **Fedorenko, V.**, Castellon, J., Bechelany, M., Laurentie, J. C., Balme, S., Fréchet, M., Ramonda, M., Arinero, R., *Characterization of Dielectric Nanocomposites with Electrostatic Force Microscopy*. Scanning, Volume 2017 (2017), 14 pages.
URL: <https://doi.org/10.1155/2017/4198519>
- Tereshchenko, A., **Fedorenko, V.**, Smyntyna, V., Konup, I., Konup, A., Eriksson, M., Yakimova, R., Ramanavicius, A., Balme, S., Bechelany, M., *ZnO films formed by atomic layer deposition as an optical biosensor platform for the detection of Grapevine virus A-type proteins*. Biosensors and Bioelectronics 2017, 92, 763-769.
URL: <http://www.sciencedirect.com/science/article/pii/S0956566316309563>
- **Fedorenko, V.**, Bechelany, M., Janot, J.-M., Smyntyna, V., Balme, S., *Large-scale protein/antibody patterning with limiting unspecific adsorption*, Journal of Nanoparticle research, 2017, 19(10), 351.
URL: <https://link.springer.com/article/10.1007/s11051-017-4053-x>

- **Fedorenko, V.**, Viter, R., Iatsunskyi, I., Nowaczyk, G., Graniel, O., Załęski, K., Jurga, S., Smyntyna, V., Miele, P., Ramanavicius, A., Balme, S., Bechelany, M., *Optical properties of ZnO deposited by atomic layer deposition (ALD) on Si nanowires*, Materials Science and Engineering B – Submitted

Participation in conferences

Oral communications

- *ALD on 3D Si substrates for optical biosensors applications*, The 8-th NanoSchool “Application of Nanolaminates for Biosensors Design”, October 6-8, 2015, Vilnius, Lithuania.
- *Synthesis of silicon nanowires by metal-assisted chemical etching combined with nanosphere lithography for optical biosensors applications*, II-ème Journée des doctorants de l’IEM, May 3, 2016, Montpellier, France.
- *Structure and optical properties of ZnO deposited by atomic layer deposition (ALD) on Si nanopillars, formed by sphere lithography*, COST action, workshop, ALD nanotechnology: advances, prospects and applications, May 22-23, 2017, Riga, Latvia.

References

1. Kim, H., *Atomic layer deposition of metal and nitride thin films: Current research efforts and applications for semiconductor device processing*. Journal of Vacuum Science & Technology B: Microelectronics and Nanometer Structures Processing, Measurement, and Phenomena, 2003. **21**(6): p. 2231-2261.
2. Niinistö, L., M. Ritala, and M. Leskelä, *Synthesis of oxide thin films and overlayers by atomic layer epitaxy for advanced applications*. Materials Science and Engineering: B, 1996. **41**(1): p. 23-29.
3. Chaaya, A.A., et al., *Evolution of microstructure and related optical properties of ZnO grown by atomic layer deposition*. Beilstein journal of nanotechnology, 2013. **4**: p. 690.
4. Abou Chaaya, A., et al., *Enhanced ionic transport mechanism by gramicidin a confined inside nanopores tuned by atomic layer deposition*. The Journal of Physical Chemistry C, 2013. **117**(29): p. 15306-15315.
5. Cabello-Aguilar, S., et al., *Slow translocation of polynucleotides and their discrimination by α -hemolysin inside a single track-etched nanopore designed by atomic layer deposition*. Nanoscale, 2013. **5**(20): p. 9582-9586.
6. Raghavan, R., et al., *Nanocrystalline-to-amorphous transition in nanolaminates grown by low temperature atomic layer deposition and related mechanical properties*. Applied Physics Letters, 2012. **100**(19): p. 191912.
7. Elam, J. and S. George, *Growth of ZnO/Al₂O₃ alloy films using atomic layer deposition techniques*. Chemistry of Materials, 2003. **15**(4): p. 1020-1028.
8. Elam, J., Z. Sechrist, and S. George, *ZnO/Al₂O₃ nanolaminates fabricated by atomic layer deposition: growth and surface roughness measurements*. Thin Solid Films, 2002. **414**(1): p. 43-55.
9. Suntola, T. and J. Antson, *Method for producing compound thin films*. 1977, Google Patents.
10. Nishizawa, J.i., H. Abe, and T. Kurabayashi, *Molecular layer epitaxy*. Journal of the Electrochemical Society, 1985. **132**(5): p. 1197-1200.
11. Bedair, S., et al., *Atomic layer epitaxy of III-V binary compounds*. Applied Physics Letters, 1985. **47**(1): p. 51-53.
12. Puurunen, R.L., *Surface chemistry of atomic layer deposition: A case study for the trimethylaluminum/water process*. Journal of applied physics, 2005. **97**(12): p. 9.

13. Leskela, M., *Atomic layer epitaxy in the growth of polycrystalline and amorphous films*. ACTA POLYTECHNICA SCANDINAVICA-CHEMICAL TECHNOLOGY SERIES, 1990(195): p. 67-80.
14. Ahonen, M., M. Pessa, and T. Suntola, *A study of ZnTe films grown on glass substrates using an atomic layer evaporation method*. Thin Solid Films, 1980. **65**(3): p. 301-307.
15. Aoyagi, Y., et al., *Atomic-layer growth of GaAs by modulated-continuous-wave laser metal-organic vapor-phase epitaxy*. Journal of Vacuum Science & Technology B: Microelectronics Processing and Phenomena, 1987. **5**(5): p. 1460-1464.
16. Egorov, A., et al., *FORMATION OF TITANIUM-DIOXIDE FILMS IN THE COURSE OF CHEMICAL ASSEMBLY*. 1984, PLENUM PUBL CORP CONSULTANTS BUREAU 233 SPRING ST, NEW YORK, NY 10013. p. 2395-2396.
17. Aleskovskii, V., *Electrical Properties of the Surface of Germanium in Contact With Transition-Metal Oxides Formed by Molecular Deposition Method*. Sov. Phys. Semicond., 1979. **13**(7): p. 817-819.
18. Kopylov, V., et al., *SPECTROSCOPIC STUDY OF THE INTERACTION OF AN EPOXY-RESIN WITH THE SURFACE OF GLASS FILLERS MODIFIED BY MOLECULAR LAMINATION*. JOURNAL OF APPLIED CHEMISTRY OF THE USSR, 1981. **54**(2): p. 186-189.
19. Nishizawa, J.-i., H. Abe, and T. Kurabayashi, *Molecular Layer Epitaxy*.
20. Shevyakov, A., G. Kuznetsova, and V. Aleskovskii. *Interaction of titanium and germanium tetrachlorides with hydrated silica*. in *Chemistry of High Temperature Materials. Proceedings of 2nd USSR Conference on High Temperature Chemistry of Oxides, Leningrad, USSR*. 1965.
21. Malygin, A., S. Koltsov, and V. Aleskovskii, *CHEMICAL-COMPOSITION OF CHROMIUM AND PHOSPHORUS-CONTAINING SILICA, SYNTHESIZED BY MOLECULAR STRATIFICATION METHOD*. ZHURNAL OBSHCHEI KHIMII, 1980. **50**(12): p. 2633-2636.
22. Leskelä, M. and M. Ritala, *Atomic layer deposition (ALD): from precursors to thin film structures*. Thin solid films, 2002. **409**(1): p. 138-146.
23. George, S.M., *Atomic layer deposition: an overview*. Chemical reviews, 2009. **110**(1): p. 111-131.
24. Ritala, M., et al., *Perfectly conformal TiN and Al₂O₃ films deposited by atomic layer deposition*. Chem. Vap. Deposition, 1999. **5**(1): p. 7-9.

25. Miikkulainen, V., et al., *Crystallinity of inorganic films grown by atomic layer deposition: Overview and general trends*. Journal of Applied Physics, 2013. **113**(2): p. 2.
26. Bunn, C., *The lattice-dimensions of zinc oxide*. Proceedings of the Physical Society, 1935. **47**(5): p. 835.
27. Yang, P., et al., *Controlled growth of ZnO nanowires and their optical properties*. Advanced Functional Materials, 2002. **12**(5): p. 323.
28. Koch, U., et al., *Photochemistry of semiconductor colloids. Preparation of extremely small ZnO particles, fluorescence phenomena and size quantization effects*. Chemical Physics Letters, 1985. **122**(5): p. 507-510.
29. Tonon, C., et al., *Degradation of the optical properties of ZnO-based thermal control coatings in simulated space environment*. Journal of Physics D: Applied Physics, 2001. **34**(1): p. 124.
30. Chen, M.-J., J.-R. Yang, and M. Shiojiri, *ZnO-based ultra-violet light emitting diodes and nanostructures fabricated by atomic layer deposition*. Semiconductor Science and Technology, 2012. **27**(7): p. 074005.
31. Chaaya, A.A., et al., *ZnO 1D nanostructures designed by combining atomic layer deposition and electrospinning for UV sensor applications*. Journal of Materials Chemistry A, 2014. **2**(48): p. 20650-20658.
32. Elias, J., et al., *Urchin-inspired zinc oxide as building blocks for nanostructured solar cells*. Nano Energy, 2012. **1**(5): p. 696-705.
33. Elias, J., et al., *Hollow Urchin-like ZnO thin Films by Electrochemical Deposition*. Advanced Materials, 2010. **22**(14): p. 1607-1612.
34. Elias, J., et al., *Electrochemical growth of ZnO nanowires on atomic layer deposition coated polystyrene sphere templates*. Electrochimica Acta, 2013. **110**: p. 387-392.
35. Viter, R., et al., *Application of room temperature photoluminescence from ZnO nanorods for salmonella detection*. IEEE Sensors Journal, 2014. **14**(6): p. 2028-2034.
36. Tammenmaa, M., et al., *Zinc chalcogenide thin films grown by the atomic layer epitaxy technique using zinc acetate as source material*. Thin Solid Films, 1985. **124**(2): p. 125-128.
37. Lujala, V., et al., *Atomic layer epitaxy growth of doped zinc oxide thin films from organometals*. Applied surface science, 1994. **82**: p. 34-40.
38. Yousfi, E.B., J. Fouache, and D. Lincot, *Study of atomic layer epitaxy of zinc oxide by in-situ quartz crystal microgravimetry*. Applied Surface Science, 2000. **153**(4): p. 223-234.

39. Ellmer, K., *Resistivity of polycrystalline zinc oxide films: current status and physical limit*. Journal of Physics D: Applied Physics, 2001. **34**(21): p. 3097.
40. Özgür, Ü., et al., *A comprehensive review of ZnO materials and devices*. Journal of applied physics, 2005. **98**(4): p. 11.
41. Libera, J., J. Elam, and M. Pellin, *Conformal ZnO coatings on high surface area silica gel using atomic layer deposition*. Thin Solid Films, 2008. **516**(18): p. 6158-6166.
42. Shvareva, T.Y., et al., *Thermochemistry of nanoparticles on a substrate: Zinc oxide on amorphous silica*. Journal of Materials Research, 2008. **23**(07): p. 1907-1915.
43. Park, S., et al., *Preparation of one dimensional Bi₂O₃-core/ZnO-shell structures by thermal evaporation and atomic layer deposition*. Solid State Communications, 2009. **149**(7): p. 315-318.
44. Elam, J., D. Routkevitch, and S. George, *Properties of ZnO/Al₂O₃ Alloy Films Grown Using Atomic Layer Deposition Techniques*. Journal of the Electrochemical Society, 2003. **150**(6): p. G339-G347.
45. Tynell, T. and M. Karppinen, *Atomic layer deposition of ZnO: a review*. Semiconductor Science and Technology, 2014. **29**(4): p. 043001.
46. Kobayashi, K. and S. Okudaira, *Preparation of ZnO films on sapphire (0001) substrates by alternate supply of zinc acetate and H₂O*. Chemistry letters, 1997. **26**(6): p. 511-512.
47. Kopalko, K., et al., *Growth by atomic layer epitaxy and characterization of thin films of ZnO*. physica status solidi (c), 2005. **2**(3): p. 1125-1130.
48. Wójcik, A., et al., *Controlling of preferential growth mode of ZnO thin films grown by atomic layer deposition*. Journal of Crystal Growth, 2008. **310**(2): p. 284-289.
49. Guziewicz, E., et al., *ZnO grown by atomic layer deposition: A material for transparent electronics and organic heterojunctions*. Journal of Applied Physics, 2009. **105**(12): p. 122413.
50. Sang, B. and M. Konagai, *Growth of transparent conductive oxide ZnO films by atomic layer deposition*. Japanese journal of applied physics, 1996. **35**(5B): p. L602.
51. Yamada, A., B. Sang, and M. Konagai, *Atomic layer deposition of ZnO transparent conducting oxides*. Applied Surface Science, 1997. **112**: p. 216-222.
52. Saito, K., et al., *Photo atomic layer deposition of transparent conductive ZnO films*. Solar energy materials and solar cells, 1997. **49**(1-4): p. 187-193.
53. Ott, A. and R. Chang, *Atomic layer-controlled growth of transparent conducting ZnO on plastic substrates*. Materials Chemistry and Physics, 1999. **58**(2): p. 132-138.

54. Park, S.-H.K. and Y.E. Lee, *Controlling preferred orientation of ZnO thin films by atomic layer deposition*. Journal of materials science, 2004. **39**(6): p. 2195-2197.
55. Kim, S.K., et al., *Comparison between ZnO films grown by atomic layer deposition using H₂O or O₃ as oxidant*. Thin Solid Films, 2005. **478**(1): p. 103-108.
56. Lee, S., et al., *Structural and optical properties of high quality ZnO films on Si grown by atomic layer deposition at low temperatures*. Superlattices and Microstructures, 2006. **39**(1): p. 24-32.
57. Park, S.-H.K., et al., *Characteristics of ZnO thin films by means of plasma-enhanced atomic layer deposition*. Electrochemical and solid-state letters, 2006. **9**(10): p. G299-G301.
58. Lim, J. and C. Lee, *Effects of substrate temperature on the microstructure and photoluminescence properties of ZnO thin films prepared by atomic layer deposition*. Thin Solid Films, 2007. **515**(7): p. 3335-3338.
59. Guziewicz, E., et al., *Extremely low temperature growth of ZnO by atomic layer deposition*. Journal of Applied Physics, 2008. **103**(3): p. 033515.
60. Jeon, S., et al., *Structural and electrical properties of ZnO thin films deposited by atomic layer deposition at low temperatures*. Journal of the Electrochemical Society, 2008. **155**(10): p. H738-H743.
61. Lin, P.-Y., et al., *Optical and structural characteristics of ZnO films grown on (0001) sapphire substrates by ALD using DEZn and N₂O*. Journal of Crystal Growth, 2008. **310**(12): p. 3024-3028.
62. Makino, H., et al., *Effects of surface pretreatment on growth of ZnO on glass substrate*. physica status solidi (a), 2008. **205**(8): p. 1971-1974.
63. Pung, S.-Y., et al., *Preferential growth of ZnO thin films by the atomic layer deposition technique*. Nanotechnology, 2008. **19**(43): p. 435609.
64. Kim, C., et al., *Effects of annealing temperature of buffer layer on structural and optical properties of ZnO thin film grown by atomic layer deposition*. Solid State Communications, 2008. **148**(9): p. 395-398.
65. Makino, H., et al., *Influence of substrate temperature and Zn-precursors on atomic layer deposition of polycrystalline ZnO films on glass*. Thin Solid Films, 2009. **517**(10): p. 3138-3142.
66. Krajewski, T., et al., *The influence of growth temperature and precursors' doses on electrical parameters of ZnO thin films grown by atomic layer deposition technique*. Microelectronics Journal, 2009. **40**(2): p. 293-295.

67. Rowlette, P.C., et al., *Plasma-Enhanced Atomic Layer Deposition of Semiconductor Grade ZnO Using Dimethyl Zinc*. Chemical Vapor Deposition, 2009. **15**(1-3): p. 15-20.
68. Lin, Y.-T., et al., *Self-limiting growth of ZnO films on (0001) sapphire substrates by atomic layer deposition at low temperatures using diethyl-zinc and nitrous oxide*. Applied Surface Science, 2009. **256**(3): p. 819-822.
69. Chung, P.-H., et al., *Observation of self-limiting regime in the atomic layer deposition of ZnO films using nitrous oxide as the oxygen supply*. ECS Transactions, 2009. **19**(3): p. 167-174.
70. Yen, K.-Y., et al., *On the Characteristics of Zinc Oxide Films Grown on (11-20) Sapphire Substrates by Atomic Layer Deposition Using Diethylzinc and Nitrous Oxide*. ECS Transactions, 2009. **19**(2): p. 843-853.
71. Kwon, S.-K., et al., *Effect of process parameters on remote PEALD for highly transparent ZnO film growth*. J Korean Phys Soc, 2009. **55**: p. 999-1004.
72. Luka, G., et al., *Transparent and conductive undoped zinc oxide thin films grown by atomic layer deposition*. physica status solidi (a), 2010. **207**(7): p. 1568-1571.
73. Guziewicz, E., et al., *Zinc oxide grown by atomic layer deposition—a material for novel 3D electronics*. physica status solidi (b), 2010. **247**(7): p. 1611-1615.
74. Gong, S.C., et al., *Effects of atomic layer deposition temperatures on structural and electrical properties of ZnO films and its thin film transistors*. Metals and Materials International, 2010. **16**(6): p. 953-958.
75. Kim, J.-E., et al., *Electrical and optical properties of zinc oxide thin films deposited using atomic layer deposition*. Journal of the Korean Ceramic Society, 2010. **47**(4): p. 353-356.
76. Min, Y.-S., et al., *Growth and characterization of conducting ZnO thin films by atomic layer deposition*. Bulletin of the Korean Chemical Society, 2010. **31**(9): p. 2503-2508.
77. Kim, D., et al., *The properties of plasma-enhanced atomic layer deposition (ALD) ZnO thin films and comparison with thermal ALD*. Applied Surface Science, 2011. **257**(8): p. 3776-3779.
78. Chiang, T.-Y., C.-L. Dai, and D.-M. Lian, *Influence of growth temperature on the optical and structural properties of ultrathin ZnO films*. Journal of Alloys and Compounds, 2011. **509**(18): p. 5623-5626.
79. Kawamura, Y., et al., *ZnO thin films fabricated by plasma-assisted atomic layer deposition*. Japanese Journal of Applied Physics, 2011. **50**(4S): p. 04DF05.

80. Kawamura, Y., et al., *Comparison between ZnO films grown by plasma-assisted atomic layer deposition using H₂O plasma and O₂ plasma as oxidant*. Journal of Vacuum Science & Technology A: Vacuum, Surfaces, and Films, 2013. **31**(1): p. 01A142.
81. Tanskanen, J.T., et al., *Influence of organozinc ligand design on growth and material properties of ZnS and ZnO deposited by atomic layer deposition*. Journal of Vacuum Science & Technology A: Vacuum, Surfaces, and Films, 2011. **29**(3): p. 031507.
82. Cheng, Y.-C., et al., *Stable p-type ZnO films grown by atomic layer deposition on GaAs substrates and treated by post-deposition rapid thermal annealing*. Thin solid films, 2011. **519**(16): p. 5558-5561.
83. Malm, J., et al., *Low-temperature atomic layer deposition of ZnO thin films: Control of crystallinity and orientation*. Thin Solid Films, 2011. **519**(16): p. 5319-5322.
84. Kudrawiec, R., et al., *Contactless electroreflectance of ZnO layers grown by atomic layer deposition at low temperature*. Semiconductor Science and Technology, 2011. **26**(7): p. 075012.
85. Janocha, E. and C. Pettenkofer, *ALD of ZnO using diethylzinc as metal-precursor and oxygen as oxidizing agent*. Applied Surface Science, 2011. **257**(23): p. 10031-10035.
86. Tapily, K., et al., *Mechanical and structural characterization of atomic layer deposition-based ZnO films*. Semiconductor Science and Technology, 2011. **26**(11): p. 115005.
87. Lin, M.-C., et al., *Structural and Photoluminescence Properties of ZnO Films Grown on 6H-SiC Substrates by Low-Temperature Atomic Layer Deposition*. Journal of The Electrochemical Society, 2011. **158**(12): p. H1213-H1217.
88. Nam, T., et al., *Low-temperature atomic layer deposition of TiO₂, Al₂O₃, and ZnO thin films*. J. Korean Phys. Soc, 2011. **59**(2): p. 452-457.
89. Pradhan, K. and P.F. Lyman, *Study of Atomic Layer Deposition of ZnO on a Polar Oxide Substrate by In Situ Quartz Crystal Microbalance*. ECS Transactions, 2011. **41**(2): p. 247-253.
90. Wang, T., et al., *Growth, optical, and electrical properties of nonpolar m-plane ZnO on p-Si substrates with Al₂O₃ buffer layers*. Applied Physics Letters, 2012. **100**(1): p. 011901.
91. Illiberi, A., F. Roozeboom, and P. Poodt, *Spatial atomic layer deposition of zinc oxide thin films*. ACS applied materials & interfaces, 2011. **4**(1): p. 268-272.
92. Mousa, M.B.M., et al., *Effect of temperature and gas velocity on growth per cycle during Al₂O₃ and ZnO atomic layer deposition at atmospheric pressure*. Journal of Vacuum Science & Technology A: Vacuum, Surfaces, and Films, 2012. **30**(1): p. 01A155.

93. Thomas, M. and J. Cui, *Highly tunable electrical properties in undoped ZnO grown by plasma enhanced thermal-atomic layer deposition*. ACS applied materials & interfaces, 2012. **4**(6): p. 3122-3128.
94. Chai, Z., X. Lu, and D. He, *Atomic layer deposition of zinc oxide films: Effects of nanocrystalline characteristics on tribological performance*. Surface and Coatings Technology, 2012. **207**: p. 361-366.
95. Baji, Z.f., et al., *Nucleation and growth modes of ALD ZnO*. Crystal Growth & design, 2012. **12**(11): p. 5615-5620.
96. Sultan, S.M., et al., *Remote plasma enhanced atomic layer deposition of ZnO for thin film electronic applications*. Microelectronic Engineering, 2012. **97**: p. 162-165.
97. Huang, H.-W., et al., *Growth of controllable ZnO film by atomic layer deposition technique via inductively coupled plasma treatment*. Journal of applied physics, 2012. **112**(12): p. 124102.
98. Yuan, N., et al., *The influence of deposition temperature on growth mode, optical and mechanical properties of ZnO films prepared by the ALD method*. Journal of Crystal Growth, 2013. **366**: p. 43-46.
99. Singh, T., et al., *Thickness dependence of optoelectronic properties in ALD grown ZnO thin films*. Applied Surface Science, 2014. **289**: p. 27-32.
100. Sun, X., et al., *Synthesis of ZnO quantum dot/graphene nanocomposites by atomic layer deposition with high lithium storage capacity*. Journal of Materials Chemistry A, 2014. **2**(20): p. 7319-7326.
101. Moret, M., et al., *Atomic Layer Deposition of zinc oxide for solar cell applications*. Superlattices and Microstructures, 2014. **75**: p. 477-484.
102. Jędrzejewska-Szczerska, M., et al., *ALD thin ZnO layer as an active medium in a fiber-optic Fabry–Perot interferometer*. Sensors and Actuators A: Physical, 2015. **221**: p. 88-94.
103. Zhang, Y., et al., *Well-ordered ZnO nanotube arrays and networks grown by atomic layer deposition*. Applied Surface Science, 2015. **340**: p. 120-125.
104. Boichot, R., et al., *Evolution of crystal structure during the initial stages of ZnO atomic layer deposition*. Chemistry of Materials, 2016. **28**(2): p. 592-600.
105. Di Mauro, A., et al., *Low temperature atomic layer deposition of ZnO: Applications in photocatalysis*. Applied Catalysis B: Environmental, 2016. **196**: p. 68-76.
106. Sampath, S., et al., *Photoelectrocatalytic activity of ZnO coated nano-porous silicon by atomic layer deposition*. RSC Advances, 2016. **6**(30): p. 25173-25178.

107. Pal, D., et al., *Tunable optical properties in atomic layer deposition grown ZnO thin films*. Journal of Vacuum Science & Technology A: Vacuum, Surfaces, and Films, 2017. **35**(1): p. 01B108.
108. Tereshchenko, A., et al., *ZnO films formed by atomic layer deposition as an optical biosensor platform for the detection of Grapevine virus A-type proteins*. Biosensors and Bioelectronics, 2017. **92**: p. 763-769.
109. Chaaya, A.A., et al., *Evolution of microstructure and related optical properties of ZnO grown by atomic layer deposition*. Beilstein Journal of Nanotechnology, 2013. **4**(1): p. 690-698.
110. Viter, R., et al., *Tuning of ZnO 1D nanostructures by atomic layer deposition and electrospinning for optical gas sensor applications*. Nanotechnology, 2015. **26**(10): p. 105501.
111. Groner, M., et al., *Low-temperature Al₂O₃ atomic layer deposition*. Chemistry of Materials, 2004. **16**(4): p. 639-645.
112. Groner, M., et al., *Electrical characterization of thin Al₂O₃ films grown by atomic layer deposition on silicon and various metal substrates*. Thin Solid Films, 2002. **413**(1): p. 186-197.
113. Elam, J., M. Groner, and S. George, *Viscous flow reactor with quartz crystal microbalance for thin film growth by atomic layer deposition*. Review of Scientific Instruments, 2002. **73**(8): p. 2981-2987.
114. Marin, E., et al., *Atomic layer deposition: state-of-the-art and research/industrial perspectives*. Corrosion Reviews, 2011. **29**(5-6): p. 191-208.
115. Im, H., et al., *Atomic layer deposition: A versatile technique for plasmonics and nanobiotechnology*. Journal of materials research, 2012. **27**(04): p. 663-671.
116. Higashi, G. and C. Fleming, *Sequential surface chemical reaction limited growth of high quality Al₂O₃ dielectrics*. Applied Physics Letters, 1989. **55**(19): p. 1963-1965.
117. Groner, M., et al., *Gas diffusion barriers on polymers using Al₂O₃ atomic layer deposition*. Applied Physics Letters, 2006. **88**(5): p. 051907.
118. Park, S.-H.K., et al., *Ultrathin film encapsulation of an OLED by ALD*. Electrochemical and solid-state letters, 2005. **8**(2): p. H21-H23.
119. Dillon, A., et al., *Surface chemistry of Al₂O₃ deposition using Al(CH₃)₃ and H₂O in a binary reaction sequence*. Surface Science, 1995. **322**(1-3): p. 230-242.
120. Ott, A., et al., *Al₂O₃ thin film growth on Si(100) using binary reaction sequence chemistry*. Thin Solid Films, 1997. **292**(1): p. 135-144.

121. Niinistö, L., et al., *Advanced electronic and optoelectronic materials by Atomic Layer Deposition: An overview with special emphasis on recent progress in processing of high-k dielectrics and other oxide materials*. *physica status solidi (a)*, 2004. **201**(7): p. 1443-1452.
122. Yun, S.J., et al., *Dependence of atomic layer-deposited Al₂O₃ films characteristics on growth temperature and Al precursors of Al(CH₃)₃ and AlCl₃*. *Journal of Vacuum Science & Technology A: Vacuum, Surfaces, and Films*, 1997. **15**(6): p. 2993-2997.
123. Ott, A., et al., *Atomic layer controlled deposition of Al₂O₃ films using binary reaction sequence chemistry*. *Applied Surface Science*, 1996. **107**: p. 128-136.
124. Kim, Y., et al., *Substrate dependence on the optical properties of Al₂O₃ films grown by atomic layer deposition*. *Applied Physics Letters*, 1997. **71**(25): p. 3604-3606.
125. Rahtu, A., T. Alaranta, and M. Ritala, *In situ quartz crystal microbalance and quadrupole mass spectrometry studies of atomic layer deposition of aluminum oxide from trimethylaluminum and water*. *Langmuir*, 2001. **17**(21): p. 6506-6509.
126. Gosset, L., et al., *Interface and material characterization of thin Al₂O₃ layers deposited by ALD using TMA/H₂O*. *Journal of non-crystalline solids*, 2002. **303**(1): p. 17-23.
127. Lee, J., et al., *Al₂O₃ nanotubes and nanorods fabricated by coating and filling of carbon nanotubes with atomic-layer deposition*. *Journal of crystal growth*, 2003. **254**(3): p. 443-448.
128. Mayer, T., et al., *Atomic-layer deposition of wear-resistant coatings for microelectromechanical devices*. *Applied Physics Letters*, 2003. **82**(17): p. 2883-2885.
129. Ferguson, J., A. Weimer, and S. George, *Atomic layer deposition of Al₂O₃ films on polyethylene particles*. *Chemistry of materials*, 2004. **16**(26): p. 5602-5609.
130. Wilson, C., R. Grubbs, and S. George, *Nucleation and growth during Al₂O₃ atomic layer deposition on polymers*. *Chemistry of Materials*, 2005. **17**(23): p. 5625-5634.
131. Zhang, X., et al., *Ultrastable substrates for surface-enhanced Raman spectroscopy: Al₂O₃ overlayers fabricated by atomic layer deposition yield improved anthrax biomarker detection*. *Journal of the American Chemical Society*, 2006. **128**(31): p. 10304-10309.
132. Langereis, E., et al., *Plasma-assisted atomic layer deposition of Al₂O₃ moisture permeation barriers on polymers*. *Applied physics letters*, 2006. **89**(8): p. 081915.

133. Elliott, S., et al., *Ozone-based atomic layer deposition of alumina from TMA: Growth, morphology, and reaction mechanism*. Chemistry of materials, 2006. **18**(16): p. 3764-3773.
134. Peng, Q., et al., *Atomic layer deposition on electrospun polymer fibers as a direct route to Al₂O₃ microtubes with precise wall thickness control*. Nano letters, 2007. **7**(3): p. 719-722.
135. Goldstein, D.N., J.A. McCormick, and S.M. George, *Al₂O₃ atomic layer deposition with trimethylaluminum and ozone studied by in situ transmission FTIR spectroscopy and quadrupole mass spectrometry*. The Journal of Physical Chemistry C, 2008. **112**(49): p. 19530-19539.
136. Lee, B., et al., *Conformal Al₂O₃ dielectric layer deposited by atomic layer deposition for graphene-based nanoelectronics*. Applied Physics Letters, 2008. **92**(20): p. 203102.
137. Poodt, P., et al., *High-speed spatial atomic-layer deposition of aluminum oxide layers for solar cell passivation*. Advanced Materials, 2010. **22**(32): p. 3564-3567.
138. Jung, Y.S., et al., *Ultrathin direct atomic layer deposition on composite electrodes for highly durable and safe Li-ion batteries*. Advanced Materials, 2010. **22**(19): p. 2172-2176.
139. Prasittichai, C. and J.T. Hupp, *Surface modification of SnO₂ photoelectrodes in dye-sensitized solar cells: significant improvements in photovoltage via Al₂O₃ atomic layer deposition*. The Journal of Physical Chemistry Letters, 2010. **1**(10): p. 1611-1615.
140. Abdulagatov, A., et al., *Al₂O₃ and TiO₂ atomic layer deposition on copper for water corrosion resistance*. ACS applied materials & interfaces, 2011. **3**(12): p. 4593-4601.
141. Jen, S.-H., J.A. Bertrand, and S.M. George, *Critical tensile and compressive strains for cracking of Al₂O₃ films grown by atomic layer deposition*. Journal of Applied Physics, 2011. **109**(8): p. 084305.
142. Lee, K., et al., *Mechanisms for hydrophilic/hydrophobic wetting transitions on cellulose cotton fibers coated using Al₂O₃ atomic layer deposition*. Journal of Vacuum Science & Technology A: Vacuum, Surfaces, and Films, 2012. **30**(1): p. 01A163.
143. Otto, M., et al., *Extremely low surface recombination velocities in black silicon passivated by atomic layer deposition*. Applied Physics Letters, 2012. **100**(19): p. 191603.
144. Gong, B. and G.N. Parsons, *Quantitative in situ infrared analysis of reactions between trimethylaluminum and polymers during Al₂O₃ atomic layer deposition*. Journal of Materials Chemistry, 2012. **22**(31): p. 15672-15682.

145. Cheng, L., et al., *Atomic layer deposition of a high-k dielectric on MoS₂ using trimethylaluminum and ozone*. ACS applied materials & interfaces, 2014. **6**(15): p. 11834-11838.
146. Mousa, M.B.M., C.J. Oldham, and G.N. Parsons, *Atmospheric pressure atomic layer deposition of Al₂O₃ using trimethyl aluminum and ozone*. Langmuir, 2014. **30**(13): p. 3741-3748.
147. Kozen, A.C., et al., *Next-generation lithium metal anode engineering via atomic layer deposition*. ACS nano, 2015. **9**(6): p. 5884-5892.
148. Zhu, H., et al., *Al₂O₃ on black phosphorus by atomic layer deposition: an in situ interface study*. ACS applied materials & interfaces, 2015. **7**(23): p. 13038-13043.
149. Iatsunskiy, I., et al., *Structural and XPS characterization of ALD Al₂O₃ coated porous silicon*. Vacuum, 2015. **113**: p. 52-58.
150. Sharma, K., et al., *Spatial atomic layer deposition on flexible porous substrates: ZnO on anodic aluminum oxide films and Al₂O₃ on Li ion battery electrodes*. Journal of Vacuum Science & Technology A: Vacuum, Surfaces, and Films, 2016. **34**(1): p. 01A146.
151. Kot, M., et al., *Room-Temperature Atomic Layer Deposition of Al₂O₃: Impact on Efficiency, Stability and Surface Properties in Perovskite Solar Cells*. ChemSusChem, 2016. **9**(24): p. 3401-3406.
152. Masango, S.S., et al., *High-Resolution Distance Dependence Study of Surface-Enhanced Raman Scattering Enabled by Atomic Layer Deposition*. Nano letters, 2016. **16**(7): p. 4251-4259.
153. Choi, H., et al., *Fast spatial atomic layer deposition of Al₂O₃ at low temperature (< 100° C) as a gas permeation barrier for flexible organic light-emitting diode displays*. Journal of Vacuum Science & Technology A: Vacuum, Surfaces, and Films, 2016. **34**(1): p. 01A121.
154. Park, J.H., et al., *Atomic layer deposition of Al₂O₃ on WSe₂ functionalized by titanyl phthalocyanine*. ACS nano, 2016. **10**(7): p. 6888-6896.
155. Ma, L., et al., *Experimental Study of Process Emissions From Atomic Layer Deposition of Al₂O₃ Under Various Temperatures and Purge Time*. Journal of Manufacturing Science and Engineering, 2017. **139**(5): p. 051013.
156. Hackler, R.A., et al., *Identification of Dimeric Methylalumina Surface Species during Atomic Layer Deposition Using Operando Surface-Enhanced Raman Spectroscopy*. Journal of the American Chemical Society, 2017. **139**(6): p. 2456-2463.

157. Zazpe, R., et al., *Atomic Layer Deposition Al₂O₃ Coatings Significantly Improve Thermal, Chemical, and Mechanical Stability of Anodic TiO₂ Nanotube Layers*. *Langmuir*, 2017. **33**(13): p. 3208-3216.
158. Franke, S., et al., *Silicon stabilized alumina thin films as gas permeation barriers prepared by spatial atomic layer deposition*. *MRS Advances*, 2017: p. 1-6.
159. Marichy, C., M. Bechelany, and N. Pinna, *Atomic Layer Deposition of Nanostructured Materials for Energy and Environmental Applications*. *Advanced Materials*, 2012. **24**(8): p. 1017-1032.
160. Freyman, C.A. and Y.-W. Chung, *Synthesis and characterization of hardness-enhanced multilayer oxide films for high-temperature applications*. *Surface and Coatings Technology*, 2008. **202**(19): p. 4702-4708.
161. Rowlette, P.C. and C.A. Wolden, *Pulsed plasma-enhanced chemical vapor deposition of Al₂O₃-TiO₂ nanolaminates*. *Thin Solid Films*, 2010. **518**(12): p. 3337-3341.
162. Seo, S.-W., et al., *Optimization of Al₂O₃/ZrO₂ nanolaminate structure for thin-film encapsulation of OLEDs*. *Organic Electronics*, 2012. **13**(11): p. 2436-2441.
163. Kukli, K., et al., *Properties of Ta₂O₅-Based Dielectric Nanolaminates Deposited by Atomic Layer Epitaxy*. *Journal of The Electrochemical Society*, 1997. **144**(1): p. 300-306.
164. Karvonen, L., et al., *Enhancement of the third-order optical nonlinearity in ZnO/Al₂O₃ nanolaminates fabricated by atomic layer deposition*. *Applied Physics Letters*, 2013. **103**(3): p. 031903.
165. Chaaya, A.A., et al., *Tuning optical properties of Al₂O₃/ZnO nanolaminates synthesized by atomic layer deposition*. *The Journal of Physical Chemistry C*, 2014. **118**(7): p. 3811-3819.
166. Viter, R., et al., *Optical properties of ultrathin Al₂O₃/ZnO nanolaminates*. *Thin Solid Films*, 2015. **594**: p. 96-100.
167. Li, M.-Y., et al., *Effect of process pressure on atomic layer deposition of Al₂O₃*. *Journal of the Electrochemical Society*, 2007. **154**(11): p. H967-H972.
168. Lim, J.-W., H.-S. Park, and S.-W. Kang, *Kinetic modeling of film growth rate in atomic layer deposition*. *Journal of The Electrochemical Society*, 2001. **148**(6): p. C403-C408.
169. Elam, J., et al., *Surface chemistry and film growth during TiN atomic layer deposition using TDMAT and NH₃*. *Thin Solid Films*, 2003. **436**(2): p. 145-156.
170. Ritala, M., et al., *Atomic layer epitaxy growth of TiN thin films*. *Journal of The Electrochemical Society*, 1995. **142**(8): p. 2731-2737.

171. Yousfi, E., et al., *Atomic layer deposition of zinc oxide and indium sulfide layers for Cu (In, Ga) Se 2 thin-film solar cells*. Thin Solid Films, 2001. **387**(1): p. 29-32.
172. Kim, H. and W.-J. Maeng, *Applications of atomic layer deposition to nanofabrication and emerging nanodevices*. Thin Solid Films, 2009. **517**(8): p. 2563-2580.
173. Iatsunskiy, I., et al., *Tailoring the structural, optical, and photoluminescence properties of porous silicon/TiO₂ nanostructures*. The Journal of Physical Chemistry C, 2015. **119**(13): p. 7164-7171.
174. Iatsunskiy, I., et al., *Study on structural, mechanical, and optical properties of Al₂O₃-TiO₂ nanolaminates prepared by atomic layer deposition*. The Journal of Physical Chemistry C, 2015. **119**(35): p. 20591-20599.
175. Baitimirova, M., et al., *Tuning of Structural and Optical Properties of Graphene/ZnO Nanolaminates*. The Journal of Physical Chemistry C, 2016. **120**(41): p. 23716-23725.
176. Viter, R., et al., *The influence of localized plasmons on the optical properties of Au/ZnO nanostructures*. Journal of Materials Chemistry C, 2015. **3**(26): p. 6815-6821.
177. Viter, R., et al., *Enhancement of electronic and optical properties of ZnO/Al₂O₃ nanolaminate coated electrospun nanofibers*. The Journal of Physical Chemistry C, 2016. **120**(9): p. 5124-5132.
178. Nasr, M., et al., *Synthesis of novel ZnO/ZnAl₂O₄ multi co-centric nanotubes and their long-term stability in photocatalytic application*. RSC Advances, 2016. **6**(105): p. 103692-103699.
179. Niu, W., et al., *Applications of atomic layer deposition in solar cells*. Nanotechnology, 2015. **26**(6): p. 064001.
180. Zardetto, V., et al., *Atomic layer deposition for perovskite solar cells: research status, opportunities and challenges*. Sustainable Energy & Fuels, 2017. **1**(1): p. 30-55.
181. Guérin, V.-M., et al., *Ordered networks of ZnO-nanowire hierarchical urchin-like structures for improved dye-sensitized solar cells*. Physical Chemistry Chemical Physics, 2012. **14**(37): p. 12948-12955.
182. Ahmadzada, T., et al., *Atomic layer deposition of Al₂O₃ and Al₂O₃/TiO₂ barrier coatings to reduce the water vapour permeability of polyetheretherketone*. Thin Solid Films, 2015. **591**: p. 131-136.
183. Johansson, P., et al., *Protecting an atomic layer deposited aluminum oxide barrier coating on a flexible polymer substrate*. Thin Solid Films, 2017. **621**: p. 151-155.
184. Behrendt, A., et al., *Stress Management in Thin-Film Gas-Permeation Barriers*. ACS Applied Materials & Interfaces, 2016. **8**(6): p. 4056-4061.

185. Ke, M., et al., *Properties of slow traps of ALD Al₂O₃/GeO_x/Ge nMOSFETs with plasma post oxidation*. Applied Physics Letters, 2016. **109**(3): p. 032101.
186. Huang, J., et al., *Enhanced electrical and reliability characteristics in HfON gated Ge p-MOSFETs with H₂ and NH₃ plasma treated interfacial layers*. Vacuum, 2016.
187. Lepoitevin, M., et al., *Combining a sensor and a pH-gated nanopore based on an avidin-biotin system*. Chemical Communications, 2015. **51**(27): p. 5994-5997.
188. Cabello-Aguilar, S., et al., *Dynamics of polymer nanoparticles through a single artificial nanopore with a high-aspect-ratio*. Soft Matter, 2014. **10**(42): p. 8413-8419.
189. Tereshchenko, A., et al., *ZnO films formed by atomic layer deposition as an optical biosensor platform for the detection of Grapevine virus A-type proteins*. Biosensors and Bioelectronics, 2016.
190. Majchrowicz, D., et al., *Application of Thin ZnO ALD Layers in Fiber-Optic Fabry-Pérot Sensing Interferometers*. Sensors, 2016. **16**(3): p. 416.
191. Humayun, M.T., et al., *ZnO functionalization of multiwalled carbon nanotubes for methane sensing at single parts per million concentration levels*. Journal of Vacuum Science & Technology B, Nanotechnology and Microelectronics: Materials, Processing, Measurement, and Phenomena, 2015. **33**(6): p. 06FF01.
192. Boyadjiev, S.I., et al., *Preparation and characterization of ALD deposited ZnO thin films studied for gas sensors*. Applied Surface Science, 2016. **387**: p. 1230-1235.
193. Yu, C.H., P. Su, and C.T. Chuang, *Performance and Stability Benchmarking of Monolithic 3-D Logic Circuits and SRAM Cells With Monolayer and Few-Layer Transition Metal Dichalcogenide MOSFETs*. IEEE Transactions on Electron Devices, 2017. **PP**(99): p. 1-7.
194. Marichy, C. and N. Pinna, *Atomic Layer Deposition to Materials for Gas Sensing Applications*. Advanced Materials Interfaces, 2016.
195. Shao, D., et al., *Flexible, thorn-like ZnO-multiwalled carbon nanotube hybrid paper for efficient ultraviolet sensing and photocatalyst applications*. Nanoscale, 2014. **6**(22): p. 13630-13636.
196. Iatsunskiy, I., et al., *Tailoring of the electronic properties of ZnO-polyacrylonitrile nanofibers: Experiment and theory*. Applied Surface Science.
197. Tereshchenko, A., et al., *Optical biosensors based on ZnO nanostructures: advantages and perspectives. A review*. Sensors and Actuators B: Chemical, 2016. **229**: p. 664-677.
198. Shavanova, K., et al., *Application of 2D non-graphene materials and 2D oxide nanostructures for biosensing technology*. Sensors, 2016. **16**(2): p. 223.

199. Nakashima, Y., et al., *Fabrication process of carbon nanotube field effect transistors using atomic layer deposition passivation for biosensors*. Journal of nanoscience and nanotechnology, 2010. **10**(6): p. 3805-3809.
200. Sultan, S.M., et al. *Top-down fabricated ZnO nanowire transistors for application in biosensors*. in *Solid-State Device Research Conference (ESSDERC), 2012 Proceedings of the European*. 2012. IEEE.
201. Ramesh, A., et al., *Towards in vivo biosensors for low-cost protein sensing*. Electronics Letters, 2013. **49**(7): p. 450-451.
202. Couniot, N., et al., *Lytic enzymes as selectivity means for label-free, microfluidic and impedimetric detection of whole-cell bacteria using ALD-Al₂O₃ passivated microelectrodes*. Biosensors and Bioelectronics, 2015. **67**: p. 154-161.
203. Bajpai, R., et al. *Synthesis and assembly of ZnO nanorods grown by ALD for biosensor application*. in *Semiconductor Device Research Symposium, 2009. ISDRS'09. International*. 2009. IEEE.
204. Guo, D., et al., *GaN nanowire functionalized with atomic layer deposition techniques for enhanced immobilization of biomolecules*. Langmuir, 2010. **26**(23): p. 18382-18391.
205. Zhao, Y., et al., *Refractive index sensitivity enhancement of optical fiber cladding mode by depositing nanofilm via ALD technology*. Optics express, 2013. **21**(22): p. 26136-26143.
206. Purniawan, A., et al., *TiO₂ ALD nanolayer as evanescent waveguide for biomedical sensor applications*. Procedia Engineering, 2010. **5**: p. 1131-1135.
207. Cha, H., et al., *Surface passivation of a photonic crystal band-edge laser by atomic layer deposition of SiO₂ and its application for biosensing*. Nanoscale, 2015. **7**(8): p. 3565-3571.
208. Watanabe, K., et al., *Simultaneous detection of refractive index and surface charges in nanolaser biosensors*. Applied Physics Letters, 2015. **106**(2): p. 021106.
209. Shen, S.-H., et al., *An enhancement of high-k/oxide stacked dielectric structure for silicon-based multi-nanowire biosensor in cardiac troponin I detection*. Sensors and Actuators B: Chemical, 2015. **218**: p. 303-309.
210. Lu, Y., et al., *Synthesis High Sensitivity ZnO Cholesterol Biosensor with One Dimensional Nanostructures*. Advanced Science, Engineering and Medicine, 2016. **8**(10): p. 771-774.
211. Saleem, M., et al. *Bio-molecular sensors based on guided mode resonance filters*. in *IOP Conference Series: Materials Science and Engineering*. 2016. IOP Publishing.

212. Zhang, C., et al., *Electrochemical Biosensor Based on Nanoporous Au/CoO Core–Shell Material with Synergistic Catalysis*. ChemPhysChem, 2016. **17**(1): p. 98-104.
213. Rasson, J., et al., *Quantitative characterization of biofunctionalization layers by robust image analysis for biosensor applications*. Sensors and Actuators B: Chemical, 2016. **222**: p. 980-986.
214. Popov, V., et al., *Biosensor properties of SOI nanowire transistors with a PEALD Al₂O₃ dielectric protective layer*. Semiconductors, 2016. **50**(5): p. 632-638.
215. Nam, H., et al., *Two different device physics principles for operating MoS₂ transistor biosensors with femtomolar-level detection limits*. Applied Physics Letters, 2015. **107**(1): p. 012105.
216. Lee, K.-L., et al., *Visualization of biosensors using enhanced surface plasmon resonances in capped silver nanostructures*. Analyst, 2016. **141**(3): p. 974-980.
217. Hirsch, M., et al., *Low-coherence interferometric fiber-optic sensors with potential applications as biosensors*. Sensors, 2017. **17**(2): p. 261.
218. Chen, Z., et al., *DNA translocation through an array of kinked nanopores*. Nature Materials, 2010. **9**(8): p. 667-675.
219. dela Torre, R., et al., *Fabrication and characterization of solid-state nanopore arrays for high-throughput DNA sequencing*. Nanotechnology, 2012. **23**(38): p. 385308.
220. Chen, P., et al., *Atomic layer deposition to fine-tune the surface properties and diameters of fabricated nanopores*. Nano Letters, 2004. **4**(7): p. 1333-1337.
221. Lepoitevin, M., et al., *Influence of nanopore surface charge and magnesium ion on polyadenosine translocation*. Nanotechnology, 2015. **26**(14): p. 144001.
222. Abou Chaaya, A., et al., *Enhanced Ionic Transport Mechanism by Gramicidin A Confined Inside Nanopores Tuned by Atomic Layer Deposition*. Journal of Physical Chemistry C, 2013. **117**(29): p. 15306-15315.
223. Perez, I., et al., *TEM-based metrology for HfO₂ layers and nanotubes formed in anodic aluminum oxide nanopore structures*. Small, 2008. **4**(8): p. 1223-1232.
224. Elam, J.W., et al., *Conformal coating on ultrahigh-aspect-ratio nanopores of anodic alumina by atomic layer deposition*. Chemistry of Materials, 2003. **15**(18): p. 3507-3517.
225. Thangaraj, V., et al., *Detection of short ssDNA and dsDNA by current-voltage measurements using conical nanopores coated with Al₂O₃ by atomic layer deposition*. Microchimica Acta, 2016. **183**(3): p. 1011-1017.

226. Cabello-Aguilar, S., et al., *Slow translocation of polynucleotides and their discrimination by alpha-hemolysin inside a single track-etched nanopore designed by atomic layer deposition*. *Nanoscale*, 2013. **5**(20): p. 9582-9586.
227. Balme, S., et al., *Ionic transport through sub 10 nm hydrophobic nanopore : experiment, theory and simulation*. *scientific reports*, 2015: p. 10135.
228. Lepoitevin, M., et al., *Non-Fluorescence label protein sensing with track-etched nanopore decorated by avidin/biotin system*. *electrochimica acta*, 2016. **211**: p. 611–618.
229. Lepoitevin, M., et al., *Combining a sensor and pH-gated Nanopore based on an Avidin-biotin system* *Chemical Communications*, 2015. **51**: p. 5994-5997
230. Thangaraj, V., et al., *Detection of short ss- and dsDNA using Al₂O₃ conical nanopore designed by atomic layer deposition*. *Microchimica Acta*, 2016. **183**: p. 1011-1017.
231. Venkatesan, B.M., et al., *DNA Sensing Using Nanocrystalline Surface-Enhanced Al₂O₃ Nanopore Sensors*. *Advanced Functional Materials*, 2010. **20**(8): p. 1266-1275.
232. Lepoitevin, M., et al., *Influence of Nanopore Surface Charge and Magnesium ion on PolyAdenosine Translocation*. *Nanotechnology*, 2015. **26**: p. 144001.
233. Picaud, F., et al., *Discrimination of Polynucleotide Transport Through a Highly Hydrophobic Uncharged Nanopore*. *journal of Physical Chemistry C*, 2017. **121**(13): p. 7525–7532.
234. Leskelä, M. and M. Ritala, *Atomic layer deposition chemistry: recent developments and future challenges*. *Angewandte Chemie International Edition*, 2003. **42**(45): p. 5548-5554.
235. Poedt, P., et al., *Ultrafast atomic layer deposition of alumina layers for solar cell passivation*. *Journal of The Electrochemical Society*, 2011. **158**(9): p. H937-H940.
236. Werner, F., et al., *Very low surface recombination velocities on p-and n-type c-Si by ultrafast spatial atomic layer deposition of aluminum oxide*. *Applied Physics Letters*, 2010. **97**(16): p. 162103.
237. Johnson, R.W., A. Hultqvist, and S.F. Bent, *A brief review of atomic layer deposition: from fundamentals to applications*. *Materials today*, 2014. **17**(5): p. 236-246.
238. Levy, D.H., S.F. Nelson, and D. Freeman, *Oxide electronics by spatial atomic layer deposition*. *Journal of Display Technology*, 2009. **5**(12): p. 484-494.
239. Xie, S., et al., *Atomic layer-by-layer deposition of Pt on Pd nanocubes for catalysts with enhanced activity and durability toward oxygen reduction*. *Nano letters*, 2014. **14**(6): p. 3570-3576.

240. Hämäläinen, J., et al., *Low temperature atomic layer deposition of noble metals using ozone and molecular hydrogen as reactants*. *Thin Solid Films*, 2013. **531**: p. 243-250.
241. Sun, S., et al., *Single-atom catalysis using Pt/graphene achieved through atomic layer deposition*. *Scientific reports*, 2013. **3**.
242. Park, J., et al., *Atomic layer-by-layer deposition of platinum on palladium octahedra for enhanced catalysts toward the oxygen reduction reaction*. *ACS nano*, 2015. **9**(3): p. 2635-2647.
243. Wang, H., et al., *Precisely-controlled synthesis of Au@ Pd core-shell bimetallic catalyst via atomic layer deposition for selective oxidation of benzyl alcohol*. *Journal of Catalysis*, 2015. **324**: p. 59-68.
244. Leus, K., et al., *Atomic layer deposition of Pt nanoparticles within the cages of MIL-101: A mild and recyclable hydrogenation catalyst*. *Nanomaterials*, 2016. **6**(3): p. 45.
245. Dasgupta, N.P., et al., *Atomic layer deposition of platinum catalysts on nanowire surfaces for photoelectrochemical water reduction*. *Journal of the American Chemical Society*, 2013. **135**(35): p. 12932-12935.
246. Minjauw, M.M., et al., *Atomic layer deposition of ruthenium at 100° C using the RuO 4-precursor and H 2*. *Journal of Materials Chemistry C*, 2015. **3**(1): p. 132-137.
247. Ramachandran, R.K., et al., *Atomic Layer Deposition Route To Tailor Nanoalloys of Noble and Non-noble Metals*. *ACS nano*, 2016. **10**(9): p. 8770-8777.
248. Griffiths, M.B., et al., *Atomic layer deposition of gold metal*. *Chemistry of Materials*, 2015. **28**(1): p. 44-46.
249. Mäkelä, M., et al., *Potential gold (I) precursors evaluated for atomic layer deposition*. *Journal of Vacuum Science & Technology A: Vacuum, Surfaces, and Films*, 2017. **35**(1): p. 01B112.
250. Hämäläinen, J., M. Ritala, and M. Leskelä, *Atomic layer deposition of noble metals and their oxides*. *Chemistry of Materials*, 2013. **26**(1): p. 786-801.
251. Muñoz-Rojas, D. and J. MacManus-Driscoll, *Spatial atmospheric atomic layer deposition: a new laboratory and industrial tool for low-cost photovoltaics*. *Materials Horizons*, 2014. **1**(3): p. 314-320.
252. Van Delft, J., D. Garcia-Alonso, and W. Kessels, *Atomic layer deposition for photovoltaics: applications and prospects for solar cell manufacturing*. *Semiconductor Science and Technology*, 2012. **27**(7): p. 074002.

253. Palmstrom, A.F., P.K. Santra, and S.F. Bent, *Atomic layer deposition in nanostructured photovoltaics: tuning optical, electronic and surface properties*. *Nanoscale*, 2015. **7**(29): p. 12266-12283.
254. Macco, B., et al. *Status and prospects for atomic layer deposited metal oxide thin films in passivating contacts for c-Si photovoltaics*. in *Photovoltaic Specialists Conference (PVSC), 2016 IEEE 43rd*. 2016. IEEE.
255. Bhardwaj, N. and S.C. Kundu, *Electrospinning: a fascinating fiber fabrication technique*. *Biotechnology advances*, 2010. **28**(3): p. 325-347.
256. Shi, Y., et al., *Electrospun polyacrylonitrile nanofibers loaded with silver nanoparticles by silver mirror reaction*. *Materials Science and Engineering: C*, 2015. **51**: p. 346-355.
257. Mikhael, B., et al., *New silicon architectures by gold-assisted chemical etching*. *ACS applied materials & interfaces*, 2011. **3**(10): p. 3866-3873.
258. Huang, Z., et al., *Metal-assisted chemical etching of silicon: a review*. *Advanced materials*, 2011. **23**(2): p. 285-308.
259. Deckman, H. and J. Dunsmuir, *Natural lithography*. *Applied Physics Letters*, 1982. **41**(4): p. 377-379.
260. Sakamoto, S., et al., *Ordered hexagonal array of Au nanodots on Si substrate based on colloidal crystal templating*. *Nanotechnology*, 2008. **19**(40).
261. Bechelany, M., et al., *Extended domains of organized nanorings of silver grains as surface-enhanced Raman scattering sensors for molecular detection*. *Nanotechnology*, 2009. **20**(45).
262. Wünsch, J.R., *Polystyrene: Synthesis, production and applications*. Vol. 112. 2000: iSmithers Rapra Publishing.
263. Velev, O. and E. Kaler, *In situ assembly of colloidal particles into miniaturized biosensors*. *Langmuir*, 1999. **15**(11): p. 3693-3698.
264. Rogach, A., et al., *Nano-and Microengineering: 3-D Colloidal Photonic Crystals Prepared from Sub- μm -sized Polystyrene Latex Spheres Pre-Coated with Luminescent Polyelectrolyte/Nanocrystal Shells*. *Advanced Materials*, 2000. **12**(5): p. 333-337.
265. Boal, A.K., et al., *Self-assembly of nanoparticles into structured spherical and network aggregates*. *Nature*, 2000. **404**(6779): p. 746-748.
266. Florence, A.T., *Issues in oral nanoparticle drug carrier uptake and targeting*. *Journal of drug targeting*, 2004. **12**(2): p. 65-70.
267. Mallon, C.T., et al., *Protein nanopatterning and release from gold nano-cavity arrays*. *Chemical Communications*, 2010. **46**(1): p. 106-108.

268. Wang, C., F.L. Yap, and Y. Zhang, *Micropatterning of polystyrene nanoparticles and its bioapplications*. Colloids and Surfaces B-Biointerfaces, 2005. **46**(4): p. 255-260.
269. Taylor, Z.R., et al., *Independently Controlling Protein Dot Size and Spacing in Particle Lithography*. Langmuir, 2012. **28**(25): p. 9656-9663.
270. Balme, S., et al., *Influence of adsorption on proteins and amyloids detection by silicon nitride nanopore*. Langmuir, 2016. **accepted**.
271. Balme, S., et al., *Potentialities of confocal fluorescence for investigating protein adsorption on mica and in ultrafiltration membranes*. Journal of Membrane Science, 2006. **284**(1-2): p. 198-204.
272. Washburn, A.L., et al., *Quantitative, label-free detection of five protein biomarkers using multiplexed arrays of silicon photonic microring resonators*. Analytical chemistry, 2009. **82**(1): p. 69-72.
273. Bog, U., et al., *Densely Packed Microgoblet Laser Pairs for Cross-Referenced Biomolecular Detection*. Advanced Science, 2015. **2**(10).
274. Hamming, L.M. and P.B. Messersmith, *Fouling resistant biomimetic poly (ethylene glycol) based grafted polymer coatings*. Mater. Matters, 2008. **3**: p. 52.
275. Soteropoulos, C.E., et al., *Tailoring the protein adsorption properties of whispering gallery mode optical biosensors*. Langmuir, 2012. **28**(44): p. 15743-15750.
276. Obermeier, B., et al., *Multifunctional poly (ethylene glycol) s*. Angewandte Chemie International Edition, 2011. **50**(35): p. 7988-7997.
277. Uchida, K., et al., *A reactive poly (ethylene glycol) layer to achieve specific surface plasmon resonance sensing with a high S/N ratio: the substantial role of a short underbrushed PEG layer in minimizing nonspecific adsorption*. Analytical chemistry, 2005. **77**(4): p. 1075-1080.
278. Zalipsky, S. and J. Milton Harris. *Introduction to chemistry and biological applications of poly (ethylene glycol)*. in ACS Symposium Series. 1997. American Chemical Society.
279. Chapman, R.G., et al., *Surveying for surfaces that resist the adsorption of proteins*. Journal of the American Chemical Society, 2000. **122**(34): p. 8303-8304.
280. Ma, H., et al., *"Non-Fouling" Oligo (ethylene glycol)-Functionalized Polymer Brushes Synthesized by Surface-Initiated Atom Transfer Radical Polymerization*. Advanced Materials, 2004. **16**(4): p. 338-341.
281. Ostuni, E., et al., *A survey of structure-property relationships of surfaces that resist the adsorption of protein*. Langmuir, 2001. **17**(18): p. 5605-5620.

282. Gudipati, C.S., et al., *The antifouling and fouling-release performance of hyperbranched fluoropolymer (HBFP)-poly (ethylene glycol)(PEG) composite coatings evaluated by adsorption of biomacromolecules and the green fouling alga ulva*. *Langmuir*, 2005. **21**(7): p. 3044-3053.
283. Aswal, D., et al., *Self assembled monolayers on silicon for molecular electronics*. *Analytica chimica acta*, 2006. **568**(1): p. 84-108.
284. Ulman, A., *Formation and structure of self-assembled monolayers*. *Chemical reviews*, 1996. **96**(4): p. 1533-1554.
285. Dubois, L.H. and R.G. Nuzzo, *Synthesis, structure, and properties of model organic surfaces*. *Annual review of physical chemistry*, 1992. **43**(1): p. 437-463.
286. Bain, C.D. and G.M. Whitesides, *Modeling organic surfaces with self-assembled monolayers*. *Angewandte Chemie International Edition in English*, 1989. **28**(4): p. 506-512.
287. Love, J.C., et al., *Self-assembled monolayers of thiolates on metals as a form of nanotechnology*. *Chemical reviews*, 2005. **105**(4): p. 1103-1170.
288. Bishop, A.R. and R.G. Nuzzo, *Self-assembled monolayers: Recent developments and applications*. *Current Opinion in Colloid & Interface Science*, 1996. **1**(1): p. 127-136.
289. Bain, C.D., et al., *Formation of monolayer films by the spontaneous assembly of organic thiols from solution onto gold*. *Journal of the American Chemical Society*, 1989. **111**(1): p. 321-335.
290. Mikhael, B., et al., *New silicon architectures by gold-assisted chemical etching*. *ACS Applied Materials & Interfaces*, 2011. **3**(10): p. 3866-3873.
291. Rybczynski, J., M. Hilgendorff, and M. Giersig, *Nanosphere lithography—Fabrication of various periodic magnetic particle arrays using versatile nanosphere masks*, in *Low-Dimensional Systems: Theory, Preparation, and Some Applications*. 2003, Springer. p. 163-172.
292. Danov, K.D., B. Pouligny, and P.A. Kralchevsky, *Capillary forces between colloidal particles confined in a liquid film: the finite-meniscus problem*. *Langmuir*, 2001. **17**(21): p. 6599-6609.
293. Goszczynski, D.E., *Complete genome sequence of a natural mutant of grapevine virus A (GVA)*. *Archives of Virology*, 2014. **159**(9): p. 2523-2528.
294. Du Preez, J., et al., *The grapevine-infecting vitiviruses, with particular reference to grapevine virus A*. *Archives of Virology*, 2011. **156**(9): p. 1495-1503.

295. Mediterr, P., *Molecular characterization of Grapevine virus A isolates from Jordan*. *Phytopathol. Mediterr*, 2007. **46**: p. 195-200.
296. Tereshchenko, A., et al., *Optical Biosensors Based on ZnO Nanostructures: Advantages and Perspectives. A Review*. *Sensors and Actuators B: Chemical*, 2016.
297. Yakimova, R., et al., *ZnO materials and surface tailoring for biosensing*. *Frontiers in bioscience (Elite edition)*, 2012. **4**(1): p. 254-278.
298. Iyer, M.A., et al., *Scanning fluorescence-based ultrasensitive detection of dengue viral DNA on ZnO thin films*. *Sensors and Actuators B: Chemical*, 2014. **202**: p. 1338-1348.
299. Shukla, S., N.K. Sharma, and V. Sajal, *Sensitivity enhancement of a surface plasmon resonance based fiber optic sensor using ZnO thin film: a theoretical study*. *Sensors and Actuators B: Chemical*, 2015. **206**: p. 463-470.
300. Kang, Z., et al., *Enhanced photoelectrochemical property of ZnO nanorods array synthesized on reduced graphene oxide for self-powered biosensing application*. *Biosensors and Bioelectronics*, 2015. **64**: p. 499-504.
301. Picciolini, S., et al., *Branched gold nanoparticles on ZnO 3D architecture as biomedical SERS sensors*. *RSC Advances*, 2015. **5**(113): p. 93644-93651.
302. Politi, J., et al., *Versatile synthesis of ZnO nanowires for quantitative optical sensing of molecular biorecognition*. *Sensors and Actuators B: Chemical*, 2015. **220**: p. 705-711.
303. Elhag, S., et al., *Habit-modifying additives and their morphological consequences on photoluminescence and glucose sensing properties of ZnO nanostructures, grown via aqueous chemical synthesis*. *Vacuum*, 2015. **116**: p. 21-26.
304. Sodzel, D., et al., *Continuous sensing of hydrogen peroxide and glucose via quenching of the UV and visible luminescence of ZnO nanoparticles*. *Microchimica Acta*, 2015. **182**(9-10): p. 1819-1826.
305. Viter, R., et al., *Application of room temperature photoluminescence from ZnO nanorods for salmonella detection*. *Sensors Journal, IEEE*, 2014. **14**(6): p. 2028-2034.
306. Viter, R., et al., *The influence of localized plasmons on the optical properties of Au/ZnO nanostructures*. *Journal of Materials Chemistry C*, 2015. **3**(26): p. 6815-6821.
307. Bechelany, M., S. Balme, and P. Miele, *Atomic layer deposition of biobased nanostructured interfaces for energy, environmental and health applications*. *Pure and Applied Chemistry*, 2015. **87**(8): p. 751-758.
308. Viter, R., et al., *Enhancement of Electronic and Optical Properties of ZnO/Al₂O₃ Nanolaminate Coated Electrospun Nanofibers*. *The Journal of Physical Chemistry C*, 2016. **120**(9): p. 5124-5132.

309. Viter, R., et al., *Novel Immune TiO₂ Photoluminescence Biosensors for Leucosis Detection*. Procedia Engineering, 2012. **47**: p. 338-341.
310. Politi, J., et al. *Photoluminescence characterization of ZnO nanowires functionalization*. in *SPIE Optics+ Optoelectronics*. 2015. International Society for Optics and Photonics.
311. Yan, X., et al., *Detection of HCG-antigen based on enhanced photoluminescence of hierarchical ZnO arrays*. Colloids and Surfaces B: Biointerfaces, 2012. **89**: p. 86-92.
312. Dumcenco, D., et al., *Photoluminescence characterization of vertically aligned ZnO microrods*. Journal of Luminescence, 2012. **132**(8): p. 1890-1895.
313. Zhao, Y. and Y. Jiang, *Investigation of room temperature UV emission of ZnO films with different defect densities induced by laser irradiation*. Spectrochimica Acta Part A: Molecular and Biomolecular Spectroscopy, 2010. **76**(3): p. 336-340.
314. Wang, J., et al., *Gas phase growth of wurtzite ZnS nanobelts on a large scale*. Journal of Nanomaterials, 2013. **2013**: p. 1.
315. Ramanavicius, A., et al., *Stabilization of (CdSe) ZnS quantum dots with polypyrrole formed by UV/VIS irradiation initiated polymerization*. Journal of Nanoscience and Nanotechnology, 2009. **9**(3): p. 1909-1915.
316. Balevicius, Z., et al., *Evaluation of intact-and fragmented-antibody based immunosensors by total internal reflection ellipsometry*. Sensors and Actuators B: Chemical, 2011. **160**(1): p. 555-562.
317. Baniukevic, J., et al., *Application of oriented and random antibody immobilization methods in immunosensor design*. Sensors and Actuators B: Chemical, 2013. **189**: p. 217-223.
318. Baleviciute, I., et al., *Study of antibody/antigen binding kinetics by total internal reflection ellipsometry*. Biosensors and Bioelectronics, 2013. **39**(1): p. 170-176.
319. Makaraviciute, A., et al., *Antibody fragment immobilization on planar gold and gold nanoparticle modified quartz crystal microbalance with dissipation sensor surfaces for immunosensor applications*. Analytical Methods, 2014. **6**(7): p. 2134-2140.
320. Baniukevic, J., et al., *Magnetic gold nanoparticles in SERS-based sandwich immunoassay for antigen detection by well oriented antibodies*. Biosensors and Bioelectronics, 2013. **43**: p. 281-288.
321. Kausaite-Minkstimiene, A., et al., *A surface plasmon resonance immunosensor for human growth hormone based on fragmented antibodies*. Analytical Methods, 2013. **5**(18): p. 4757-4763.

322. Peng, K.-Q., et al., *Silicon nanowires for advanced energy conversion and storage*. Nano Today, 2013. **8**(1): p. 75-97.
323. Cui, Y., et al., *High Performance Silicon Nanowire Field Effect Transistors*. Nano Letters, 2003. **3**(2): p. 149-152.
324. Goldberger, J., et al., *Silicon Vertically Integrated Nanowire Field Effect Transistors*. Nano Letters, 2006. **6**(5): p. 973-977.
325. Chen, L.J., *Silicon nanowires: the key building block for future electronic devices*. Journal of Materials Chemistry, 2007. **17**(44): p. 4639-4643.
326. Cui, L.-F., et al., *Crystalline-Amorphous Core–Shell Silicon Nanowires for High Capacity and High Current Battery Electrodes*. Nano Letters, 2009. **9**(1): p. 491-495.
327. Pavlenko, M., et al., *Enhancement of optical and mechanical properties of Si nanopillars by ALD TiO₂ coating*. RSC Advances, 2016. **6**(99): p. 97070-97076.
328. Hochbaum, A.I., et al., *Enhanced thermoelectric performance of rough silicon nanowires*. Nature, 2008. **451**(7175): p. 163-167.
329. Abramson, A.R., et al., *Fabrication and characterization of a nanowire/polymer-based nanocomposite for a prototype thermoelectric device*. Journal of Microelectromechanical Systems, 2004. **13**(3): p. 505-513.
330. Boukai, A.I., et al., *Silicon nanowires as efficient thermoelectric materials*. Nature, 2008. **451**(7175): p. 168-171.
331. Cui, Y., et al., *Nanowire Nanosensors for Highly Sensitive and Selective Detection of Biological and Chemical Species*. Science, 2001. **293**(5533): p. 1289-1292.
332. Kim, D.R. and X. Zheng, *Numerical characterization and optimization of the microfluidics for nanowire biosensors*. Nano letters, 2008. **8**(10): p. 3233-3237.
333. Patolsky, F., G. Zheng, and C.M. Lieber, *Nanowire-Based Biosensors*. Analytical Chemistry, 2006. **78**(13): p. 4260-4269.
334. Bae, T.-E., et al., *High Performance of Silicon Nanowire-Based Biosensors using a High-k Stacked Sensing Thin Film*. ACS applied materials & interfaces, 2013. **5**(11): p. 5214-5218.
335. Treuting, R. and S. Arnold, *Orientation habits of metal whiskers*. Acta Metallurgica, 1957. **5**(10): p. 598.
336. Wagner, R.S. and W.C. Ellis, *VAPOR-LIQUID-SOLID MECHANISM OF SINGLE CRYSTAL GROWTH*. Applied Physics Letters, 1964. **4**(5): p. 89-90.
337. Peng, K.-Q., et al., *Synthesis of large-area silicon nanowire arrays via self-assembling nanoelectrochemistry*. Advanced Materials, 2002. **14**(16): p. 1164.

338. Lerose, D., et al., *Ordered arrays of epitaxial silicon nanowires produced by nanosphere lithography and chemical vapor deposition*. Journal of Crystal Growth, 2010. **312**(20): p. 2887-2891.
339. Fukata, N., et al., *Synthesis of silicon nanowires using laser ablation method and their manipulation by electron beam*. Science and Technology of Advanced Materials, 2005. **6**(6): p. 628-632.
340. Fuhrmann, B., et al., *Ordered Arrays of Silicon Nanowires Produced by Nanosphere Lithography and Molecular Beam Epitaxy*. Nano Letters, 2005. **5**(12): p. 2524-2527.
341. Zhang, Y.J., W. Li, and K.J. Chen, *Application of two-dimensional polystyrene arrays in the fabrication of ordered silicon pillars*. Journal of Alloys and Compounds, 2008. **450**(1-2): p. 512-516.
342. Park, N.-M. and C.-J. Choi, *Growth of silicon nanowires in aqueous solution under atmospheric pressure*. Nano Research, 2014. **7**(6): p. 898-902.
343. Pavlenko, M., et al., *Enhancement of optical and mechanical properties of Si nanopillars by ALD TiO₂ coating*. RSC Advances, 2016. **6**(99): p. 97070-97076.
344. Han, H., Z. Huang, and W. Lee, *Metal-assisted chemical etching of silicon and nanotechnology applications*. Nano Today, 2014. **9**(3): p. 271-304.
345. Geyer, N., et al., *Influence of the doping level on the porosity of silicon nanowires prepared by metal-assisted chemical etching*. Nanotechnology, 2015. **26**(24): p. 245301.
346. Colson, P., C. Henrist, and R. Cloots, *Nanosphere lithography: a powerful method for the controlled manufacturing of nanomaterials*. Journal of Nanomaterials, 2013. **2013**: p. 21.
347. AKINOGLU, E.M., A.J. MORFA, and M. GIERSIG, *Nanosphere lithography-exploiting self-assembly on the nanoscale for sophisticated nanostructure fabrication*. Turkish Journal of Physics, 2014. **38**(3): p. 563-572.
348. Bechelany, M., et al., *ZnO nanotubes by template-assisted sol-gel route*. Journal of Nanoparticle Research, 2012. **14**(8): p. 1-7.
349. Özgür, Ü., et al., *A comprehensive review of ZnO materials and devices*. Journal of Applied Physics, 2005. **98**(4): p. 041301.
350. Roman, V., et al., *Tuning of ZnO 1D nanostructures by atomic layer deposition and electrospinning for optical gas sensor applications*. Nanotechnology, 2015. **26**(10): p. 105501.
351. Iatsunskiy, I., et al., *Atomic layer deposition TiO₂ coated porous silicon surface: Structural characterization and morphological features*. Thin Solid Films, 2015. **589**: p. 303-308.

352. Zhang, Y., et al., *Ordered nanostructures array fabricated by nanosphere lithography*. Journal of Alloys and Compounds, 2008. **452**(2): p. 473-477.
353. Kralchevsky, P.A. and K. Nagayama, *Capillary forces between colloidal particles*. Langmuir, 1994. **10**(1): p. 23-36.
354. Danov, K.D., B. Pouligny, and P.A. Kralchevsky, *Capillary Forces between Colloidal Particles Confined in a Liquid Film: The Finite-Meniscus Problem*. Langmuir, 2001. **17**(21): p. 6599-6609.
355. Shinde, S.S. and S. Park, *Oriented colloidal-crystal thin films of polystyrene spheres via spin coating*. Journal of Semiconductors, 2015. **36**(2): p. 023001.
356. Iatsunskiy, I., et al., *Study on Structural, Mechanical, and Optical Properties of Al₂O₃-TiO₂ Nanolaminates Prepared by Atomic Layer Deposition*. The Journal of Physical Chemistry C, 2015. **119**(35): p. 20591-20599.
357. Chaaya, A.A., et al., *Optical and structural properties of Al₂O₃/ZnO nanolaminates deposited by ALD method*. Physica status solidi (c), 2014. **11**(9-10): p. 1505-1508.
358. Dawood, M., et al., *Interference lithographically defined and catalytically etched, large-area silicon nanocones from nanowires*. Nanotechnology, 2010. **21**(20): p. 205305.
359. Pal, B. and P.K. Giri, *Defect Mediated Magnetic Interaction and High T_c Ferromagnetism in Co Doped ZnO Nanoparticles*. Journal of Nanoscience and Nanotechnology, 2011. **11**(10): p. 9167-9174.
360. Mohan Kumar, G., et al., *Magnetic and optical property studies on controlled low-temperature fabricated one-dimensional Cr doped ZnO nanorods*. CrystEngComm, 2010. **12**(6): p. 1887-1892.
361. Kuriakose, S., B. Satpati, and S. Mohapatra, *Enhanced photocatalytic activity of Co doped ZnO nanodisks and nanorods prepared by a facile wet chemical method*. Physical Chemistry Chemical Physics, 2014. **16**(25): p. 12741-12749.
362. Iatsunskiy, I., et al., *One and two-phonon Raman scattering from nanostructured silicon*. Optik - International Journal for Light and Electron Optics, 2015. **126**(18): p. 1650-1655.
363. Yang, Q., et al., *Size effect on morphology and optical properties of branched ZnO/Si nanowire arrays*. Physics Letters A, 2016. **380**(9): p. 1044-1048.
364. Banerjee, P., et al., *Structural, electrical, and optical properties of atomic layer deposition Al-doped ZnO films*. Journal of Applied Physics, 2010. **108**(4): p. 043504.
365. Kayaci, F., et al., *Polymer-inorganic core-shell nanofibers by electrospinning and atomic layer deposition: Flexible nylon-ZnO core-shell nanofiber mats and their photocatalytic activity*. ACS applied materials & interfaces, 2012. **4**(11): p. 6185-6194.

366. Kemnade, N., et al., *Non-destructive functionalisation for atomic layer deposition of metal oxides on carbon nanotubes: effect of linking agents and defects*. *Nanoscale*, 2015. **7**(7): p. 3028-3034.
367. Lin, Y.-H., et al., *Atomic layer deposition of zinc oxide on multiwalled carbon nanotubes for UV photodetector applications*. *Journal of The Electrochemical Society*, 2011. **158**(2): p. K24-K27.
368. Oldham, C.J., et al., *(Invited) Atomic Layer Deposition on Polymers: Applications to Physical Encapsulation of Electrospun Nylon Nanofibers*. *ECS Transactions*, 2010. **33**(2): p. 279-290.
369. Stano, K.L., et al., *Conformal atomic layer deposition of alumina on millimeter tall, vertically-aligned carbon nanotube arrays*. *ACS applied materials & interfaces*, 2014. **6**(21): p. 19135-19143.
370. Ismaila, A.F., A. Mustafa, and M.S.A. Rahaman, *Effect of Blending Temperature on the Characteristics of Modified Polyacrylonitrie Homopolymer*. *Modern Applied Science*, 2008. **2**(2): p. 131.
371. Zacharias, M. and P. Streitenberger. *Crystallization in the limit of ultra thin layers-A new crystallization model*. in *MRS Proceedings*. 2000. Cambridge Univ Press.
372. Iatsunskiy, I., et al., *Structural and XPS studies of PSi/TiO₂ nanocomposites prepared by ALD and Ag-assisted chemical etching*. *Applied Surface Science*, 2015. **347**: p. 777-783.
373. Wagner, C.D. and G. Muilenberg, *Handbook of X-ray photoelectron spectroscopy*. 1979: Perkin-Elmer.
374. Mosquera, A.A., et al., *Exciton and core-level electron confinement effects in transparent ZnO thin films*. *Scientific reports*, 2013. **3**.
375. Das, J., et al., *Micro-Raman and XPS studies of pure ZnO ceramics*. *Physica B: Condensed Matter*, 2010. **405**(10): p. 2492-2497.
376. De la Rosa, E., et al., *Controlling the growth and luminescence properties of well-faceted ZnO nanorods*. *The Journal of Physical Chemistry C*, 2007. **111**(24): p. 8489-8495.
377. Wang, H., et al., *Microstructural and optical characteristics of solution-grown Ga-doped ZnO nanorod arrays*. *Nanotechnology*, 2008. **19**(7): p. 075607.
378. Wang, H. and C. Xie, *The effects of oxygen partial pressure on the microstructures and photocatalytic property of ZnO nanoparticles*. *Physica E: Low-dimensional Systems and Nanostructures*, 2008. **40**(8): p. 2724-2729.

379. Kovalev, A.I., et al., *Size shift of XPS lines observed from PbS nanocrystals*. Surface and Interface Analysis, 2010. **42**(6-7): p. 850-854.
380. Sharma, A., et al., *Effect of surface groups on the luminescence property of ZnO nanoparticles synthesized by sol-gel route*. Surface Science, 2012. **606**(3): p. L13-L17.
381. Zhang, X., et al., *Effect of aspect ratio and surface defects on the photocatalytic activity of ZnO nanorods*. Scientific reports, 2014. **4**: p. 4596.
382. Nichols, M., et al., *Measurement of bandgap energies in low-k organosilicates*. Journal of Applied Physics, 2014. **115**(9): p. 094105.
383. Ozawa, K.-i., et al., *Angle-resolved photoelectron spectroscopy study of the anion-derived dangling-bond band on ZnO (101⁻ 0)*. Physical Review B, 2003. **68**(12): p. 125417.
384. Ren, J., et al., *High-density NiSi nanocrystals embedded in Al₂O₃/SiO₂ double-barrier for robust retention of nonvolatile memory*. Solid-State Electronics, 2012. **67**(1): p. 23-26.
385. Maragliano, C., et al., *Quantifying charge carrier concentration in ZnO thin films by Scanning Kelvin Probe Microscopy*. Scientific reports, 2014. **4**: p. 4203.
386. Medvedev, D.A., et al., *Characterization of electron donor sites on Al₂O₃ surface*. Physical Chemistry Chemical Physics, 2012. **14**(8): p. 2587-2598.
387. Liao, Z.-M., et al., *Surface effects on photoluminescence of single ZnO nanowires*. Physics Letters A, 2008. **372**(24): p. 4505-4509.
388. Lin, Y.-J. and C.-L. Tsai, *Changes in surface band bending, surface work function, and sheet resistance of undoped ZnO films due to (NH₄)₂Sx treatment*. Journal of applied physics, 2006. **100**(11): p. 113721.
389. Schlesinger, R., et al., *Controlling the work function of ZnO and the energy-level alignment at the interface to organic semiconductors with a molecular electron acceptor*. Physical Review B, 2013. **87**(15): p. 155311.
390. Kumar, S., et al., *Investigations on structural and optical properties of ZnO and ZnO: Co nanoparticles under dense electronic excitations*. RSC Advances, 2014. **4**(107): p. 62123-62131.
391. Sadewasser, S., et al., *Kelvin probe force microscopy for the nano scale characterization of chalcopyrite solar cell materials and devices*. Thin Solid Films, 2003. **431**: p. 257-261.
392. Jiang, C.-S., et al., *Local built-in potential on grain boundary of Cu (In, Ga) Se₂ thin films*. Applied physics letters, 2004. **84**(18): p. 3477-3479.